NASA/TM–2012-217337

Flight Tests of the Turbulence Prediction and Warning System (TPAWS)

David W. Hamilton, Fred H. Proctor, and Nash'at N. Ahmad
Langley Research Center, Hampton, Virginia

February 2012

NASA STI Program . . . in Profile

Since its founding, NASA has been dedicated to the advancement of aeronautics and space science. The NASA scientific and technical information (STI) program plays a key part in helping NASA maintain this important role.

The NASA STI program operates under the auspices of the Agency Chief Information Officer. It collects, organizes, provides for archiving, and disseminates NASA's STI. The NASA STI program provides access to the NASA Aeronautics and Space Database and its public interface, the NASA Technical Report Server, thus providing one of the largest collections of aeronautical and space science STI in the world. Results are published in both non-NASA channels and by NASA in the NASA STI Report Series, which includes the following report types:

- TECHNICAL PUBLICATION. Reports of completed research or a major significant phase of research that present the results of NASA programs and include extensive data or theoretical analysis. Includes compilations of significant scientific and technical data and information deemed to be of continuing reference value. NASA counterpart of peer-reviewed formal professional papers, but having less stringent limitations on manuscript length and extent of graphic presentations.

- TECHNICAL MEMORANDUM. Scientific and technical findings that are preliminary or of specialized interest, e.g., quick release reports, working papers, and bibliographies that contain minimal annotation. Does not contain extensive analysis.

- CONTRACTOR REPORT. Scientific and technical findings by NASA-sponsored contractors and grantees.

- CONFERENCE PUBLICATION. Collected papers from scientific and technical conferences, symposia, seminars, or other meetings sponsored or co-sponsored by NASA.

- SPECIAL PUBLICATION. Scientific, technical, or historical information from NASA programs, projects, and missions, often concerned with subjects having substantial public interest.

- TECHNICAL TRANSLATION. English-language translations of foreign scientific and technical material pertinent to NASA's mission.

Specialized services also include creating custom thesauri, building customized databases, and organizing and publishing research results.

For more information about the NASA STI program, see the following:

- Access the NASA STI program home page at *http://www.sti.nasa.gov*

- E-mail your question via the Internet to help@sti.nasa.gov

- Fax your question to the NASA STI Help Desk at 443-757-5803

- Phone the NASA STI Help Desk at 443-757-5802

- Write to:
  NASA STI Help Desk
  NASA Center for AeroSpace Information
  7115 Standard Drive
  Hanover, MD 21076-1320

NASA/TM–2012-217337

Flight Tests of the Turbulence Prediction and Warning System (TPAWS)

David W. Hamilton, Fred H. Proctor, and Nash'at N. Ahmad
Langley Research Center, Hampton, Virginia

National Aeronautics and
Space Administration

Langley Research Center
Hampton, Virginia 23681-2199

February 2012

Available from:

NASA Center for AeroSpace Information
7115 Standard Drive
Hanover, MD 21076-1320
443-757-5802

Contents

List of Acronyms and Abbreviations

AGL	Above Ground Level
ARIES	Airborne Research Integrated Experiments System
ATC	Air Traffic Control
ATDS	Airborne Turbulence Detection System
AvSSP	NASA's Aviation Safety and Security Program
CAT	Clear Air Turbulence
CIT	Convection Induced Turbulence
DAL	Delta Air Lines
FAA	Federal Aviation Administration
FOQA	Flight Operations Quality Assurance
FSL	Forecast Systems Lab
FY	Fiscal Year
GOES	Geostationary Operational Environmental Satellite
ICAO	International Civil Aviation Organization
IMC	Instrument Meteorological Conditions
IR	Infrared
LI	Lifted Index
MAPS	Mesoscale Analysis and Prediction System
MASS	Mesoscale Atmospheric Simulation System
MCC	Mesoscale Convective Complex
MoG	Moderate or Greater turbulence
MSL	Mean Sea Level
NAR	Nuisance Alarm Rate
NASA	National Aeronautics and Space Administration
NCAR	National Center for Atmospheric Research
NCDC	National Climate Data Center
NCEP	National Centers for Environmental Prediction
NCSU	North Carolina State University
NEXRAD	NEXt Generation RADar
NOAA	National Oceanic and Atmospheric Administration
NTSB	National Transportation Safety Board
PIREPS	Pilot Reports
POD	Probability of Detection
PPI	Plan-Position Indicator
PWS	Predictive Wind Shear
RADAR	Radio Detection and Ranging
RRF	Radar Reflectivity Factor
RMS	Root Mean Square
RUC	Rapid Update Cycle
TAS	True Air Speed
TPAWS	Turbulence Prediction And Warning System
UAL	United Air Lines
UTC	Coordinated Universal Time
VMC	Visual Meteorological Conditions
WSR	Weather Surveillance Radar
WxAP	NASA's Weather Accident and Prevention Project

Abstract

Flight tests of the National Aeronautics and Space Administration's Turbulence Prediction And Warning System (TPAWS) were conducted in the Fall of 2000 and Spring of 2002. TPAWS is a radar-based airborne turbulence detection system. During twelve flights, NASA's B-757 tallied 53 encounters with convectively induced turbulence. Analysis of data collected during 49 encounters in the Spring of 2002 showed that the TPAWS Airborne Turbulence Detection System (ATDS) successfully detected 80% of the events at least 30 seconds prior to the encounter, achieving FAA recommended performance criteria. Details of the flights, the prevailing weather conditions, and each of the turbulence events are presented in this report. Sensor and environmental characterizations are also provided.

1. Introduction

Aircraft encounters with turbulence are the leading cause of in-flight injuries (Tvaryanas 2003) and have occasionally resulted in passenger and crew fatalities. Most of these injuries are caused by sudden and unexpected encounters with severe turbulence in and around convective activity (Kaplan et al. 2005). According to the NTSB (2011), in-flight turbulence encounters accounted for over one-third of all civil aviation accident events. Although damage to aircraft from these encounters is usually minimal, injuries and even fatalities can cost the airline industry millions of dollars per year (Kauffmann 2002). These costs are incurred from 1) crew and passenger injuries (including liability claims, worker's compensation, *etc.*), 2) aircraft inspections & maintenance, 3) delays, diversions & flight cancellation, as well as 4) intangibles like airline reputation and reliability, which are difficult to measure.

Convection Induced Turbulence (CIT) is turbulence generated in the presence of convective clouds. Although aircraft encounters with turbulence may occur in clear air, Kaplan et al. (2005) have found that approximately 82% of all turbulence accidents were in the vicinity of convection. Often these encounters occur within areas of low-level radar reflectivity, regions that may not be routinely avoided by flying aircraft. In some cases of CIT, the aircraft's conventional radar may not return any radar reflectivity signature.

Although aircraft attempt to avoid flying directly into thunderstorms, unanticipated encounters with CIT can occur. These encounters may happen as aircraft: 1) try to skirt around the high reflectivity regions associated with thunderstorms in order to minimize the deviation from their planned route, 2) encounter unexpected convection that appears to be invisible or benign on the aircraft's radar display, 3) encounter storm tops that rapidly rise into the aircraft's flight path, and 4) are inadvertently vectored into convection by Air Traffic Control (ATC). An extensive review of the literature describing the mechanisms for CIT can be found in Pantley (1989). In his thesis, Pantley classifies the types of CIT considered hazardous to aircraft as: 1) updrafts and downdrafts associated with deep cumulus convection, 2) rapidly growing thunderstorms that may go undetected by airborne weather radar, 3) Kelvin-Helmholtz instability induced by thunderstorm outflows along the tropopause, 4) turbulent vortices that form due to the breaking of convectively triggered atmospheric waves above and downwind of thunderstorms, and 5) turbulent wakes caused by barrier type effects around and in the lee of thunderstorms.

The use of ground-based radar for identifying CIT has been evaluated in previous studies (Press and Binckley 1948; Thompson and Lipscomb 1960; Doviak and Lee 1985). Doviak and Lee found agreement between the spectrum width from ground-based radar and aircraft *in situ* measurements of turbulence velocity, when the aircraft were within 1 *km* of the radar resolution volume. They also found that the spectrum width exceeded 5 *m/s* within regions of moderate or severe turbulence. However, the spectrum width calculations may not be accurate if the radar reflectivity is weak or if the event is at a range greater than 60 *km* from the radar (Brewster 1984). Detection is further hindered since small areas of turbulence may be transitory and only detectable at short ranges.

Current airborne radars with Predictive Wind Shear (PWS) capability offer new opportunities. An obvious benefit of the PWS radar is that being a part of the aircraft system, it can readily sense the atmosphere just ahead of the aircraft. Therefore, unlike the ground-based radar studied by Doviak and Lee (1985), immediate detection of turbulence can be made ahead of the aircraft. If turbulence detection is made from ground radar, the product is susceptible to shortcomings discussed by Brewster (1984). In addition, the product delivery will be delayed since it has to be uplinked to the aircraft.

Turbulence sensing with airborne PWS radar can utilize methods for extracting the first and second Doppler moments that provide detection and warning capabilities with high confidence (Cornman et al. 2000). Furthermore, Bowles and Buck (2009) have provided a technical basis for relating aircraft normal loads to this new PWS radar capability. They have developed hazard metrics and aircraft dependent reference tables that enable the calculation and estimation of aircraft loads consistent with the definitions of moderate and severe levels of encountered turbulence. Given these technical advancements, a large part of the Federal Aviation Administration (FAA) Part 121 fleet now has existing capability with onboard equipment to make confident turbulence detection and load predictions; thus providing warning either for preparation of an inadvertent encounter or for tactically avoiding the hazard.

Between 2001-2005, The National Aeronautics and Space Administration (NASA), under its Aviation Safety and Security Program and the Turbulence Prediction And Warning System (TPAWS) project element, began addressing turbulence hazards through research, flight experiments, and data analysis (Hamilton and Proctor 2002a, 2002b, 2003; Proctor et al. 2002a, 2002b). The primary focus of this program element was the characterization of turbulence and its environment, as well as the development and testing of hazard-estimation algorithms for both

radar and *in situ* detection. The ultimate goal was to develop an ATDS performance metering methodology for potential FAA certification of future turbulence alerting systems. In order to provide this support, NASA tested the turbulence detection algorithms in flight. NASA also developed a set of tools and metrics required for the certification process (*e.g.*, Hamilton and Proctor 2006a, 2006b). These tools include atmospheric data sets representing turbulence environments, aircraft dynamic load models, radar simulation systems, scoring algorithms, and cockpit display concepts. Atmospheric data sets continue to be generated for development and testing of airborne radar systems (Ahmad and Proctor 2011).

The ATDS enables detection of hazardous turbulence with standard airborne PWS Doppler radar and it provides flight crews timely and accurate load estimates prior to an encounter. The ATDS development was part of a mandated effort to reduce injuries associated with weather-related aviation accidents. The ATDS discussed in this report is designed to improve upon turbulence detection technology currently in use on commercial airliners, by alerting crews to potential encounters with CIT. The FAA has set performance goals for the proposed ATDS at 80% probability of detection and a false alarm rate of less than 10%. These goals apply to the alerting of airline crews of significant turbulence encounters when the radar reflectivity is greater than 15 *dBz* with a lead-time of 30-120 seconds. To meet these goals, candidate turbulence detection algorithms were tested on NASA Langley Research Center's B-757 research aircraft (Figure 1), referred hereafter as the Airborne Research Integrated Experiments System (ARIES) (Wusk 2002). The algorithms were installed on a standard airborne weather radar system and flown in environments conducive to CIT. The ATDS was designed to work in regions of CIT when sufficient levels of radar reflectivity were present to allow for detection. The ATDS utilized spectral moments obtained from the aircraft's PWS radar and converted them to aircraft-dependent load estimates. The first campaign tested an initial version of the ATDS and included two flights in the fall of 2000. An upgraded version of the ATDS was used during the second campaign, which consisted of 10 flights in the spring of 2002. During these twelve flights, ARIES tallied 53 encounters with CIT. Analysis of the events during the second campaign showed that the ATDS successfully detected 80% of the 49 total events at least 30 seconds prior to the encounter. This demonstrated that the ATDS met the FAA recommended performance criteria.

The intensity of the atmospheric turbulence can be characterized by many parameters (*e.g.*, turbulence kinetic energy, turbulence eddy dissipation rate, velocity variance, turbulence integral length scale, *etc*). However, 1) it is difficult to characterize atmospheric turbulence with the use of just one parameter and more importantly, 2) these parameters cannot be easily related to the influence that turbulence has on aircraft response (Proctor and Hamilton 2005). Quantification of the turbulence hazard must be related to the aircraft response, and should have properties that can be estimated by onboard detection sensors. The root mean square (RMS) of the normal load acceleration ($\sigma_{\Delta n}$) is a metric that represents the influence that atmospheric turbulence has on aircraft motions. Specifically, it is defined as:

$$\sigma_{\Delta n}(t) = \left[\frac{1}{\tau} \int_{t-\tau}^{t} [\Delta n(t') - \overline{\Delta n}(t)]^2 \, dt' \right]^{\frac{1}{2}}$$

where, Δn = aircraft's normal acceleration (in units of gravity), t = time, τ = size of shifting / sliding window (5 seconds has been chosen), and

$$\overline{\Delta n}(t) = \frac{1}{\tau} \int_{t-\tau}^{t} \Delta n(t') dt'$$

In the above equation, the *in situ* calculation of $\sigma_{\Delta n}$ is simple because it can be calculated directly from measurements provided by the aircraft accelerometers. Although this metric does not directly quantify the fluid characteristics of the atmospheric turbulence, it does define the airplane response to atmospheric turbulence. This metric is preferred because: 1) it is airplane centric, 2) it's easy to calculate, 3) it statistically quantifies the sharp bumps and accelerations that passengers feel when flying in an aircraft and 4) it's understood by the airplane operators (see appendix).

For a given turbulence event, the RMS of the normal load acceleration ($\sigma_{\Delta n}$) is strongly correlated with the peak normal load ($|\Delta n|$). This correlation is shown in Figure 2. Since the relationship of the peak normal load acceleration ($|\Delta n|$) with the root mean square of the normal load accelerations is known; the hazard levels can be assigned. The

turbulence metric thresholds are subjective, but for warning pilots and dispatchers they can be categorized as follows Bowles and Buck (2009):

$\sigma_{\Delta n} \le 0.1g$	*Light Turbulence*
$0.1g < \sigma_{\Delta n} \le 0.2g$	*Moderate Turbulence*
$0.2g \le \sigma_{\Delta n} < 0.3g$	*Moderate to Severe Turbulence*
$0.3g \le \sigma_{\Delta n} < 0.6g$	*Severe Turbulence*
$0.6g \le \sigma_{\Delta n}$	*Extreme Turbulence*

Note that all of the NTSB accident reconstructions shown in Figure 2 have values for $\sigma_{\Delta n}$ greater than $0.3g$ and for peak normal load ($|\Delta n|$) greater than $1g$. Turbulence encounter intensities with $\sigma_{\Delta n} > 0.30\ g$ are designated as "Severe" or "Extreme" and may cause passengers and heavy objects in the cabin to become weightless, an obviously dangerous situation.

Figure 1. NASA Langley Research Center's B-757 ARIES.

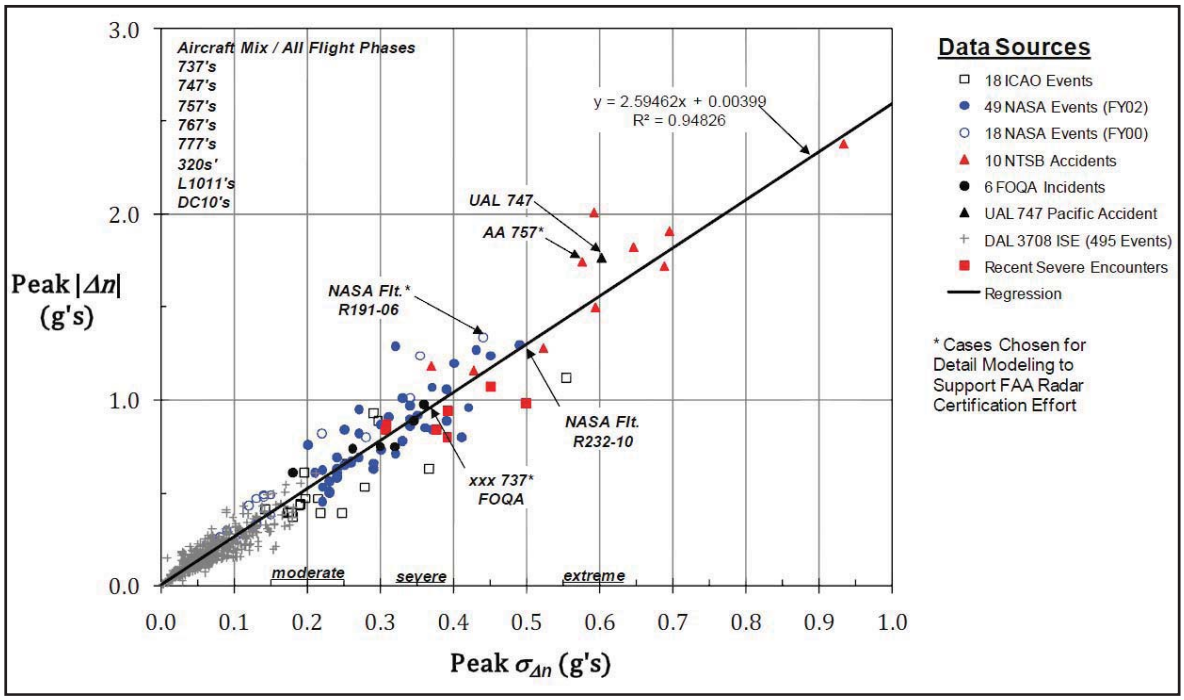

Figure 2. Relationship between the peak normal load (Δn) and the root mean square of normal load acceleration ($\sigma_{\Delta n}$) assuming a 5 second window. The dataset is constructed from measurements for 606 turbulence encounters. From Bowles and Buck (2009).

2. TPAWS Flight Experiment Summaries

Two flight campaigns were conducted by NASA to evaluate the ATDS and to determine if it could meet the FAA required performance criteria. The initial flight campaign was conducted during November and December of 2000, and the second set of flight experiments were performed during April and May of 2002. The ARIES aircraft, a B-757, was equipped with *in situ* sensors for wind, temperature and acceleration measurements (Robinson et al. 2000), and an airborne Doppler radar for forward-looking turbulence detection. The radar installed in ARIES was a Collins WXR-700 X-band radar system which is further discussed in Section 4.3.

The test procedure for the campaign was to identify regions likely to have CIT, then fly into those regions and make direct penetrations into areas of turbulence. During the flights, both radar and *in situ* data were collected for events ranging from light to severe turbulence. As a safety precaution, direct penetrations into regions with high radar reflectivity (RRF > 40 *dBz*) were purposefully avoided at all times during the flights. Commercial carriers also routinely avoid these regions, as well. Flight days for the NASA test were chosen based on the likelihood of CIT within flight range from the NASA Langley Research Center (Hampton, Virginia). The B-757 flight range included most of the southeastern United States. General locations favorable for CIT were chosen based on real-time weather predictions from various numerical weather prediction models. These models included the Forecast Systems Lab's (FSL) Rapid Update Cycle (RUC) and Mesoscale Analysis and Prediction System (MAPS) models (Benjamin 2000); and the National Center for Environmental Prediction's ETA model (Rogers et al. 1996; Nutter and Manobianco 1999). The Mesoscale Atmospheric Simulation System (MASS) developed by Kaplan et al. (2000) was also used to provide weather forecasts to support the flight experiments. The MASS model was run on a NASA workstation and it provided key indices for real-time turbulence prediction (Kaplan et al. 2006). The type of convection encountered during the flight deployments ranged from isolated to frontal convection, and was associated with squall lines, tropical systems, sea breeze fronts, mesoscale convective complexes, as well as "airmass" thunderstorms.

A detailed description (weather conditions, flight paths, *in situ* sensor data, satellite data, and airborne radar data) of the twelve days in which flights encountered hazardous turbulence are presented in this section. A summary of the key *in situ* parameters from 53 significant turbulence events is given in Table 1. Geostationary Operational Environmental Satellite (GOES-12) imagery was acquired from the Global Hydrology and Climate Center at NASA Marshall Space Flight Center in Huntsville, Alabama and the ground-based NEXRAD radar data (WSR-88D) were acquired from the National Climate Data Center (NCDC) in Asheville, North Carolina. The airborne radar data presented include flight level radar reflectivity and hazard predictions. In most events, the "hazard" predictions were derived from a three bar radar scan strategy (0°, -2°, and –4° tilts in a short pulse configuration) as described in Cornman et al. (2002). On occasion, this strategy was modified either by changing the tilt angles and/or changing the pulse length for research purposes. These modifications are delineated in each case; however, events with modified scan strategies were not included in the scoring analysis presented in Section 3. The wind recovery methods and load estimations from the *in situ* recorder are based on Robinson et al. (2000). The *in situ* turbulence measurements were quantified in terms of the peak normal load acceleration (Δn) and the RMS of the normal load acceleration, $\sigma_{\Delta n}$ (Robinson et al. 2000). An event was classified as significant turbulence if $\sigma_{\Delta n} \geq 0.2\ g$.

In general, the majority of the events were characterized by large horizontal gradients of vertical velocity associated with either rising cumulus plumes or sinking air within precipitation shafts. On a couple of occasions, moderate turbulence was experienced on the periphery of the convection. Durations of the encounters were usually brief; lasting several seconds to a minute, and coinciding with the time the aircraft was operating in the cloud. The values of radar reflectivity factor as derived from the ATDS radar were usually low, with peak values for each event ranging from 0 to 40 *dBz* (Table 1). When available, composite plots are presented that include colored intensity scans of the airborne radar reflectivity, radar predicted loads with overlays of the aircraft tracks with the *in situ* loads, and vectors representing the environmental winds experienced along the flight path.

Table 1: Summary of Significant Turbulence Events

Event	Altitude (*kft*)	Weight (*klbs*)	TAS (*m/s*)	Peak In Situ Turbulence (*g's*)			Peak Vertical Wind (ms^{-1})		Reflectivity (*dBz*)
				$\sigma_{\Delta n}$	Δn_{max}	Δn_{min}	Max	Min	
190-04	24	184.5	215	0.28	0.58	-0.8	12.15	-6.50	16
190-06	24	183.2	217	0.35	0.71	-1.24	11.18	-6.23	16
191-03	33	179.8	234	0.34	1.00	-0.90	9.32	-15.04	20
191-06	33	177.8	236	0.44	0.87	-1.4	18.41	-14.91	28
227-10*	23	171.3	210	0.22	0.37	-0.53	6.74	-2.57	18
228-04	27	182.3	225	0.41	0.63	-0.8	23.42	-4.41	10
228-06	25	181.1	215	0.26	0.66	-0.53	8.79	-10.28	30
228-09	25	179.6	216	0.21	0.47	-0.61	8.45	-4.69	19
228-10	25	178.6	215	0.33	0.56	-0.78	15.69	-5.28	32
228-11	25	177.7	215	0.32	0.65	-0.71	18.70	-2.20	30
228-12	25	176.7	214	0.4	0.7	-1.20	23.25	-4.59	30
229-05	25	179.4	219	0.23	0.51	-0.5	11.25	-7.15	32
230-02	16	192.0	192	0.25	0.4	-0.65	10.62	-6.42	10
230-04	15	188.8	186	0.29	0.63	-0.52	7.60	-10.98	8
230-06	15	187.8	185	0.35	0.92	-0.65	10.80	-12.97	0
230-08	15	187.6	187	0.24	0.63	-0.61	6.84	-12.98	8
230-10	17	186.8	193	0.27	0.95	-0.64	7.49	-9.44	32
230-12	17	186.4	193	0.30	0.73	-0.67	8.52	-11.72	21
230-15	24	183.4	213	0.34	0.86	-0.74	11.02	-7.09	20
230-19	24	181.5	213	0.37	1.02	-1.07	11.17	-12.03	28
230-20	24	180.9	214	0.33	0.71	-1.01	20.71	-4.62	32
230-21	24	180.4	212	0.35	0.65	-0.92	16.25	-6.07	22
230-23	24	179.3	211	0.42	0.79	-0.96	20.37	-14.94	40
230-24	24	178.8	212	0.24	0.47	-0.69	13.64	-4.73	16
231-04	27	186.5	225	0.24	0.61	-0.43	5.84	-5.75	24
231-08	27	184.9	224	0.24	0.58	-0.59	17.10	-3.51	32
231-10	27	184.1	224	0.25	0.61	-0.84	15.21	-3.39	22
231-12	31	180.7	237	0.24	0.58	-0.50	9.40	-5.84	16
232-03	31	182.9	238	0.3	0.69	-0.87	16.27	-8.14	20
232-04	31	182.1	238	0.31	0.91	-0.63	8.53	-8.71	6
232-05	31 to 35	181.2	227	0.26	0.67	-0.58	7.77	-8.31	4
232-06	35	179.5	236	0.27	0.62	-0.69	5.99	-12.72	2
232-08	35	178.6	235	0.27	0.82	-0.53	7.86	-8.83	8
232-10	35	177.3	235	0.45	1.24	-1.17	14.63	-21.42	22
233-01	28	188.3	227	0.32	1.29	-0.61	15.88	-7.60	22
233-04	17	176.9	194	0.23	0.48	-0.56	5.11	-5.67	4
233-05	17	176.5	194	0.23	0.56	-0.53	6.00	-3.13	10
233-06	17	175.9	195	0.25	0.57	-0.65	4.79	-7.73	18
233-07	17	174.9	193	0.39	0.89	-0.65	11.73	-7.10	22
233-09	17	172.7	194	0.24	0.58	-0.55	10.43	-5.92	16
234-05	25	180.0	219	0.20	0.76	-0.34	5.80	-3.16	13
234-06	25	179.0	218	0.43	1.27	-1.12	14.43	-9.36	22
234-09	25	175.4	219	0.29	0.65	-0.65	9.34	-7.17	16
234-11	25	174.1	220	0.34	0.97	-0.89	12.38	-8.86	24
234-12	25	173.5	218	0.34	0.86	-0.90	12.54	-7.71	22
235-02	26	179.6	224	0.23	0.43	-0.50	8.45	-4.33	22
235-03	24	178.7	216	0.36	0.81	-0.85	17.76	-7.39	32
235-05*	22 to 19	170.9	204	0.22	0.45	-0.39	11.07	-4.88	2
235-07*	19	169.4	201	0.22	0.46	-0.62	8.27	-3.04	24
235-08*	19	168.4	201	0.37	0.84	-1.14	14.18	-6.08	8
235-09*	19	167.7	200	0.23	0.51	-0.41	2.77	-10.99	8
240-03	29	181.7	235	0.39	0.96	-1.06	14.98	-2.35	4
240-09	25	179.4	218	0.49	1.30	-1.07	22.13	-2.09	32

* Events where the radar was in long pulse mode, and which are not included in radar scoring.

2.1: Flight 190, December 13, 2000

Between 1830 UTC and 1900 UTC on December 13, 2000, the ARIES investigated a thunderstorm complex near the Louisiana/Mississippi Gulf Coast (Figure 3 and Figure 4). During this time, the complex was rapidly organizing into a squall line that was oriented southwest to northeast. Eventually, the squall line prompted numerous severe weather warnings. A broad area of precipitation with embedded convective cells covered much of Louisiana. Early in the morning, pilot reports (PIREPS) of moderate turbulence were submitted over Louisiana in the vicinity of the rapidly building thunderstorms. Visual meteorological conditions prevailed at flight level in the region surrounding the complex (Figure 5).

In Figure 3, the flight path of Flight 190 is shown along with the NEXRAD radar composite from the Fort Polk, Louisiana station (KPOE). Several events with significant turbulence ($\sigma_{\Delta n} \geq 0.2$ *g*), were encountered during this flight and are marked in Figure 3. The peak turbulence levels associated with this flight are shown in Table 1. The turbulence encounters were associated with the penetration of convective turrets emanating from the stratiform cloud region that was present at lower elevations. These isolated turrets were located northwest of the large thunderstorm complex. Closer to the thunderstorm, the turrets became more numerous and had higher cloud tops due to greater local instability. Similarly, higher turbulence intensities were encountered in the turrets located closer to the main thunderstorm complex (Event 190-06). The precipitation encountered by ARIES was in the form of light snow and ice crystals as determined from external camcorders. This precipitation was detected from NEXRAD to have low-levels of radar reflectivity along the flight path (see Table 1). Large thunderstorms in the vicinity of this event had cloud tops up to 13.7 *km* (45 *kft*) MSL and generated extensive outflow anvils. Associated cloud turrets were ascending to various altitudes, depending on the intensity of the convection. The flight altitude during the data collection was between 7.3 *km* and 8.2 *km* (24 - 27 *kft*) MSL, which was well below the anvil outflow. Cell motion was towards the northeast at approximately 35 *m/s* (69 *kts*). The prevailing winds in the near storm environment were around 40 *m/s* (80 *kts*) from 240° from true North. ATDS data were not available for this case and were not included in the scoring of the airborne radar. Radar data from the KPOE NEXRAD were used to evaluate the radar reflectivity levels along the flight path.

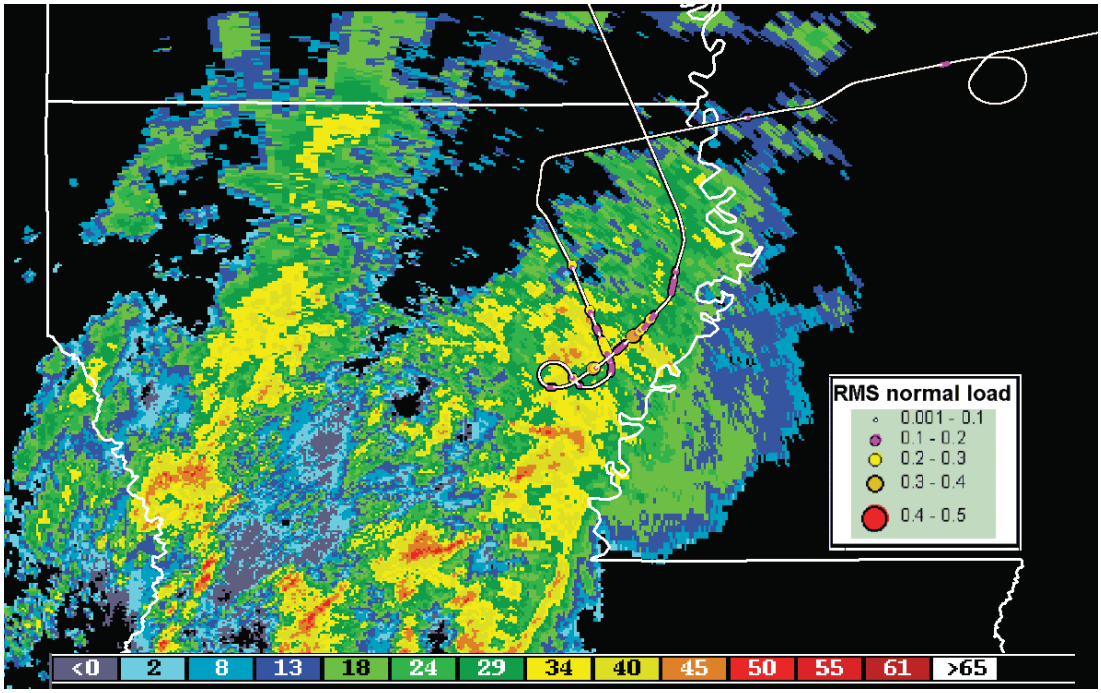

Figure 3. Path of Flight 190 and ground based composite radar reflectivity (*dBz*) from the Fort Polk, Louisiana NEXRAD radar at 18:57:48 UTC on 13 December 2000. Intensity of the radar reflectivity factor and the aircraft RMS normal loads ($\sigma_{\Delta n}$) are denoted by the legends.

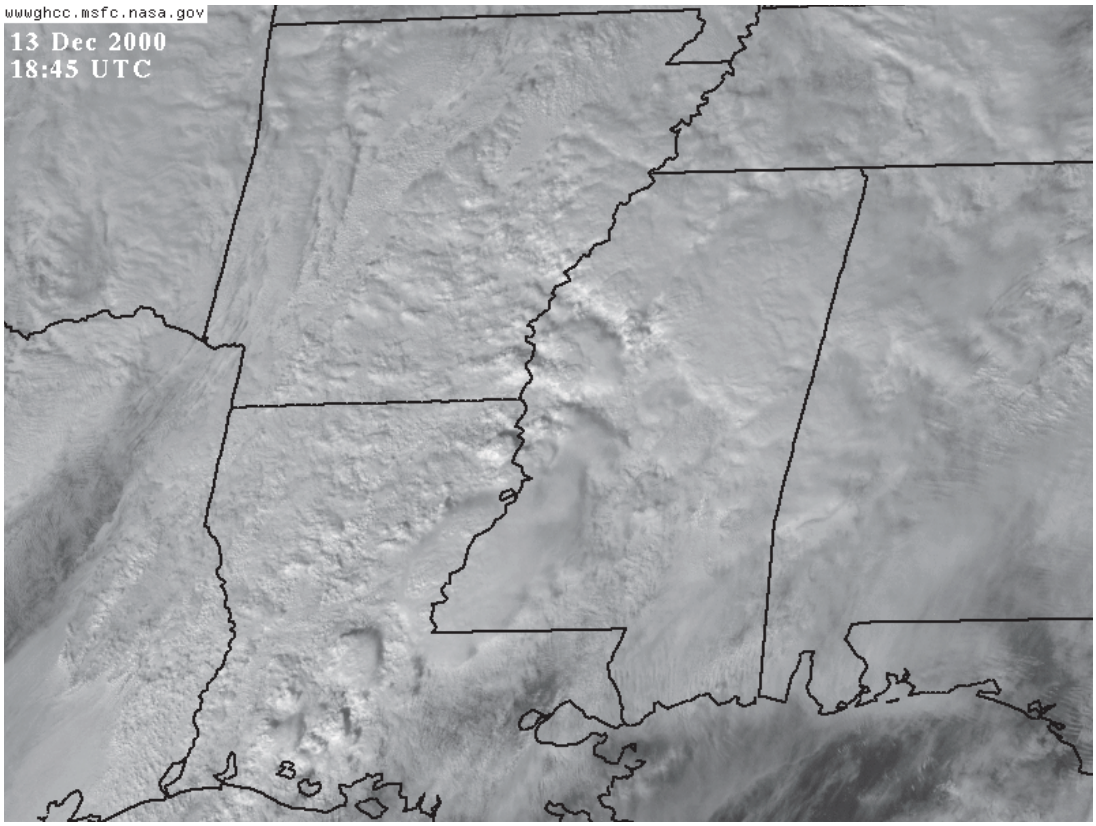

Figure 4. GOES-12 visible satellite image at 1845 UTC on 13 December 2000.

Figure 5. Photograph of a cumulonimbus that was penetrated over Louisiana. Photograph taken from aft of the ARIES during Flight 190.

2.2: Flight 191, December 14, 2000

Between 1825 and 1900 UTC on December 14, 2000, the ARIES investigated a line of convection over southern Georgia and the western Florida Panhandle. This line was a remnant of the convective complex encountered on the previous day. However, it had now weakened and manifested itself as a narrow but nearly continuous line of convection extending northeastward from the Gulf (Figure 6 and Figure 7). The line of convection contained strong thunderstorms and was located about 100 *km* ahead of a surface cold front. No PIREPS were issued in the vicinity of this system. Visual meteorological conditions (VMC) existed on approach to the line (Figure 8); however, instrument meteorological conditions (IMC) prevailed in the data collection region.

The flight path relative to the KTLH NEXRAD radar composite associated with Flight 191 is shown in Figure 6. The aircraft flew within the thunderstorm cirrus outflow at an altitude of 10 *km* (33 *kft*). Continuous turbulence was encountered while flying within the outflow region. Two significant turbulence encounters were associated with the penetration of cumulus plumes that were rising through the outflow region. Airborne radar indicated that moderate levels of radar reflectivity were associated with each of the two encounters. The precipitation encountered at flight level was in the form of snow and ice crystals. Storm tops were mostly around 10.6 *km* (35 *kft*) with occasional overshooting tops nearing 12 *km* (40 *kft*). Although the line was moving eastward with the cold front, cell motion was 17 *m/s* (25 *kts*) toward the east-northeast (from 240°), i.e., along the convective line. Prevailing winds in the near storm environment were around 36 *m/s* (70 *kts*) from 260° from true North. ATDS data was not available for this case and was therefore not included in the scoring of the airborne radar. However, data from the KTLH NEXRAD were used to evaluate the radar reflectivity levels along the flight path.

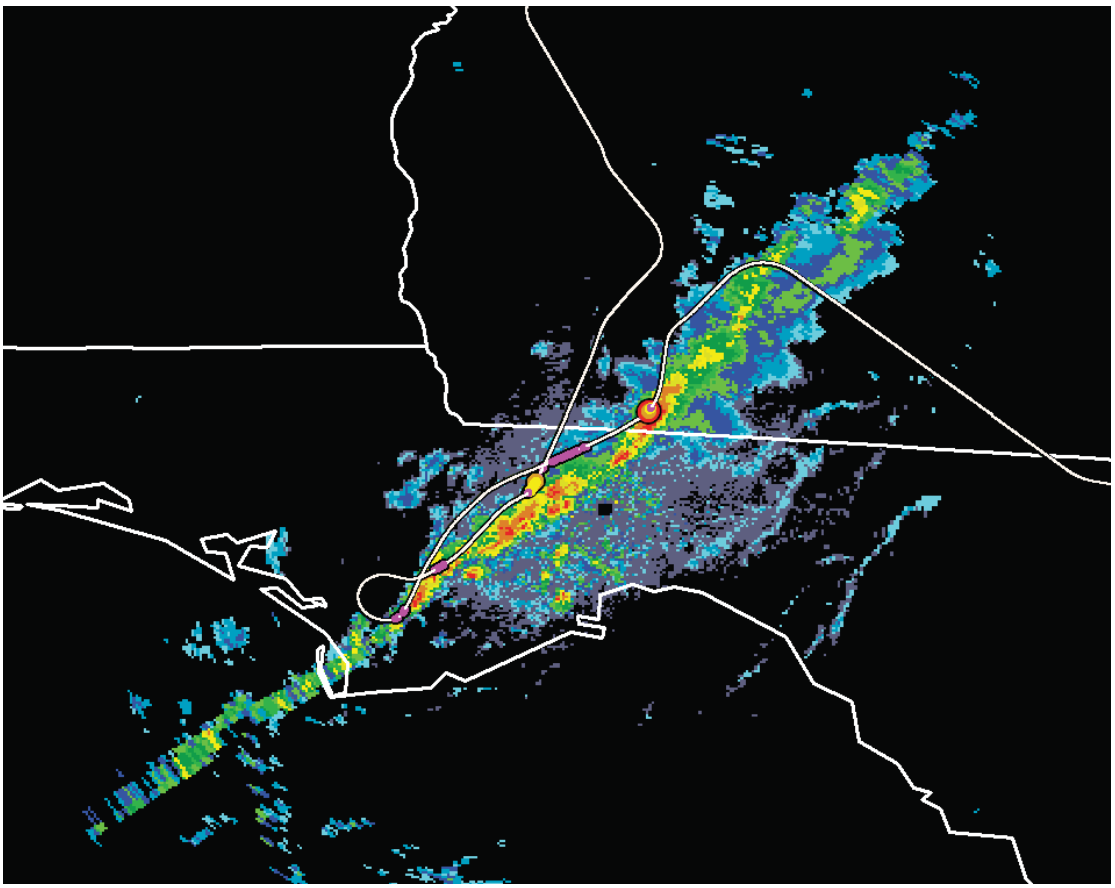

Figure 6. Path for Flight 191. Ground based composite radar reflectivity (*dBz*) from the Tallahassee, Florida NEXRAD radar at 18:44:21 UTC on 14 December 2000. The intensity of the radar reflectivity factor and the aircraft RMS normal loads are the same as denoted in the legend of Figure 3.

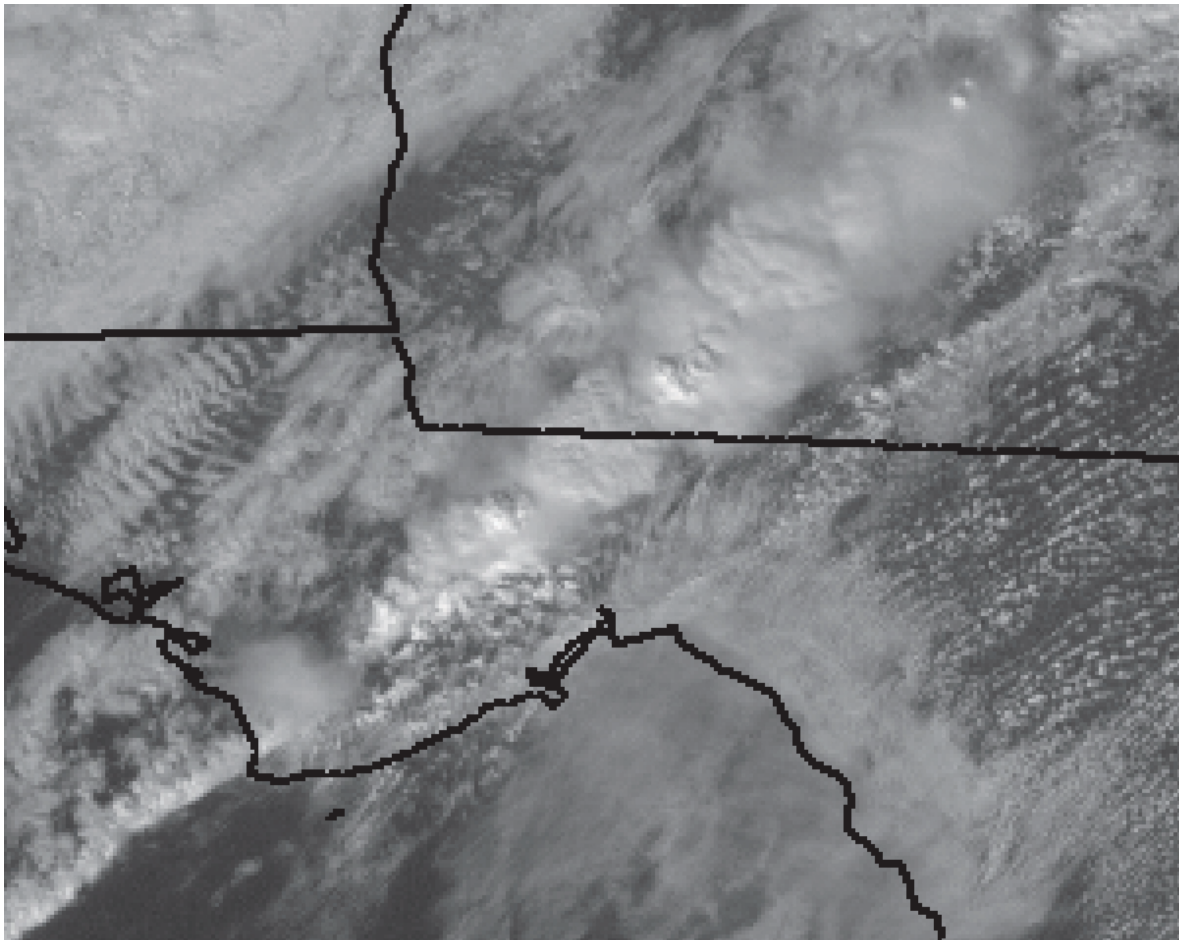

Figure 7. GOES-12 visible satellite image at 1845 UTC on 14 December 2000.

Figure 8. Photograph of the convective line as viewed from the northwest. Photograph taken from the cockpit of ARIES during Flight 191.

2.3: Flight 227, April 2, 2002

Between 2010 and 2110 UTC on April 2, 2002 the ARIES investigated a mesoscale convective complex (MCC) located over central Indiana (Figure 9 and Figure 10). The MCC presented a line of deep convection along its southern leading edge, which was oriented southwest to northeast. A broad area of stratiform precipitation with embedded convective cells was located north of the leading convective line. ARIES worked several of these embedded convective cells in the stratiform precipitation region of the MCC, and avoided the stronger convection along the southern leading edge. Light to moderate turbulence encounters were reported from PIREPS in the vicinity of this system (Figure 11). Instrument meteorological conditions prevailed in the data collection region with intermittent periods of marginal visibility.

ARIES encountered significant turbulence associated with the penetration of a convective cell embedded within the stratiform precipitation region. Unfortunately, ATDS data was not available for this case, and therefore, was not included in the scoring of the radar. However, weak airborne radar reflectivity was associated with this cell as deduced by NEXRAD radar. The precipitation encountered at flight level was in the form of snow and ice crystals. Storm tops were mostly around 9 *km* (30 *kft*) with occasional higher tops of about 10.6 *km* (35 *kft*). The flight altitude during the data collection was below the storm tops. The flight altitude was initially 8 *km* (27 *kft*) and later changed to 7 *km* (23 *kft*) due to the weak levels of turbulence intensity at the higher altitude. In general, nonhazardous turbulence characterized the overall stratiform region. Cell motion was towards the east-northeast at 34 *m/s* (66 *kts*). The prevailing winds in the near storm environment were around 36 *m/s* (70 *kts*) from 260° from true North.

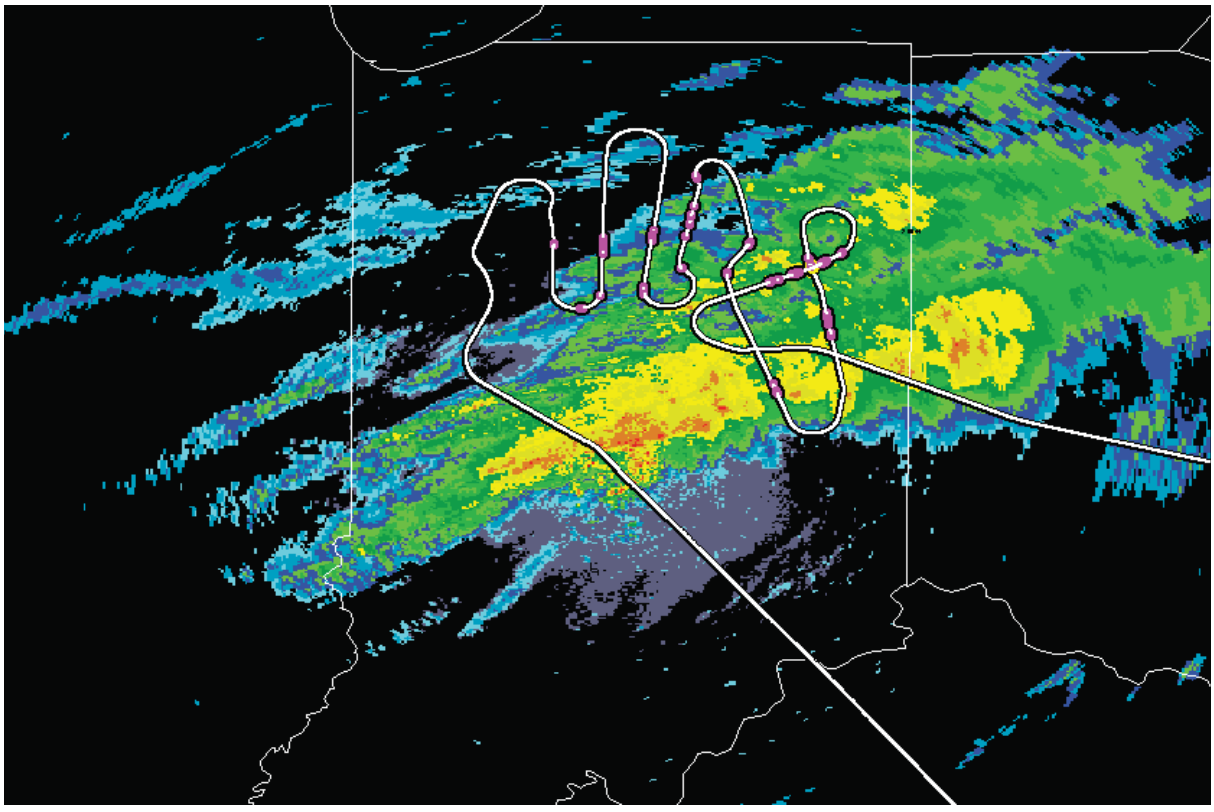

Figure 9. Path for Flight 227. Ground based composite radar reflectivity (*dBz*) from the KIND (Indianapolis, Indiana) NEXRAD radar at 21:00:32 UTC on 2 April 2002. The intensity of the radar reflectivity factor and the aircraft RMS normal loads are the same as denoted in the legend of Figure 3.

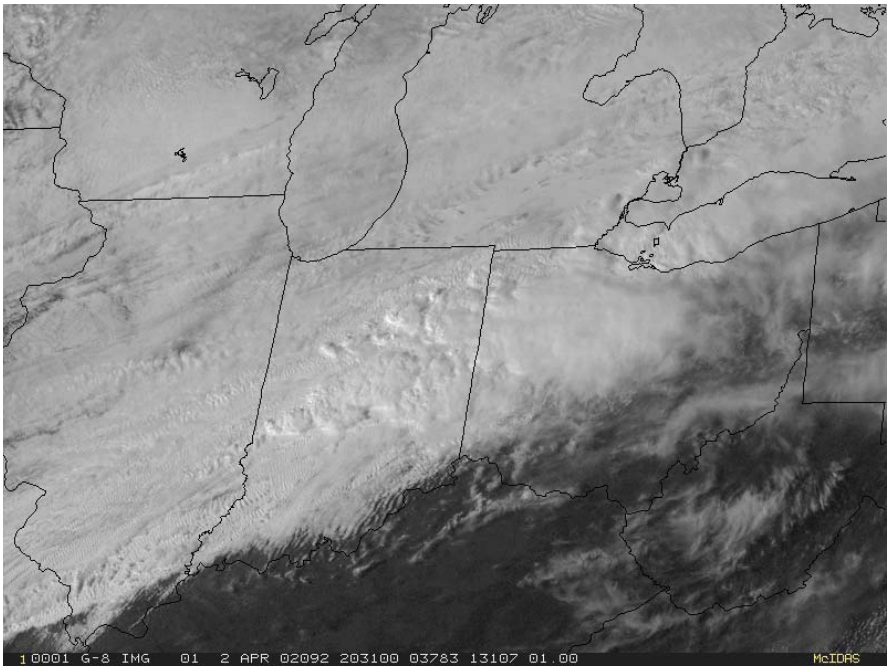

Figure 10. GOES-12 visible satellite image at 2031 UTC on 02 April 2002.

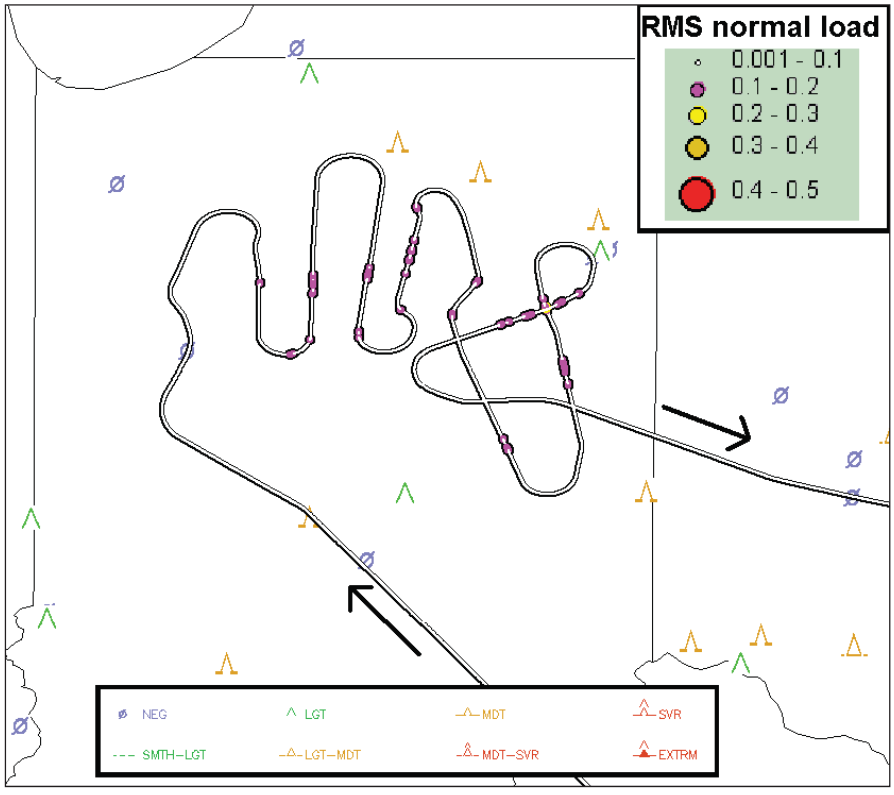

Figure 11. RMS normal loads encountered along the path for Flight 227 with turbulence PIREPS for 02 April 2002.

2.4: Flight 228, April 3, 2002

Between 1830 and 1920 UTC on April 3, 2002, the ARIES investigated an isolated convective cell located on the South Carolina coast near Georgetown, South Carolina (Figure 12 and Figure 13). This cell was triggered by a sea breeze and remained nearly stationary throughout the data collection period. No pilot reports of turbulence were issued in the vicinity (Figure 14) and visual meteorological conditions prevailed in the data collection region.

Six significant turbulence encounters were associated with ARIES penetrations of the upwind periphery of the convective cell. Strong radar reflectivity was detected with the airborne radar along the upwind edges of the cell (Figure 15 - Figure 26). Estimates of storm top altitude are not provided due to the unavailability of ground based NEXRAD image. However, the aircraft penetrated just below the storm top at a flight altitude of 7.6 *km* (25 *kft*). Prevailing winds at the altitude were around 23 *m/s* (45 *kts*) from 240° relative to true North.

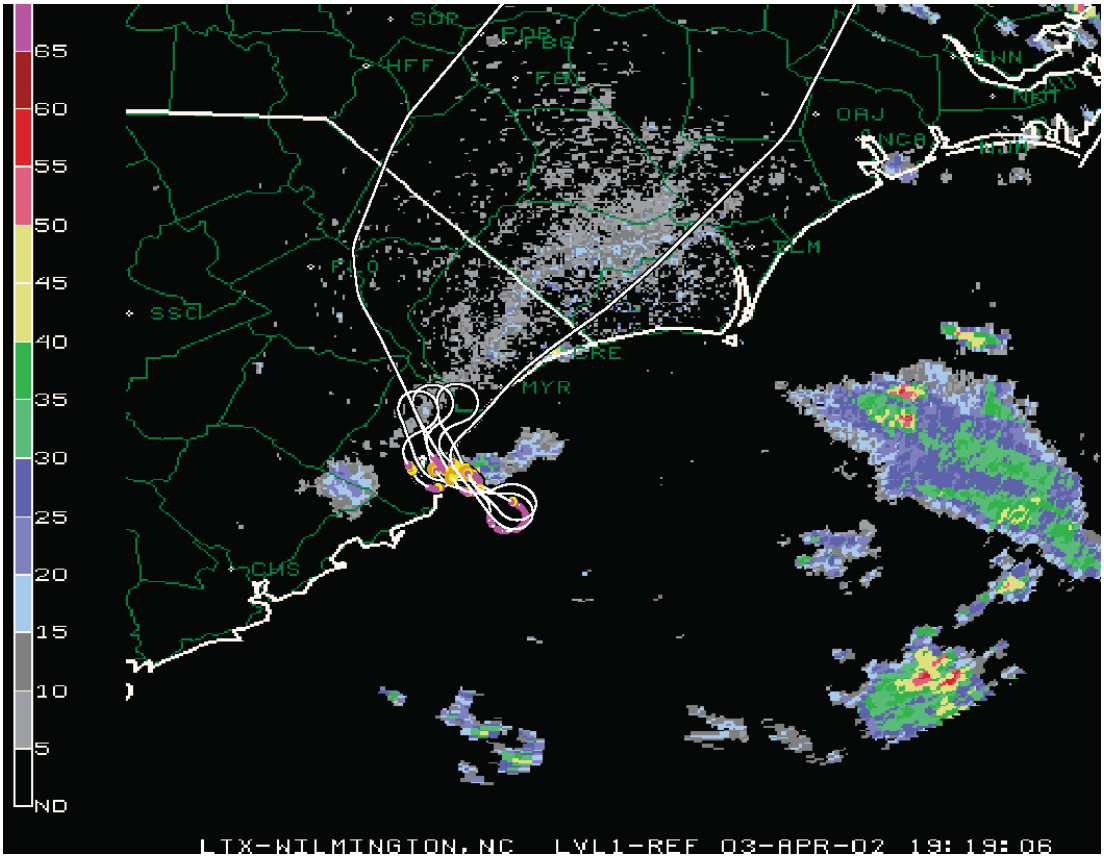

Figure 12. Path for Flight 228. Ground based composite radar reflectivity (*dBz*) from the Wilmington, North Carolina (KLTX) NEXRAD radar at 19:19:06 on 03 April 2002. See Figure 3 for legend to intensity of the aircraft RMS normal loads.

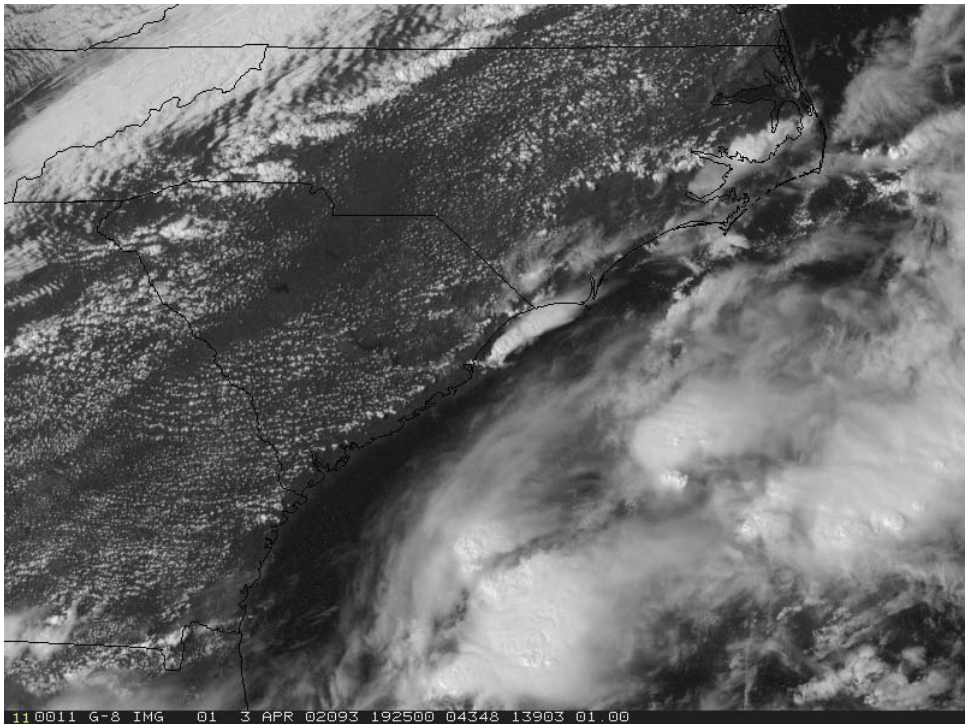

Figure 13. GOES-12 visible satellite image at 19:25:00 UTC on 03 April 2002. The cell investigated by ARIES is located in the center of the figure.

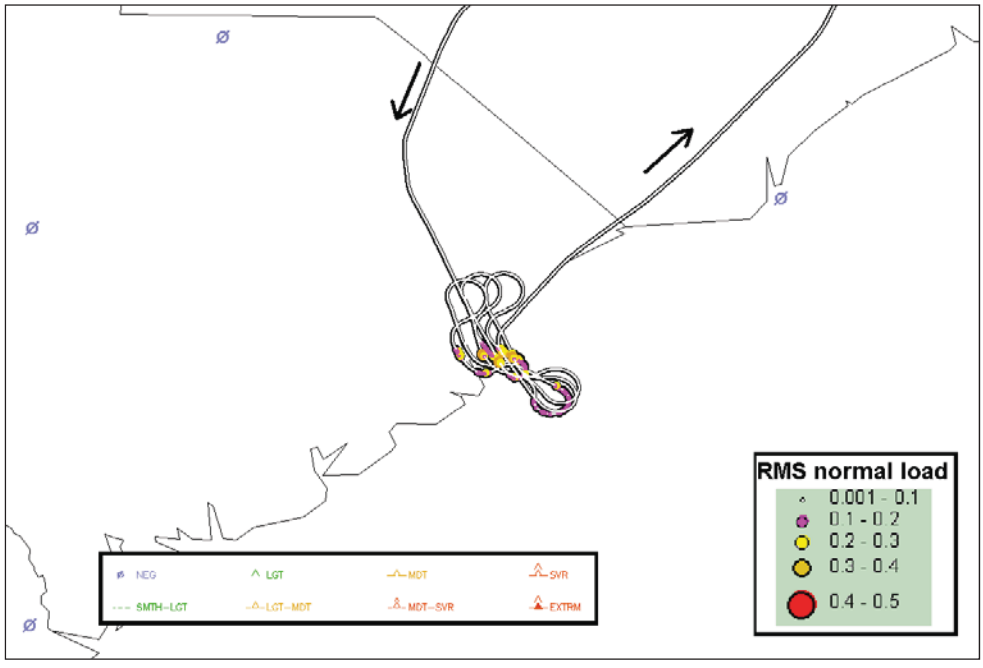

Figure 14. RMS normal loads encountered along the path for Flight 228 with turbulence PIREPS for 03 April 2002.

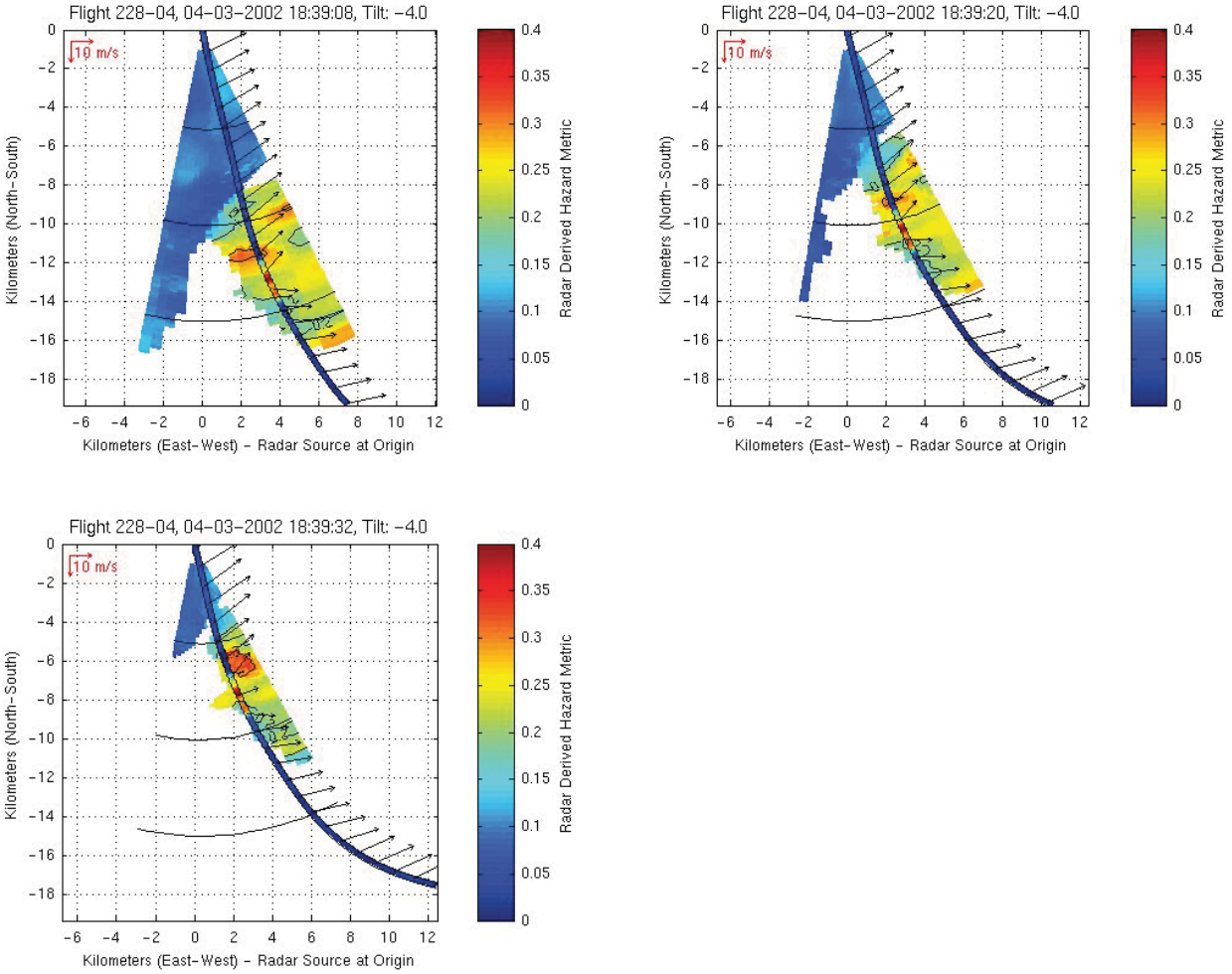

Figure 15. Sequential scans at 12*s* intervals for airborne radar predicted $\sigma_{\Delta n}$ (color contour cones) and *in situ* $\sigma_{\Delta n}$ (color on flight path line) for Event 228-04. Ambient wind vectors are shown along path.

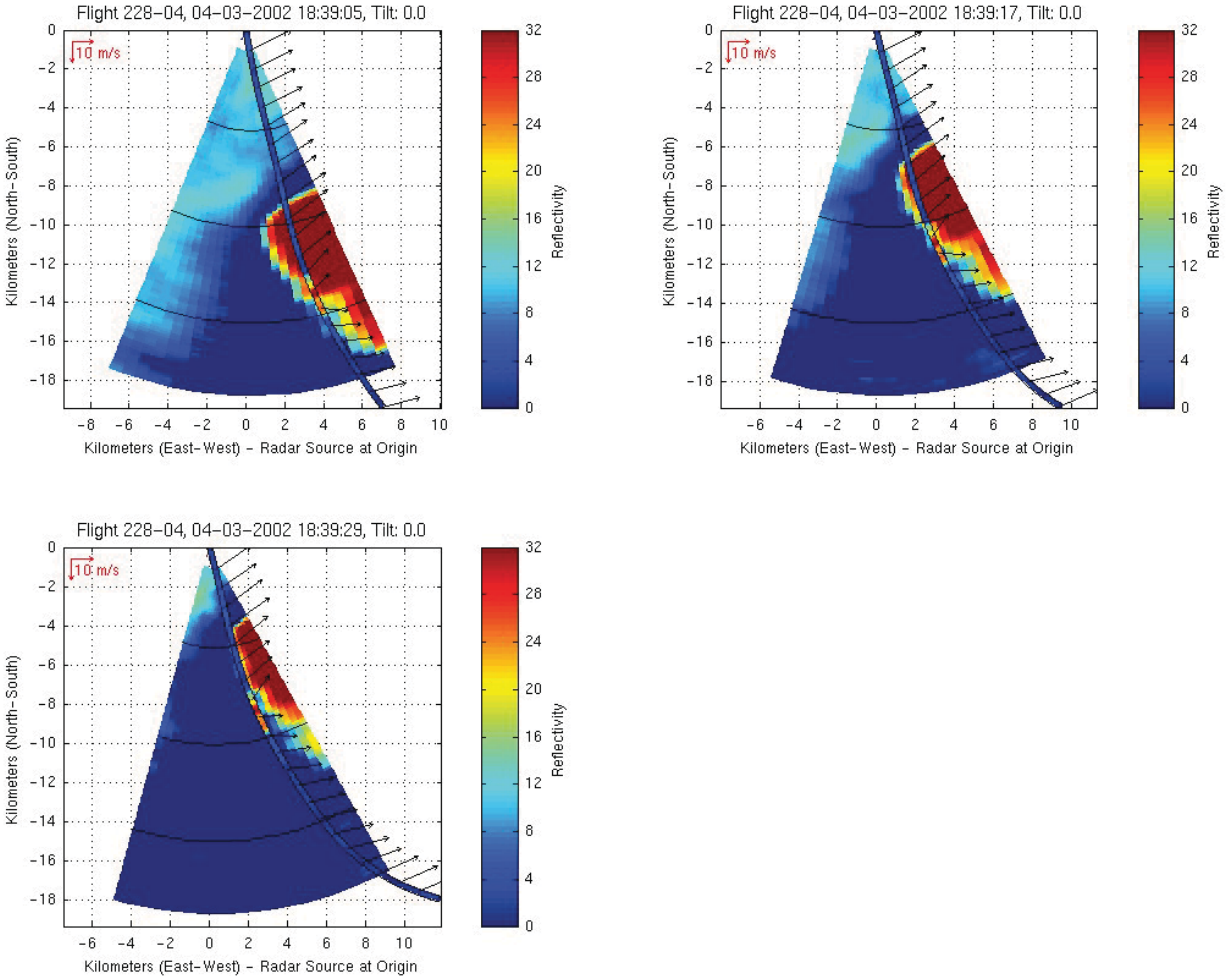

Figure 16. Sequential scans at 12*s* interval for airborne radar reflectivity factor (color contour cones) and *in situ* $\sigma_{\Delta n}$ (color on flight path line) for Event 228-04. Ambient wind vectors are shown along path.

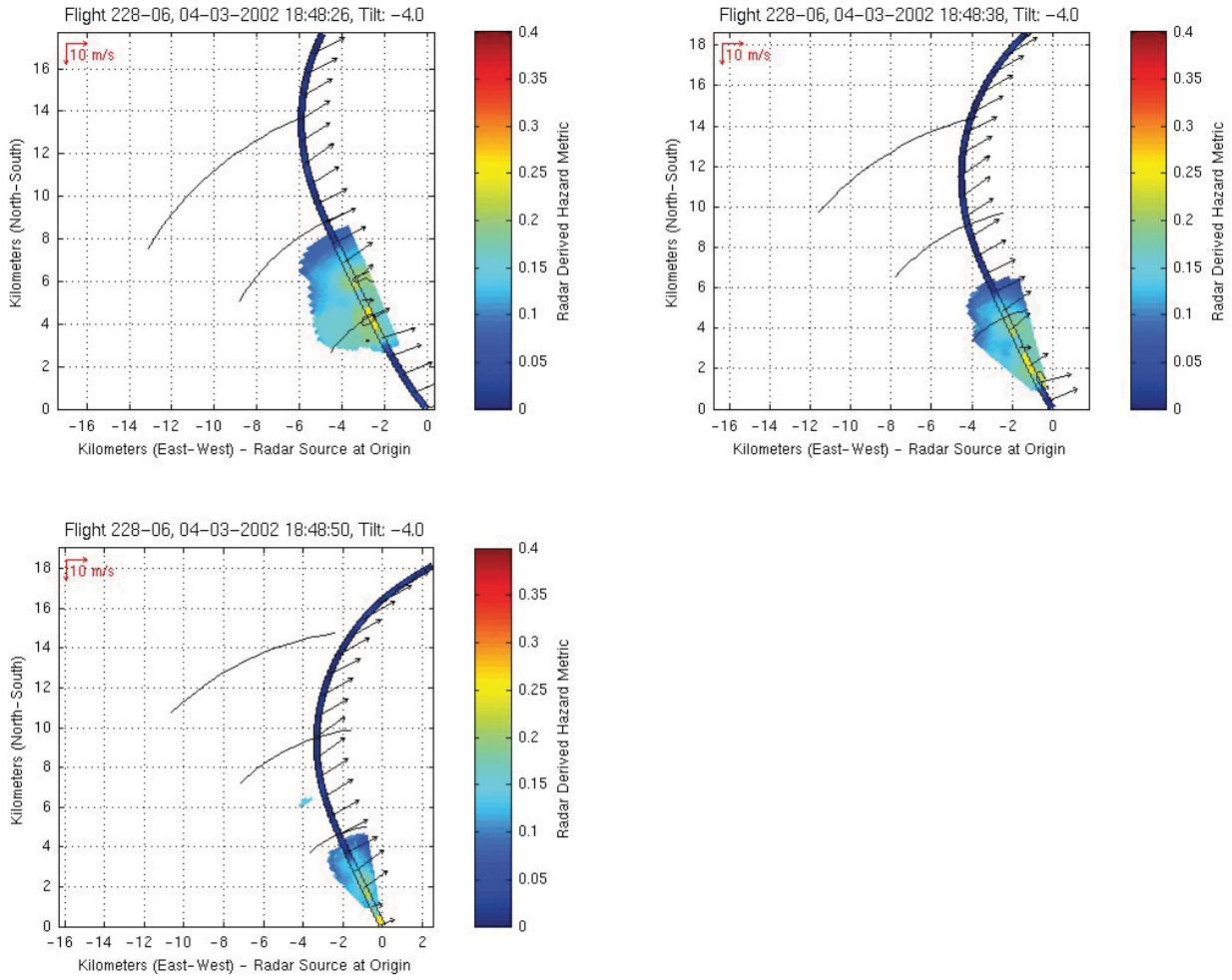

Figure 17. Sequential scans at 12*s* intervals for airborne radar predicted $\sigma_{\Delta n}$ (color contour cones) and *in situ* $\sigma_{\Delta n}$ (color on flight path line) for Event 228-06. Ambient wind vectors are shown along path.

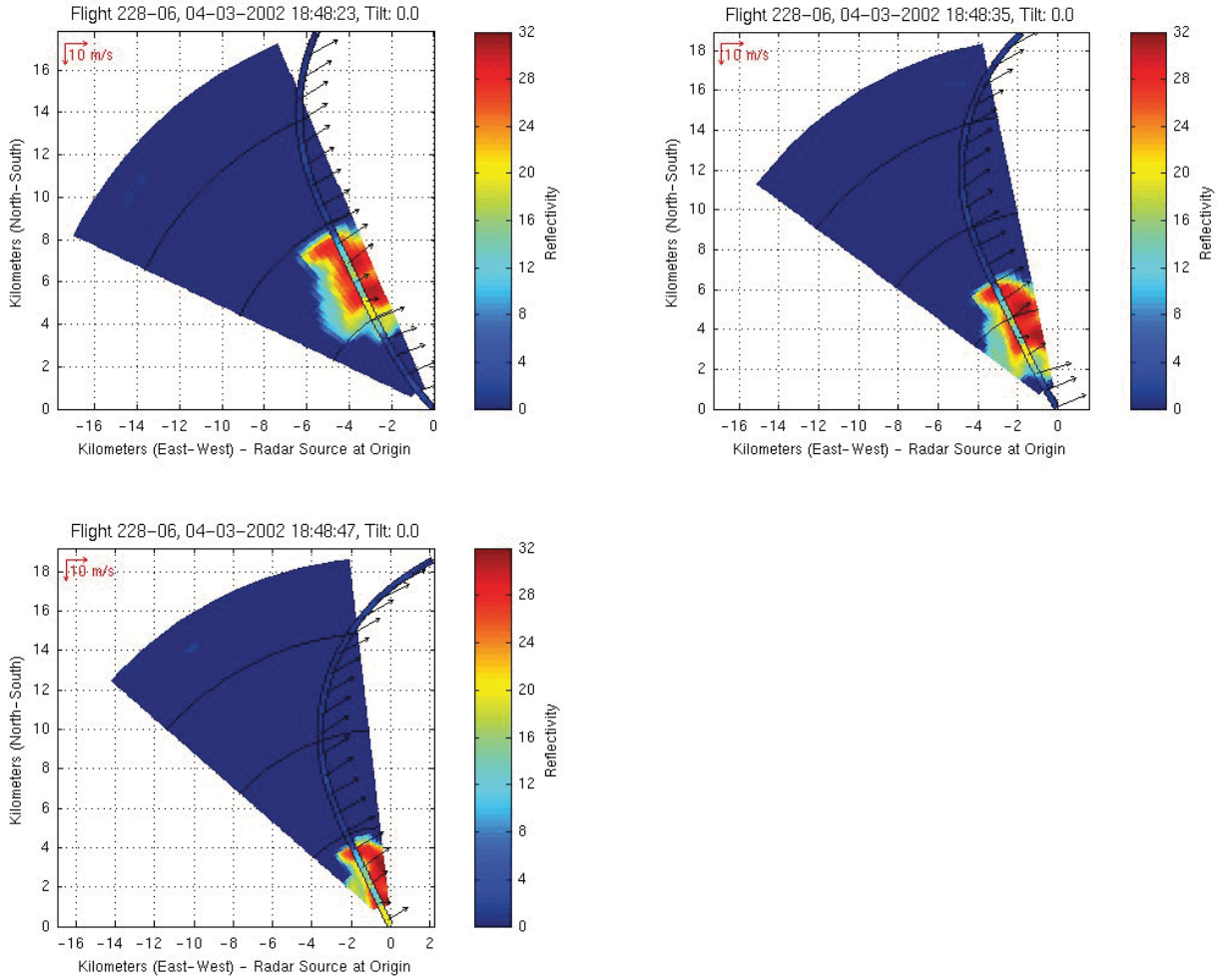

Figure 18. Sequential scans at 12*s* interval for airborne radar reflectivity factor (color contour cones) and *in situ* $\sigma_{\Delta n}$ (color on flight path line) for Event 228-06. Ambient wind vectors are shown along path.

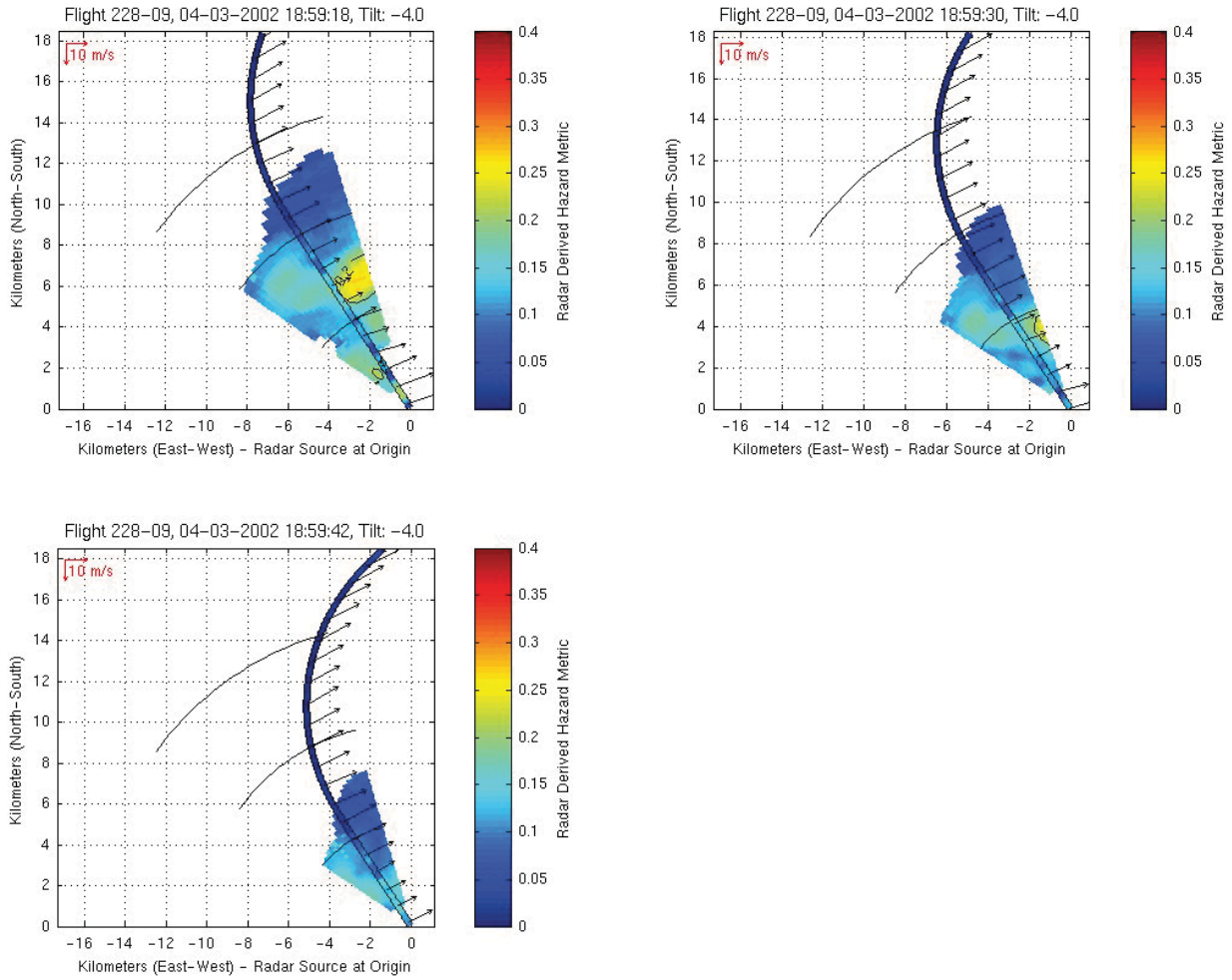

Figure 19. Sequential scans at 12*s* intervals for airborne radar predicted $\sigma_{\Delta n}$ (color contour cones) and *in situ* $\sigma_{\Delta n}$ (color on flight path line) for Event 228-09. Ambient wind vectors are shown along path.

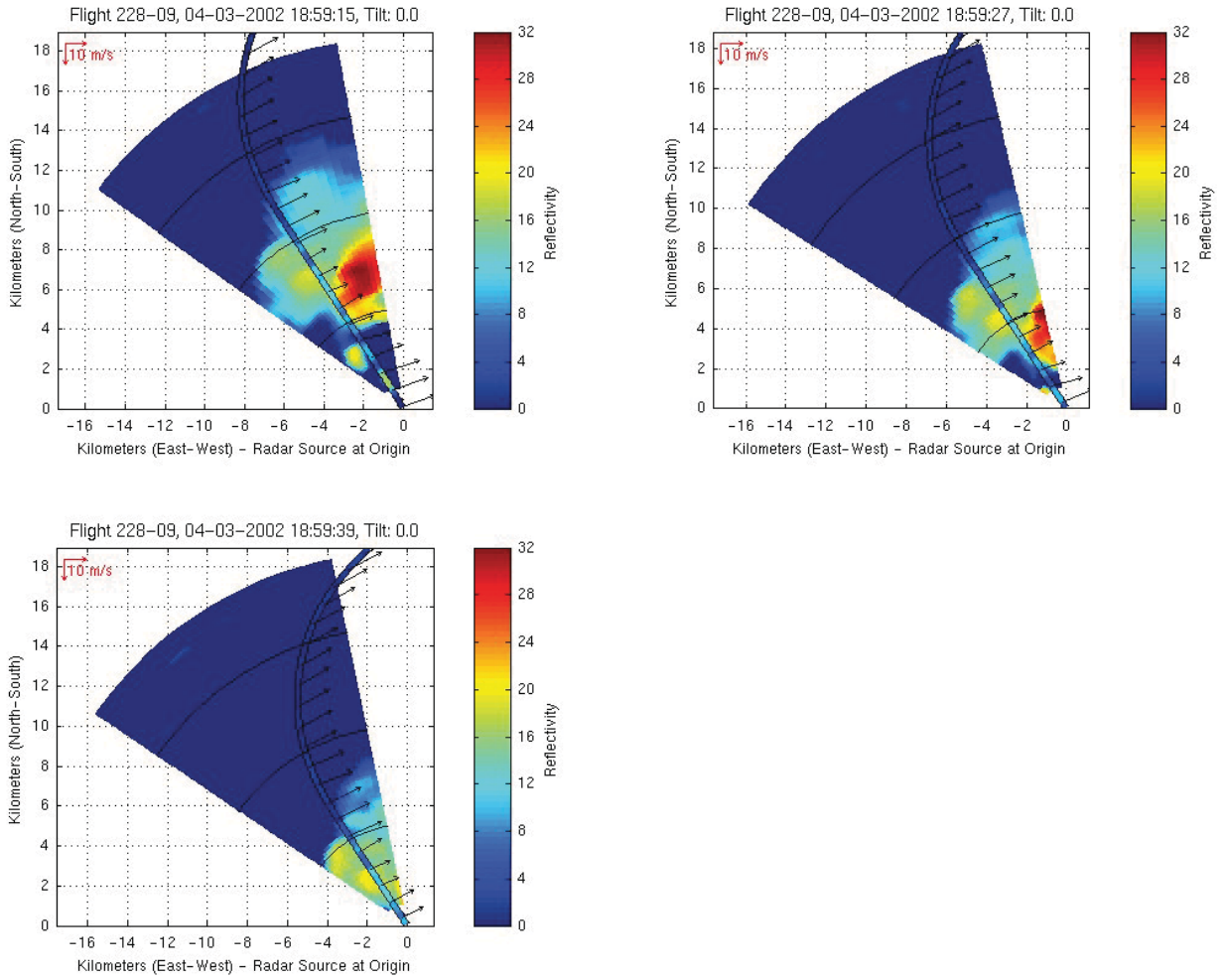

Figure 20. Sequential scans at 12*s* interval for airborne radar reflectivity factor (color contour cones) and *in situ* $\sigma_{\Delta n}$ (color on flight path line) for Event 228-09. Ambient wind vectors are shown along path.

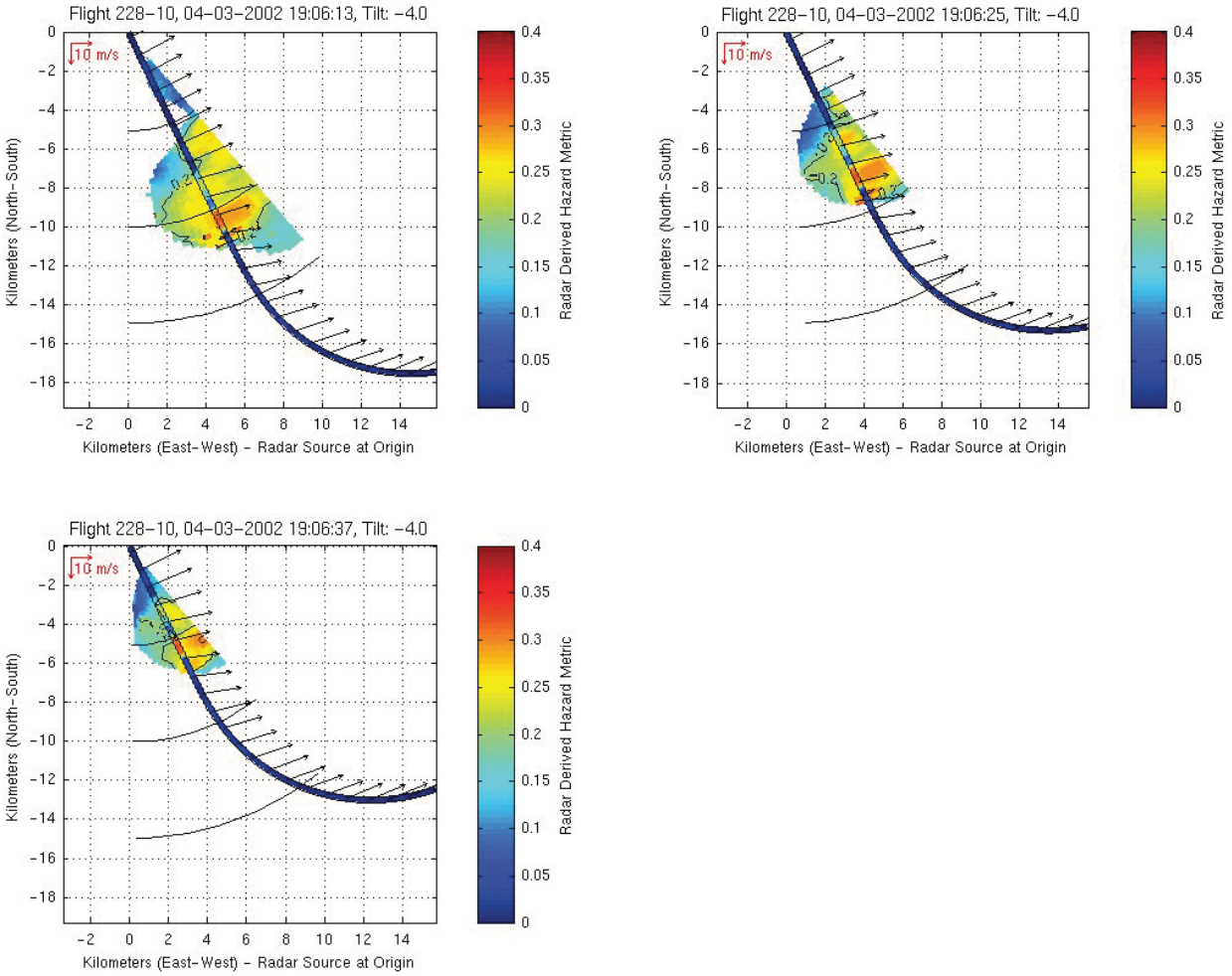

Figure 21. Sequential scans at 12*s* intervals for airborne radar predicted $\sigma_{\Delta n}$ (color contour cones) and *in situ* $\sigma_{\Delta n}$ (color on flight path line) for Event 228-10. Ambient wind vectors are shown along path.

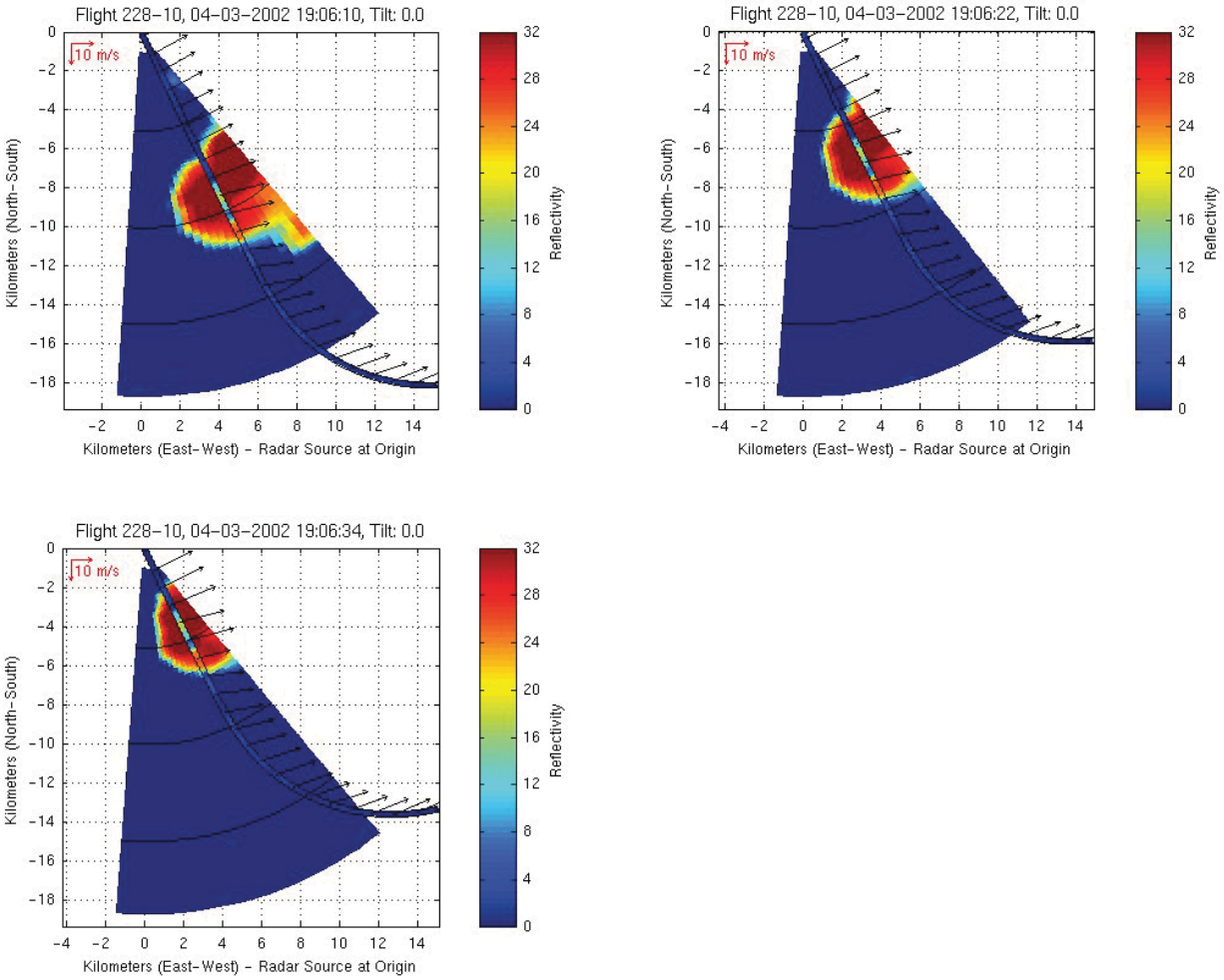

Figure 22. Sequential scans at 12*s* interval for airborne radar reflectivity factor (color contour cones) and *in situ* $\sigma_{\Delta n}$ (color on flight path line) for Event 228-10. Ambient wind vectors are shown along path.

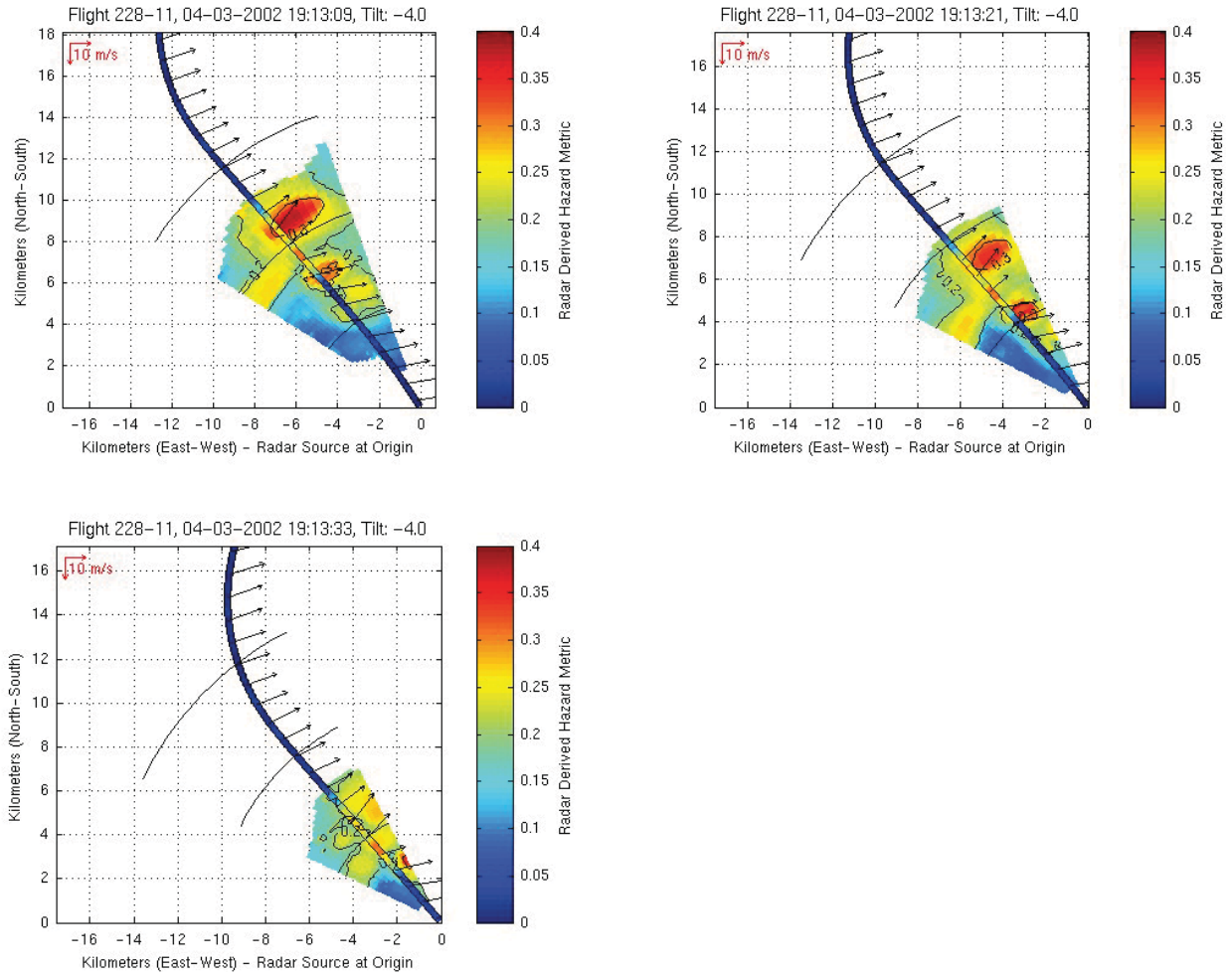

Figure 23. Sequential scans at 12*s* intervals for airborne radar predicted $\sigma_{\Delta n}$ (color contour cones) and *in situ* $\sigma_{\Delta n}$ (color on flight path line) for Event 228-11. Ambient wind vectors are shown along path.

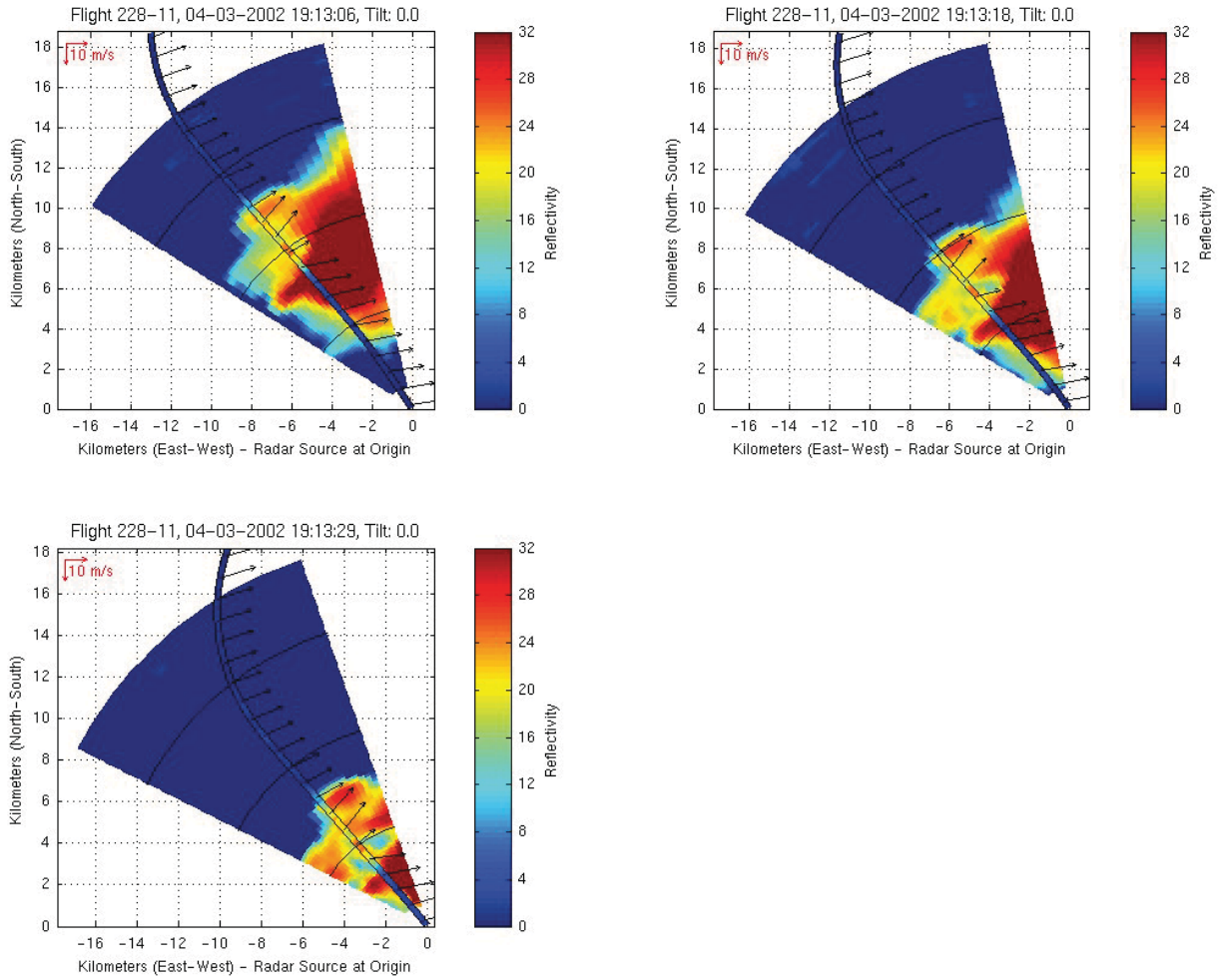

Figure 24. Sequential scans at 12*s* interval for airborne radar reflectivity factor (color contour cones) and *in situ* $\sigma_{\Delta n}$ (color on flight path line) for Event 228-11. Ambient wind vectors are shown along path.

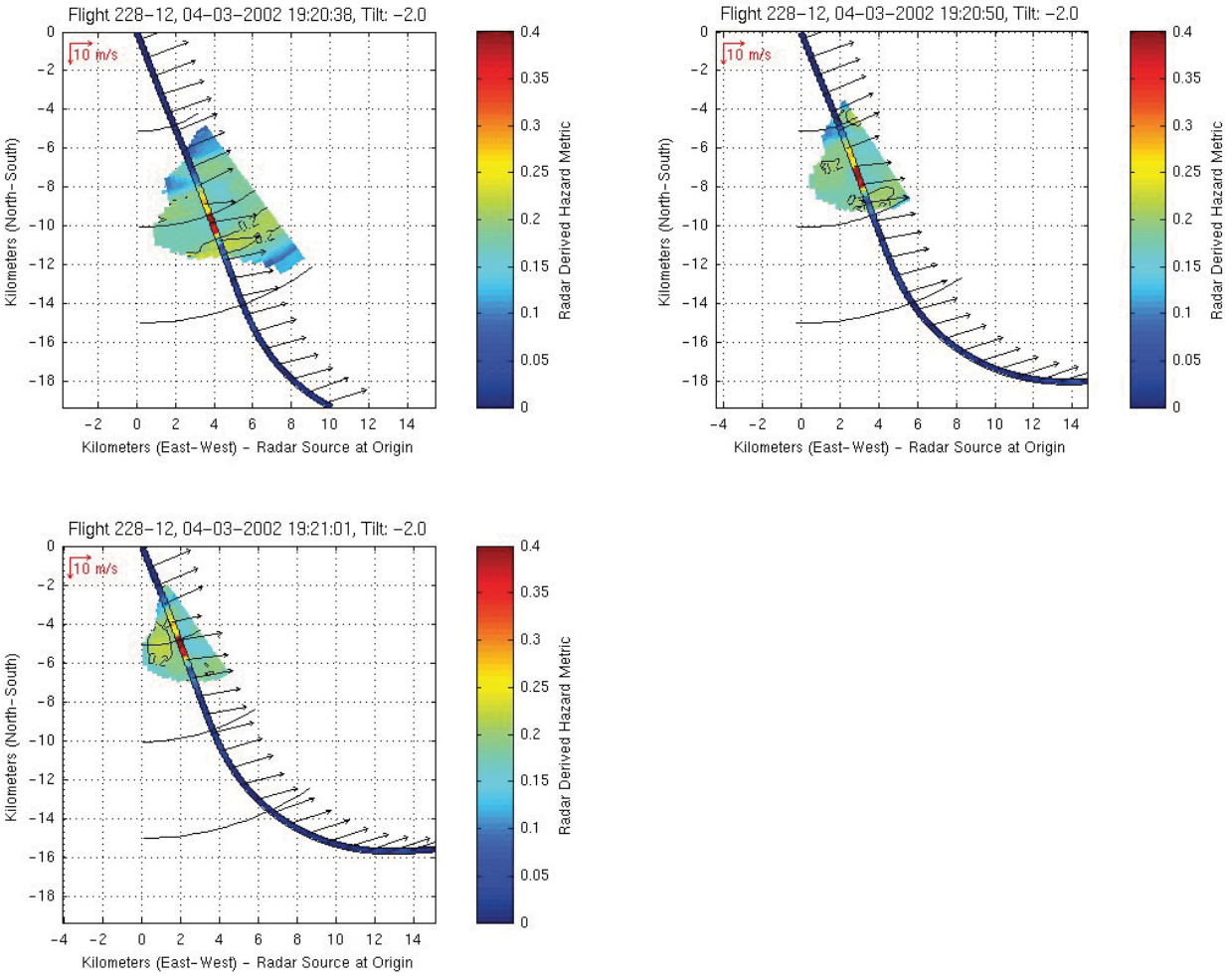

Figure 25. Sequential scans at 12*s* intervals for airborne radar predicted $\sigma_{\Delta n}$ (color contour cones) and *in situ* $\sigma_{\Delta n}$ (color on flight path line) for Event 228-12. In this event, all three scans were executed at a tilt of –2°. Ambient wind vectors are shown along path.

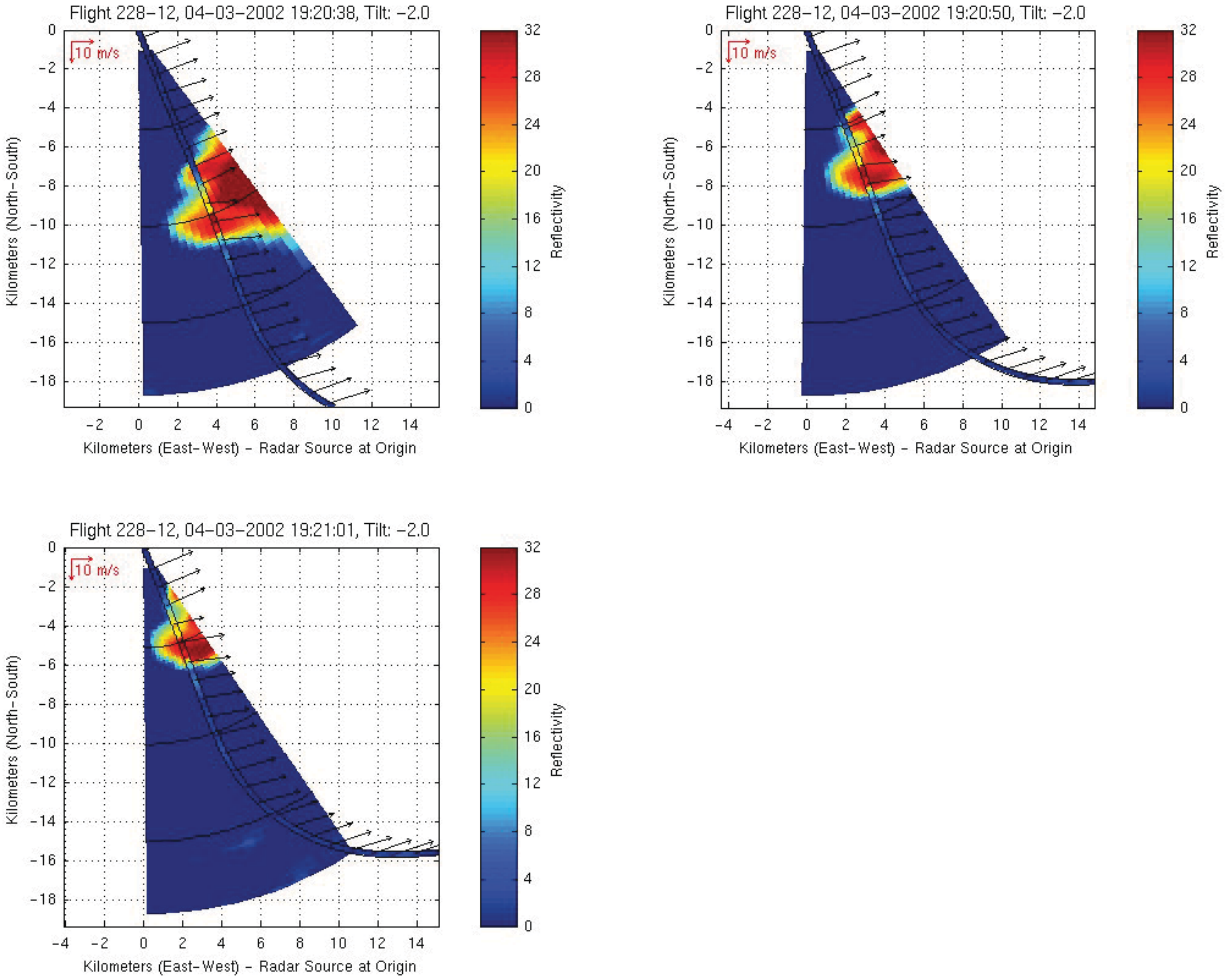

Figure 26. Sequential scans at 12*s* interval for airborne radar reflectivity factor (color contour cones) and *in situ* $\sigma_{\Delta n}$ (color on flight path line) for Event 228-12. In this event, all three scans were executed at a tilt of –2°. Ambient wind vectors are shown along path.

2.5: Flight 229, April 12, 2002

Between 1800 and 1915 UTC on April 12, 2002, ARIES encountered convection associated with a tropical disturbance along the western Florida panhandle (Figure 27 and Figure 28). This disturbance was associated with a nearly stationary tropical low located in the Gulf of Mexico, south of the western Florida panhandle. Tropical rain bands associated with this system were propagating northward, moving inland over the Gulf Coast. Heavy rain was occurring at the surface in association with the rain bands. The environment was characterized by slightly unstable convective indices with a nearly saturated column up to the tropopause. Pilot reports of moderate turbulence were reported in the vicinity of the disturbance (Figure 29, Figure 30 and Figure 31). Extensive upper-level outflow was associated with this convection and led to instrument meteorological conditions through a portion of the Deep South.

Continuous light turbulence was experienced by ARIES while flying in the vicinity of the tropical system. However, only one significant turbulence encounter occurred. This was associated with the penetration of an embedded convective cell at 7.6 *km* (25 *kft*). Low levels of radar reflectivity were detected with ATDS in association with the convective cell that was responsible for the single encounter. Although the embedded cell's storm top was 9.1 *km* (30 *kft*) most precipitation and resulting weak radar reflectivity appeared to be confined to below 6 *km* (20 *kft*). The strongest radar reflectivity was limited to below 3 *km* (10 *kft*), due to large drops and weak updrafts. Cell motion was towards the north-northwest at around 5 *m/s* (10 *kts*). The prevailing wind at flight level was 8 *m/s* (15 *kts*) from 155° relative to true North.

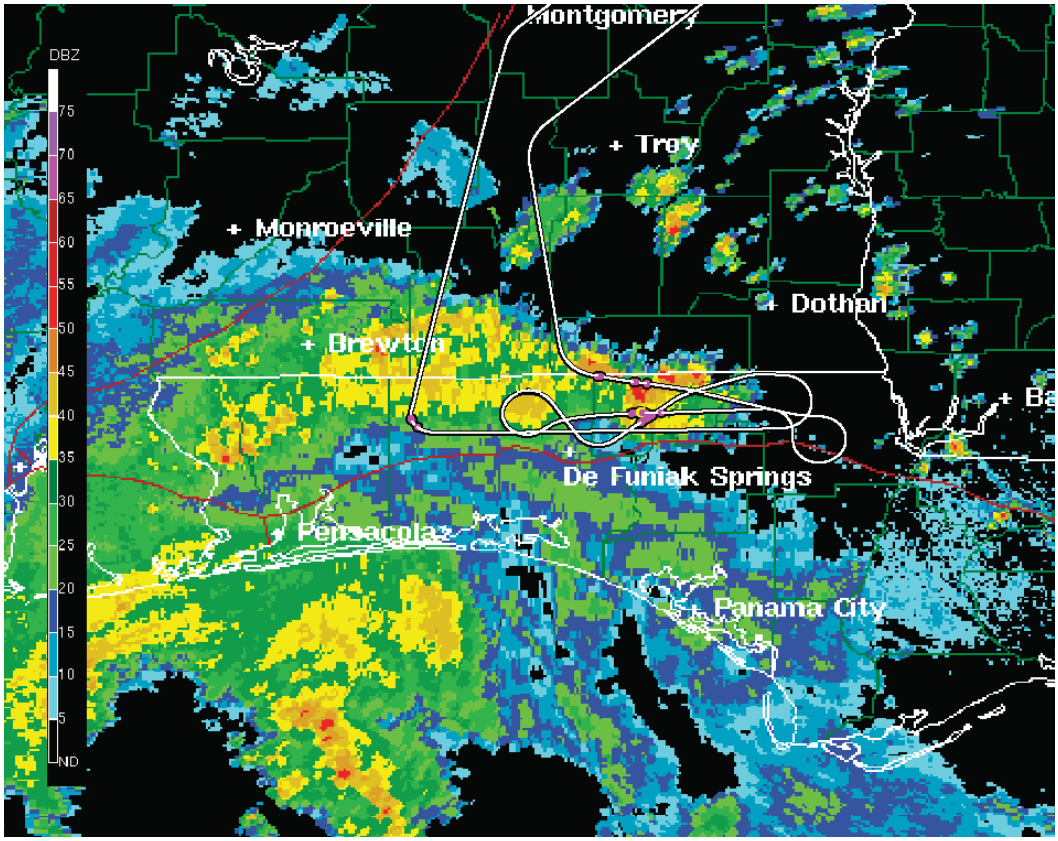

Figure 27. Path for Flight 229. Blended plot of ground based composite NEXRAD radar reflectivity (*dBz*) from the Mobile, Alabama 18:57 UTC and Tallahassee, Florida 18:56 UTC on 12 April 2002. See Figure 3 for legend to intensity of the aircraft RMS normal loads.

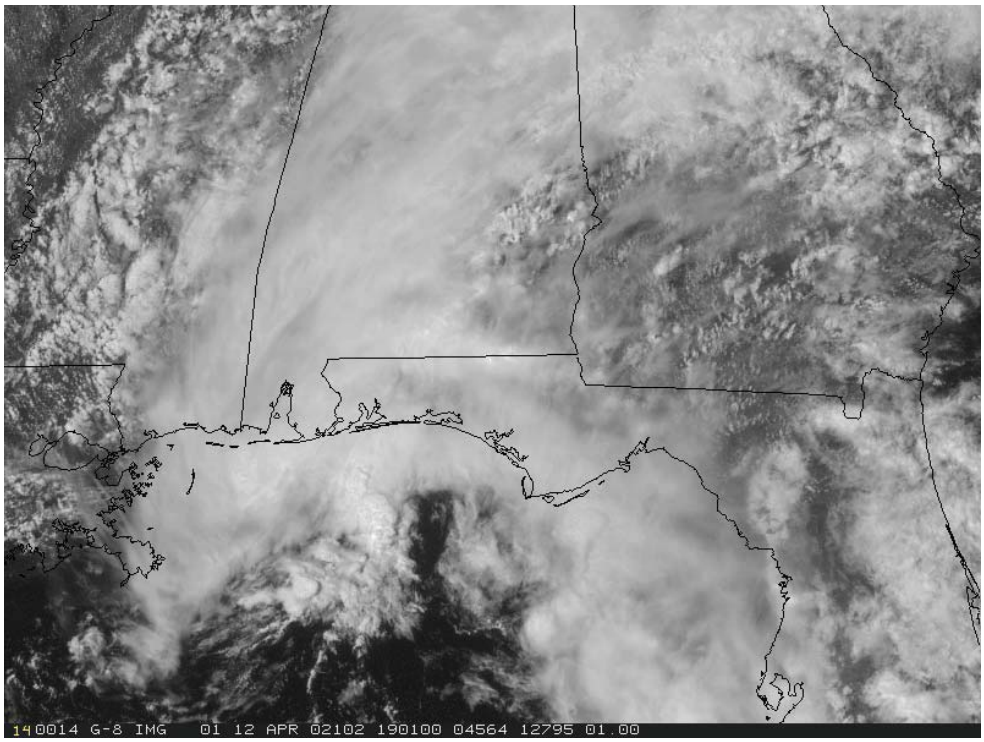

Figure 28. GOES-12 visible satellite image at 19:01:00 UTC on 12 April 2002.

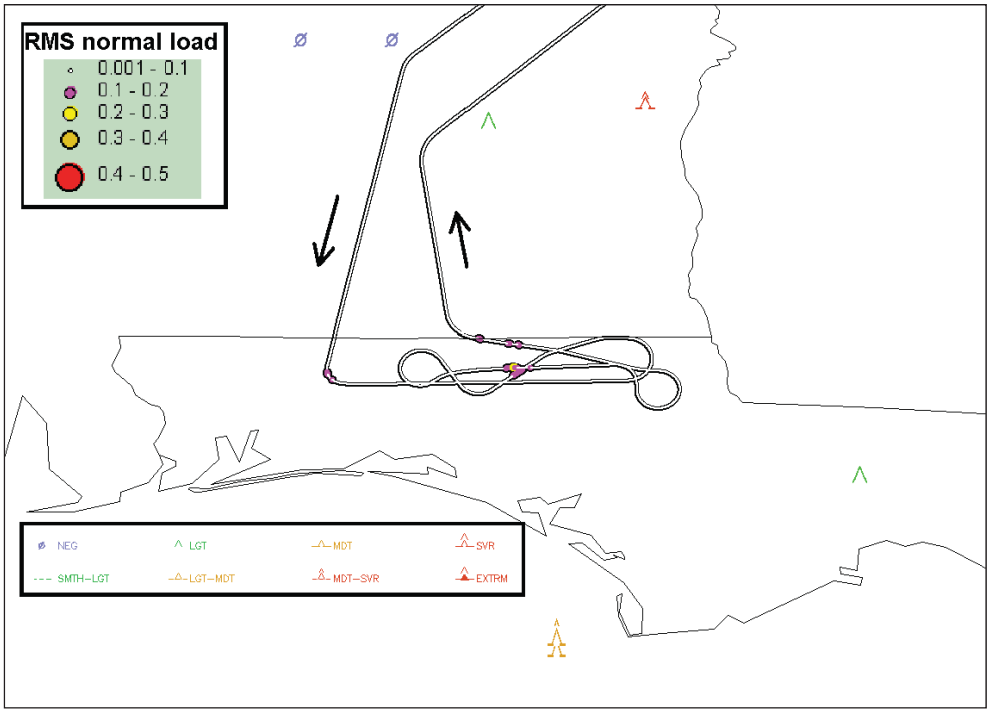

Figure 29. RMS normal loads encountered along the path for Flight 229 with turbulence PIREPS for 12 April 2002.

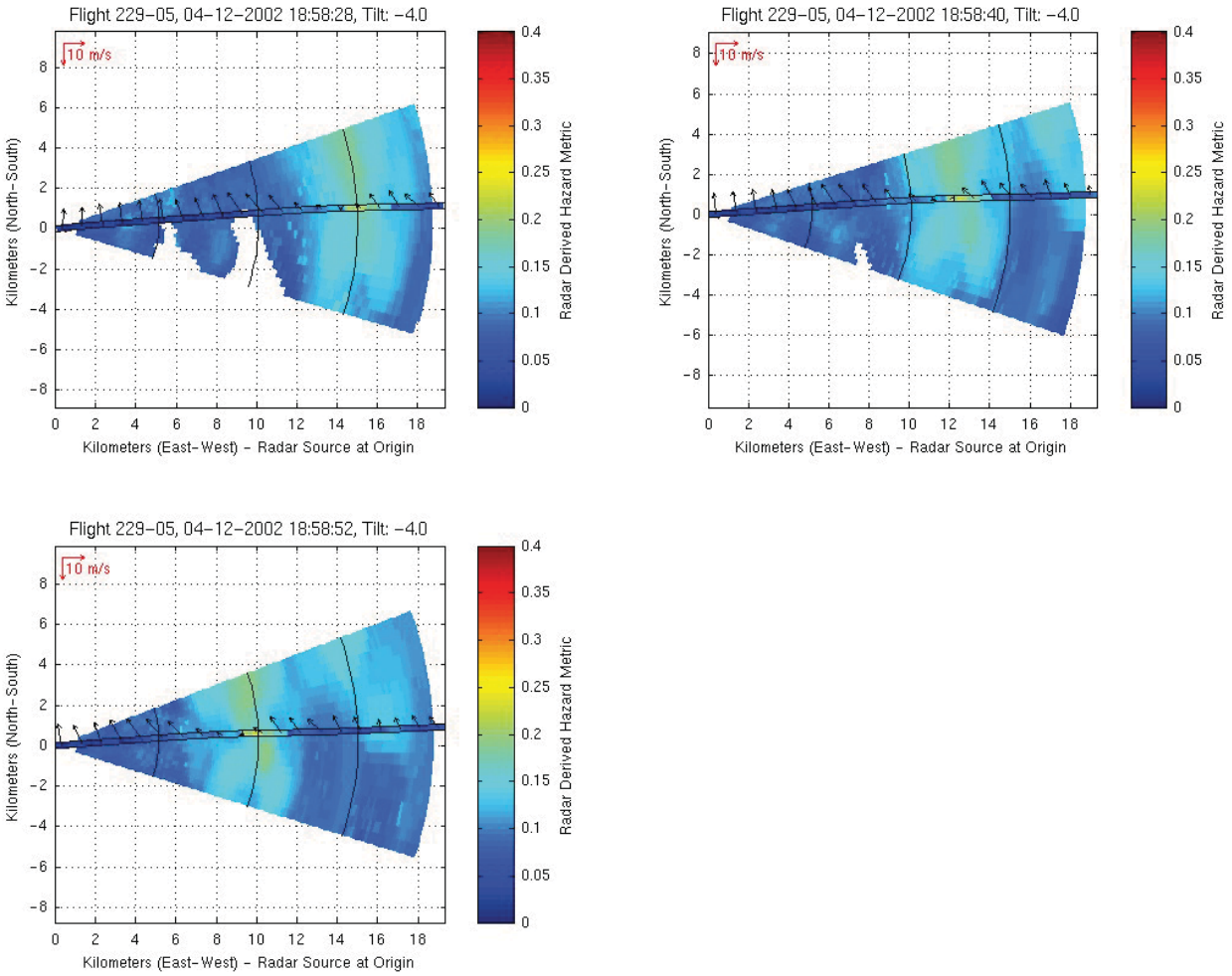

Figure 30. Sequential scans at 12*s* intervals for airborne radar predicted $\sigma_{\Delta n}$ (color contour cones) and *in situ* $\sigma_{\Delta n}$ (color on flight path line) for Event 229-05. Ambient wind vectors are shown along path.

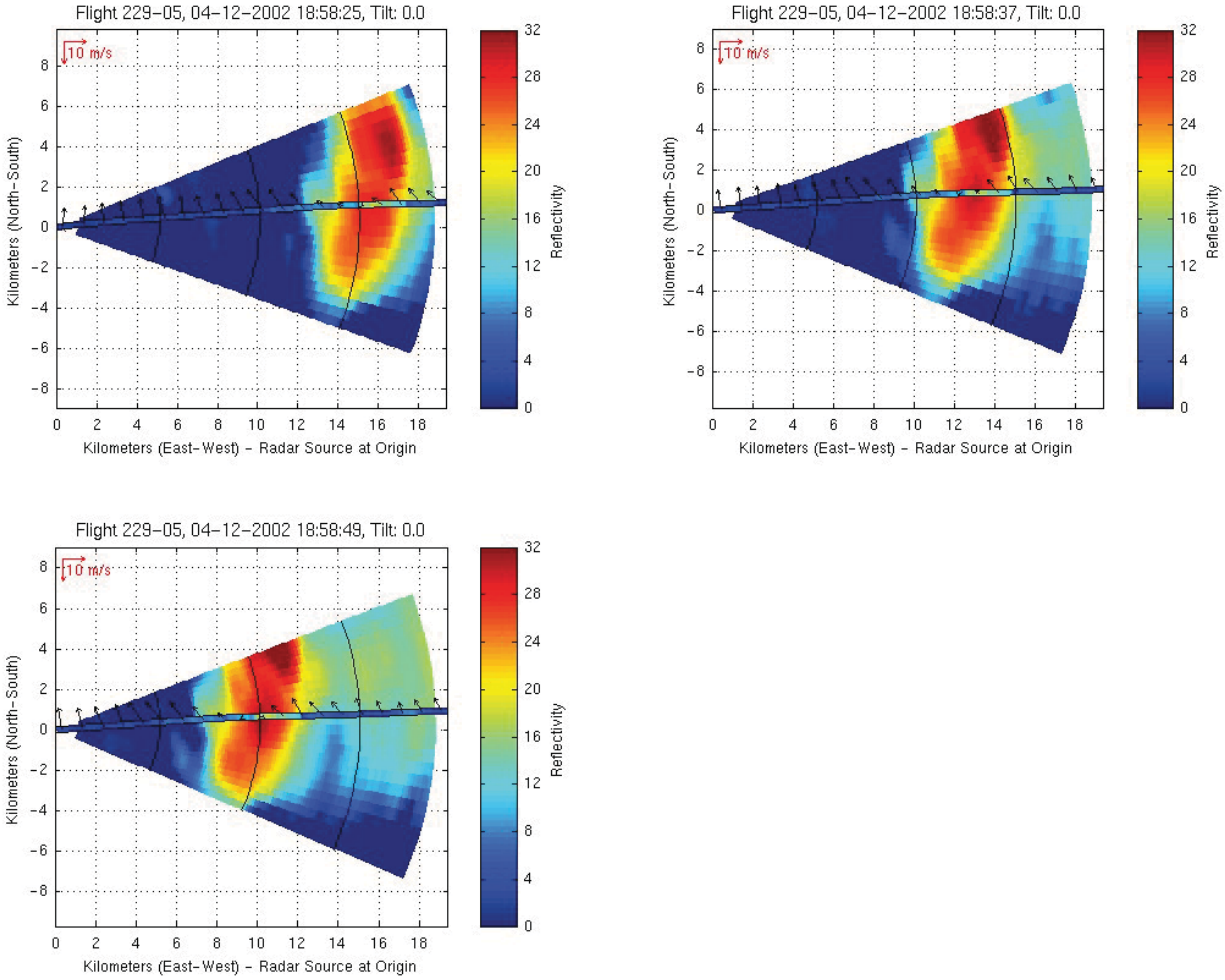

Figure 31. Sequential scans at 12*s* interval for airborne radar reflectivity factor (color contour cones) and *in situ* $\sigma_{\Delta n}$ (color on flight path line) for Event 229-05. Ambient wind vectors are shown along path.

2.6: Flight 230, April 15, 2002

Between 1900 and 2030 UTC on April 15, 2002, ARIES investigated a line of isolated convective cells along the North and South Carolina coastline (Figure 32 and Figure 33). The convective cells were triggered by a westward propagating sea breeze front. No pilot reports of significant turbulence had been issued in the vicinity of convection (Figure 34). Visual meteorological conditions prevailed during the entire flight.

Twelve significant turbulence encounters ($\sigma_{\Delta n} \geq 0.2$ *g*) were associated with the penetration of the isolated convective cells (Figure 35 - Figure 60). On one occasion (event 230-06), the ARIES experienced significant turbulence in the clear-air on the downwind edge of one of the cells (see Figure 38). Accelerometer data showed a fairly intense downdraft on this downwind edge (see Table 1) most likely associated with the compensation region outside of the intense convection. This turbulence may have been associated with the steep horizontal gradients between the compensating downdraft and cloud updraft, which apparently extended outside of the cloud periphery.

Weak to moderate reflectivity was associated with the edges and tops of the storms, which were the primary target regions. Maximum storm tops were about 13.7 *km* (45 *kft*) and cell motion was nearly stationary since the convection was anchored to the slow moving sea breeze. The turbulence encounters occurred at altitudes of 4.5, 5.2, and 7.0 *km* (15, 17, and 23 *kft*). The precipitation encountered along the flight path, as determined from the ARIES external camcorders, was in the form of heavy rain, snow, and what appeared to be large aggregates. The cells remained nearly stationary except for a slight drift towards the east-southeast. The prevailing wind at flight level was 6 *m/s* (12 *kts*) from 330° from true North for events 04, 06, 08, 10, and 12 and about 11.8 *m/s* (23 *kts*) and between 335° and 350° from true North for events 15, 19, 21, and 23. Event 230-02 is not shown since the radar "hazard" scans were taken at –6°, –8°, and –10° tilts.

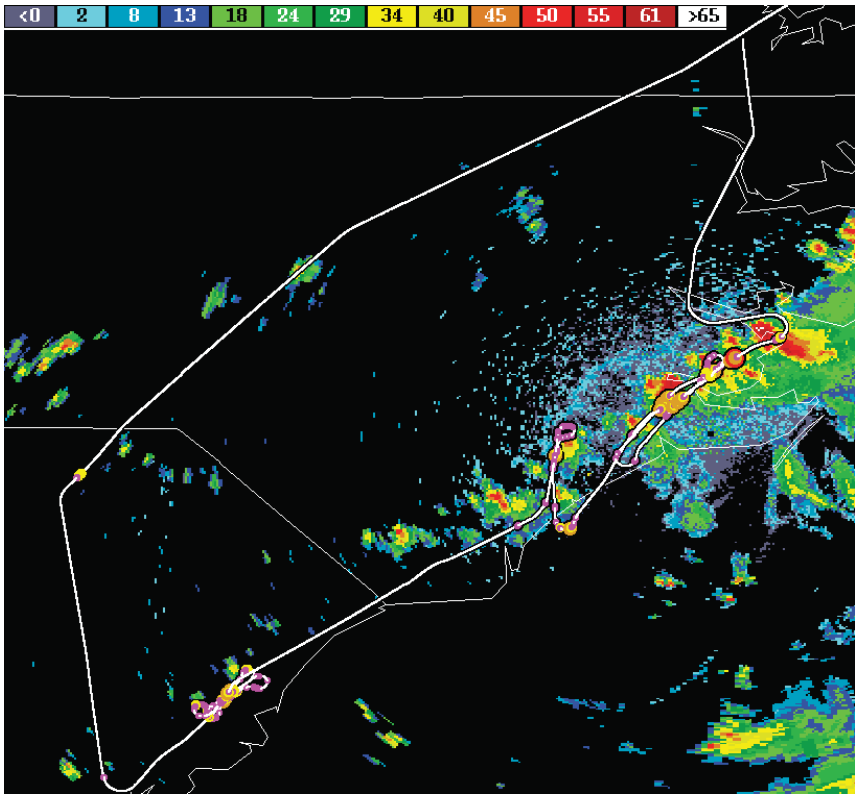

Figure 32. Path for Flight 230. Blended plot of ground based composite radar reflectivity (*dBz*) from the Wilmington, North Carolina 20:03:49 UTC and Morehead City, North Carolina 20:03:49 UTC NEXRAD radars on 15 April 2002. See Figure 3 for legend to intensity of the aircraft RMS normal loads.

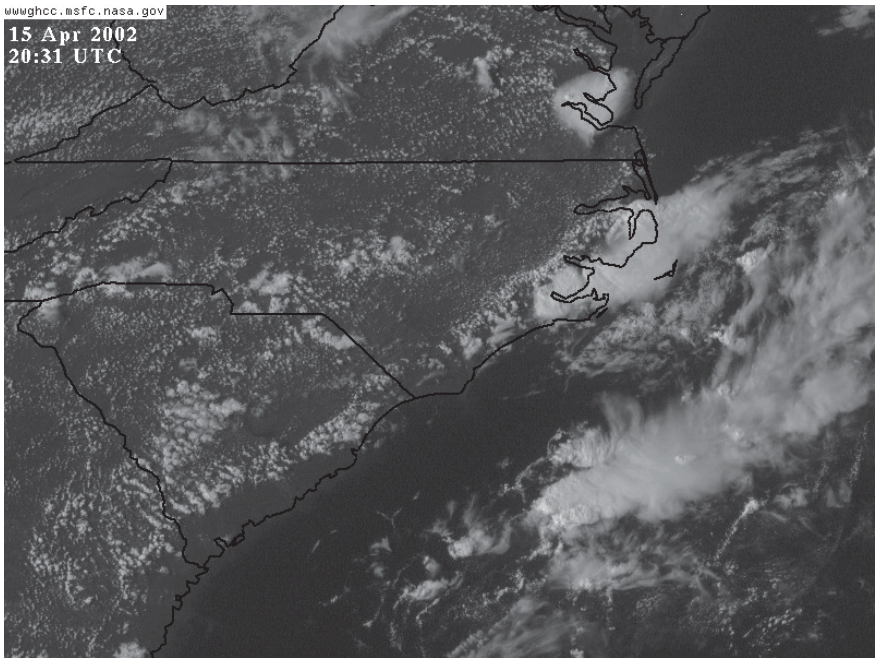

Figure 33. GOES-12 visible satellite image from 20:31 UTC on 15 April 2002.

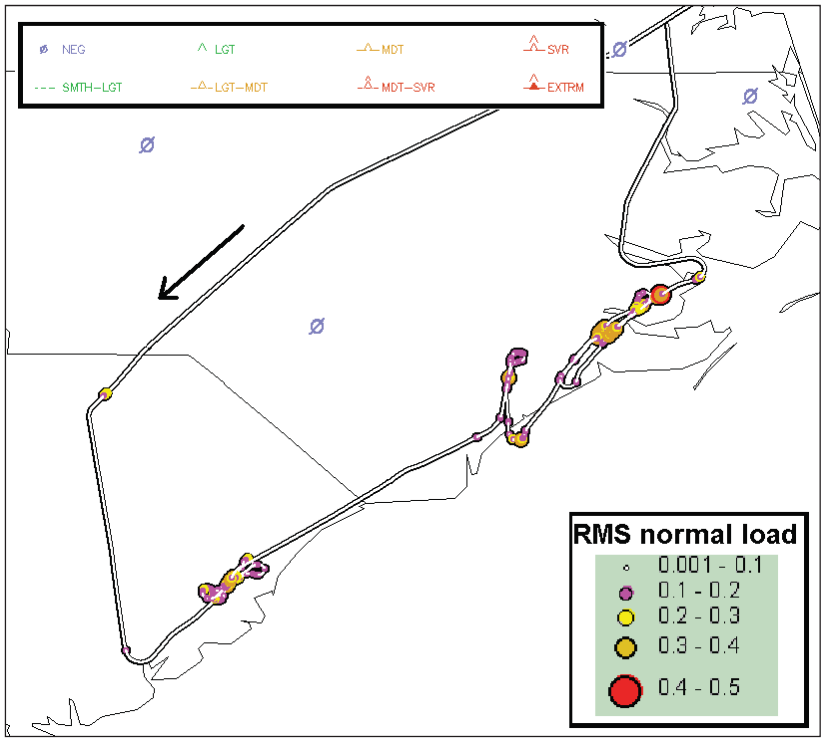

Figure 34. RMS normal loads encountered along the path for Flight 230 with turbulence PIREPS for 15 April 2002.

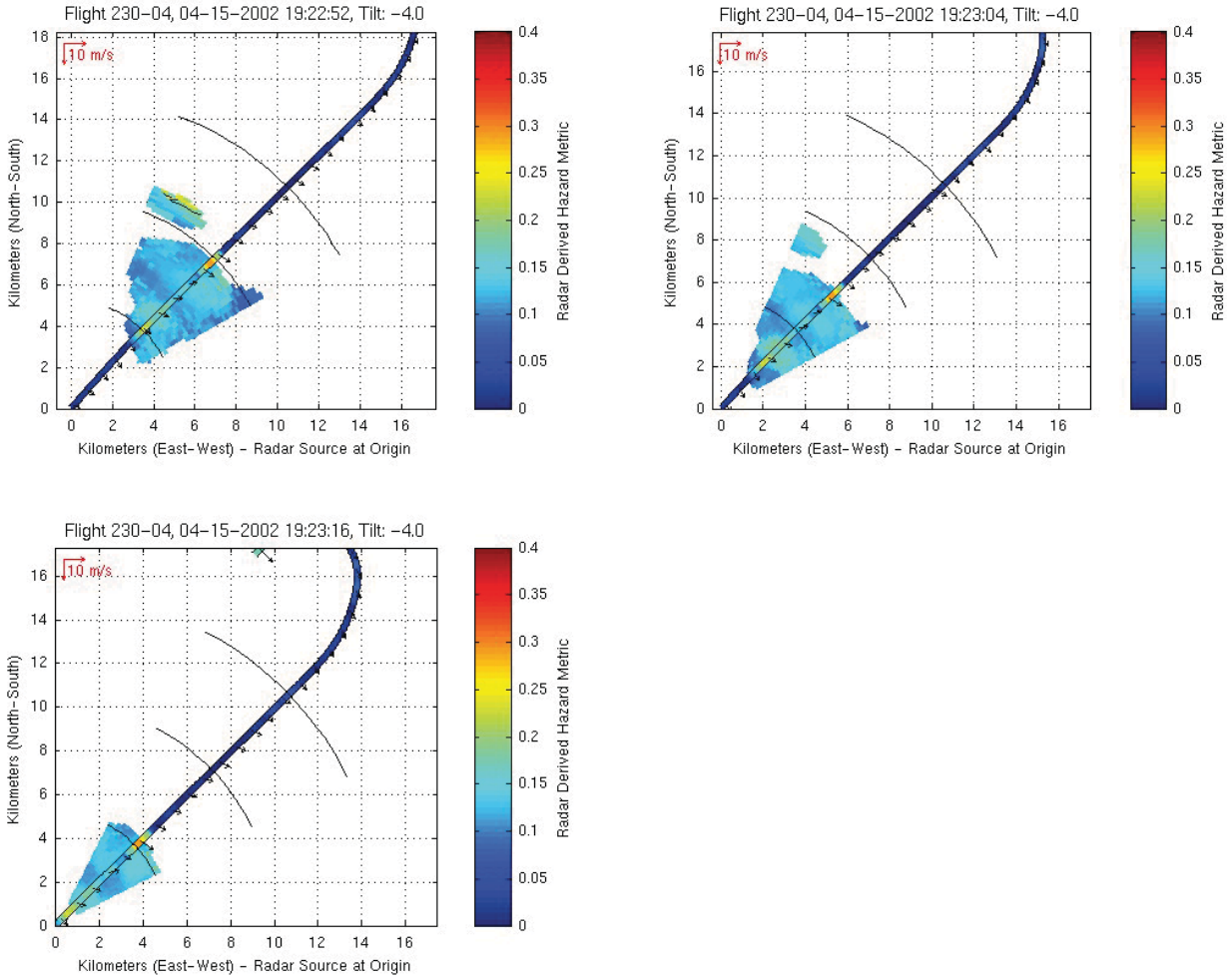

Figure 35. Sequential scans at 12*s* intervals for airborne radar predicted $\sigma_{\Delta n}$ (color contour cones) and *in situ* $\sigma_{\Delta n}$ (color on flight path line) for Event 230-04. Ambient wind vectors are shown along path.

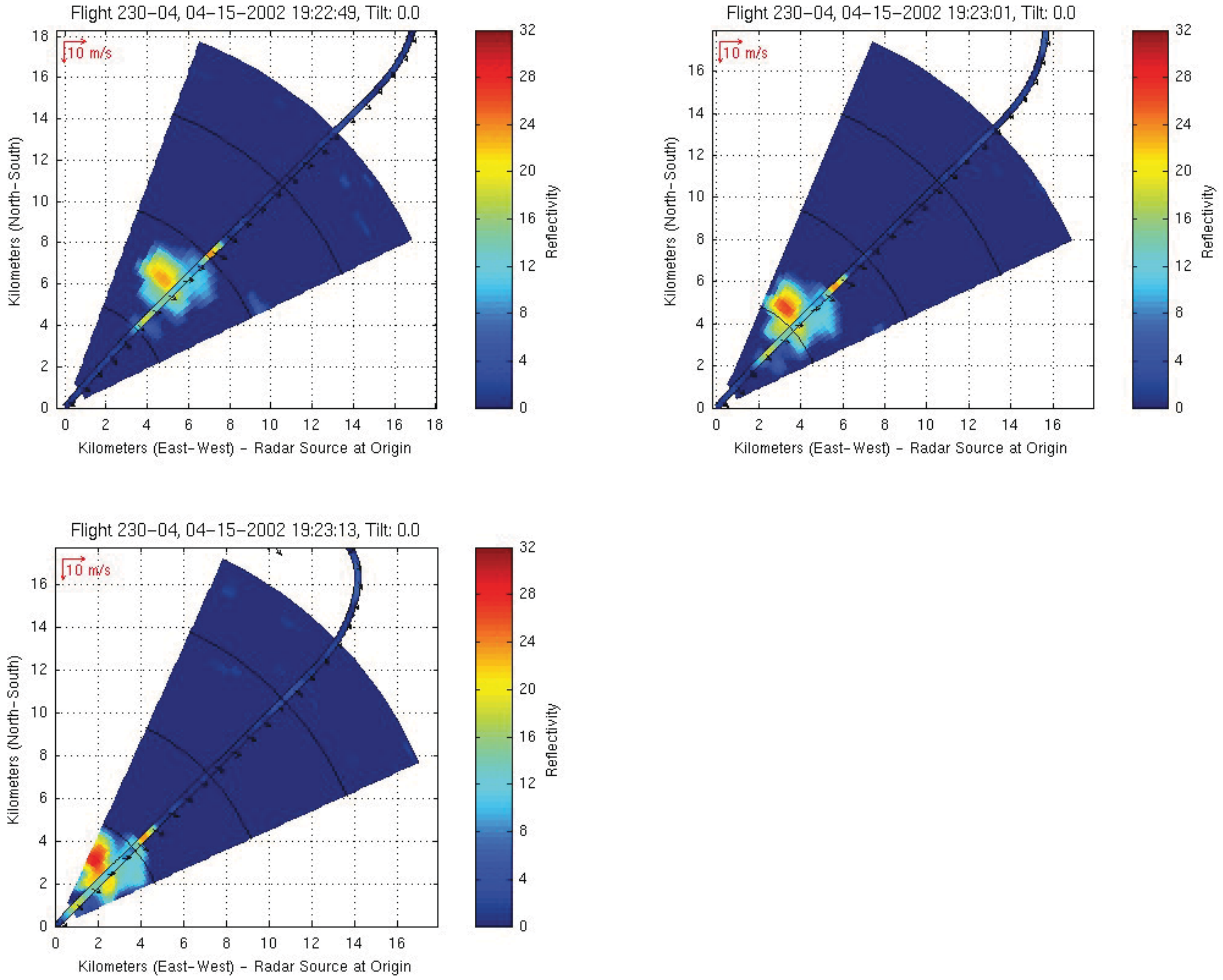

Figure 36. Sequential scans at 12*s* interval for airborne radar reflectivity factor (color contour cones) and *in situ* $\sigma_{\Delta n}$ (color on flight path line) for Event 230-04. Ambient wind vectors are shown along path.

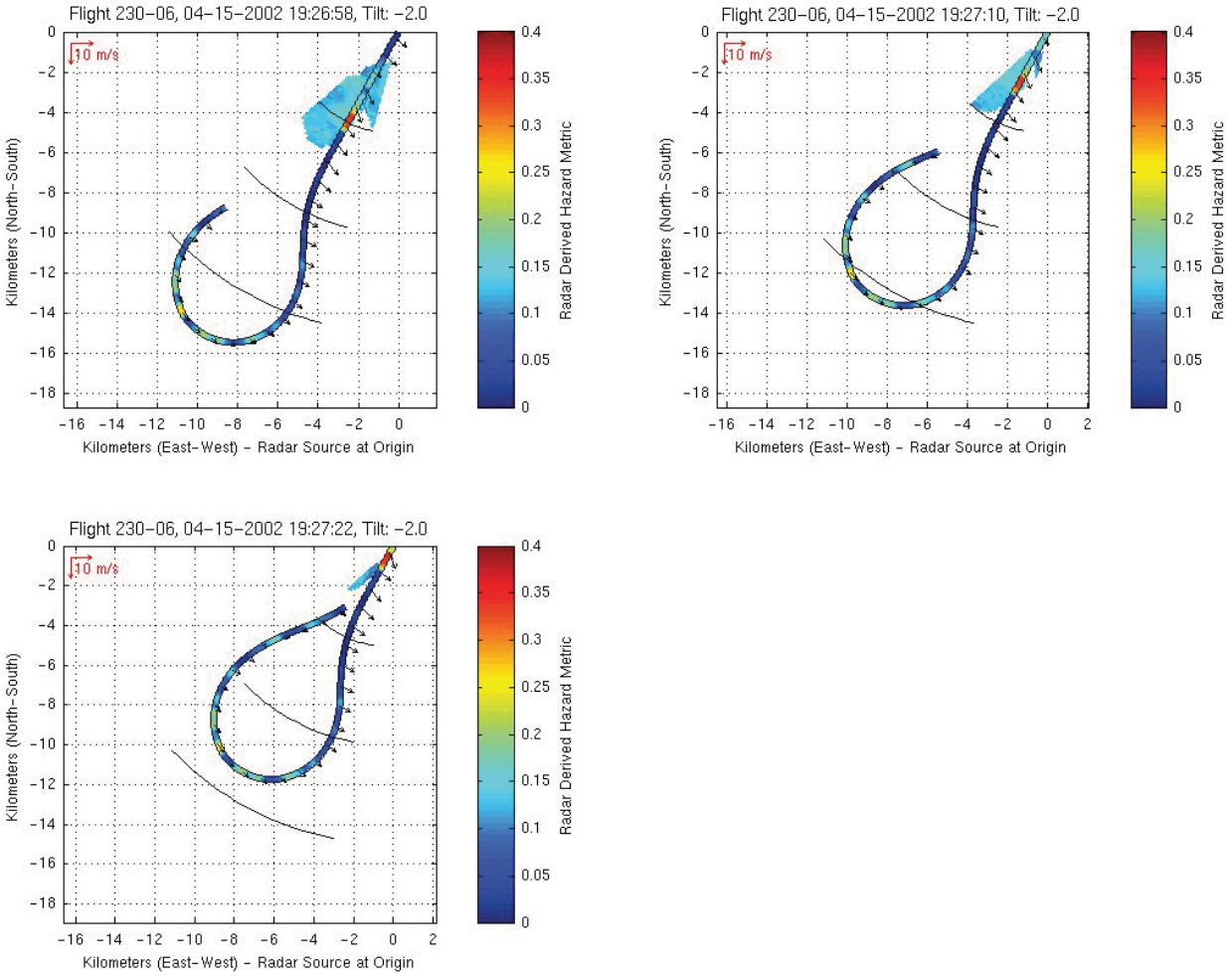

Figure 37. Sequential scans at 12*s* intervals for airborne radar predicted $\sigma_{\Delta n}$ (color contour cones) and *in situ* $\sigma_{\Delta n}$ (color on flight path line) for Event 230-06. In this event, all three "hazard" scans were executed at a tilt of –2°. Ambient wind vectors are shown along path.

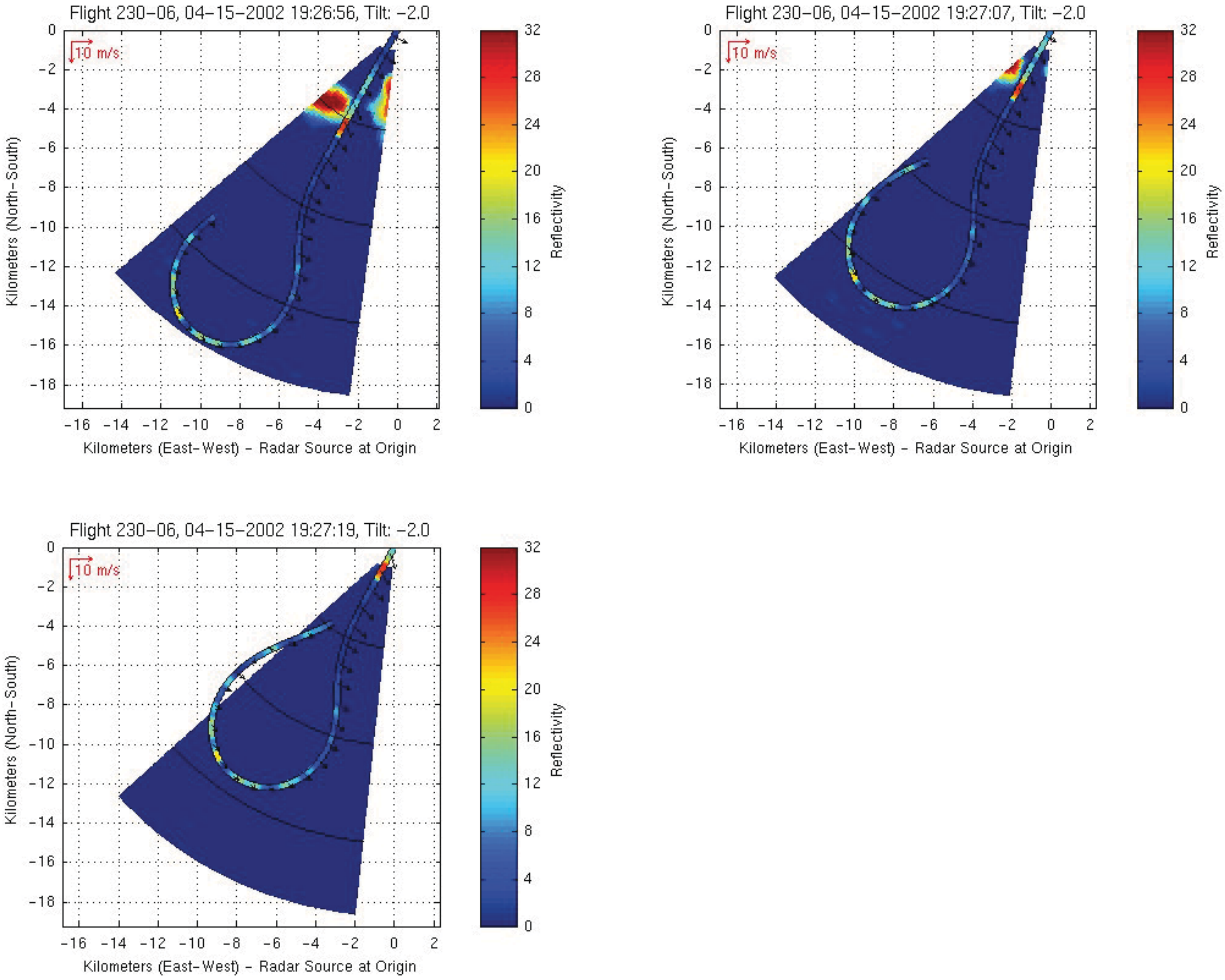

Figure 38. Sequential scans at 12*s* interval for airborne radar reflectivity factor (color contour cones) and *in situ* $\sigma_{\Delta n}$ (color on flight path line) for Event 230-06. In this event, all three scans were executed at a tilt of –2°. Ambient wind vectors are shown along path.

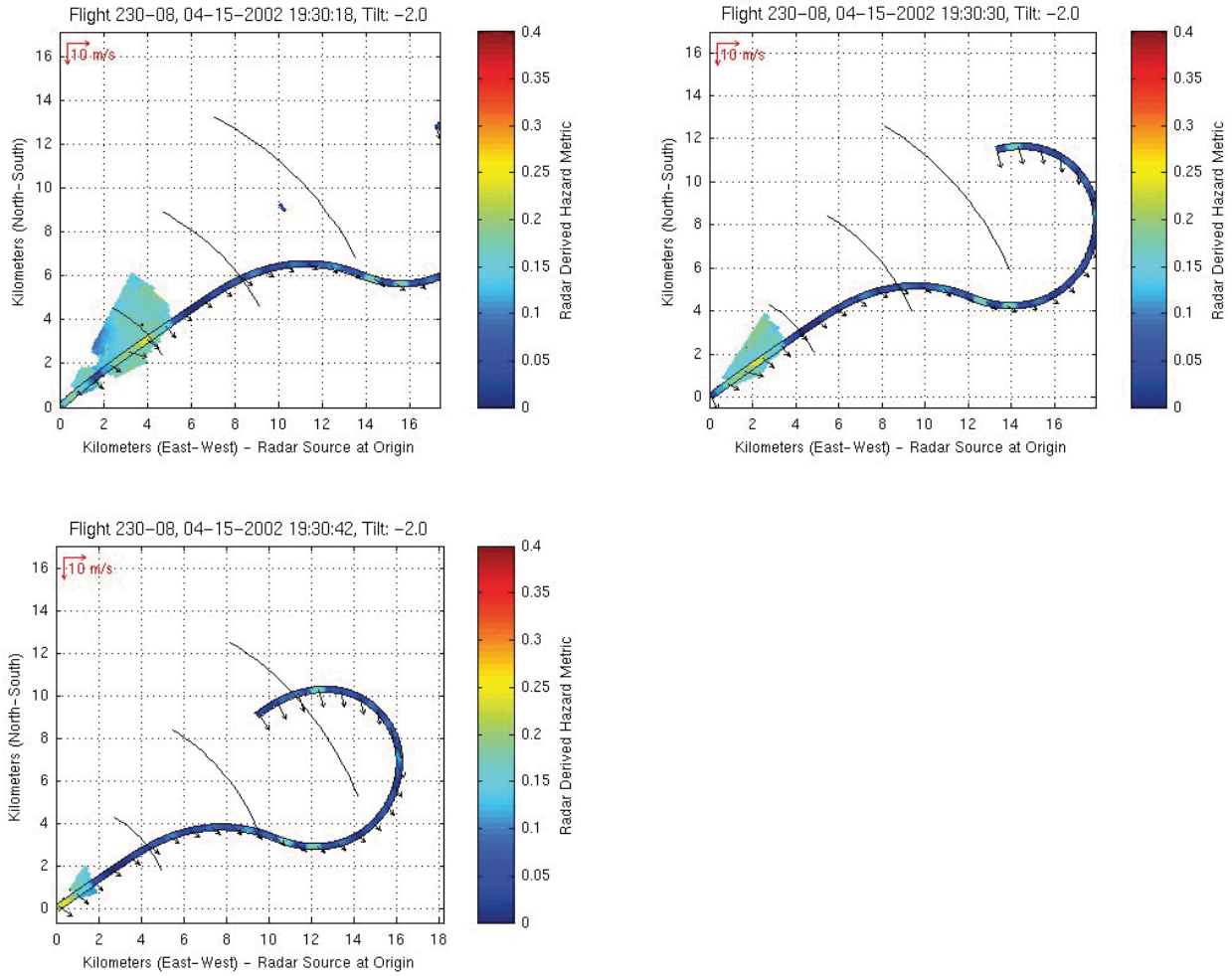

Figure 39. Sequential scans at 12*s* intervals for airborne radar predicted $\sigma_{\Delta n}$ (color contour cones) and *in situ* $\sigma_{\Delta n}$ (color on flight path line) for Event 230-08. In this event, all three "hazard" scans were executed at a tilt of –2°. Ambient wind vectors are shown along path.

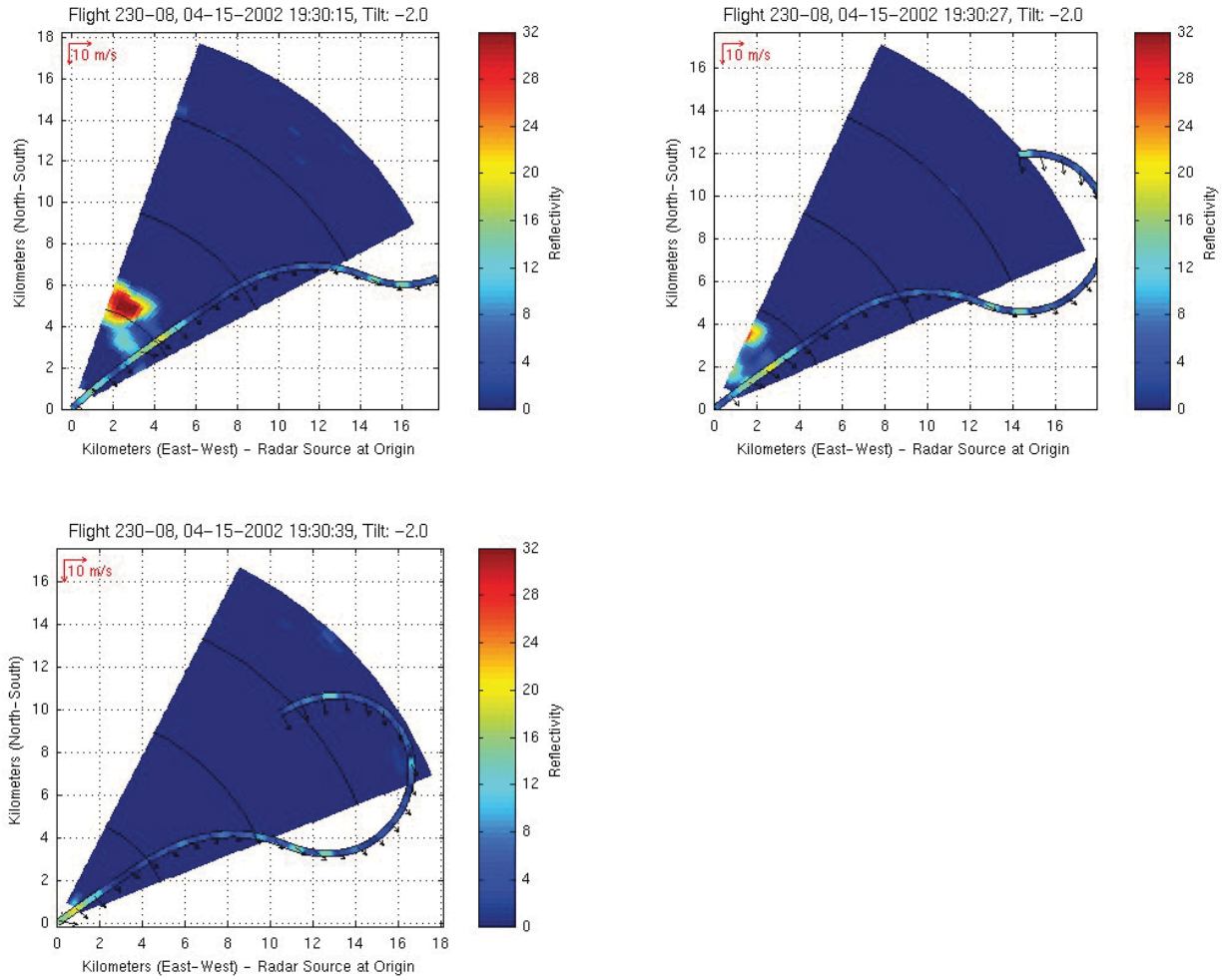

Figure 40. Sequential scans at 12*s* interval for airborne radar reflectivity factor (color contour cones) and *in situ* $\sigma_{\Delta n}$ (color on flight path line) for Event 230-08. In this event, all three scans were executed at a tilt of –2°. Ambient wind vectors are shown along path.

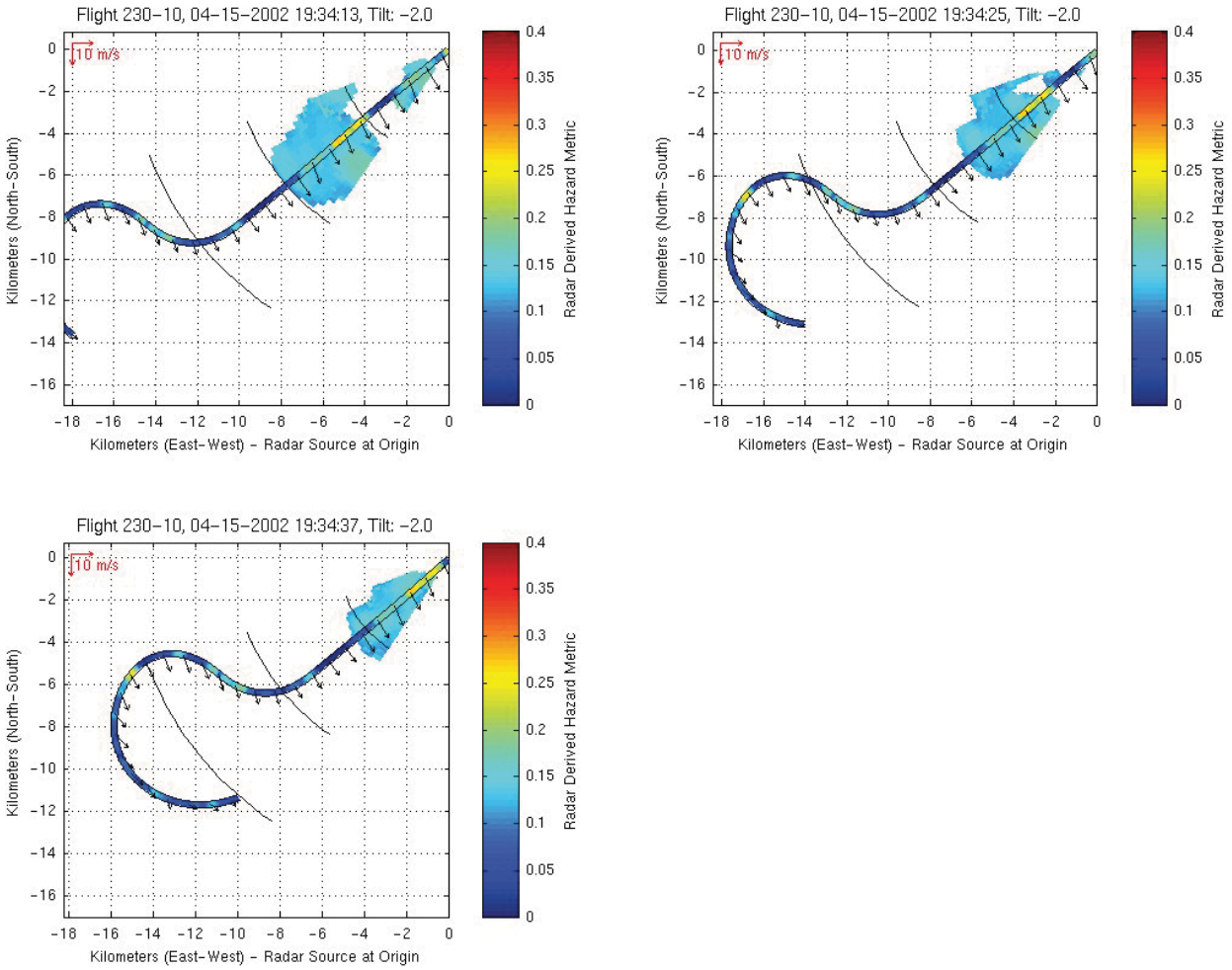

Figure 41. Sequential scans at 12*s* intervals for airborne radar predicted $\sigma_{\Delta n}$ (color contour cones) and *in situ* $\sigma_{\Delta n}$ (color on flight path line) for Event 230-10. In this event, all three "hazard" scans were executed at a tilt of –2°. Ambient wind vectors are shown along path.

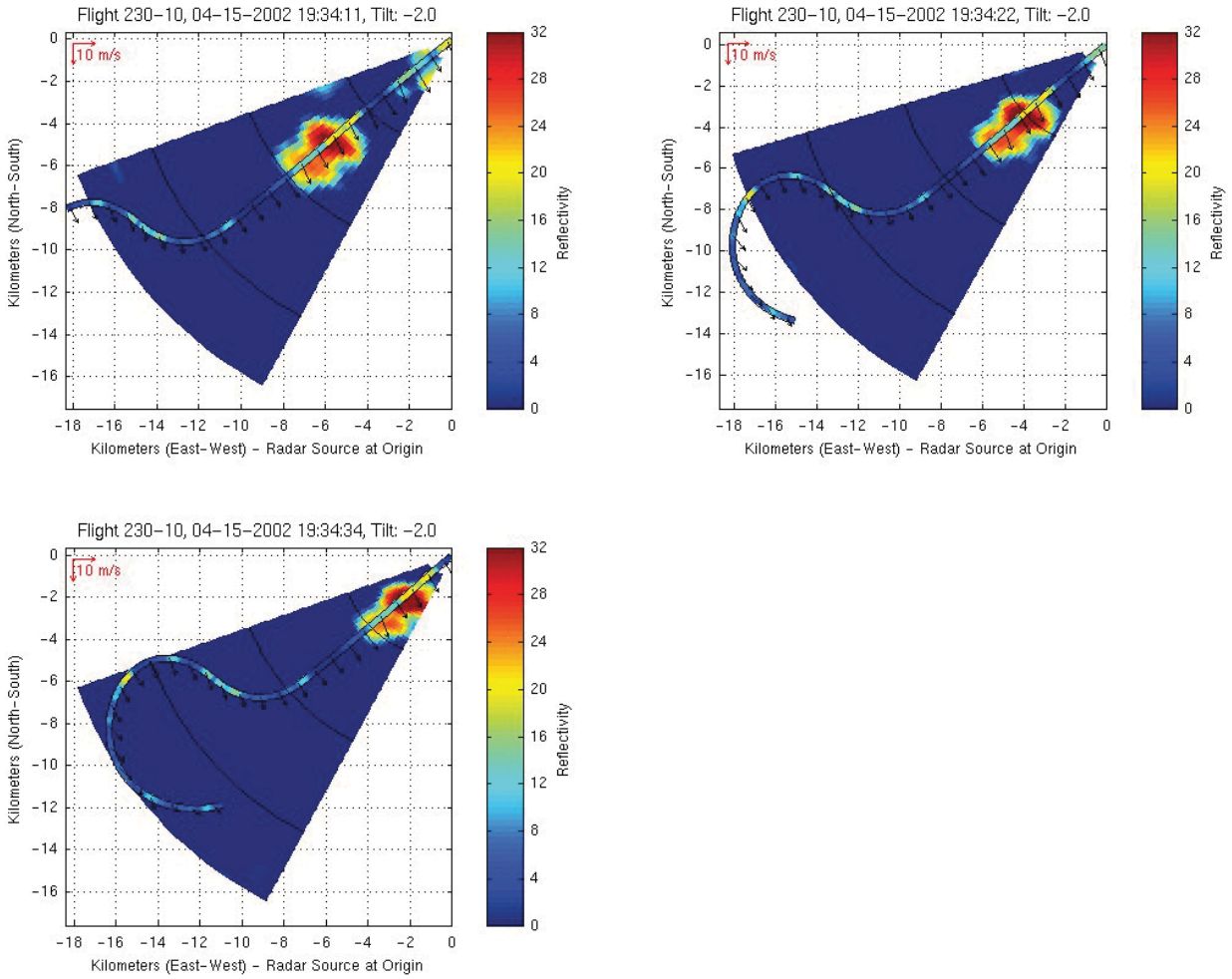

Figure 42. Sequential scans at 12*s* interval for airborne radar reflectivity factor (color contour cones) and *in situ* $\sigma_{\Delta n}$ (color on flight path line) for Event 230-10. In this event, all three scans were executed at a tilt of –2°. Ambient wind vectors are shown along path.

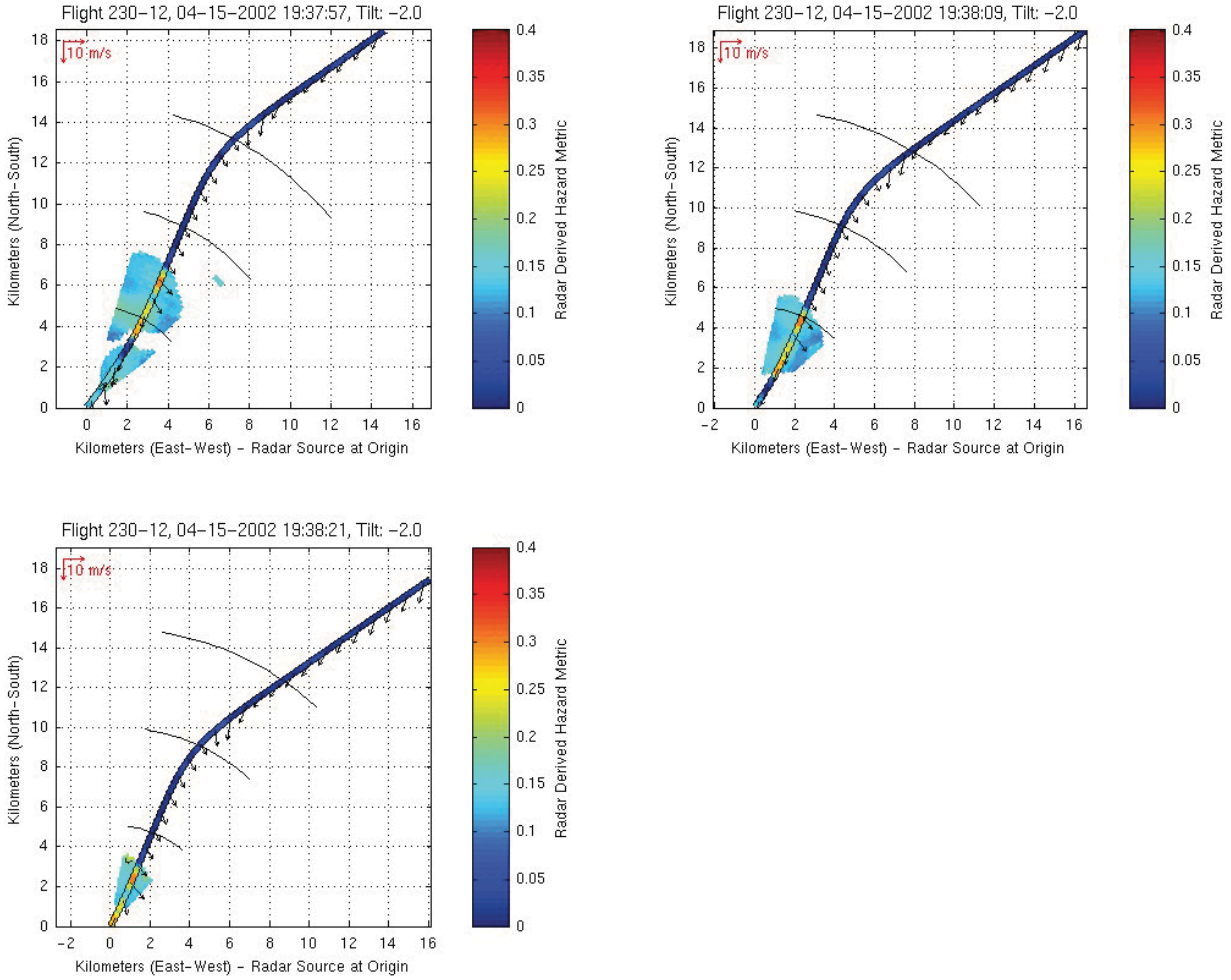

Figure 43. Sequential scans at 12*s* intervals for airborne radar predicted $\sigma_{\Delta n}$ (color contour cones) and *in situ* $\sigma_{\Delta n}$ (color on flight path line) for Event 230-12. In this event, all three "hazard" scans were executed at a tilt of –2°. Ambient wind vectors are shown along path.

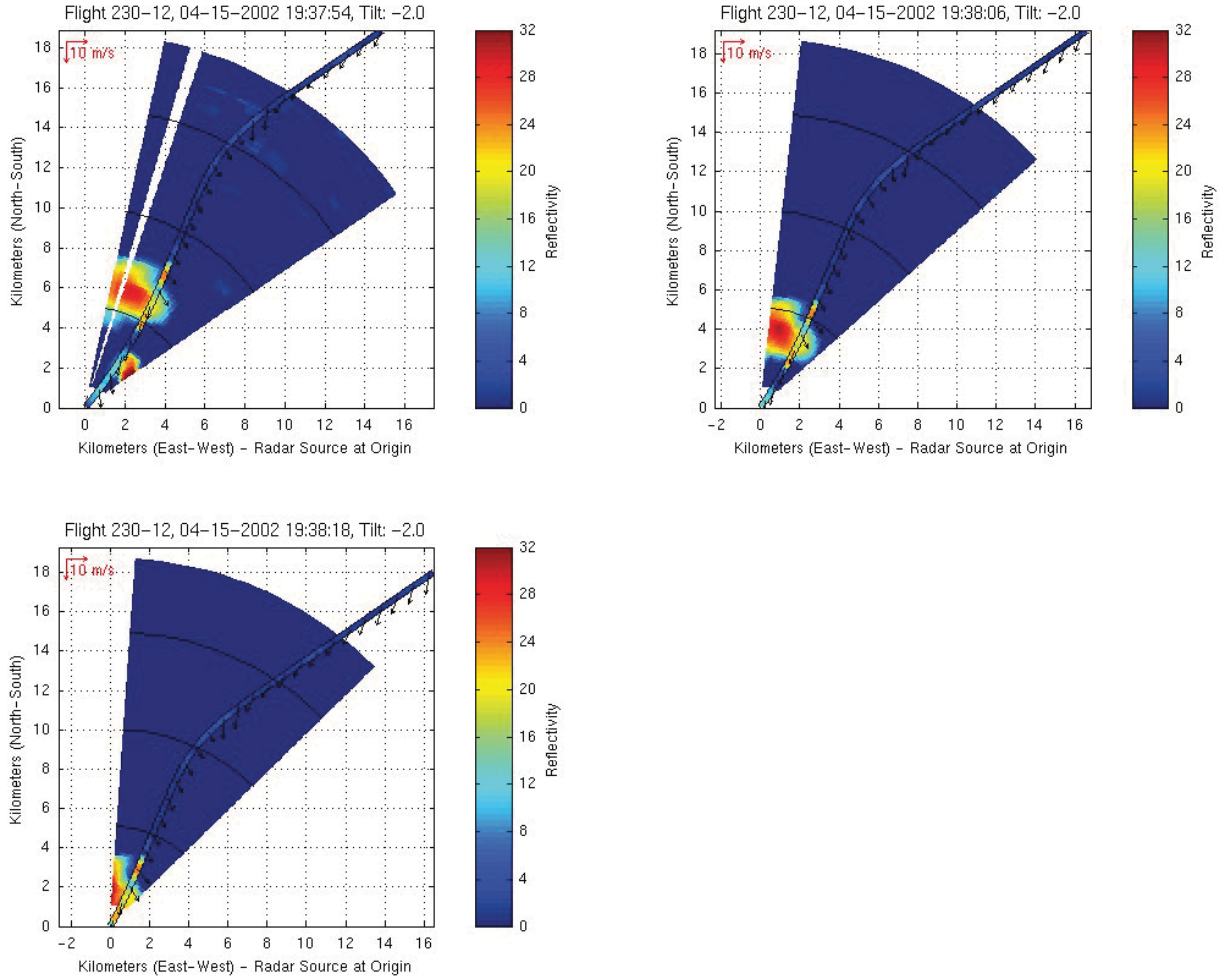

Figure 44. Sequential scans at 12*s* interval for airborne radar reflectivity factor (color contour cones) and *in situ* $\sigma_{\Delta n}$ (color on flight path line) for Event 230-12. In this event, all three scans were executed at a tilt of –2°. Ambient wind vectors are shown along path.

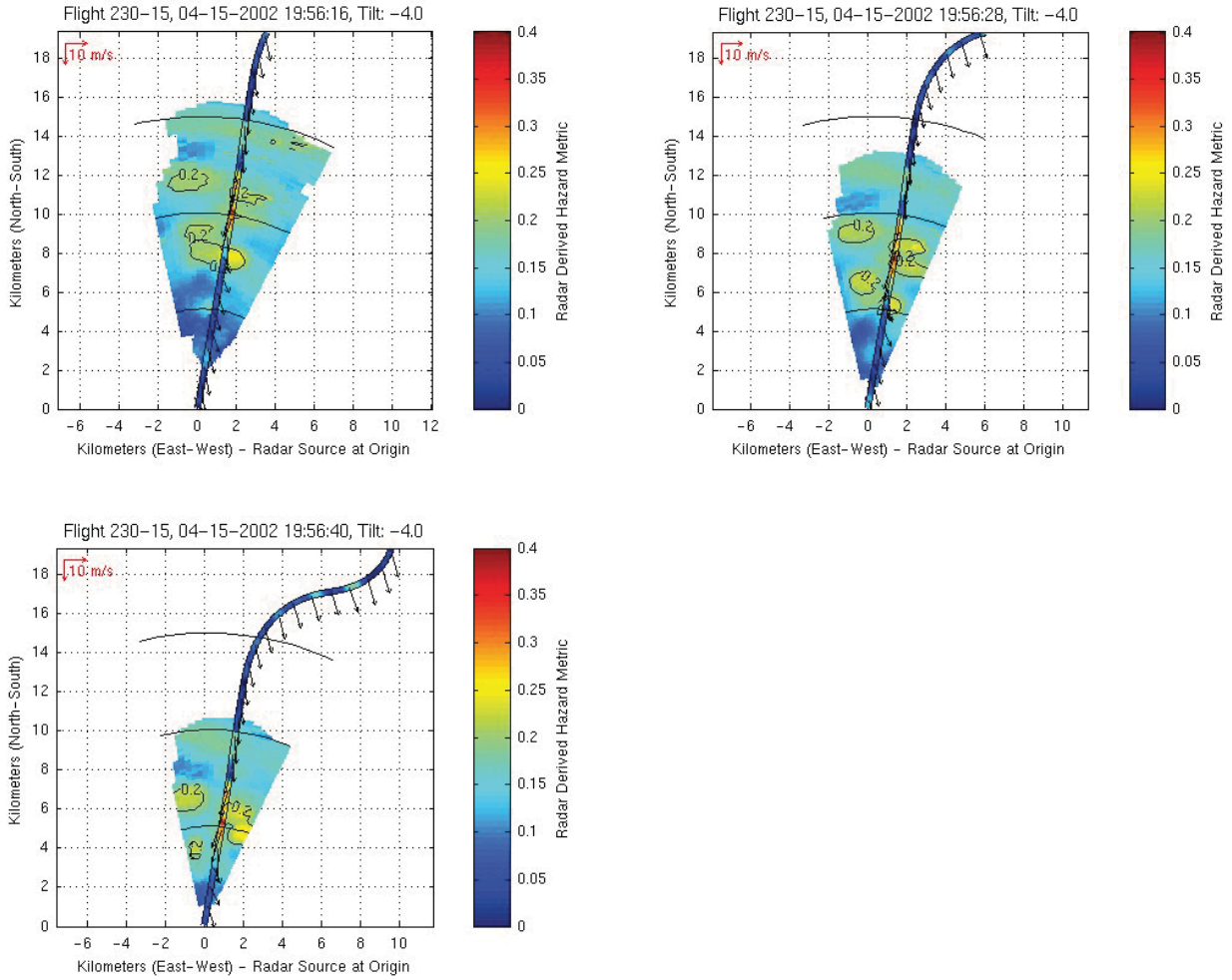

Figure 45. Sequential scans at 12*s* intervals for airborne radar predicted $\sigma_{\Delta n}$ (color contour cones) and *in situ* $\sigma_{\Delta n}$ (color on flight path line) for Event 230-15. Ambient wind vectors are shown along path.

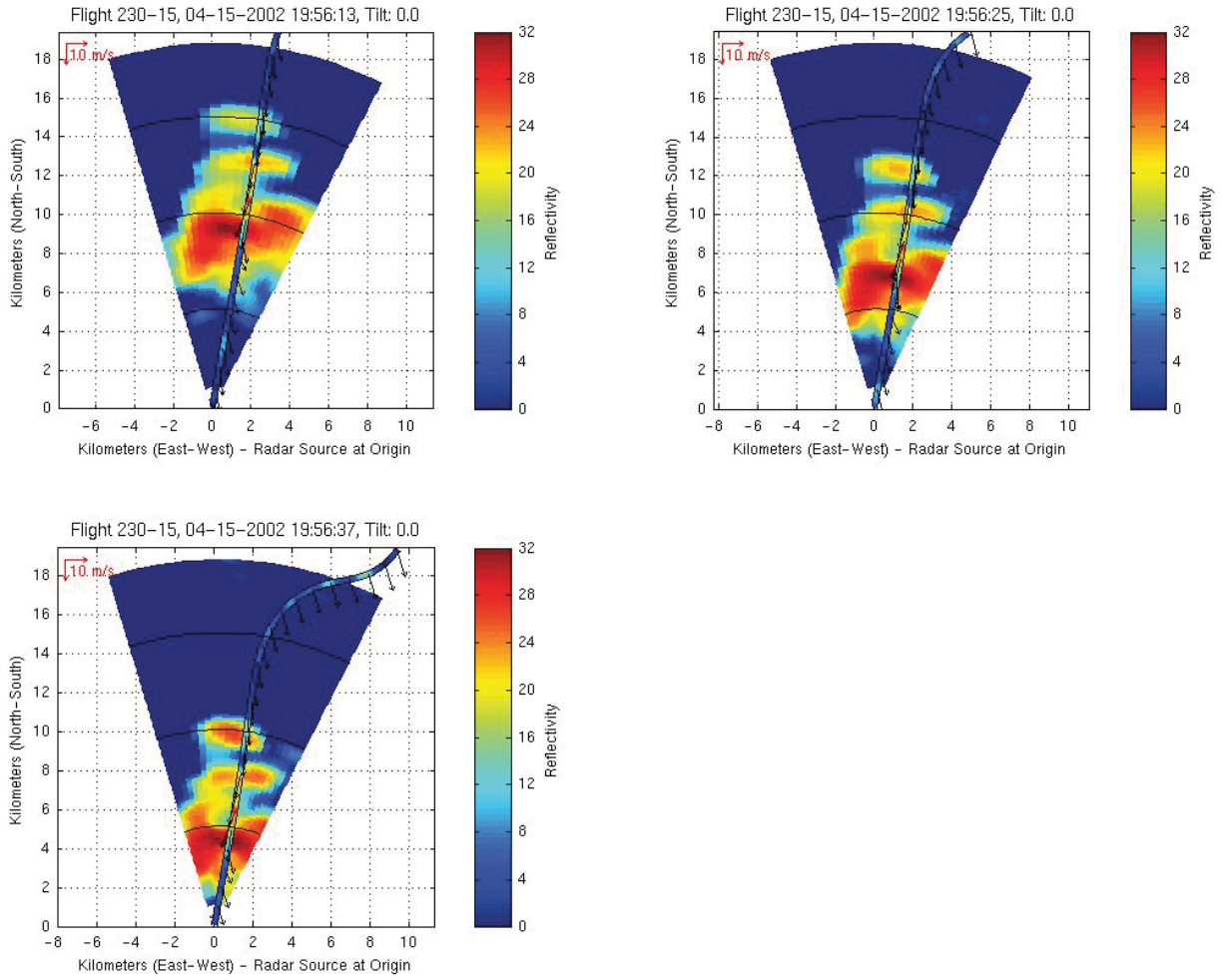

Figure 46. Sequential scans at 12*s* interval for airborne radar reflectivity factor (color contour cones) and *in situ* $\sigma_{\Delta n}$ (color on flight path line) for Event 230-15. Ambient wind vectors are shown along path.

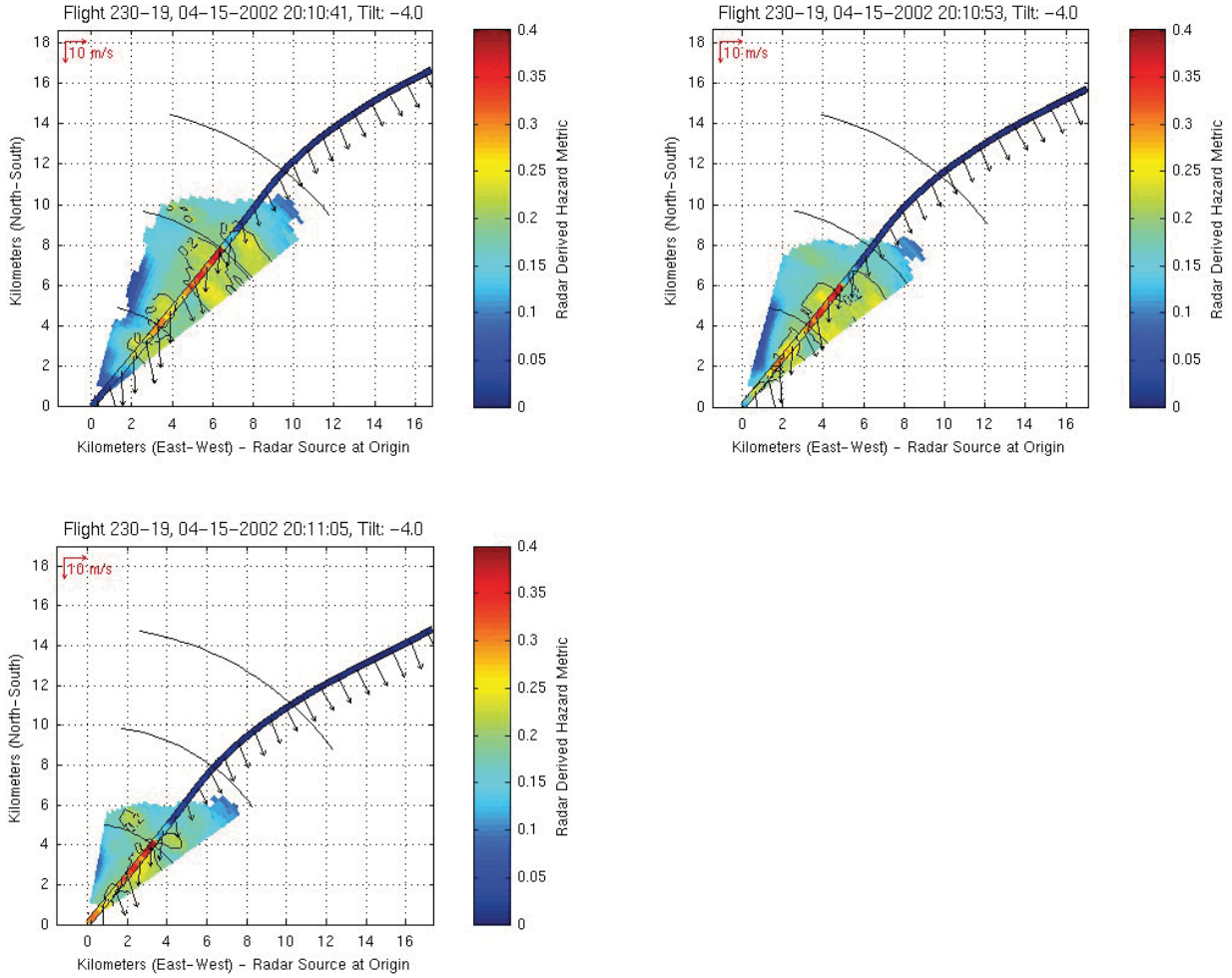

Figure 47. Sequential scans at 12*s* intervals for airborne radar predicted $\sigma_{\Delta n}$ (color contour cones) and *in situ* $\sigma_{\Delta n}$ (color on flight path line) for Event 230-19. Ambient wind vectors are shown along path.

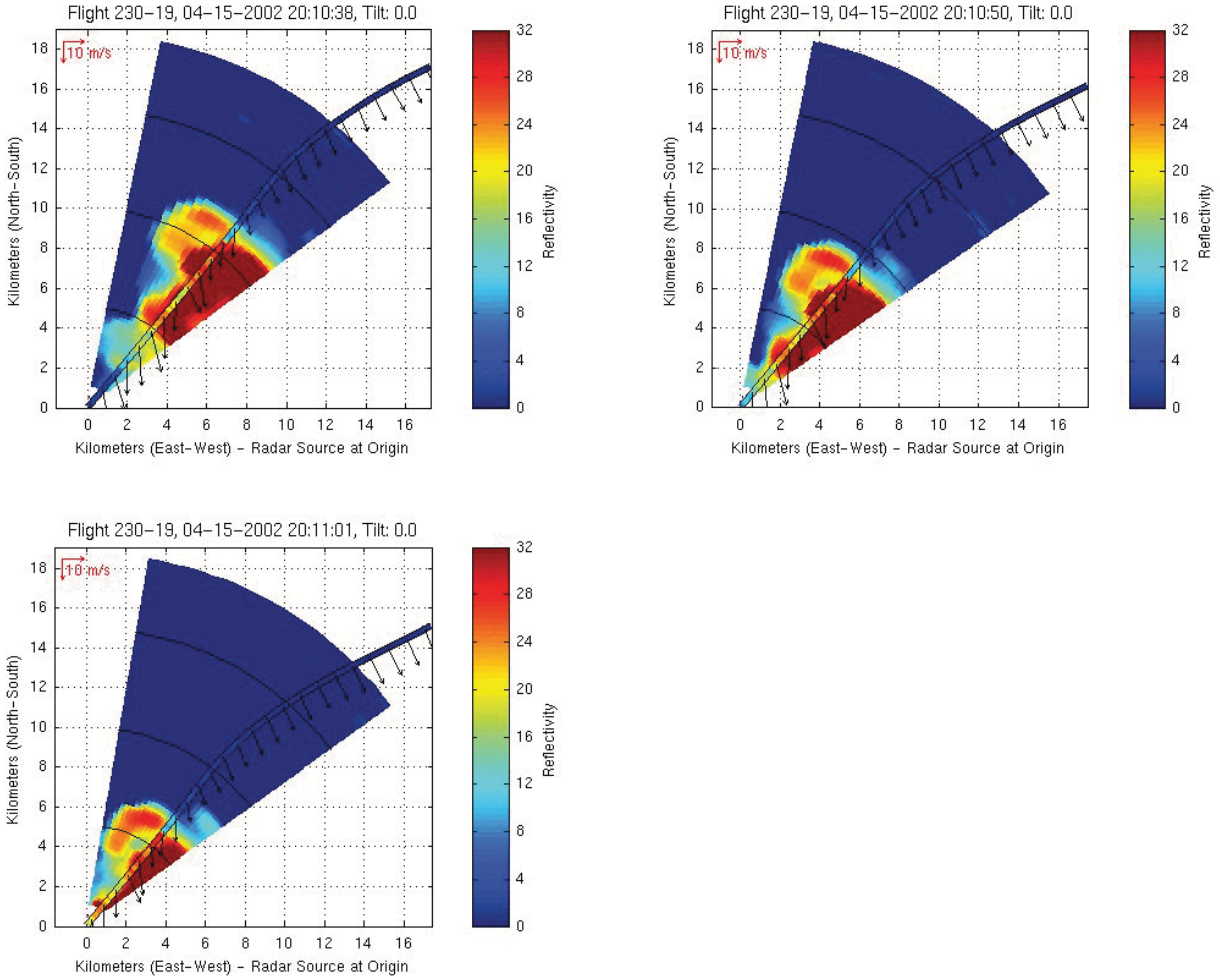

Figure 48. Sequential scans at 12*s* interval for airborne radar reflectivity factor (color contour cones) and *in situ* $\sigma_{\Delta n}$ (color on flight path line) for Event 230-19. Ambient wind vectors are shown along path.

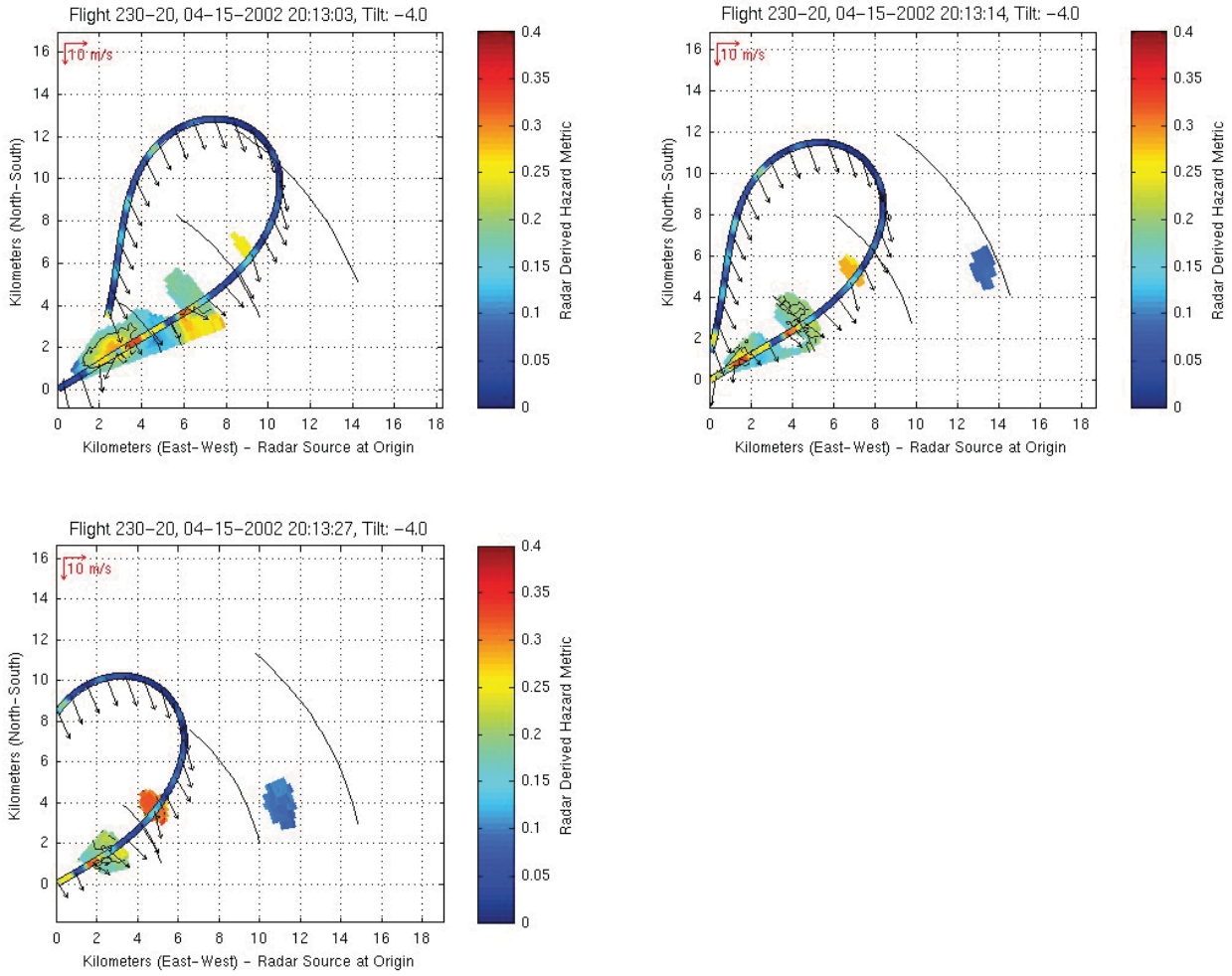

Figure 49. Sequential scans at 12*s* intervals for airborne radar predicted $\sigma_{\Delta n}$ (color contour cones) and *in situ* $\sigma_{\Delta n}$ (color on flight path line) for Event 230-20. Ambient wind vectors are shown along path.

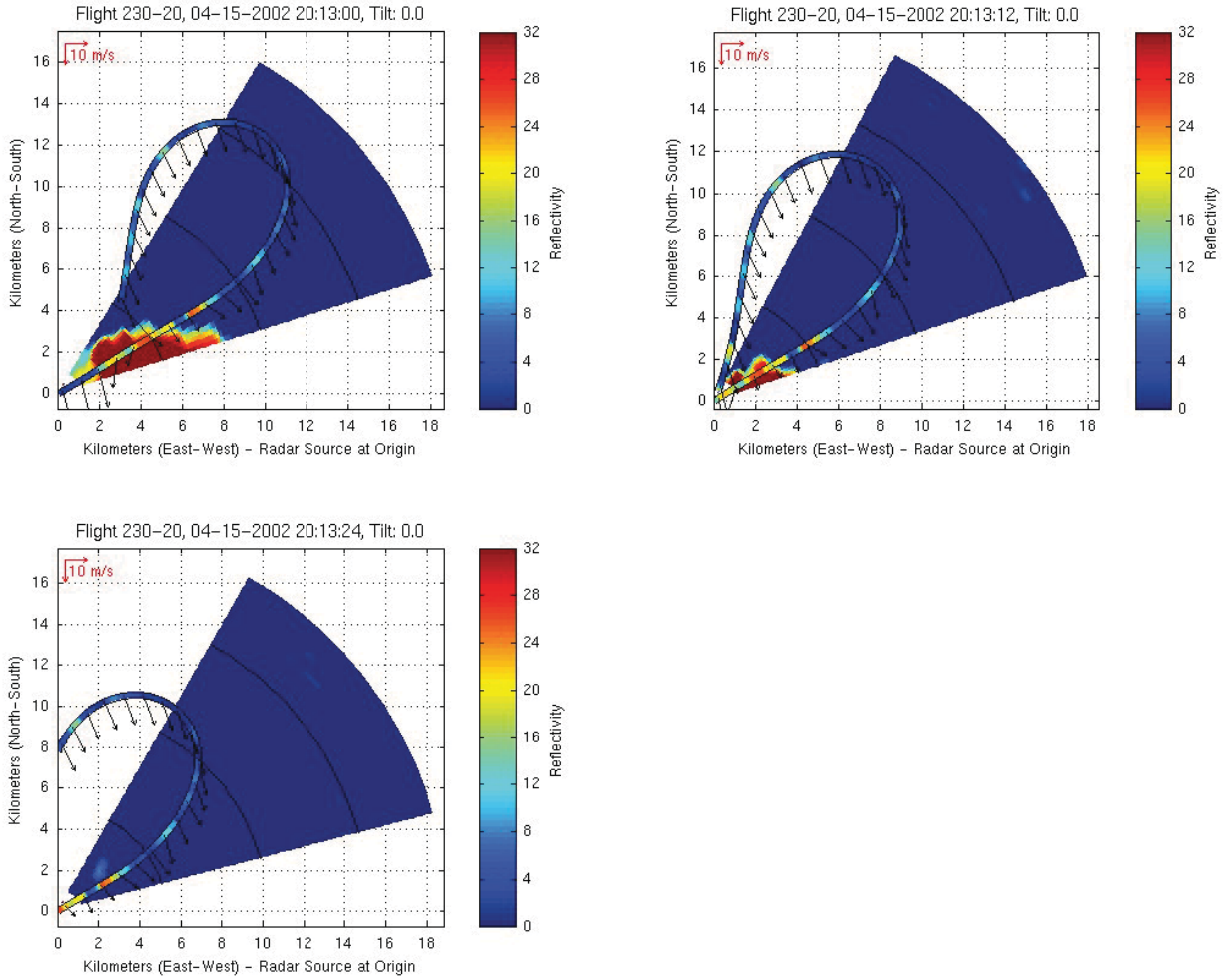

Figure 50. Sequential scans at 12*s* interval for airborne radar reflectivity factor (color contour cones) and *in situ* $\sigma_{\Delta n}$ (color on flight path line) for Event 230-20. Ambient wind vectors are shown along path.

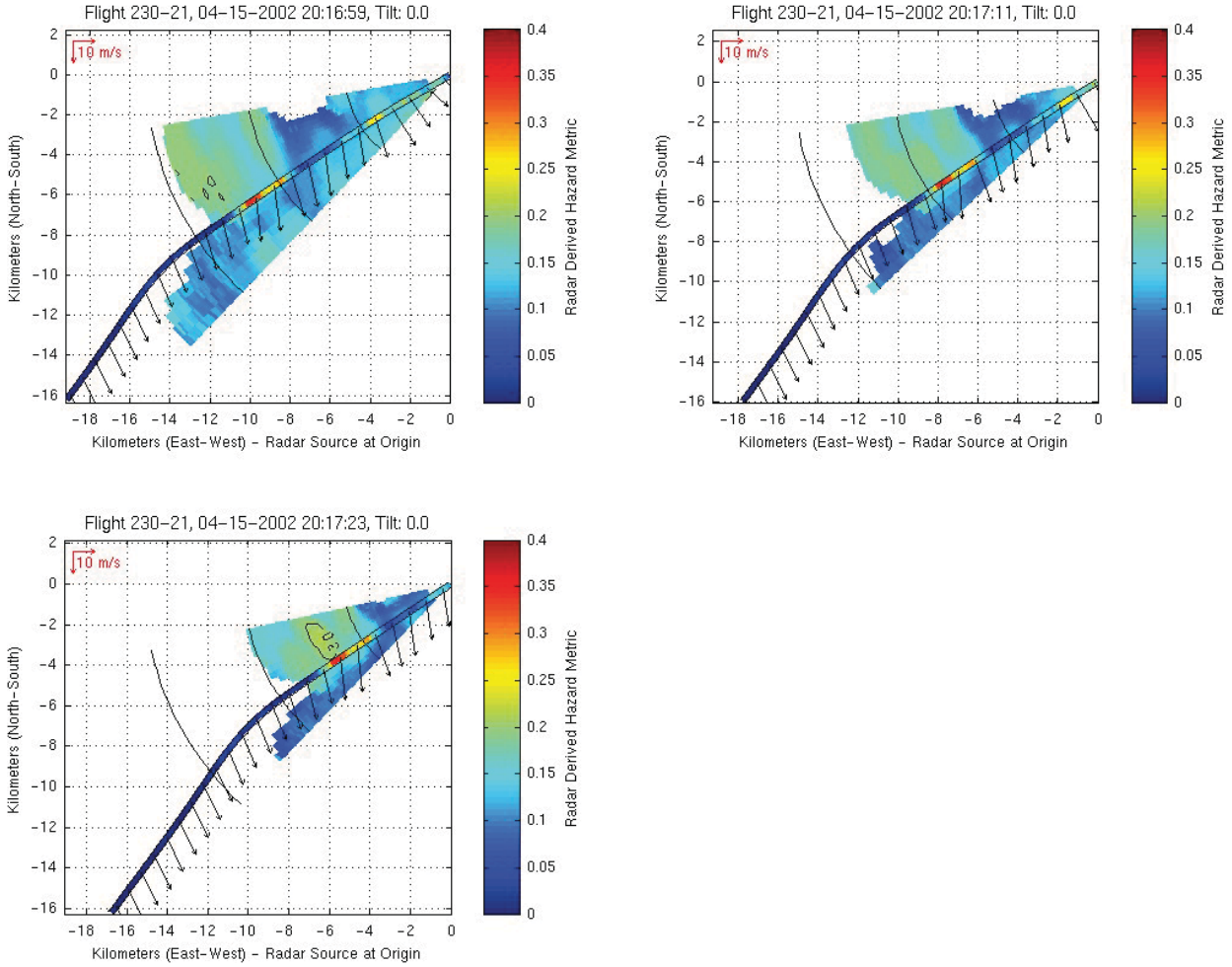

Figure 51. Sequential scans at 12*s* intervals for airborne radar predicted $\sigma_{\Delta n}$ (color contour cones) and *in situ* $\sigma_{\Delta n}$ (color on flight path line) for Event 230-21. In this event, all three "hazard" scans were executed at a tilt of 0^{o}. Ambient wind vectors are shown along path.

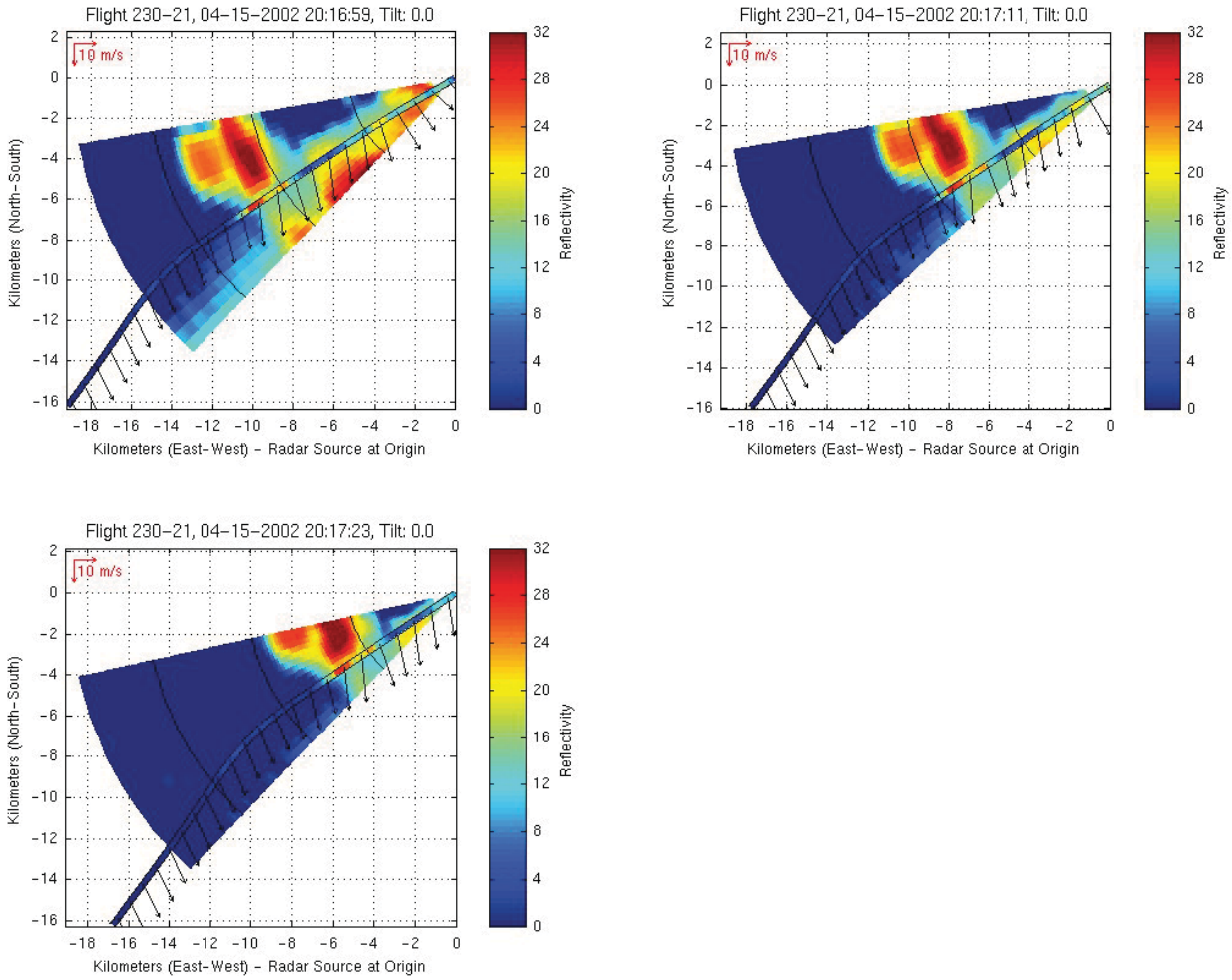

Figure 52. Sequential scans at 12*s* interval for airborne radar reflectivity factor (color contour cones) and *in situ* $\sigma_{\Delta n}$ (color on flight path line) for Event 230-21. In this event, all three scans were executed at a tilt of 0°. Ambient wind vectors are shown along path.

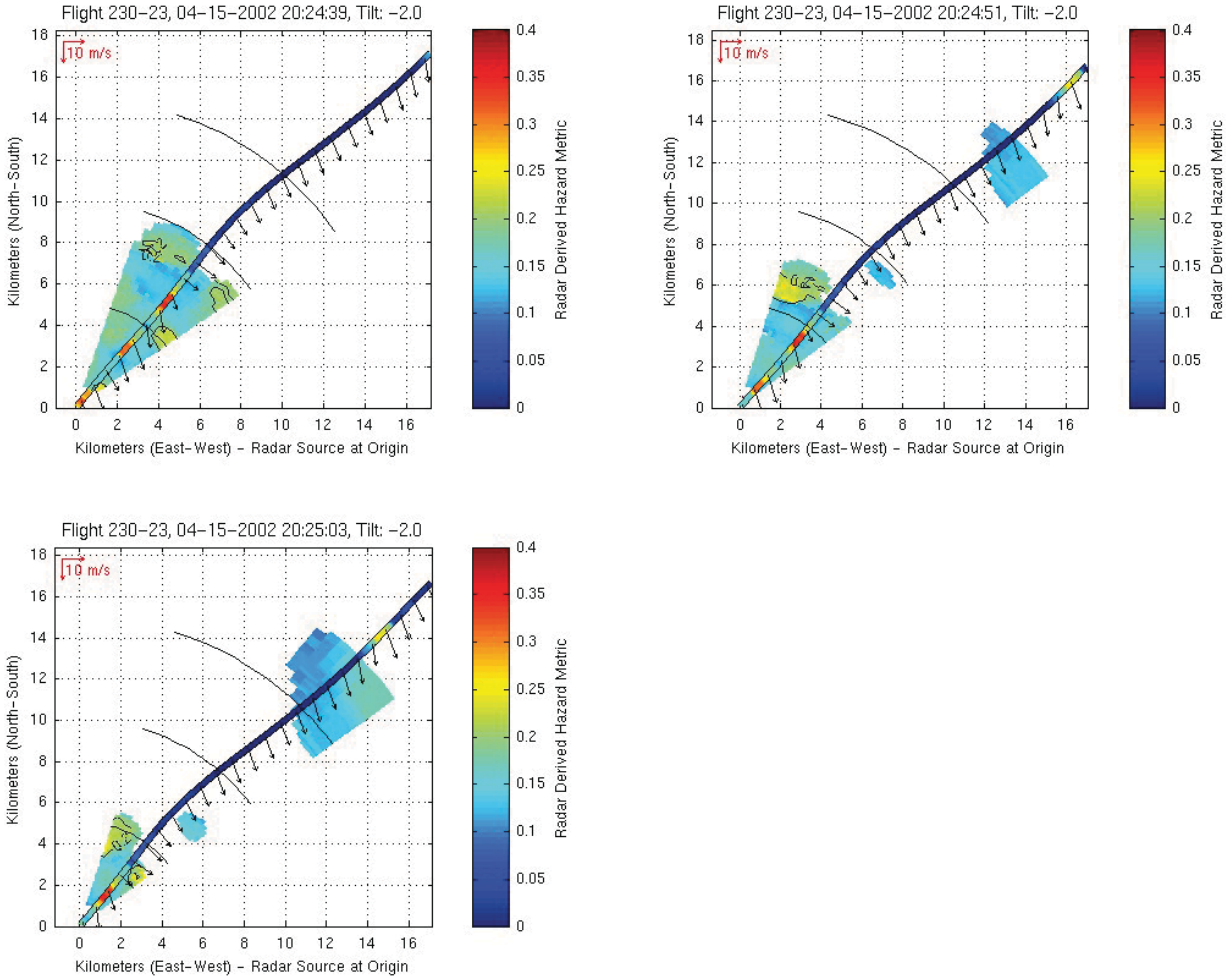

Figure 53. Sequential scans at 12*s* intervals for airborne radar predicted $\sigma_{\Delta n}$ (color contour cones) and *in situ* $\sigma_{\Delta n}$ (color on flight path line) for Event 230-23. In this event, all three "hazard" scans were executed at a tilt of –2°. Ambient wind vectors are shown along path.

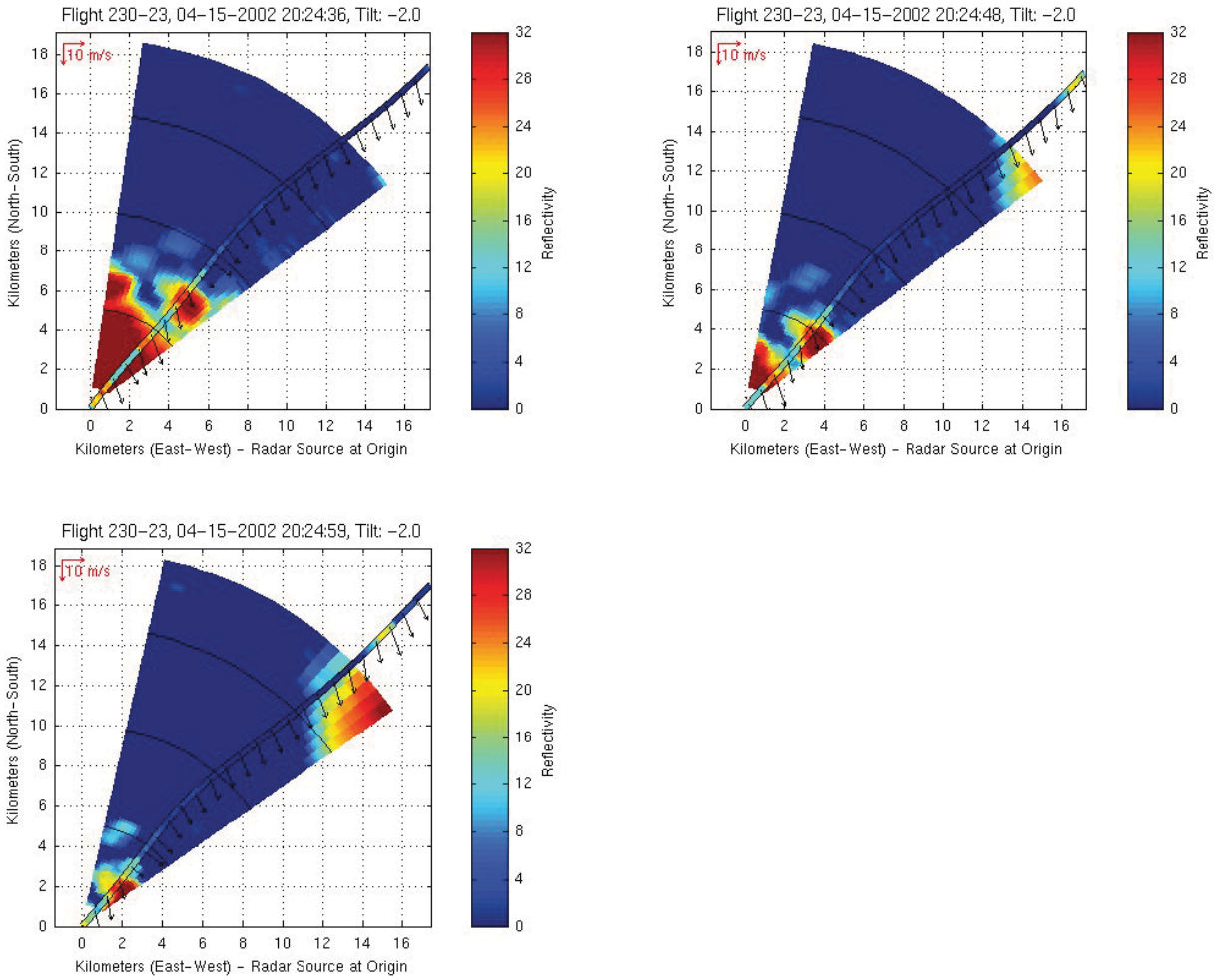

Figure 54. Sequential scans at 12*s* interval for airborne radar reflectivity factor (color contour cones) and *in situ* $\sigma_{\Delta n}$ (color on flight path line) for Event 230-23. In this event, all three scans were executed at a tilt of –2°. Ambient wind vectors are shown along path.

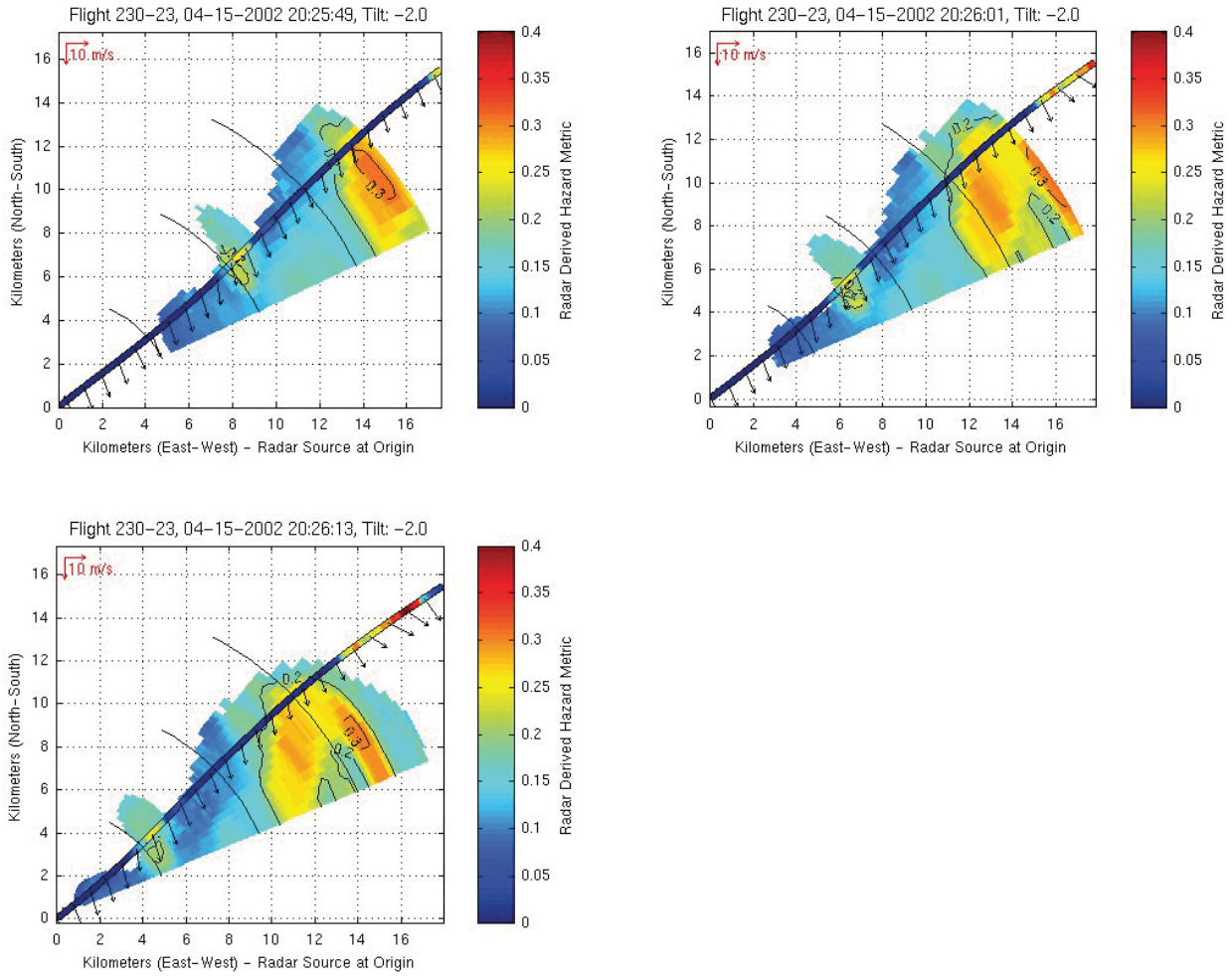

Figure 55. Sequential scans at 12*s* intervals for airborne radar predicted $\sigma_{\Delta n}$ (color contour cones) and *in situ* $\sigma_{\Delta n}$ (color on flight path line) for Event 230-23. In this event, all three "hazard" scans were executed at a tilt of –2°. Ambient wind vectors are shown along path.

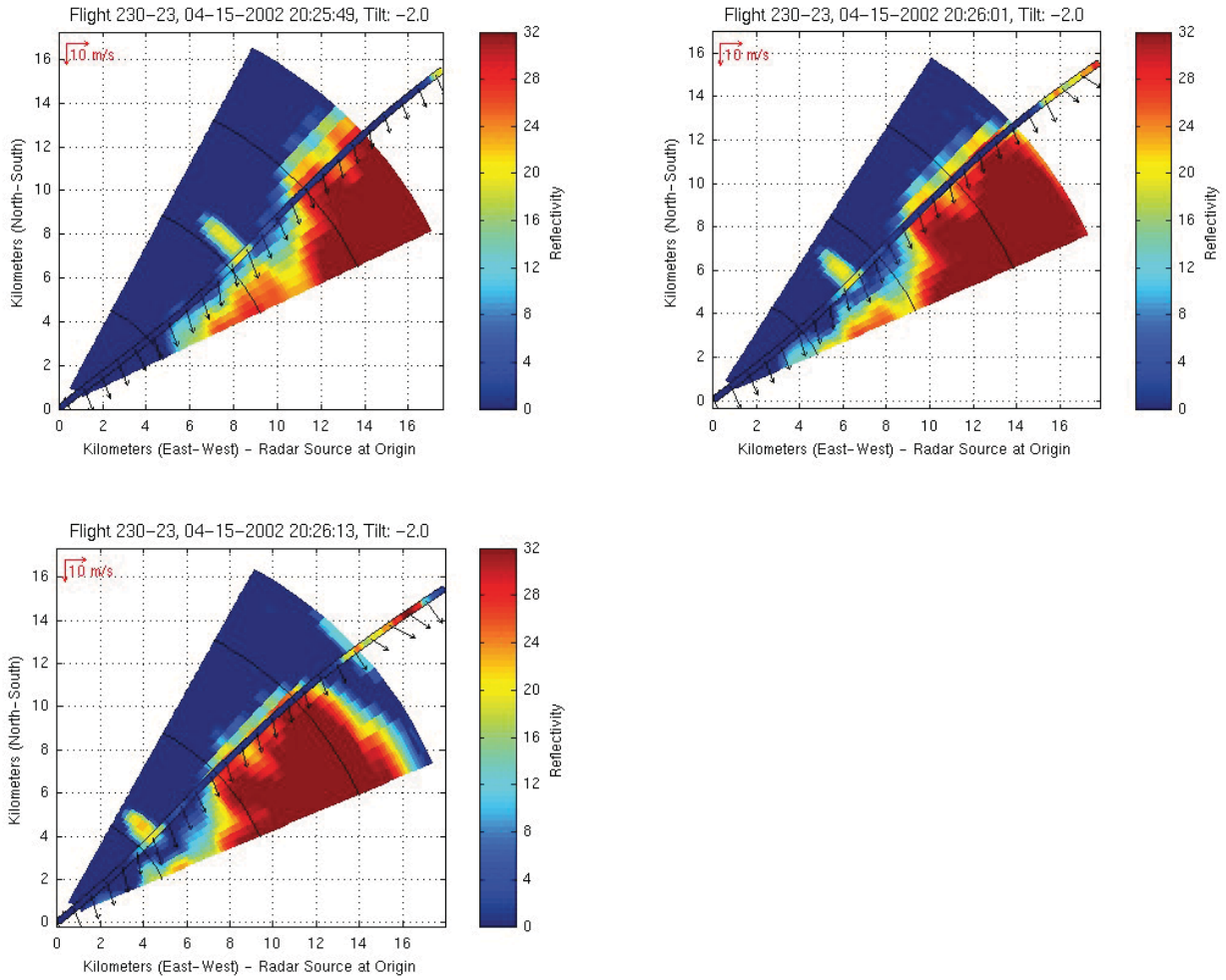

Figure 56. Sequential scans at 12*s* interval for airborne radar reflectivity factor (color contour cones) and *in situ* $\sigma_{\Delta n}$ (color on flight path line) for Event 230-23. In this event, all three scans were executed at a tilt of –2°. Ambient wind vectors are shown along path.

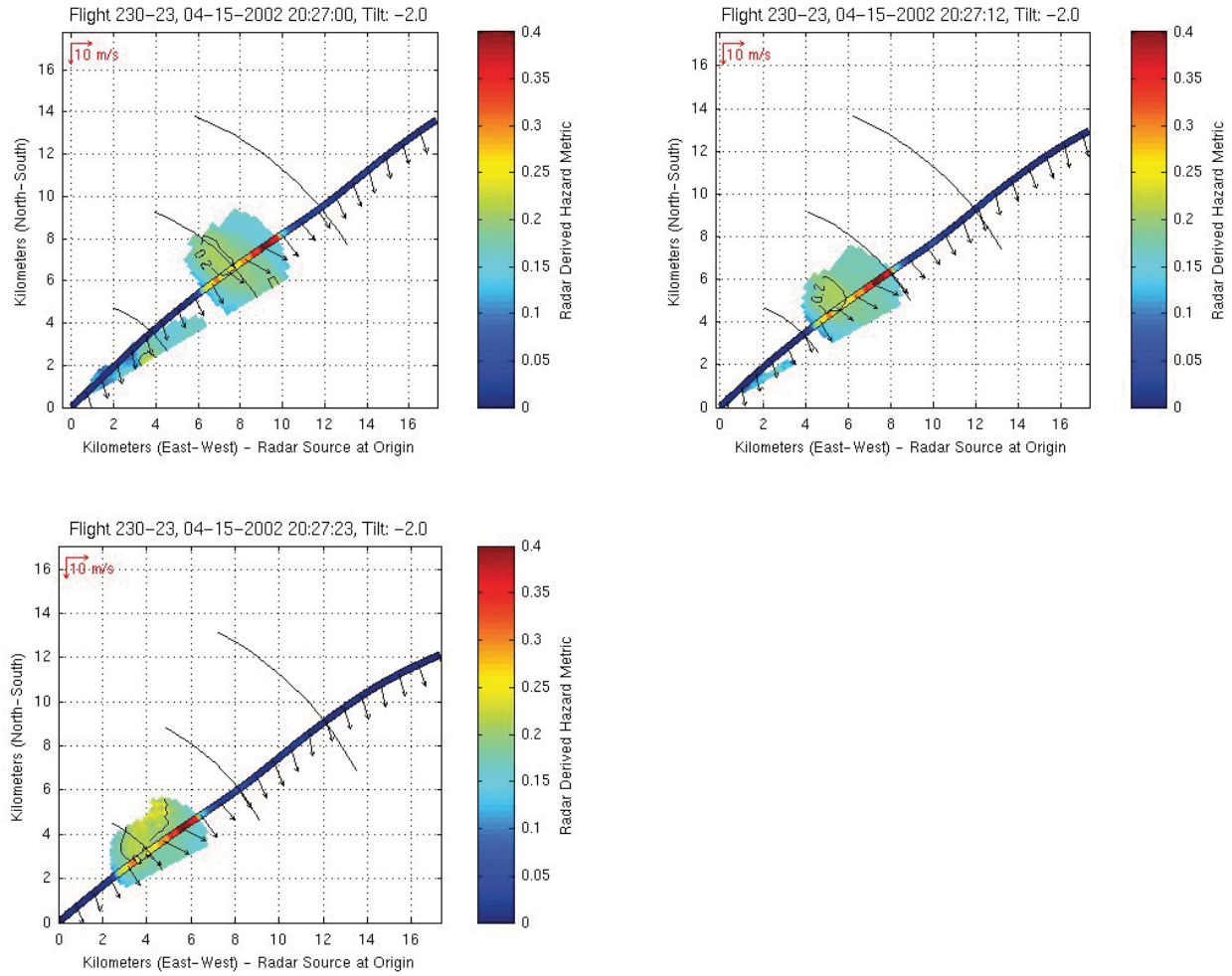

Figure 57. Sequential scans at 12*s* intervals for airborne radar predicted $\sigma_{\Delta n}$ (color contour cones) and *in situ* $\sigma_{\Delta n}$ (color on flight path line) for Event 230-23. Ambient wind vectors are shown along path.

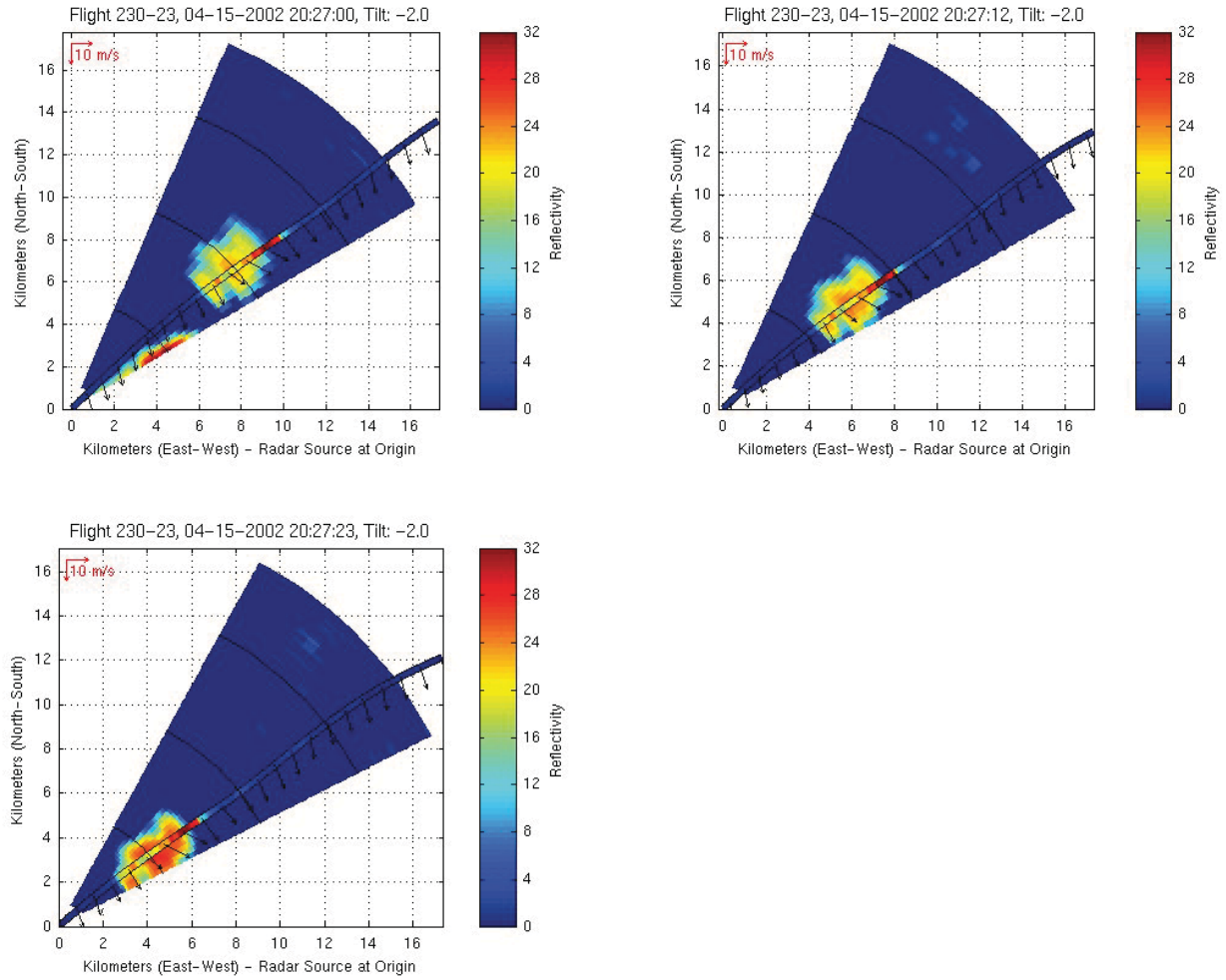

Figure 58. Sequential scans at 12*s* interval for airborne radar reflectivity factor (color contour cones) and *in situ* $\sigma_{\Delta n}$ (color on flight path line) for Event 230-23. Ambient wind vectors are shown along path.

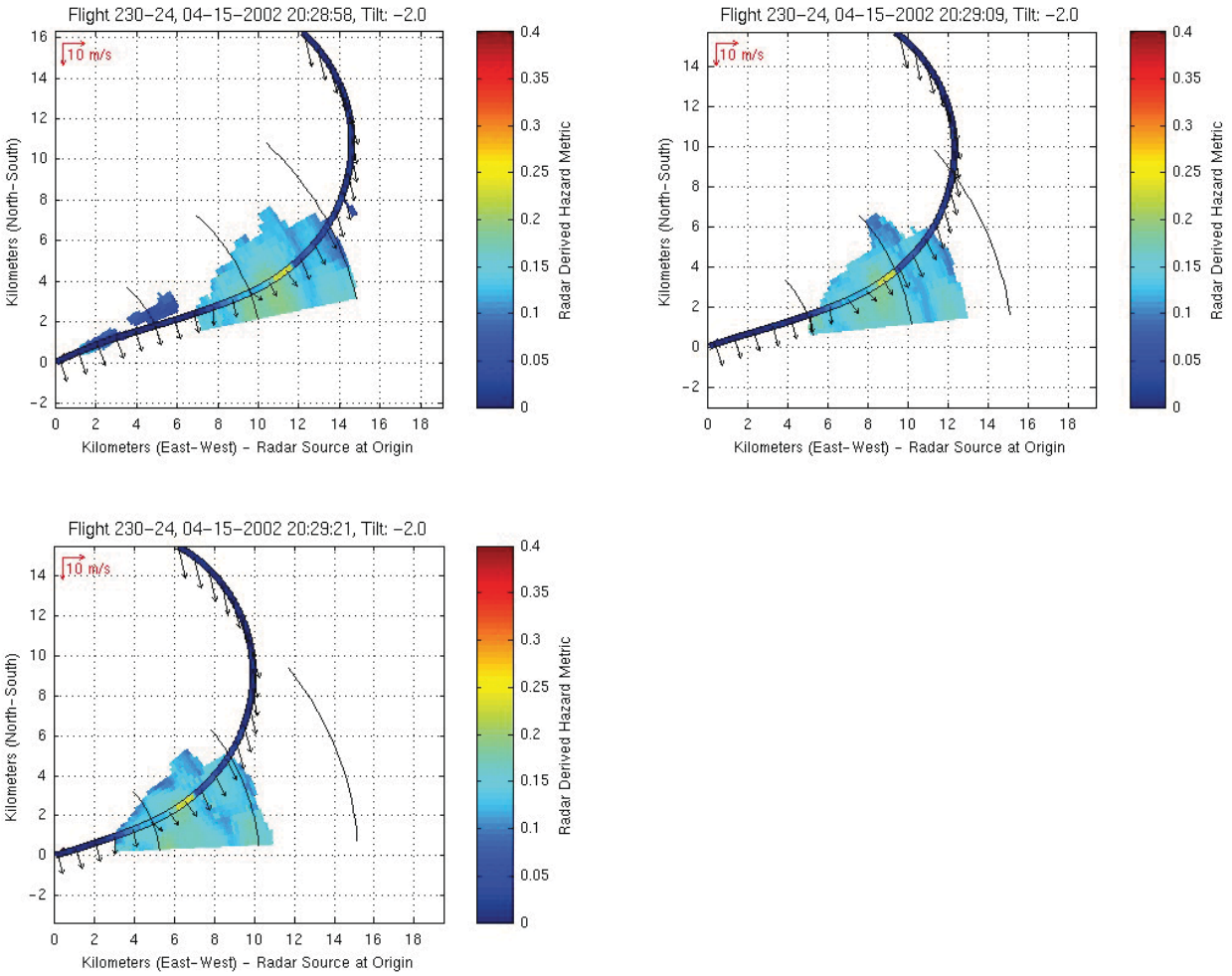

Figure 59. Sequential scans at 12*s* intervals for airborne radar predicted $\sigma_{\Delta n}$ (color contour cones) and *in situ* $\sigma_{\Delta n}$ (color on flight path line) for Event 230-24. Ambient wind vectors are shown along path.

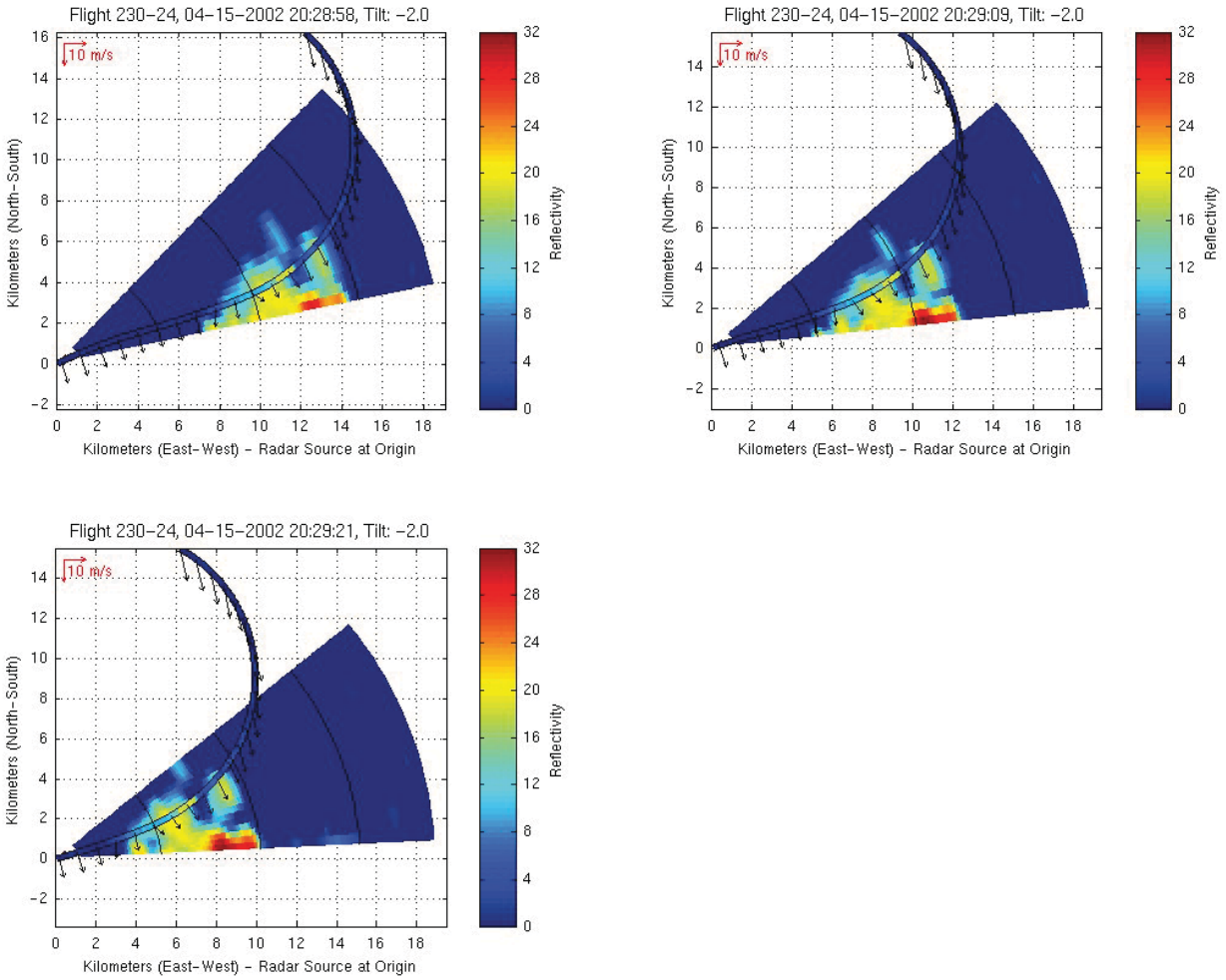

Figure 60. Sequential scans at 12*s* interval for airborne radar reflectivity factor (color contour cones) and *in situ* $\sigma_{\Delta n}$ (color on flight path line) for Event 230-24. Ambient wind vectors are shown along path.

2.7: Flight 231, April 24, 2002

Between 1800 and 1900 UTC on 24 April 2002, ARIES investigated an MCC over Central Tennessee (Figure 61 and Figure 62). The MCC had two deep convective lines located southwest of a large region of stratiform precipitation. The majority of the encounters were associated with the southernmost convective line. One penetration was made in the northern line of convection prior to dissipation of the system and the subsequent end of data collection. Pilot reports of moderate to severe turbulence had been issued in the vicinity of the MCC (Figure 63). Visibility depended upon flight altitude due to the presence of multiple convective outflow layers.

Four significant turbulence encounters were associated with the penetration of cumulonimbus towers on their periphery and overshooting tops (Figure 64 - Figure 69). Moderate airborne radar reflectivity was associated with the convective cells. The storm tops were between 11 and 12 *km* (36 and 40 *kft*) and flight altitudes ranged between 8.5 and 10 *km* (28 and 33 *kft*). Cell motion was towards the east-southeast at 25 *kts*. The prevailing winds in the altitude range were from the west-northwest (290° from true North) between 23 and 28 *m/s* (45 and 55 *kts*). Very little of the onboard radar data from Event 231-12 was processed and delivered to NASA.

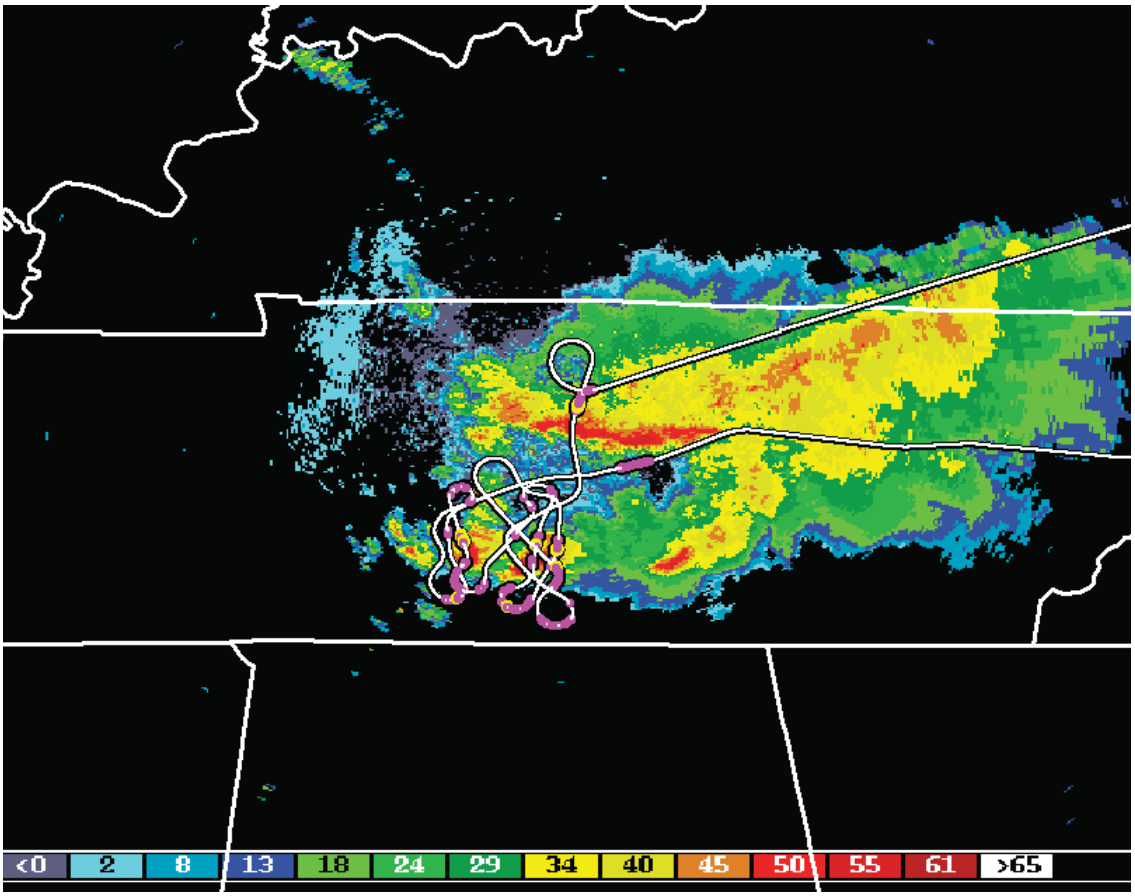

Figure 61. Path for Flight 231. Ground based composite radar reflectivity (*dBz*) from the KOHX (Nashville, Tennessee) NEXRAD radar at 18:27:30 UTC on 24 April 2002. See Figure 3 for legend to intensity of the aircraft RMS normal loads.

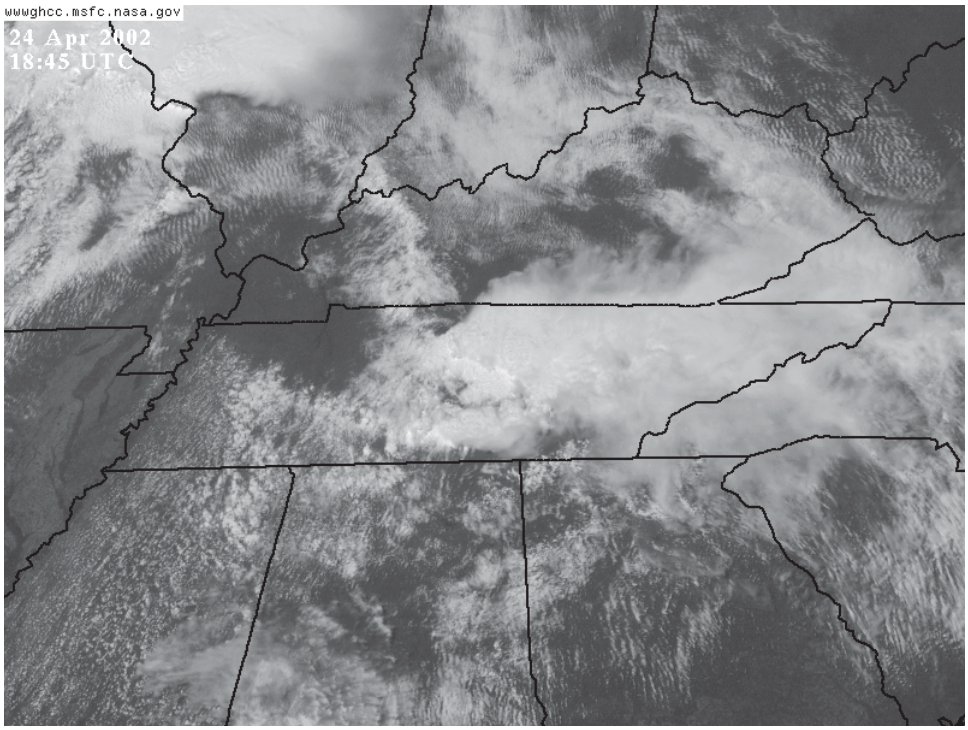

Figure 62. GOES-12 visible satellite image at 1845 UTC on 24 April 2002.

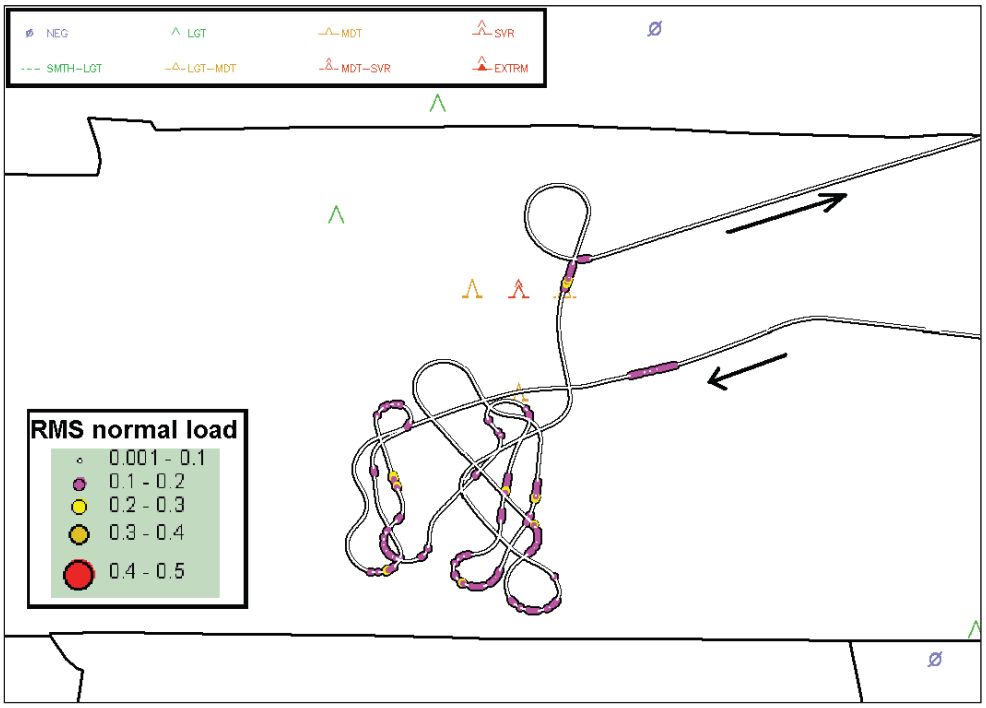

Figure 63. RMS normal loads encountered along the path for Flight 231 with turbulence PIREPS for 24 April 2002.

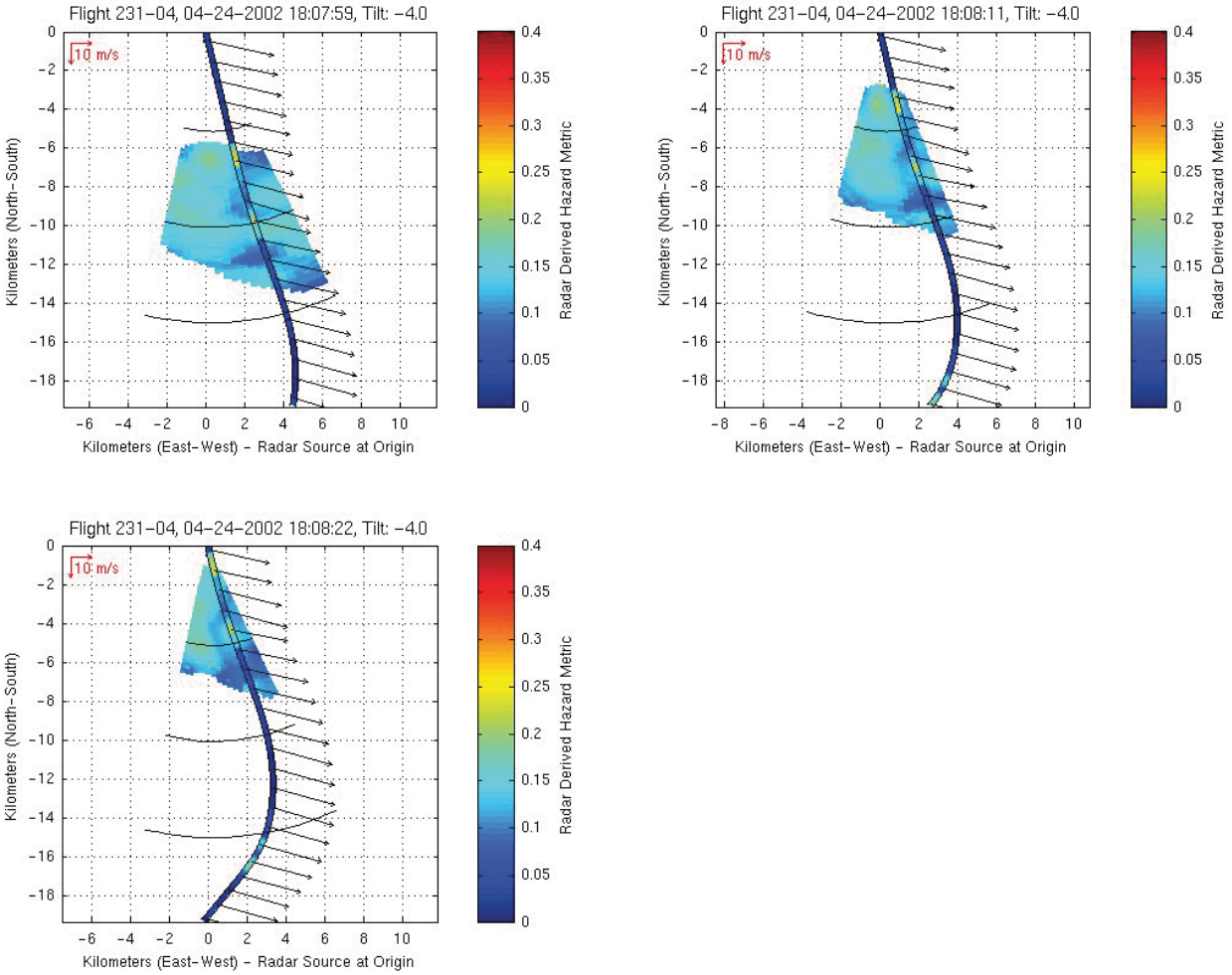

Figure 64. Sequential scans at 12*s* intervals for airborne radar predicted $\sigma_{\Delta n}$ (color contour cones) and *in situ* $\sigma_{\Delta n}$ (color on flight path line) for Event 231-04. Ambient wind vectors are shown along path.

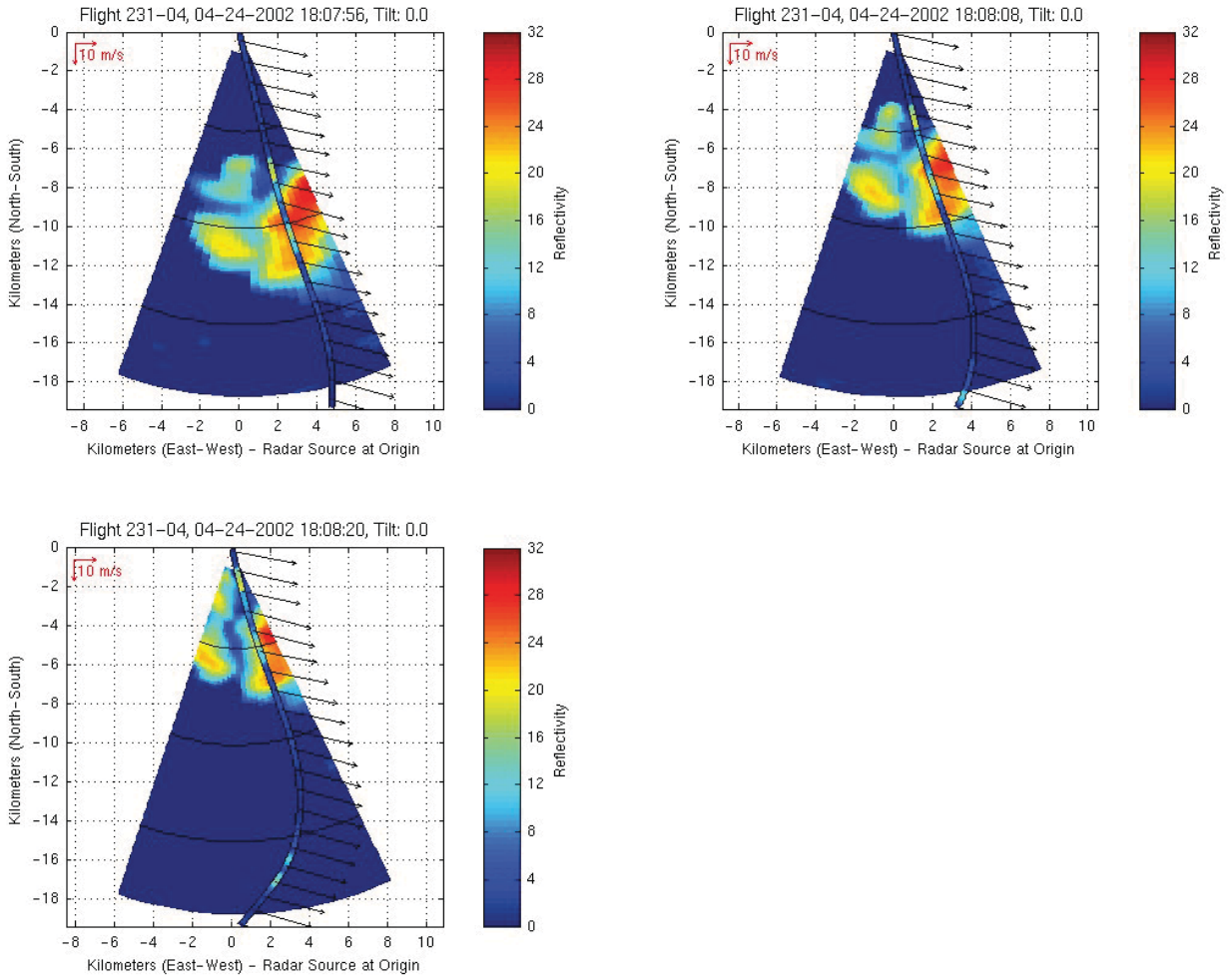

Figure 65. Sequential scans at 12*s* interval for airborne radar reflectivity factor (color contour cones) and *in situ* $\sigma_{\Delta n}$ (color on flight path line) for Event 231-04. Ambient wind vectors are shown along path.

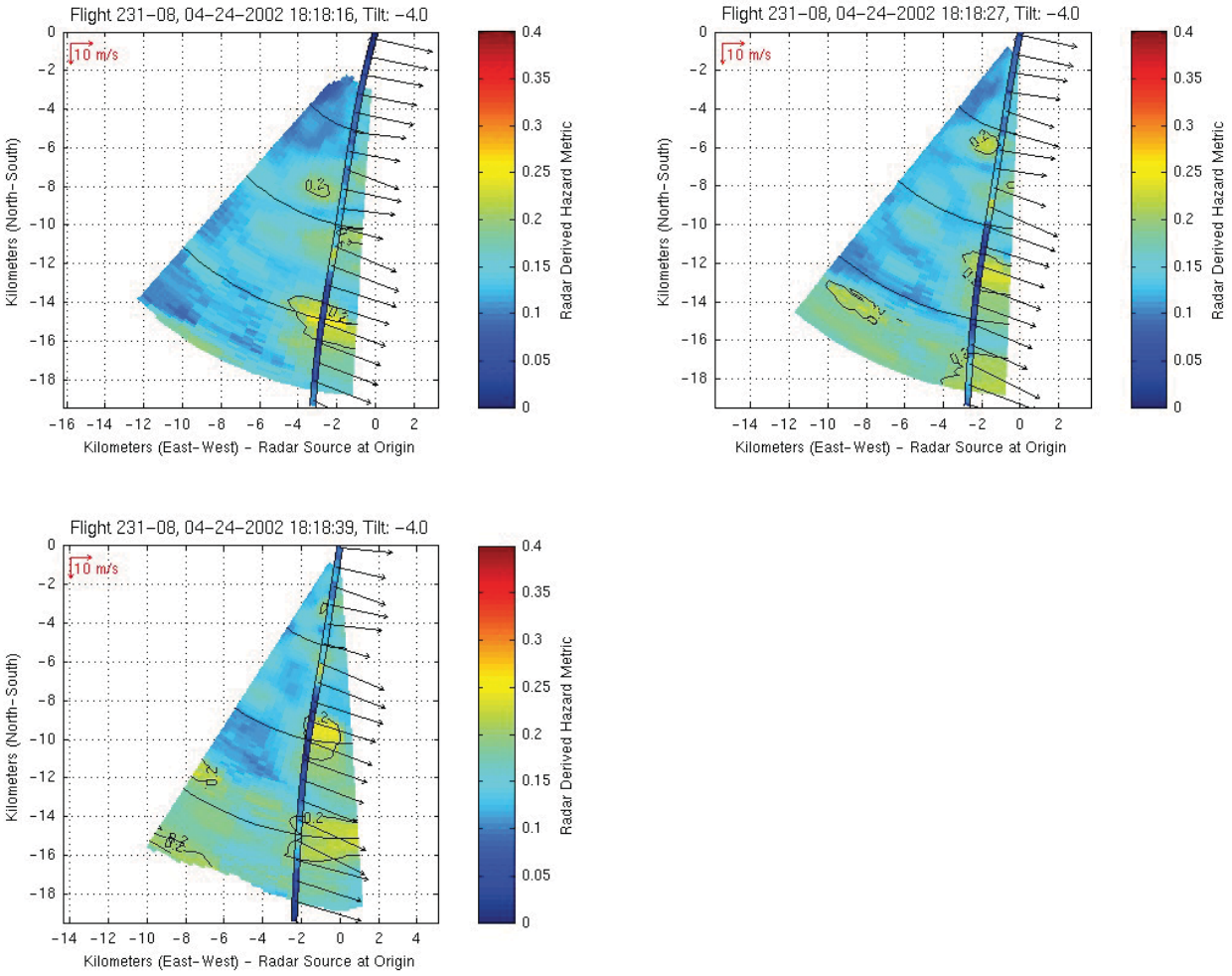

Figure 66. Sequential scans at 12*s* intervals for airborne radar predicted $\sigma_{\Delta n}$ (color contour cones) and *in situ* $\sigma_{\Delta n}$ (color on flight path line) for Event 231-08. Ambient wind vectors are shown along path.

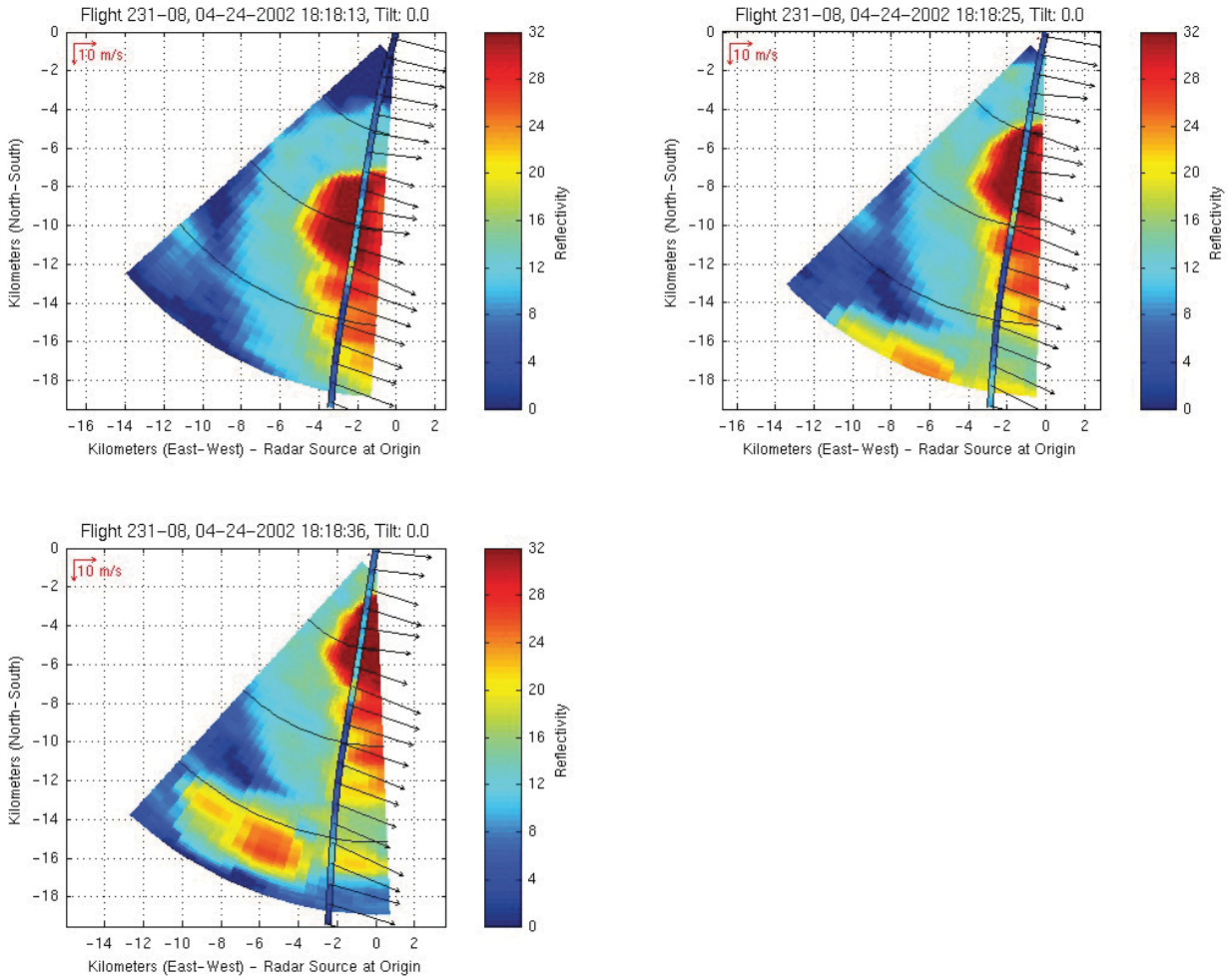

Figure 67. Sequential scans at 12*s* interval for airborne radar reflectivity factor (color contour cones) and *in situ* $\sigma_{\Delta n}$ (color on flight path line) for Event 231-08. Ambient wind vectors are shown along path.

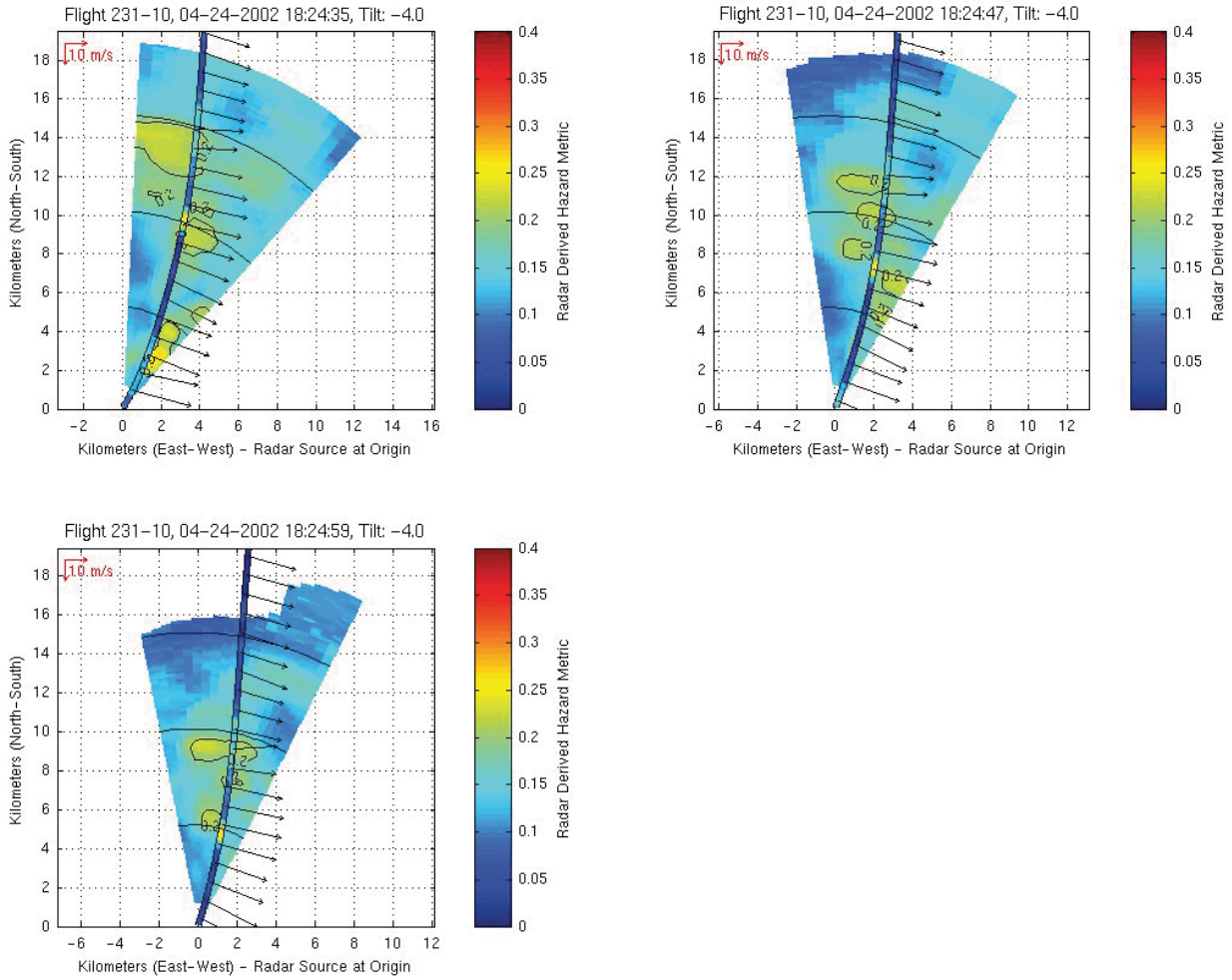

Figure 68. Sequential scans at 12*s* intervals for airborne radar predicted $\sigma_{\Delta n}$ (color contour cones) and *in situ* $\sigma_{\Delta n}$ (color on flight path line) for Event 231-10. Ambient wind vectors are shown along path.

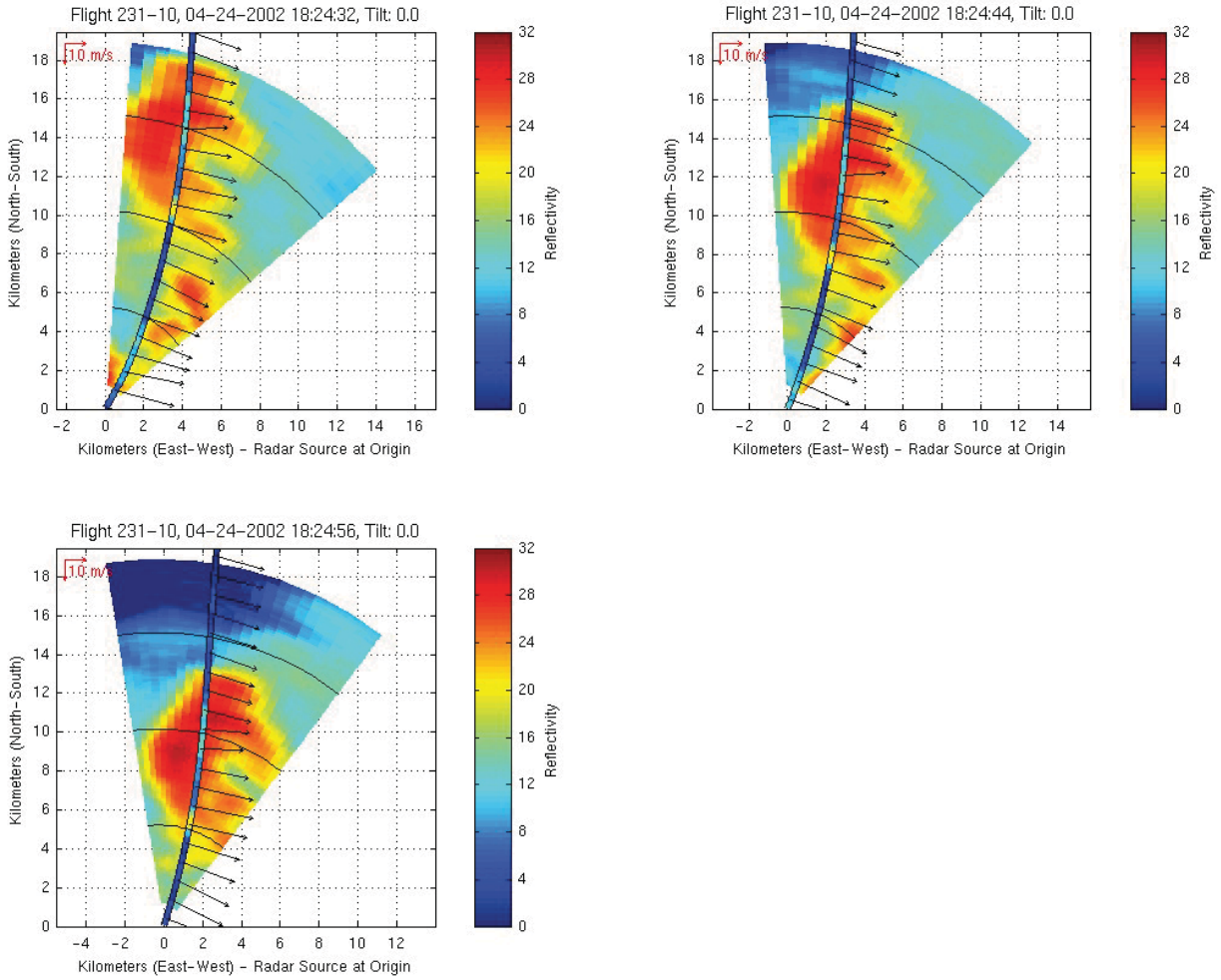

Figure 69. Sequential scans at 12*s* interval for airborne radar reflectivity factor (color contour cones) and *in situ* $\sigma_{\Delta n}$ (color on flight path line) for Event 231-10. Ambient wind vectors are shown along path.

2.8: Flight 232, April 30, 2002

Between 1800 and 1915 UTC on April 30, 2002, ARIES investigated a convective complex located over northern Alabama (Figure 70 and Figure 71). Pilot reports of moderate to severe turbulence were reported in the vicinity of the complex (Figure 72). Extensive outflow from large cells located upstream of the convective complex led to instrument meteorological conditions throughout most of the data collection period. However, marginal visibility was present south of the complex.

Continuous light turbulence was experienced in transit to and in the vicinity of the complex. Six significant turbulence encounters were associated with the penetration of rising convective plumes within the complex (Figure 73 - Figure 86). Very weak airborne radar reflectivity was associated with these plumes. At times no radar reflectivity was shown on the aircraft's weather radar display. The precipitation encountered was in the form of ice crystals and light snow. Elevations of storm tops generally were around 10.6 *km* (35 *kft*) with some overshooting tops reaching as high as 15 *km* (50 *kft*). Flight altitudes were initially 9.5 *km* (31 *kft*) and later changed to 10.6 *km* (35 *kft*). Cell motion ranged from 13 and 23 *m/s* (25 to 45 *kts*) towards the east-southeast. The prevailing winds in the vicinity of the encounters varied with altitude and horizontal position, and on average were about 56 *m/s* (110 *kts*) from 280° from true North.

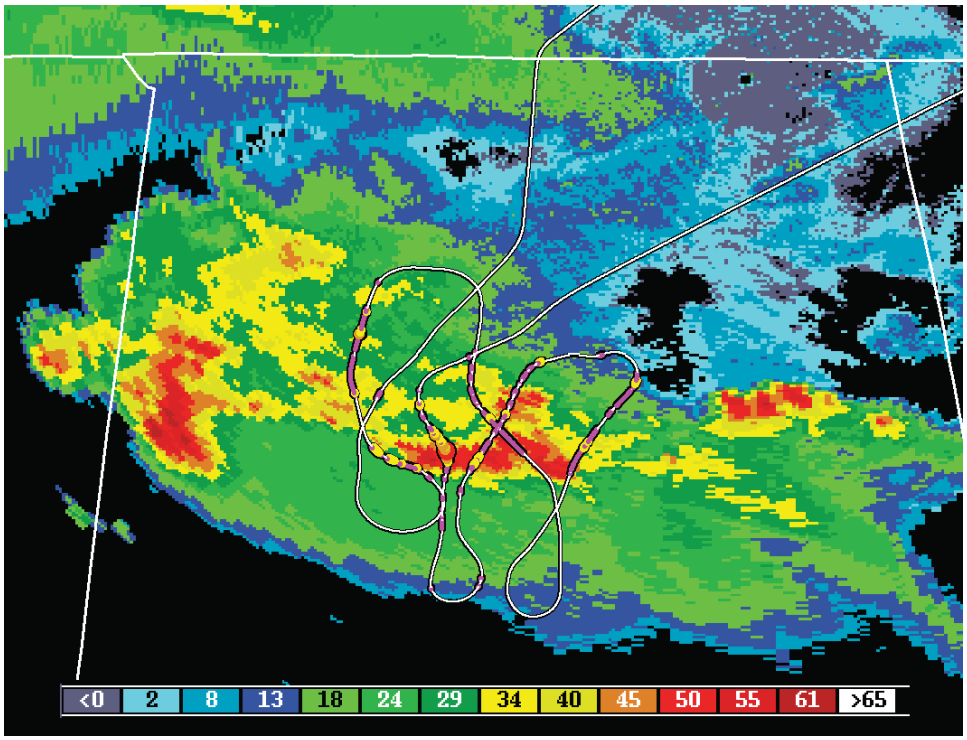

Figure 70. Path for Flight 232. Ground based composite radar reflectivity (*dBz*) from the KHTX (Huntsville, Alabama) NEXRAD radar at 19:12:34 UTC on 30 April 2002. The intensity of the aircraft RMS normal loads is the same as denoted in the legend of Figure 3.

This flight captured the 'show-case' event, 232-10, that has been used to exemplify the operational environment in which accidents occur due to turbulence (Figure 83-Figure 86). The characteristics of this event were:

1. the flight environment was IMC, so 'see and avoid' was not an option;
2. the convection at flight level had very low radar reflectivity and was not displayed on aircraft's weather radar (< 20 *dBz*);
3. the encounter was sudden, of short duration, and severe intensity;
4. no reports of severe turbulence were made prior to the time of the event; and
5. severe turbulence was detected with ATDS about 2 minutes prior to the encounter.

Shortly afterwards, two commercial aircraft, an MD-80 and an A319, both issued PIREPS for severe turbulence within 10 *km* and 30 *min* of event 232-10. The availability of an ATDS could have made the aircrews aware of the hazards from the rapidly rising storm tops of this convective system.

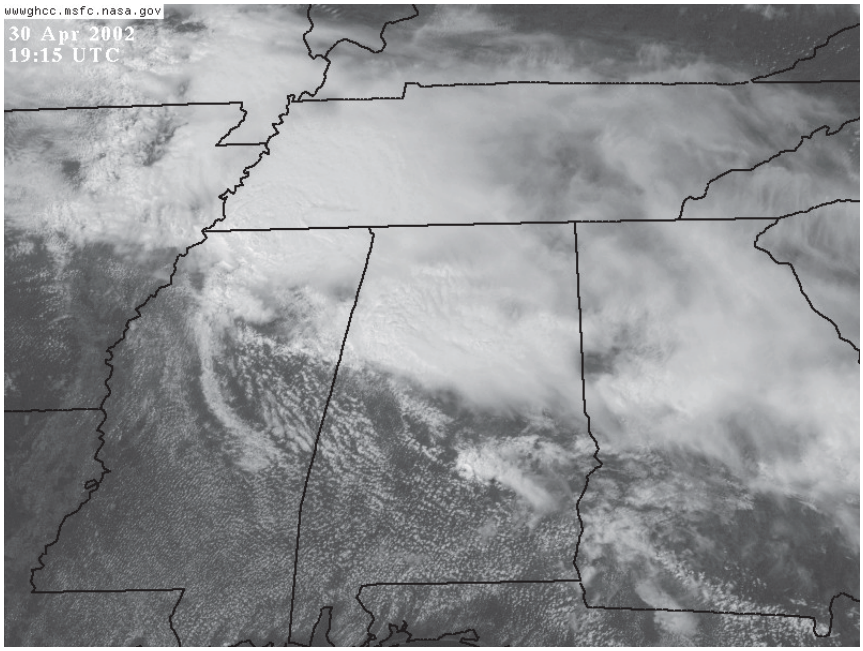

Figure 71. GOES-12 visible satellite image at 1915 UTC on 30 April 2002.

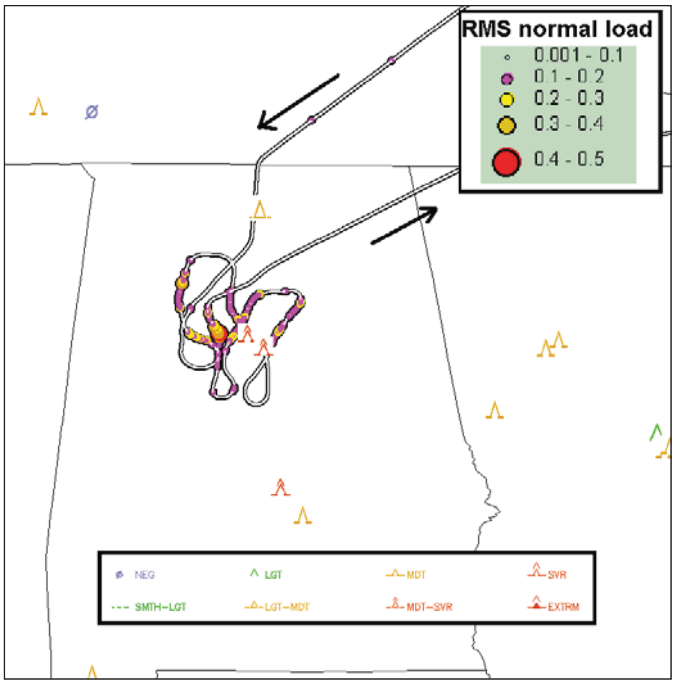

Figure 72. RMS normal loads encountered along the path for Flight 232 with turbulence PIREPS for 30 April 2002.

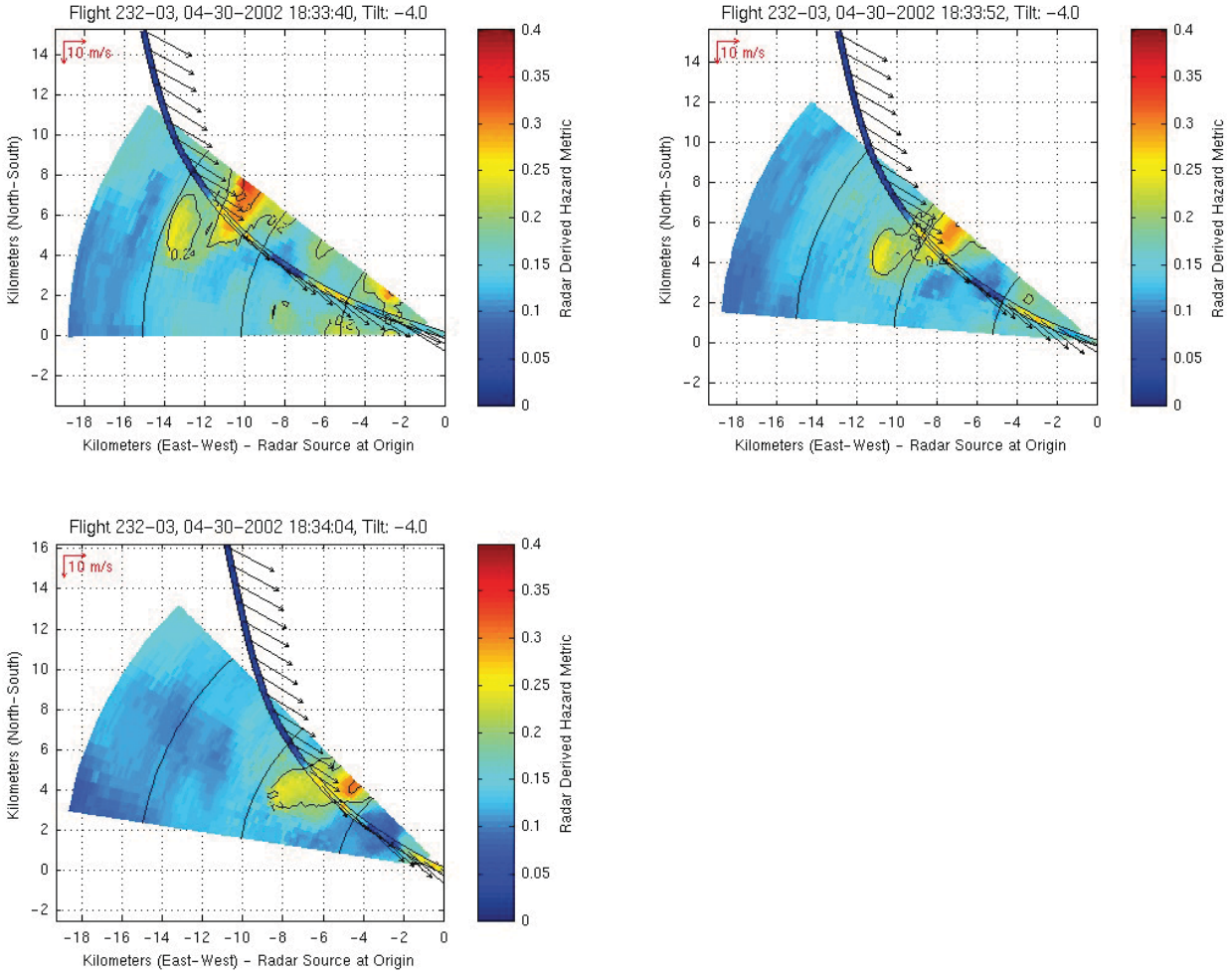

Figure 73. Sequential scans at 12*s* intervals for airborne radar predicted $\sigma_{\Delta n}$ (color contour cones) and *in situ* $\sigma_{\Delta n}$ (color on flight path line) for Event 232-03. Ambient wind vectors are shown along path.

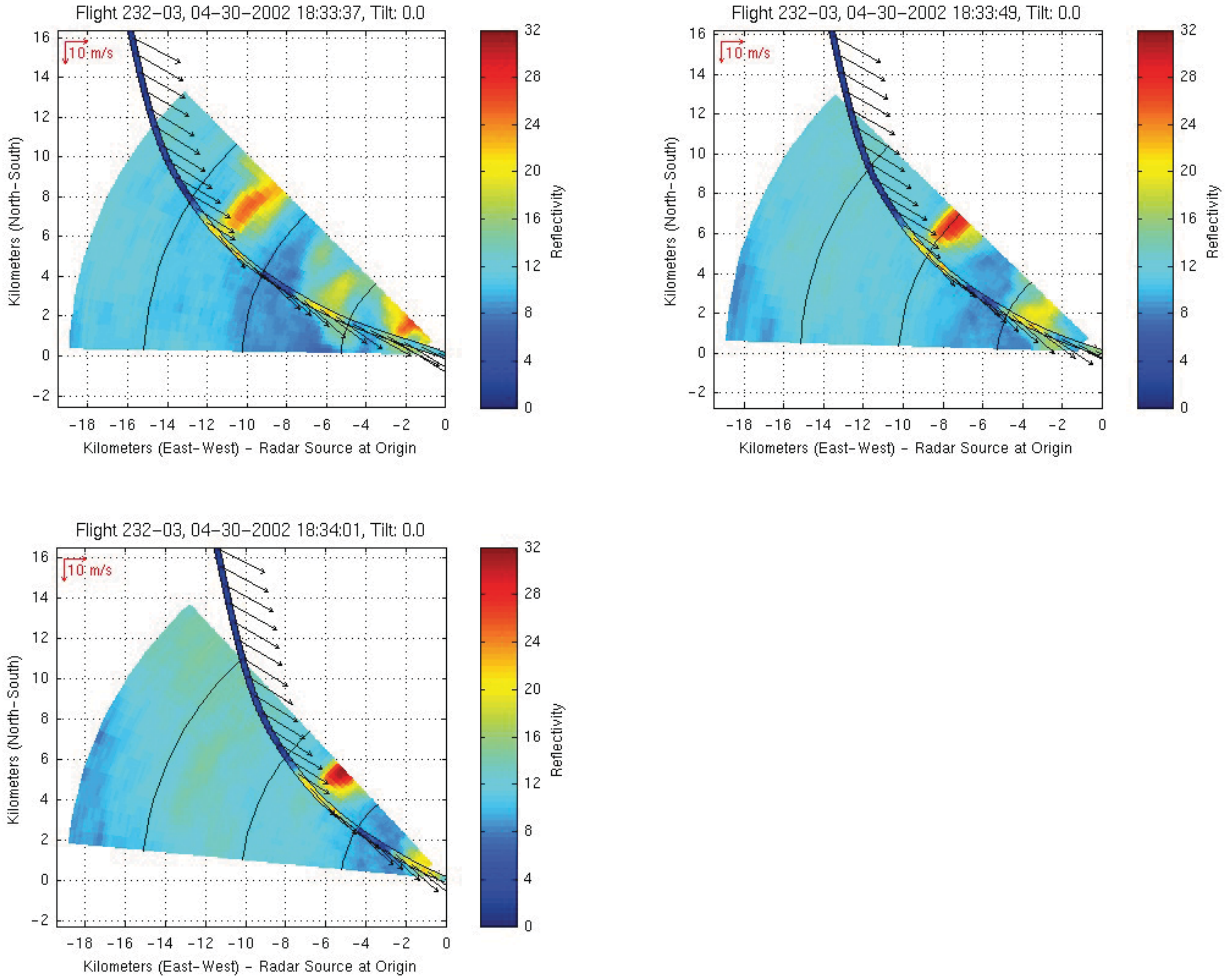

Figure 74. Sequential scans at 12*s* interval for airborne radar reflectivity factor (color contour cones) and *in situ* $\sigma_{\Delta n}$ (color on flight path line) for Event 232-03. Ambient wind vectors are shown along path.

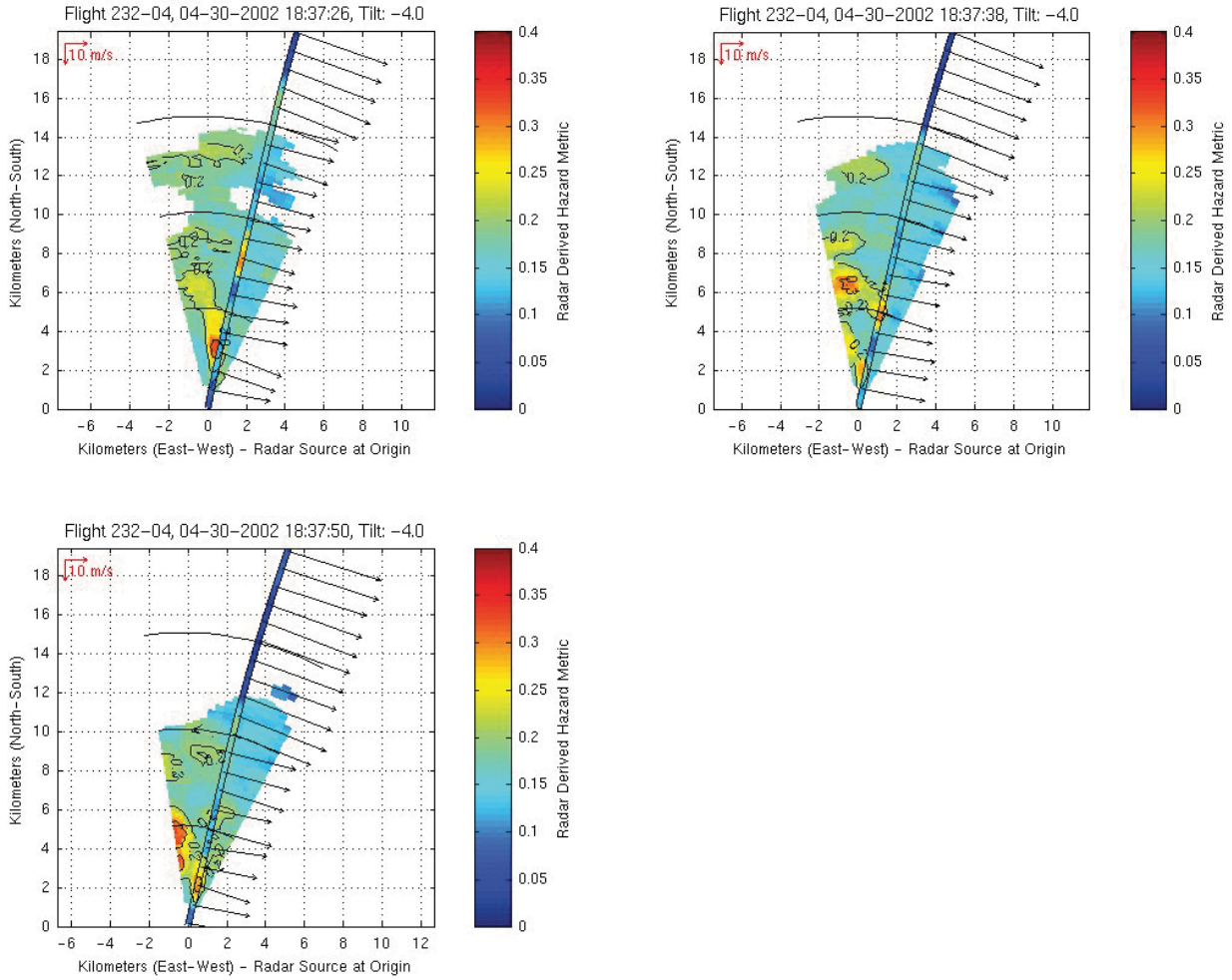

Figure 75. Sequential scans at 12*s* intervals for airborne radar predicted $\sigma_{\Delta n}$ (color contour cones) and *in situ* $\sigma_{\Delta n}$ (color on flight path line) for Event 232-04. Ambient wind vectors are shown along path.

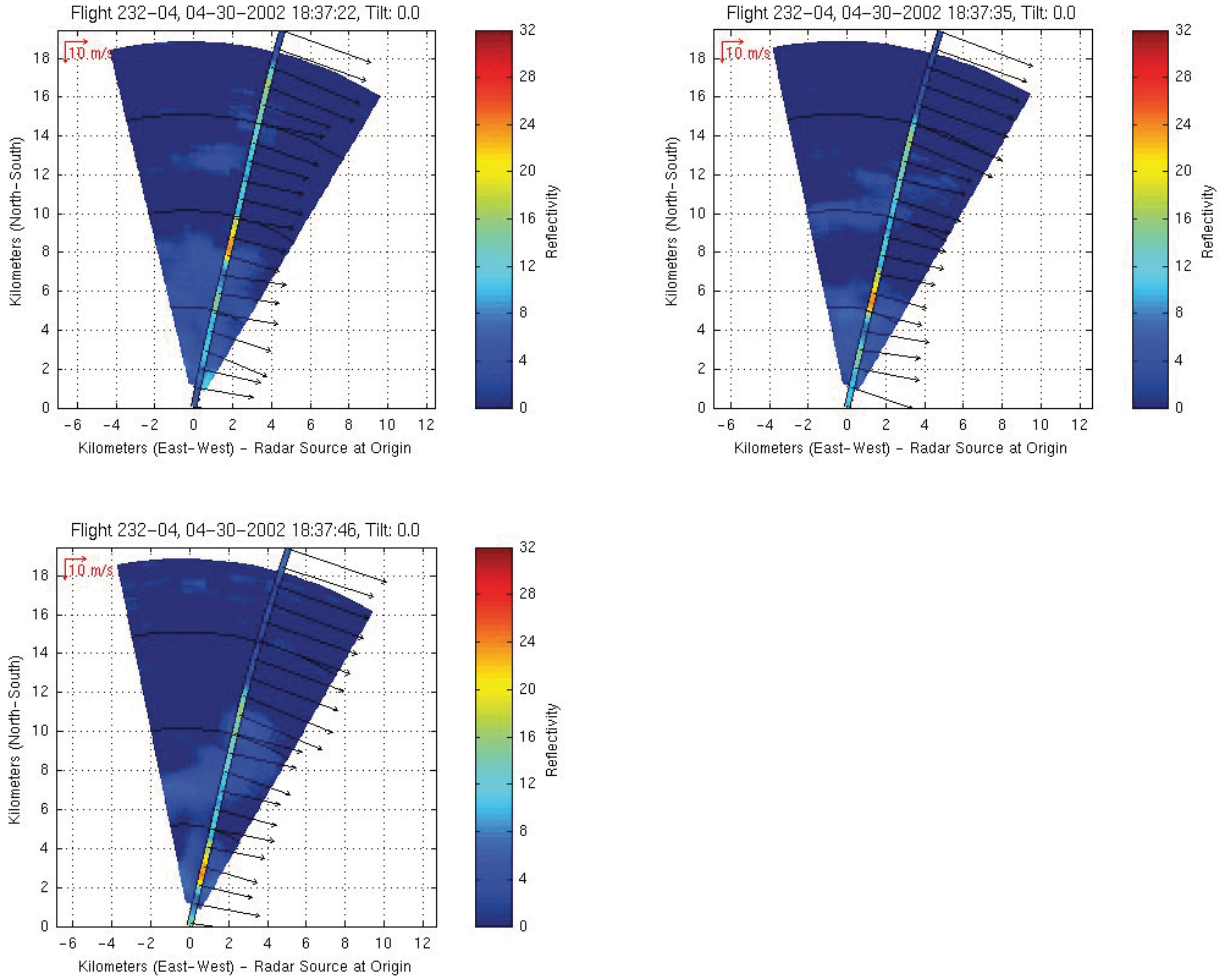

Figure 76. Sequential scans at 12*s* interval for airborne radar reflectivity factor (color contour cones) and *in situ* $\sigma_{\Delta n}$ (color on flight path line) for Event 232-04. Ambient wind vectors are shown along path.

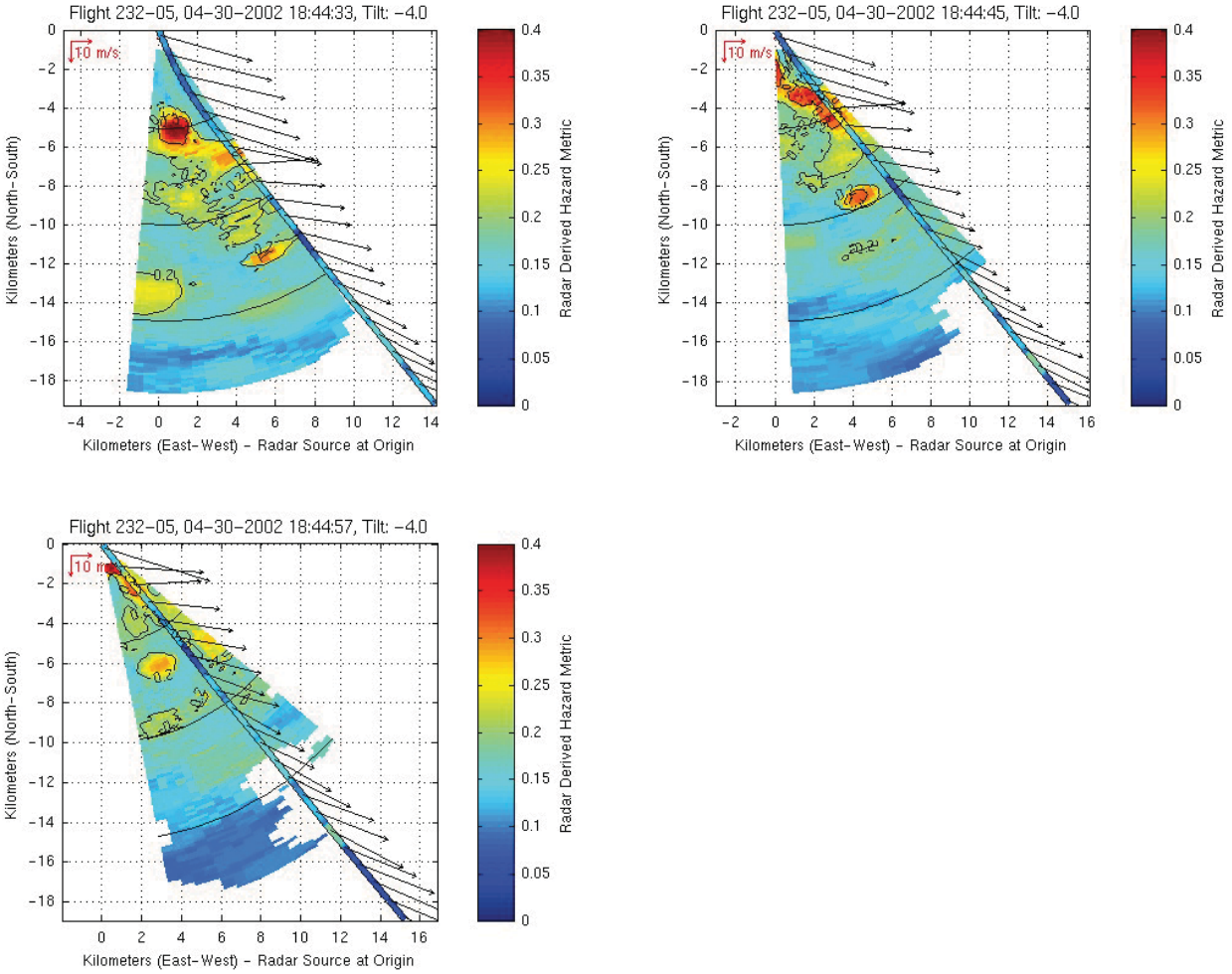

Figure 77. Sequential scans at 12*s* intervals for airborne radar predicted $\sigma_{\Delta n}$ (color contour cones) and *in situ* $\sigma_{\Delta n}$ (color on flight path line) for Event 232-05. Ambient wind vectors are shown along path.

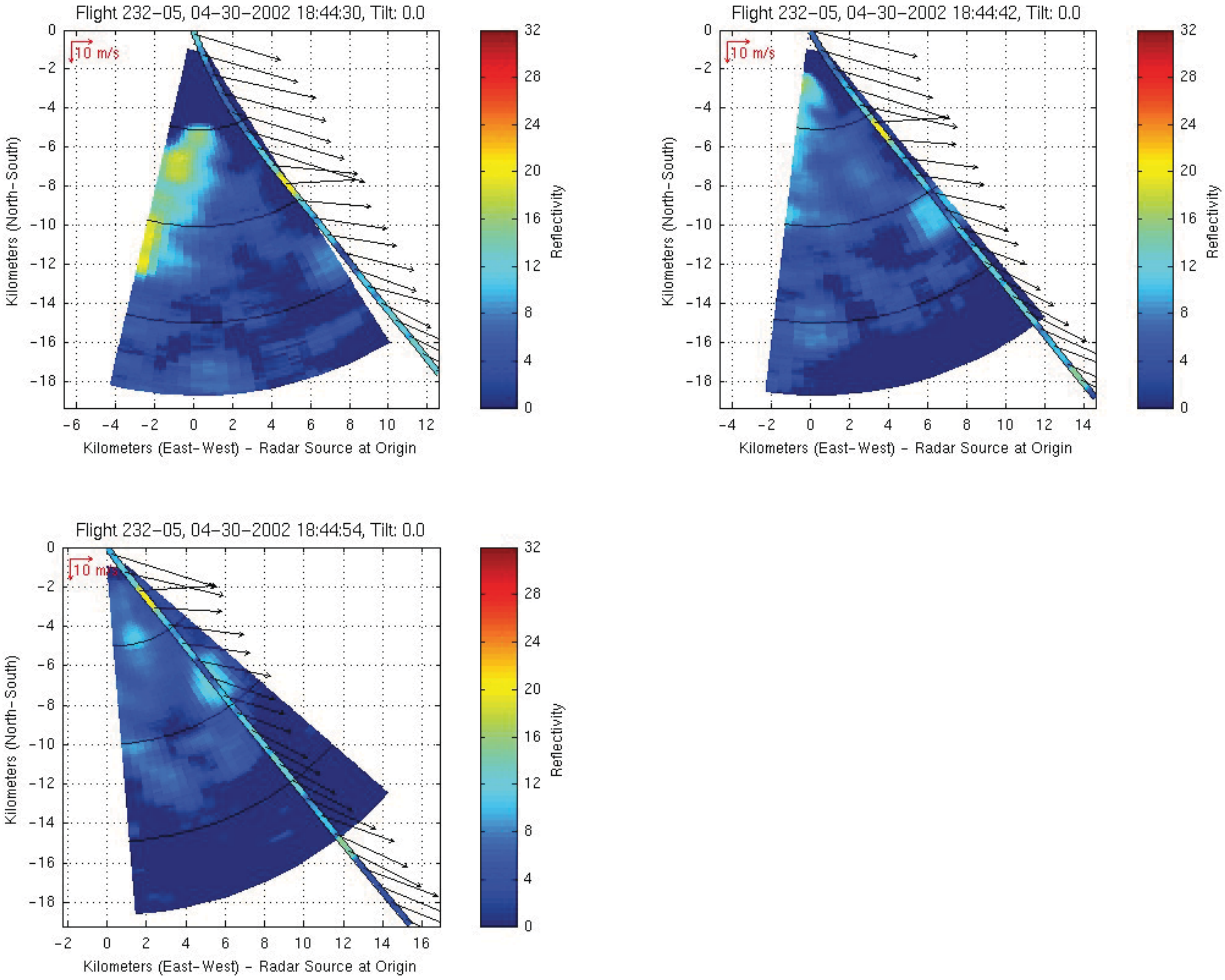

Figure 78. Sequential scans at 12*s* interval for airborne radar reflectivity factor (color contour cones) and *in situ* $\sigma_{\Delta n}$ (color on flight path line) for Event 232-05. Ambient wind vectors are shown along path.

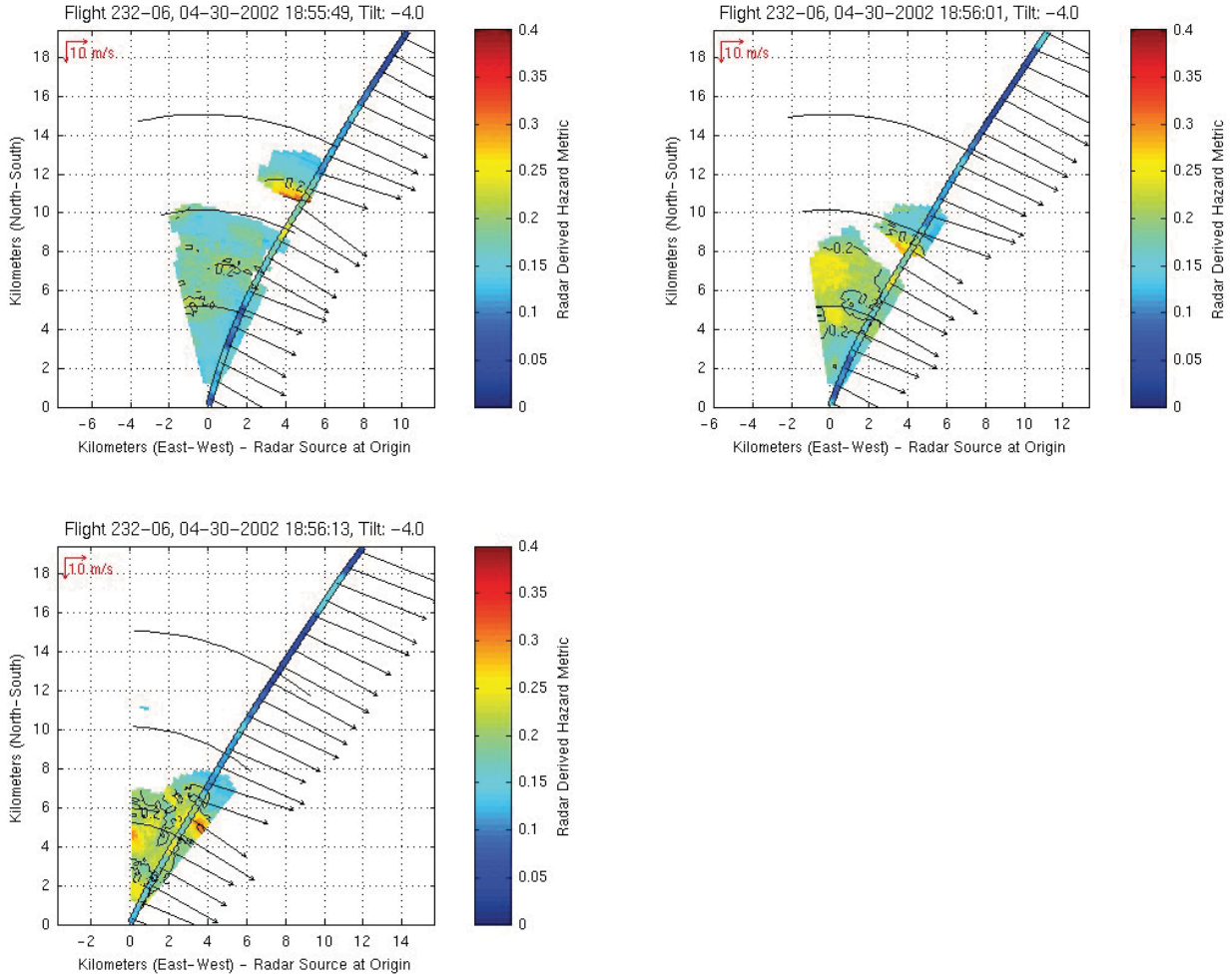

Figure 79. Sequential scans at 12*s* intervals for airborne radar predicted $\sigma_{\Delta n}$ (color contour cones) and *in situ* $\sigma_{\Delta n}$ (color on flight path line) for Event 232-06. Ambient wind vectors are shown along path.

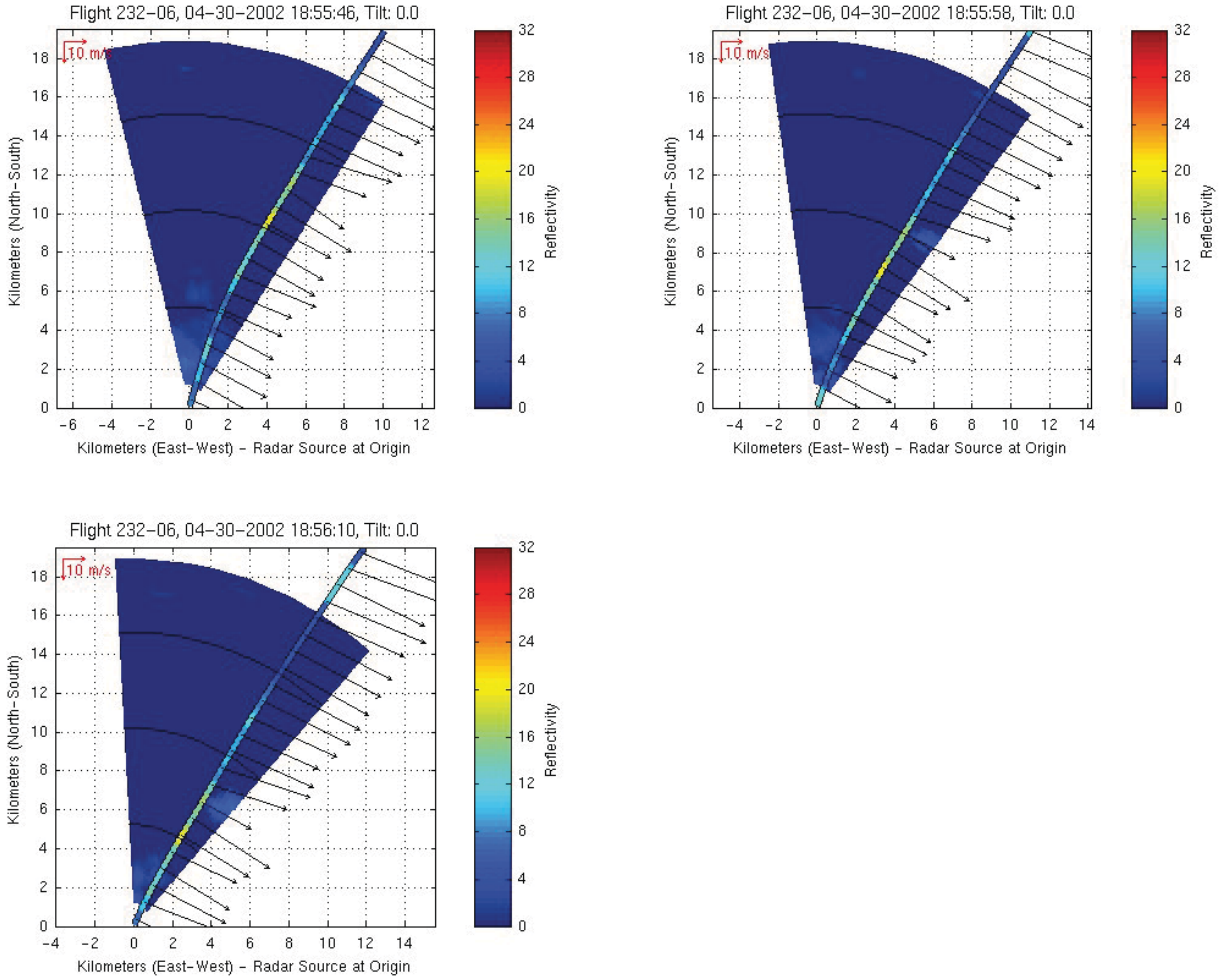

Figure 80. Sequential scans at 12*s* interval for airborne radar reflectivity factor (color contour cones) and *in situ* $\sigma_{\Delta n}$ (color on flight path line) for Event 232-06. Ambient wind vectors are shown along path.

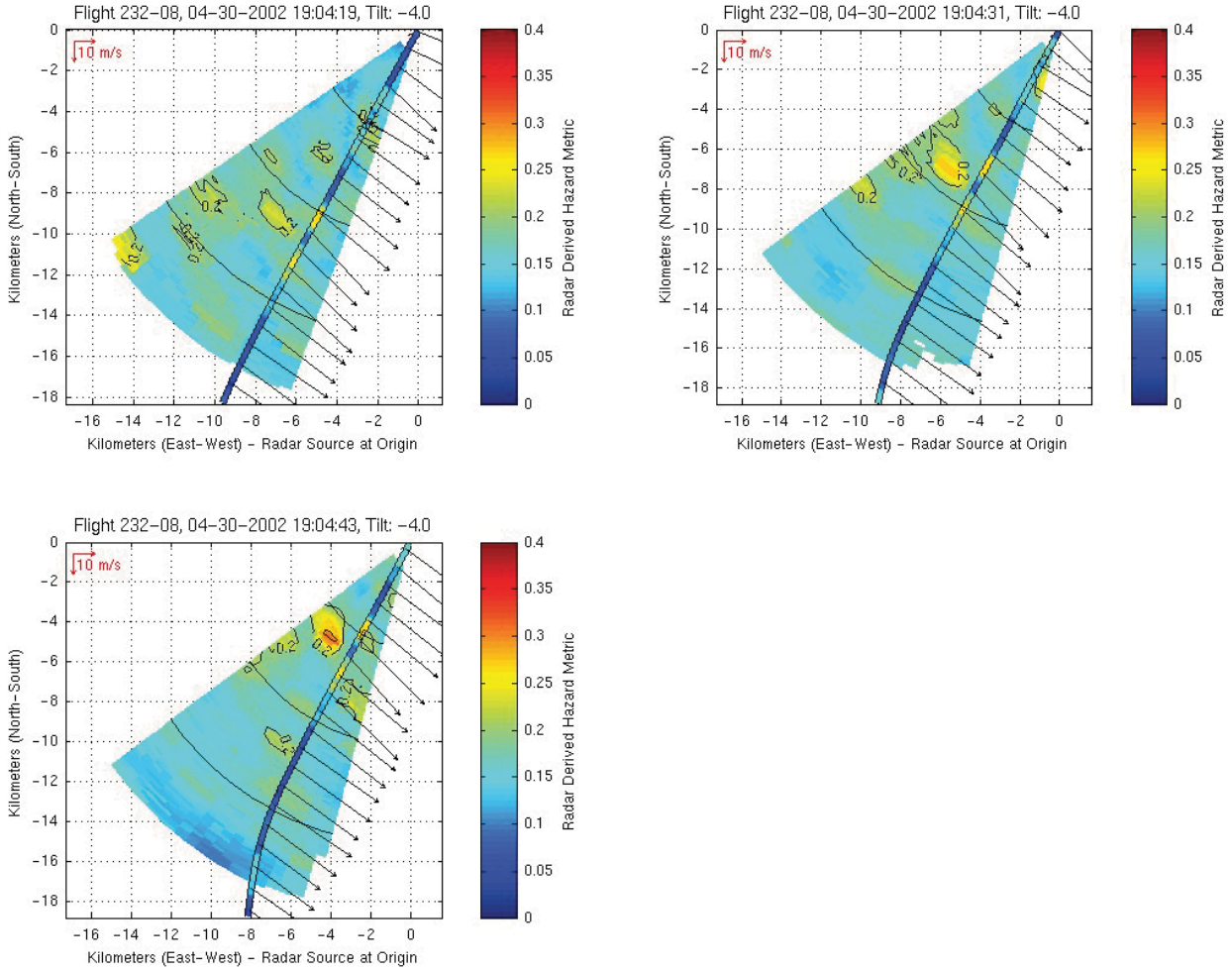

Figure 81. Sequential scans at 12*s* intervals for airborne radar predicted $\sigma_{\Delta n}$ (color contour cones) and *in situ* $\sigma_{\Delta n}$ (color on flight path line) for Event 232-08. Ambient wind vectors are shown along path.

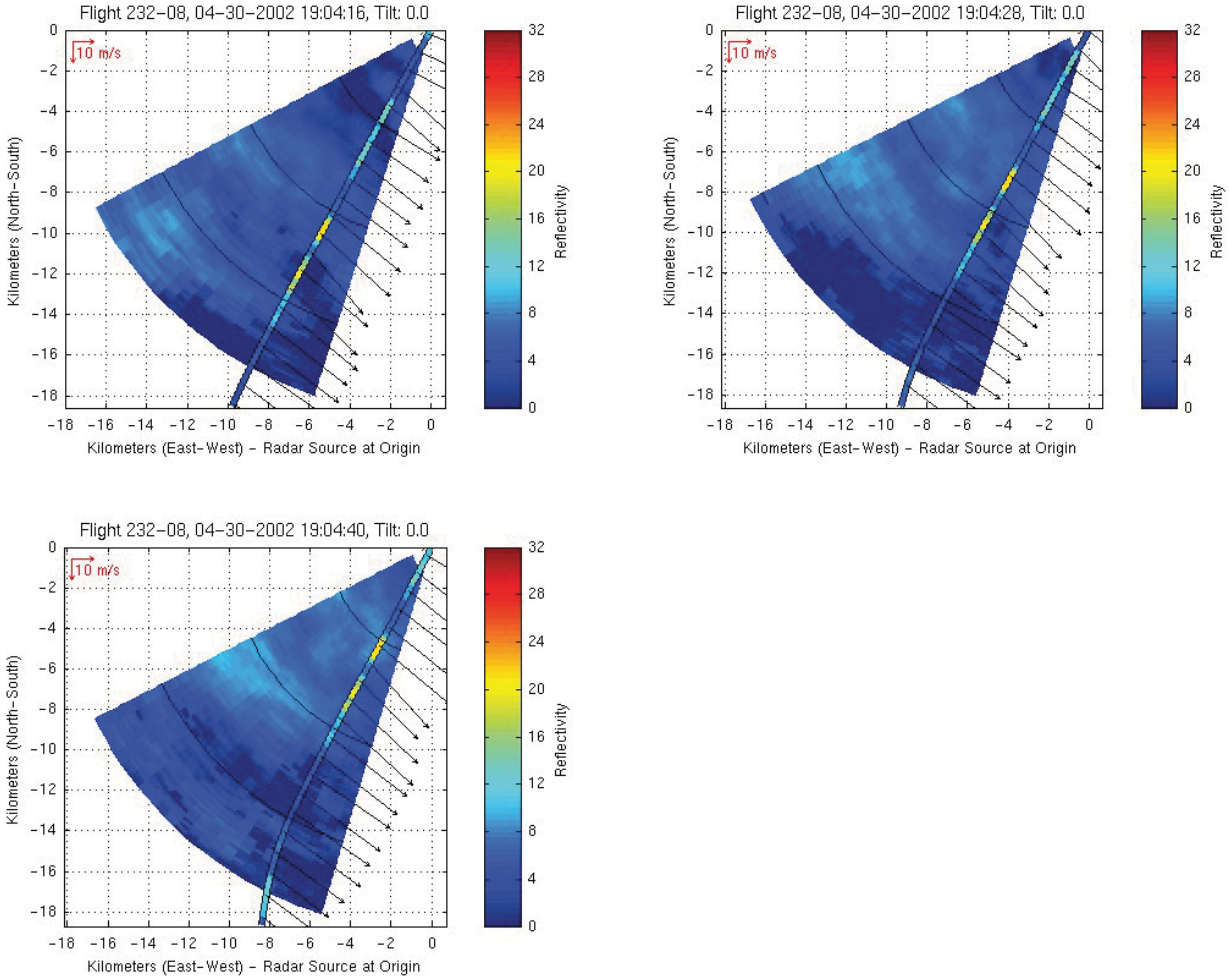

Figure 82. Sequential scans at 12*s* interval for airborne radar reflectivity factor (color contour cones) and *in situ* $\sigma_{\Delta n}$ (color on flight path line) for Event 232-08. Ambient wind vectors are shown along path.

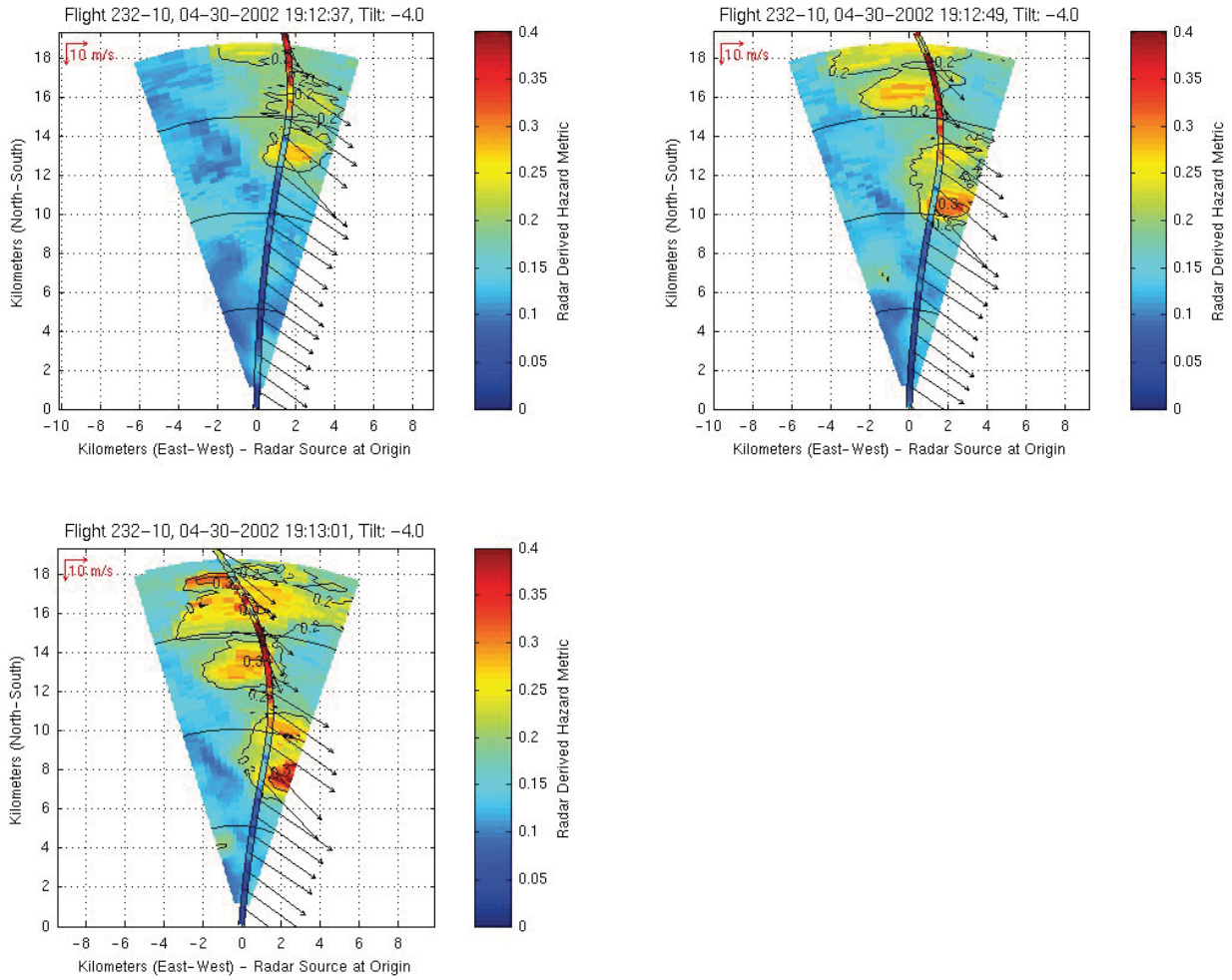

Figure 83. Sequential scans at 12*s* intervals for airborne radar predicted $\sigma_{\Delta n}$ (color contour cones) and *in situ* $\sigma_{\Delta n}$ (color on flight path line) for Event 232-10. Ambient wind vectors are shown along path.

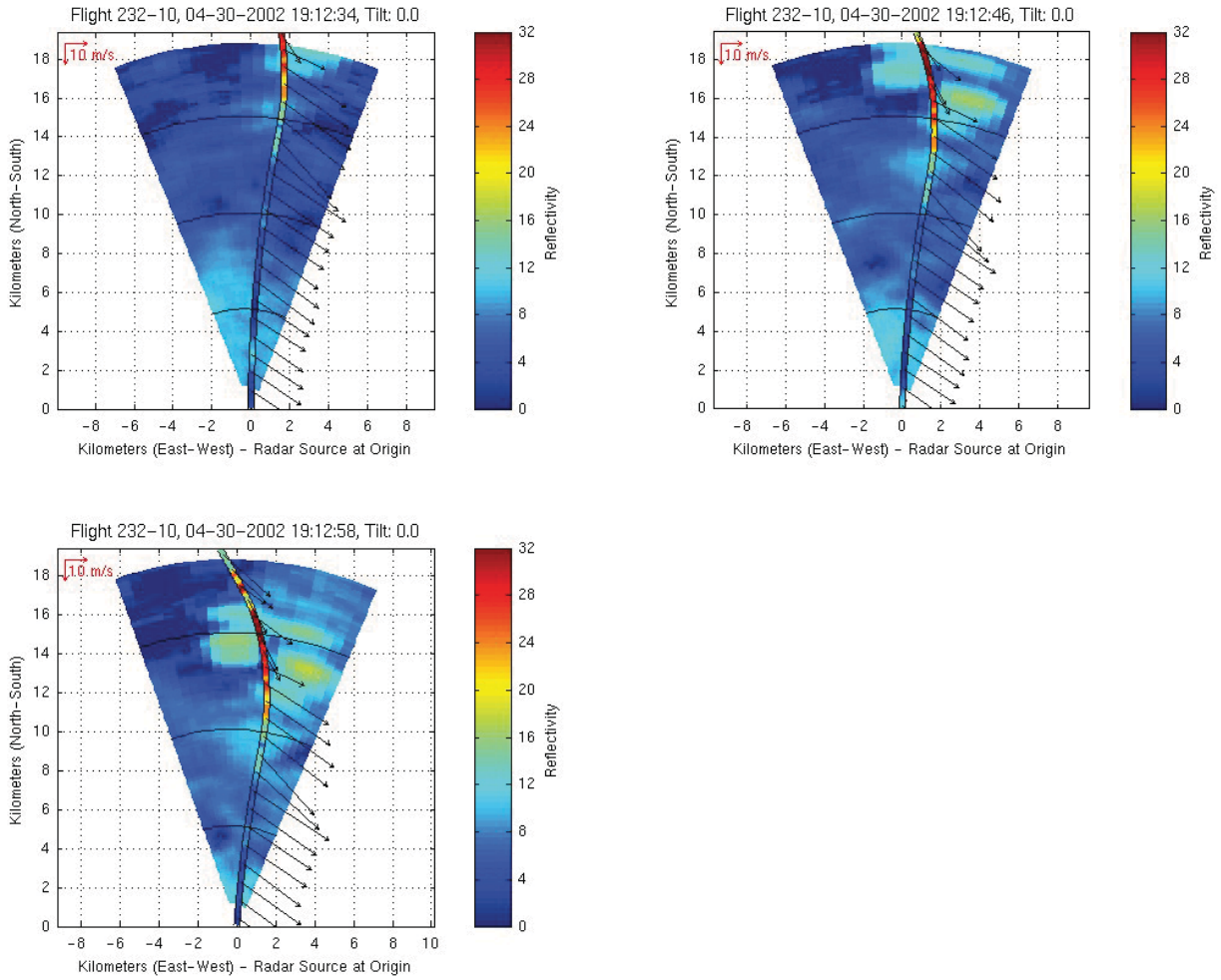

Figure 84. Sequential scans at 12*s* interval for airborne radar reflectivity factor (color contour cones) and *in situ* $\sigma_{\Delta n}$ (color on flight path line) for Event 232-10. Ambient wind vectors are shown along path.

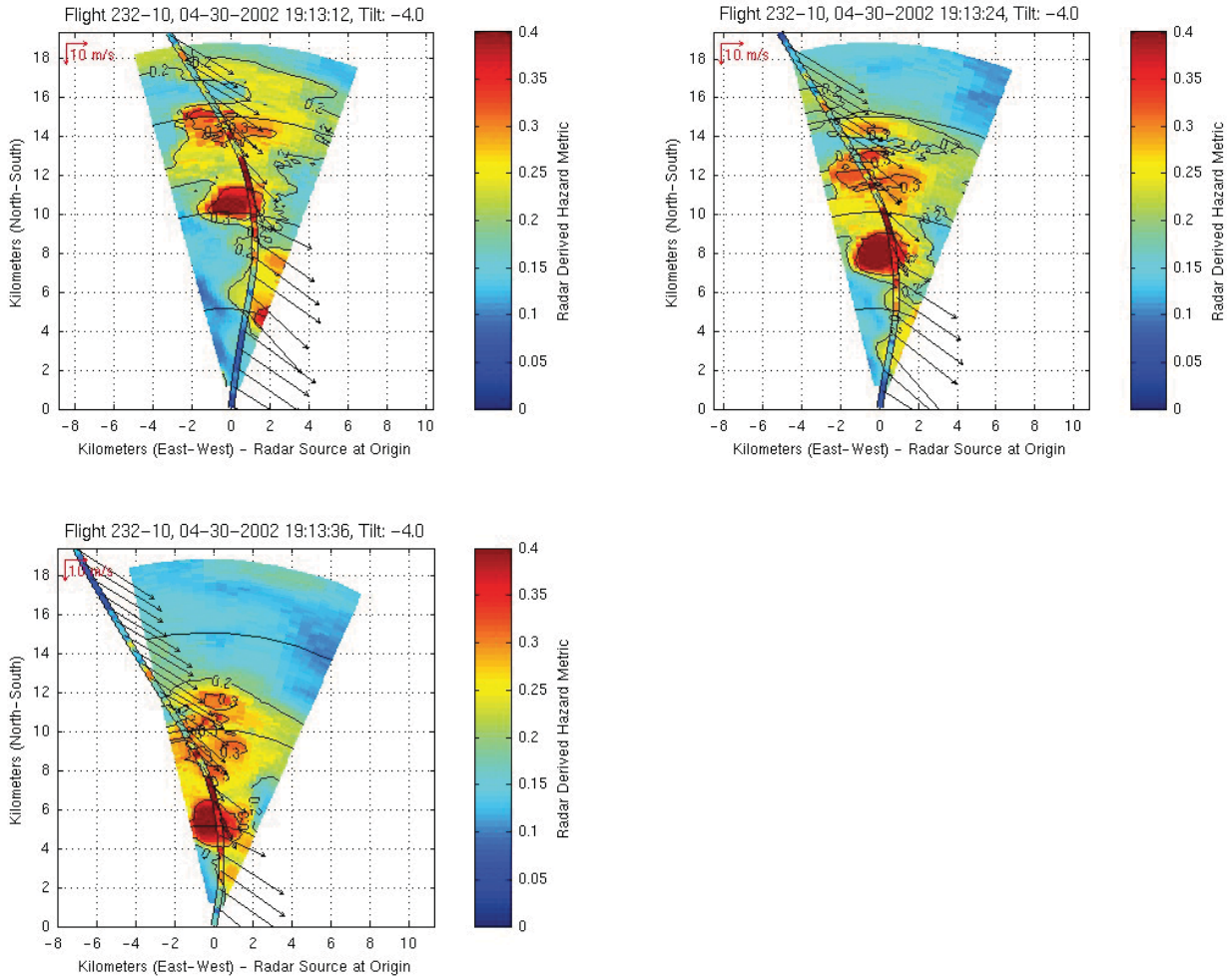

Figure 85. Sequential scans at 12*s* intervals for airborne radar predicted $\sigma_{\Delta n}$ (color contour cones) and *in situ* $\sigma_{\Delta n}$ (color on flight path line) for Event 232-10. Ambient wind vectors are shown along path.

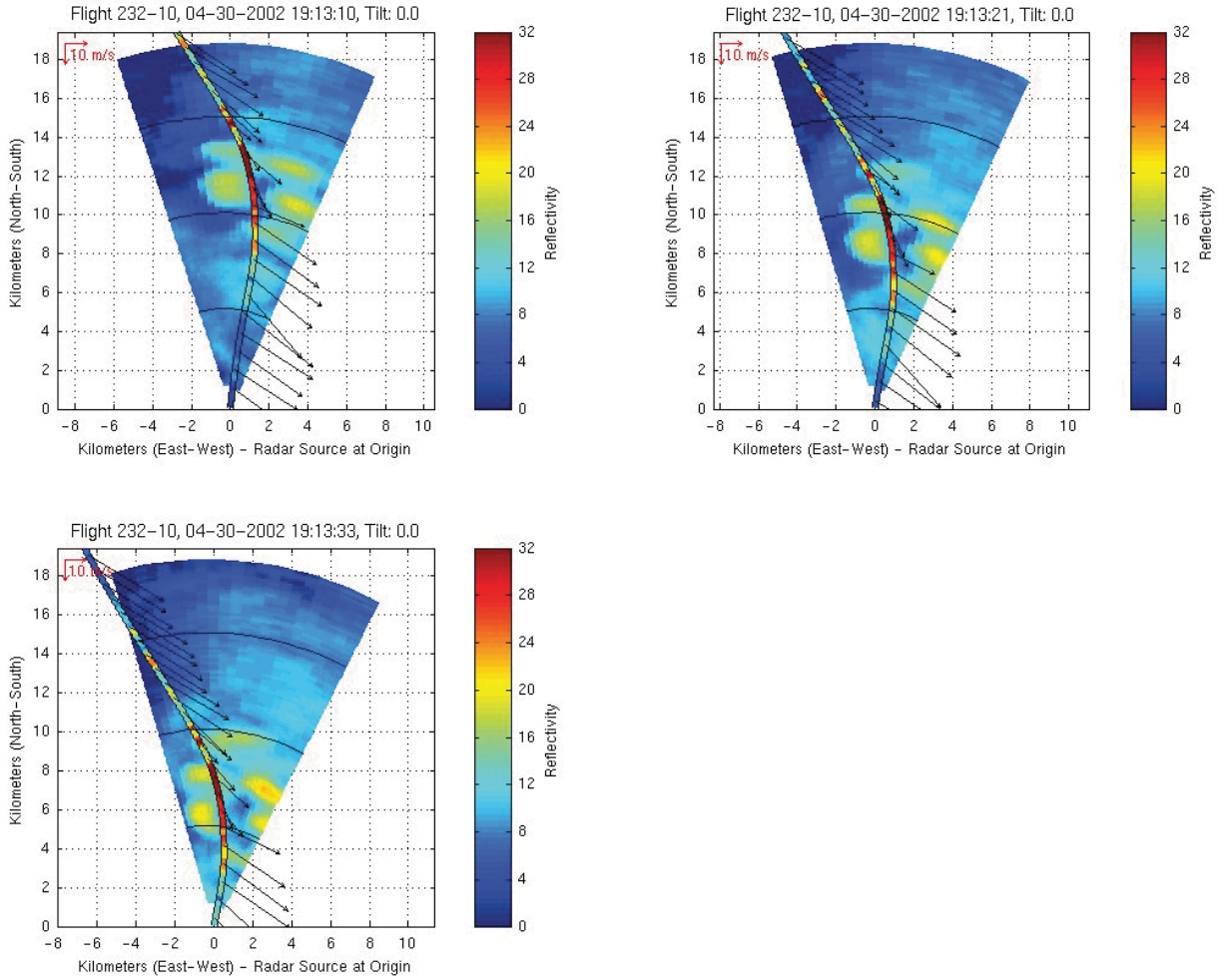

Figure 86. Sequential scans at 12*s* interval for airborne radar reflectivity factor (color contour cones) and *in situ* $\sigma_{\Delta n}$ (color on flight path line) for Event 232-10. Ambient wind vectors are shown along path.

2.9: Flight 233, May 6, 2002

Between 17:40 and 19:45 UTC on 06 May 2002, ARIES investigated two isolated convective cells in eastern Kentucky. These cells were located on the southern periphery of a MCC that was moving rapidly eastward through northern Kentucky and southern Ohio (Figure 87 and Figure 88). Pilot reports of moderate turbulence had been issued in the vicinity of the MCC (Figure 89). Visual meteorological conditions prevailed south of the MCC.

Five significant turbulence encounters were associated with the ARIES penetration of the two convective cells (Figure 90 - Figure 99). Strong airborne radar reflectivity was associated with the central updrafts of these cells. However, the aircraft avoided these regions, penetrating only the tops and periphery of the cells where radar reflectivity was relatively low. The precipitation encountered in the events was in the form of snow and ice crystals (determined from the ARIES camcorders). Initially, storm top elevations were about 10.6 *km* (35 *kft*), but lowered to 7.6 *km* (25 *kft*) as the cells weakened. Likewise, the initial flight altitude was 8.5 *km* (28 *kft*) but was reduced to 5.2 *km* (17 *kft*). Cell motion was to the east-northeast at 22 *m/s* (43 *kts*) and the prevailing winds were from 275° relative to true North, at 31 *m/s* (60 *kts*).

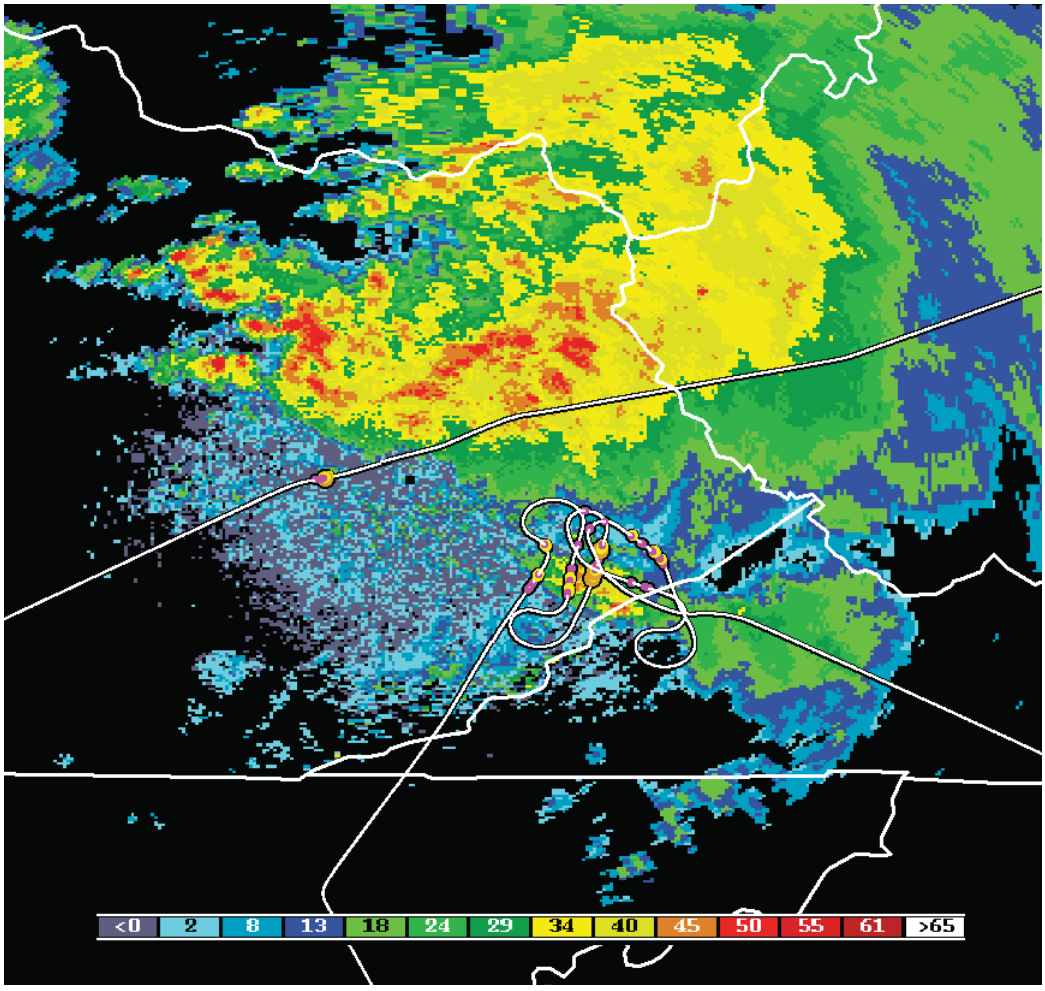

Figure 87. Path for Flight 233. Ground based composite radar reflectivity (*dBz*) from the KJKL (Jackson, Kentucky) NEXRAD radar at 19:18:40 UTC on 6 May 2002. See Figure 3 for legend to intensity of the aircraft RMS normal loads.

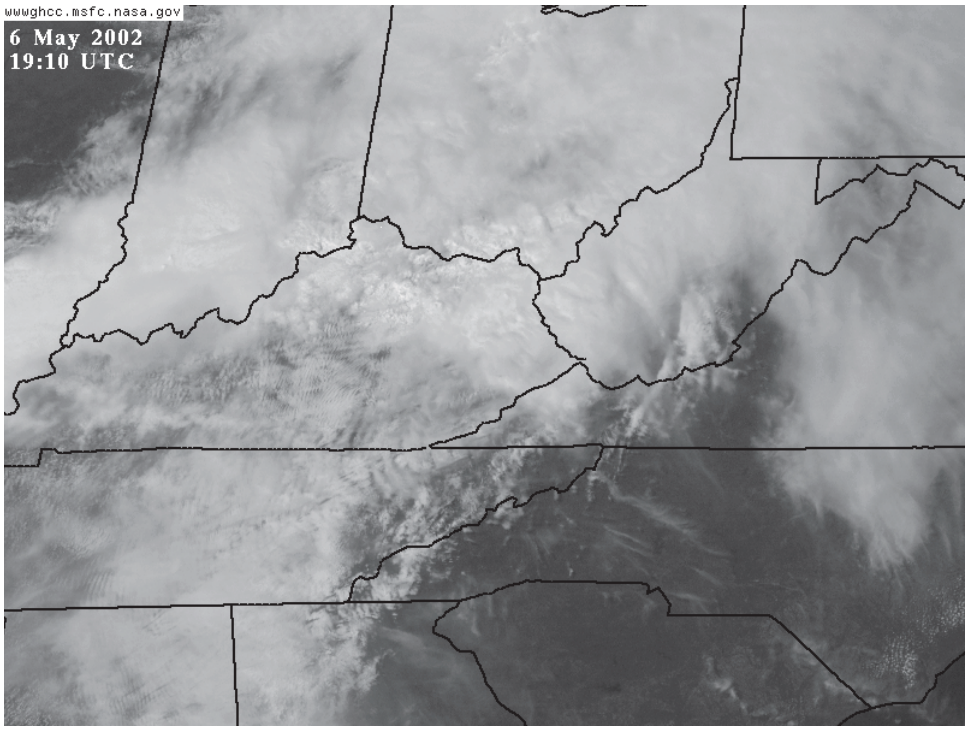

Figure 88. GOES-12 visible satellite image at 1910 UTC on 06 May 2002.

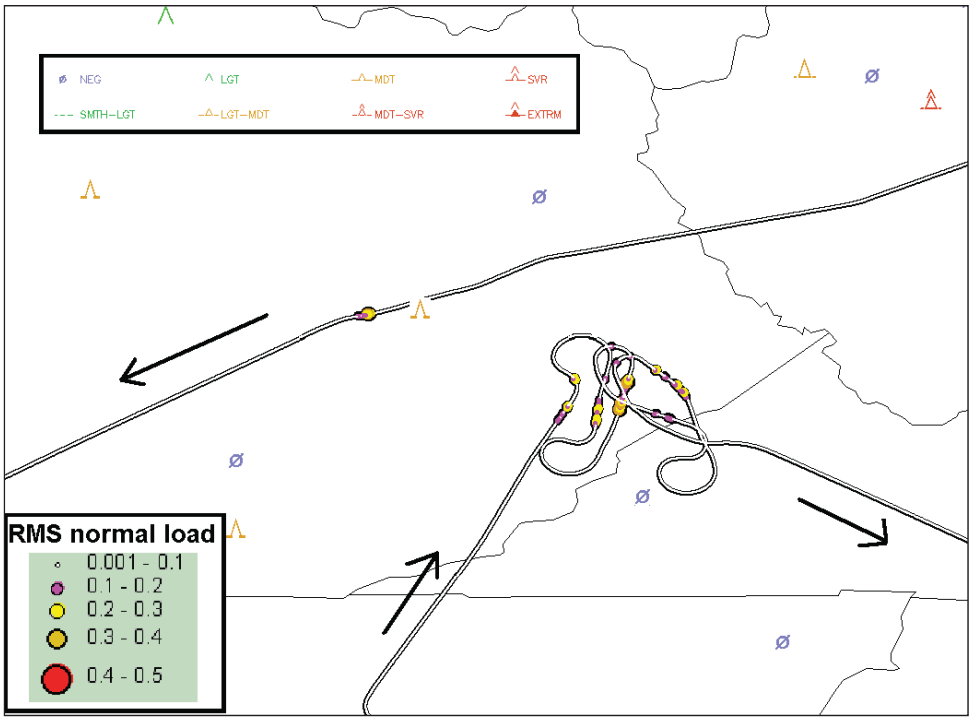

Figure 89. RMS normal loads encountered along the path for Flight 233 with turbulence PIREPS for 06 May 2002.

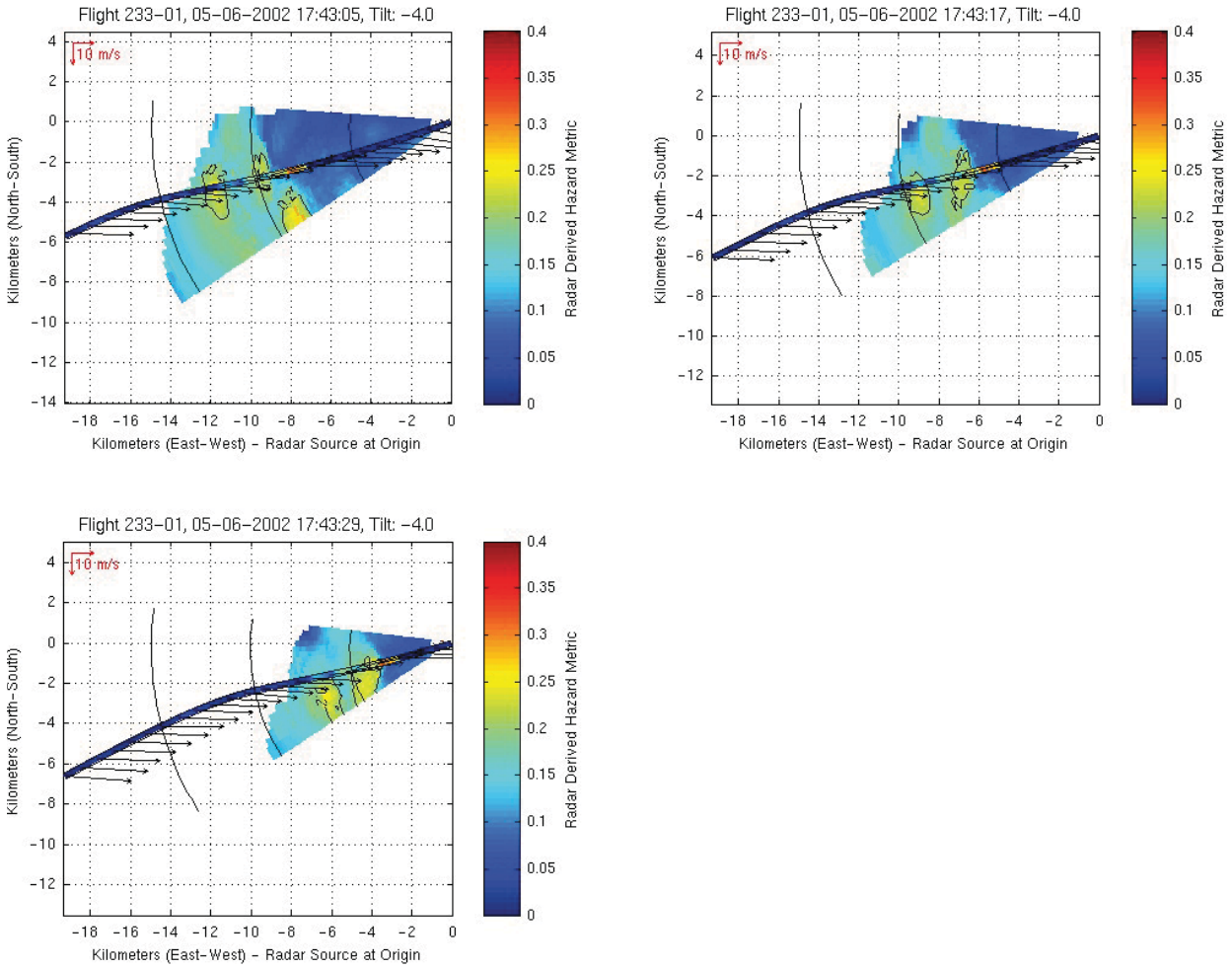

Figure 90. Sequential scans at 12*s* intervals for airborne radar predicted $\sigma_{\Delta n}$ (color contour cones) and *in situ* $\sigma_{\Delta n}$ (color on flight path line) for Event 233-01. Ambient wind vectors are shown along path.

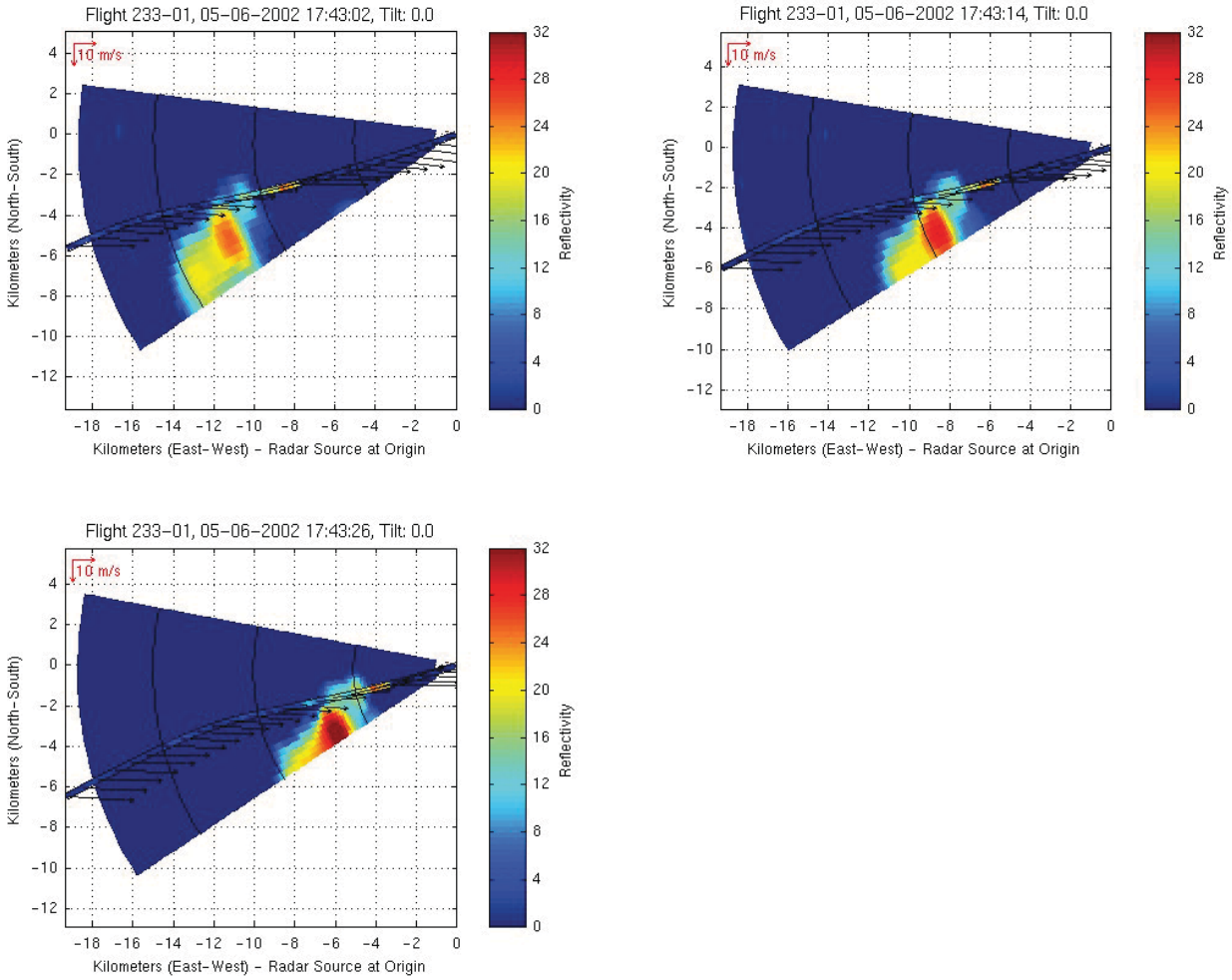

Figure 91. Sequential scans at 12*s* interval for airborne radar reflectivity factor (color contour cones) and *in situ* $\sigma_{\Delta n}$ (color on flight path line) for Event 233-01. Ambient wind vectors are shown along path.

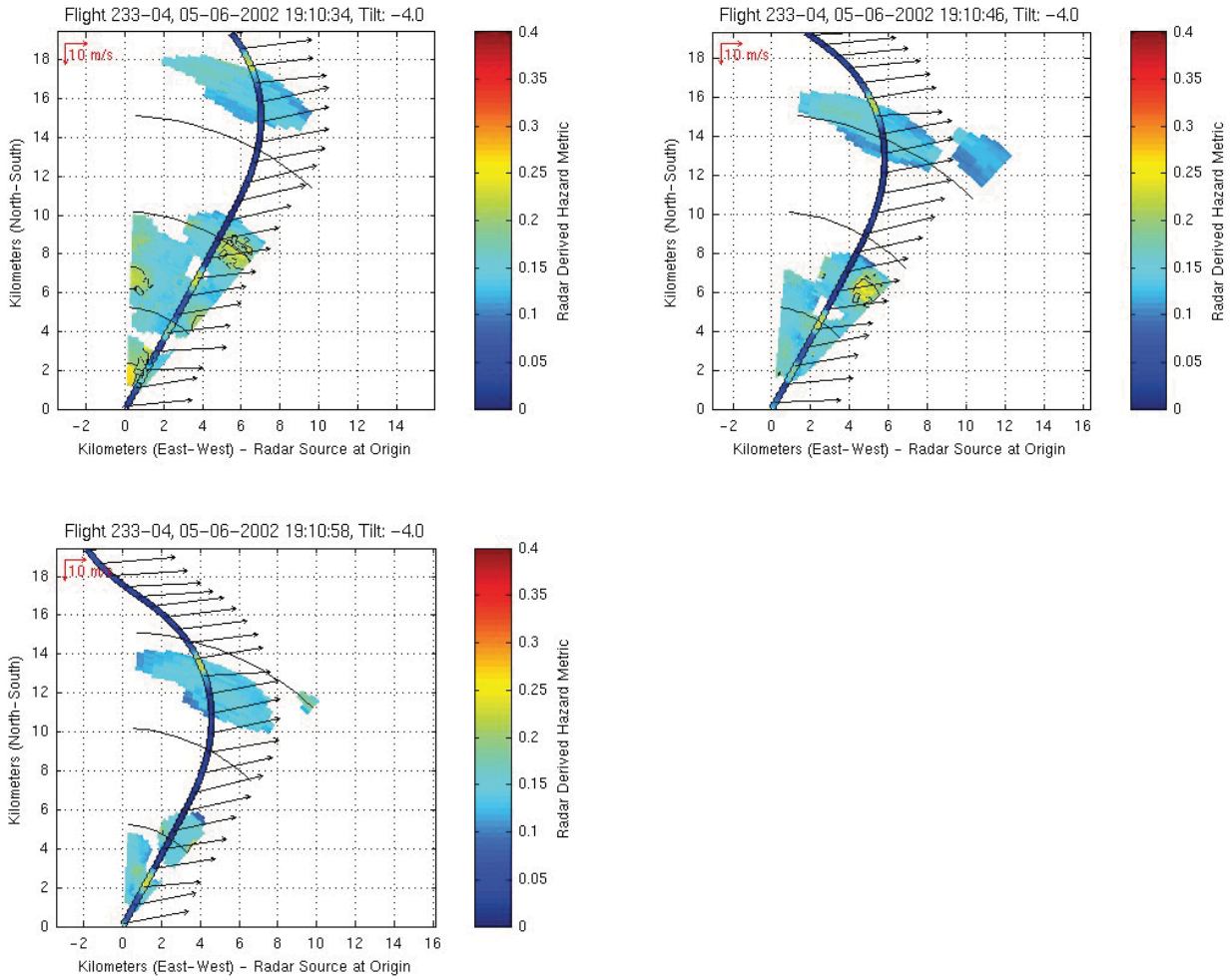

Figure 92. Sequential scans at 12*s* intervals for airborne radar predicted $\sigma_{\Delta n}$ (color contour cones) and *in situ* $\sigma_{\Delta n}$ (color on flight path line) for Event 233-04. Ambient wind vectors are shown along path.

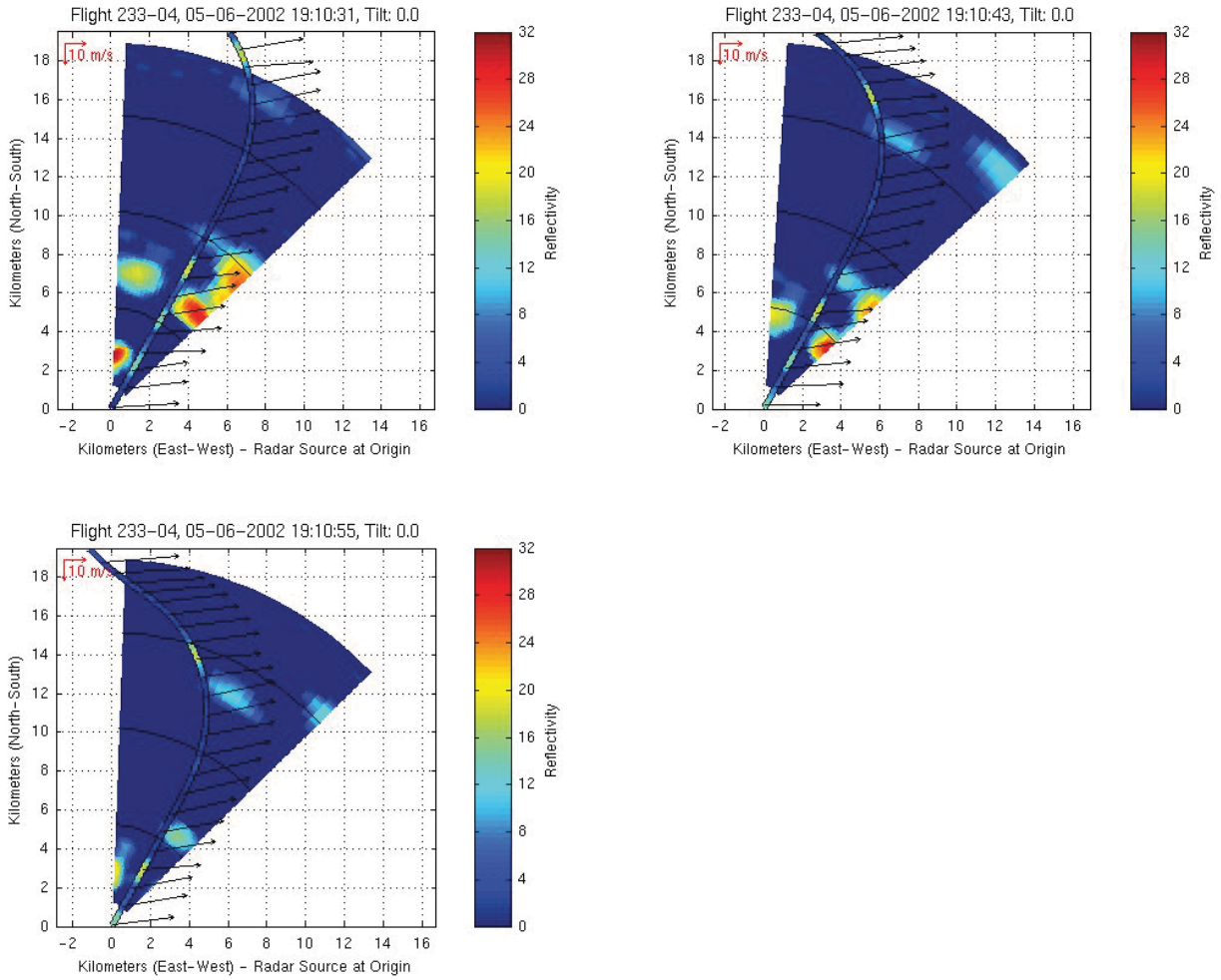

Figure 93. Sequential scans at 12*s* interval for airborne radar reflectivity factor (color contour cones) and *in situ* $\sigma_{\Delta n}$ (color on flight path line) for Event 233-04. Ambient wind vectors are shown along path.

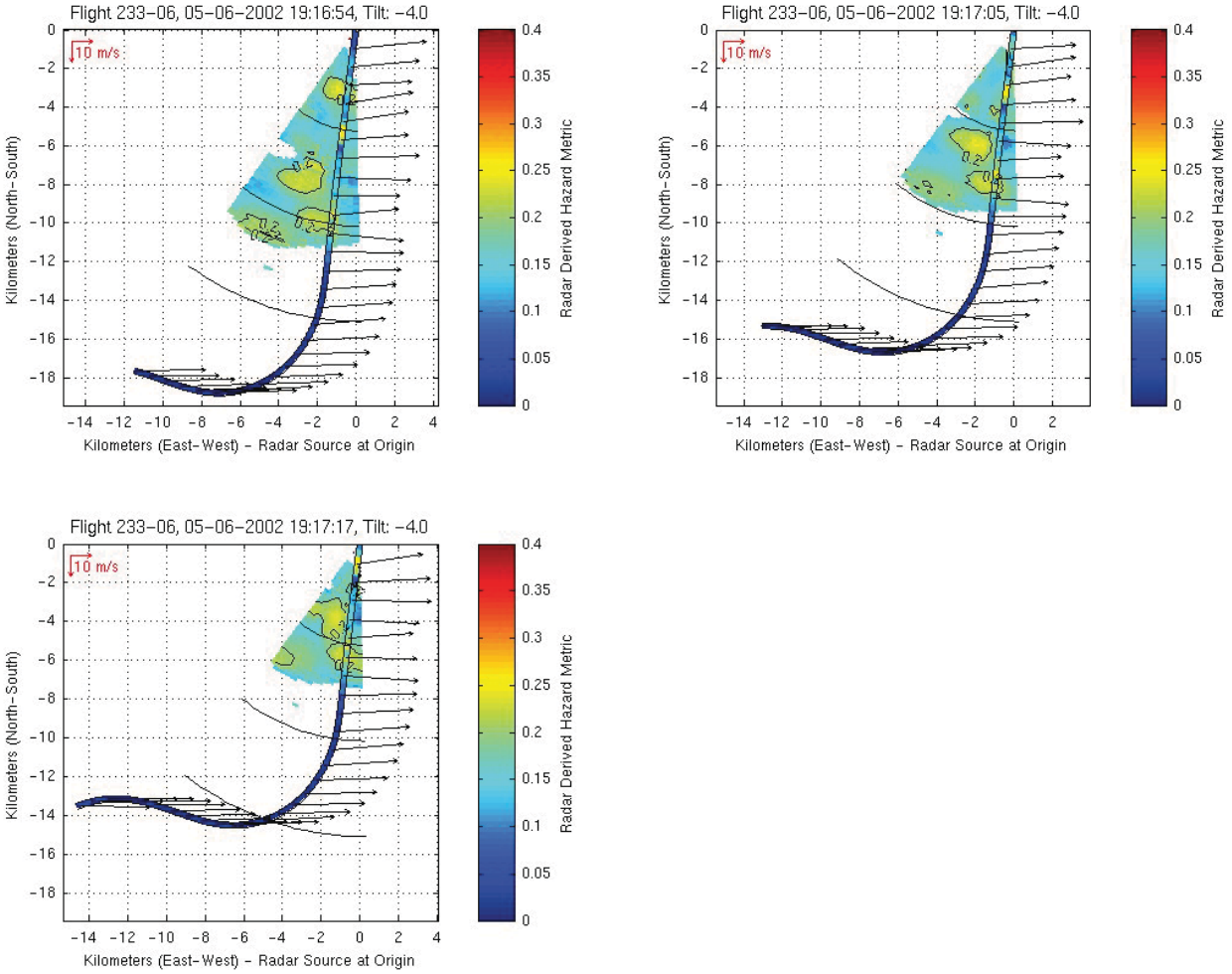

Figure 94. Sequential scans at 12*s* intervals for airborne radar predicted $\sigma_{\Delta n}$ (color contour cones) and *in situ* $\sigma_{\Delta n}$ (color on flight path line) for Event 233-06. Ambient wind vectors are shown along path.

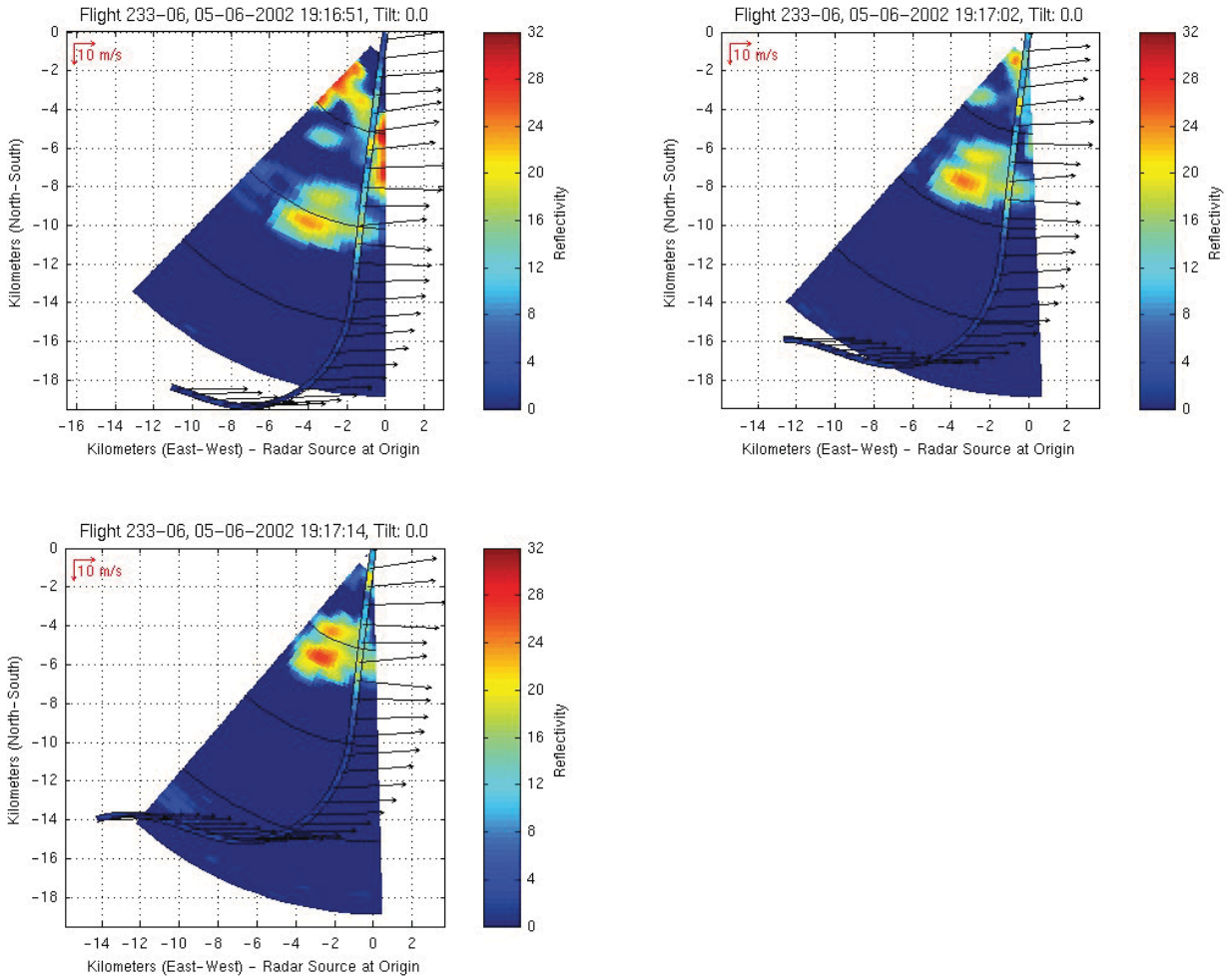

Figure 95. Sequential scans at 12*s* interval for airborne radar reflectivity factor (color contour cones) and *in situ* $\sigma_{\Delta n}$ (color on flight path line) for Event 233-06. Ambient wind vectors are shown along path.

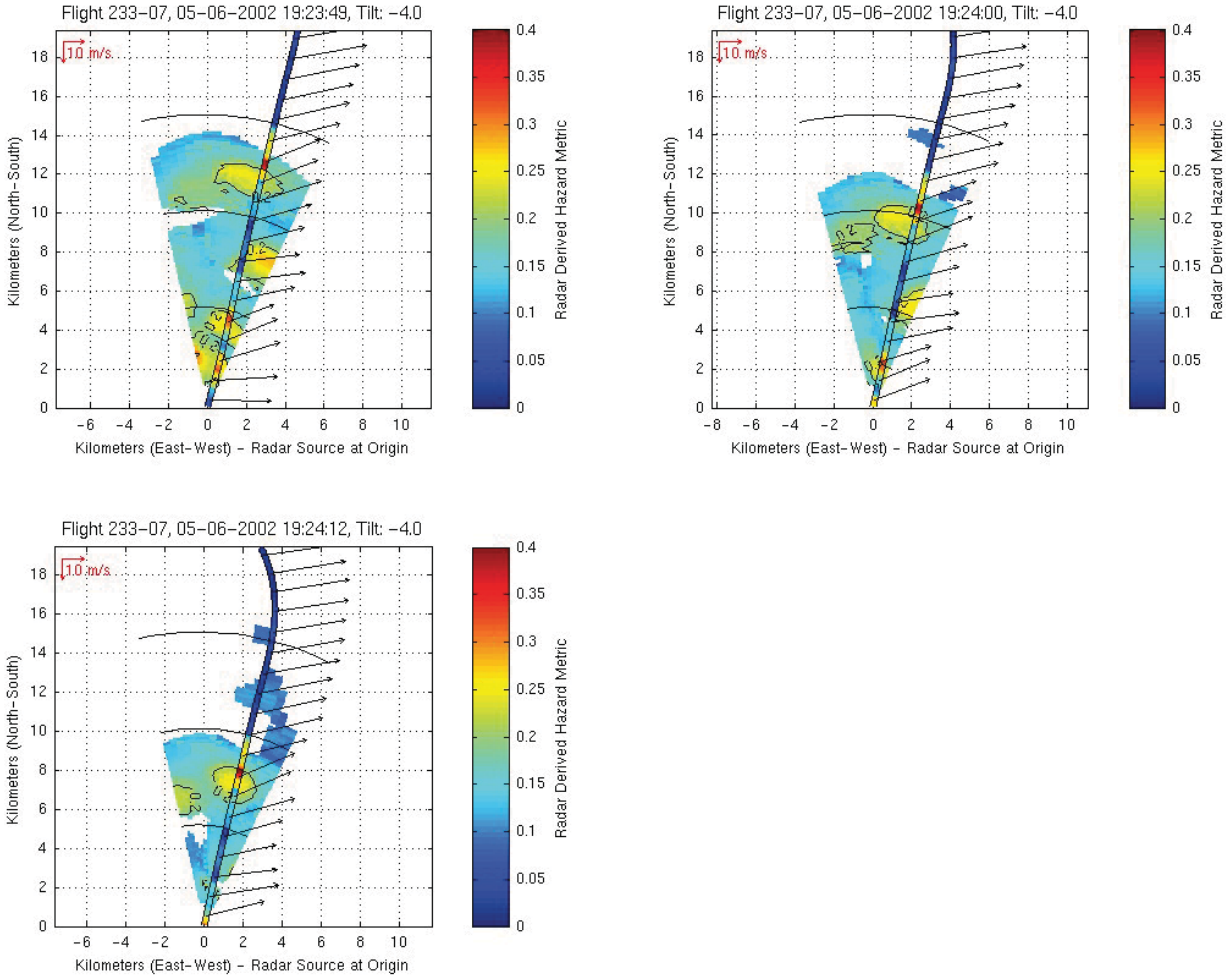

Figure 96. Sequential scans at 12*s* intervals for airborne radar predicted $\sigma_{\Delta n}$ (color contour cones) and *in situ* $\sigma_{\Delta n}$ (color on flight path line) for Event 233-07. Ambient wind vectors are shown along path.

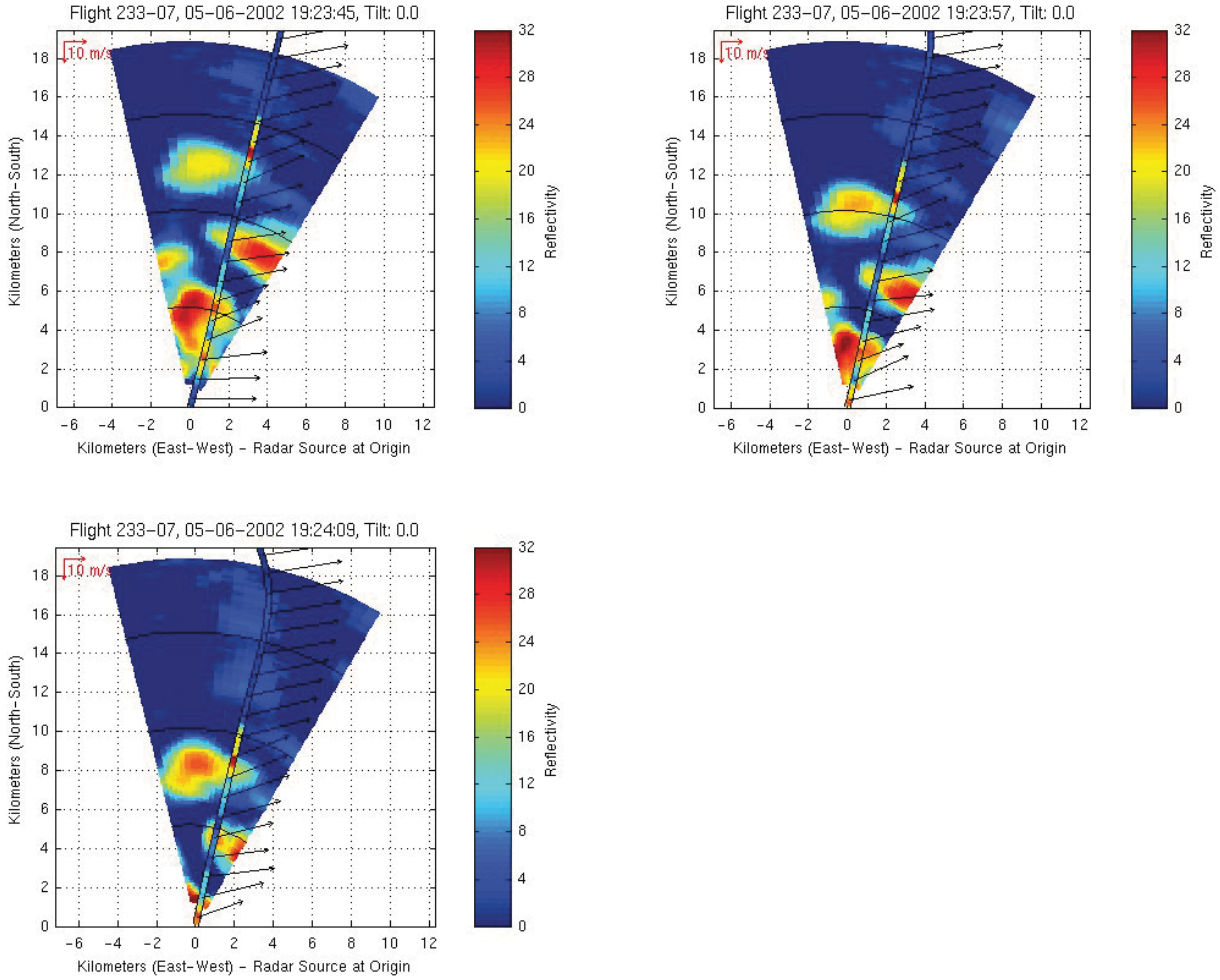

Figure 97. Sequential scans at 12*s* interval for airborne radar reflectivity factor (color contour cones) and *in situ* $\sigma_{\Delta n}$ (color on flight path line) for Event 233-07. Ambient wind vectors are shown along path.

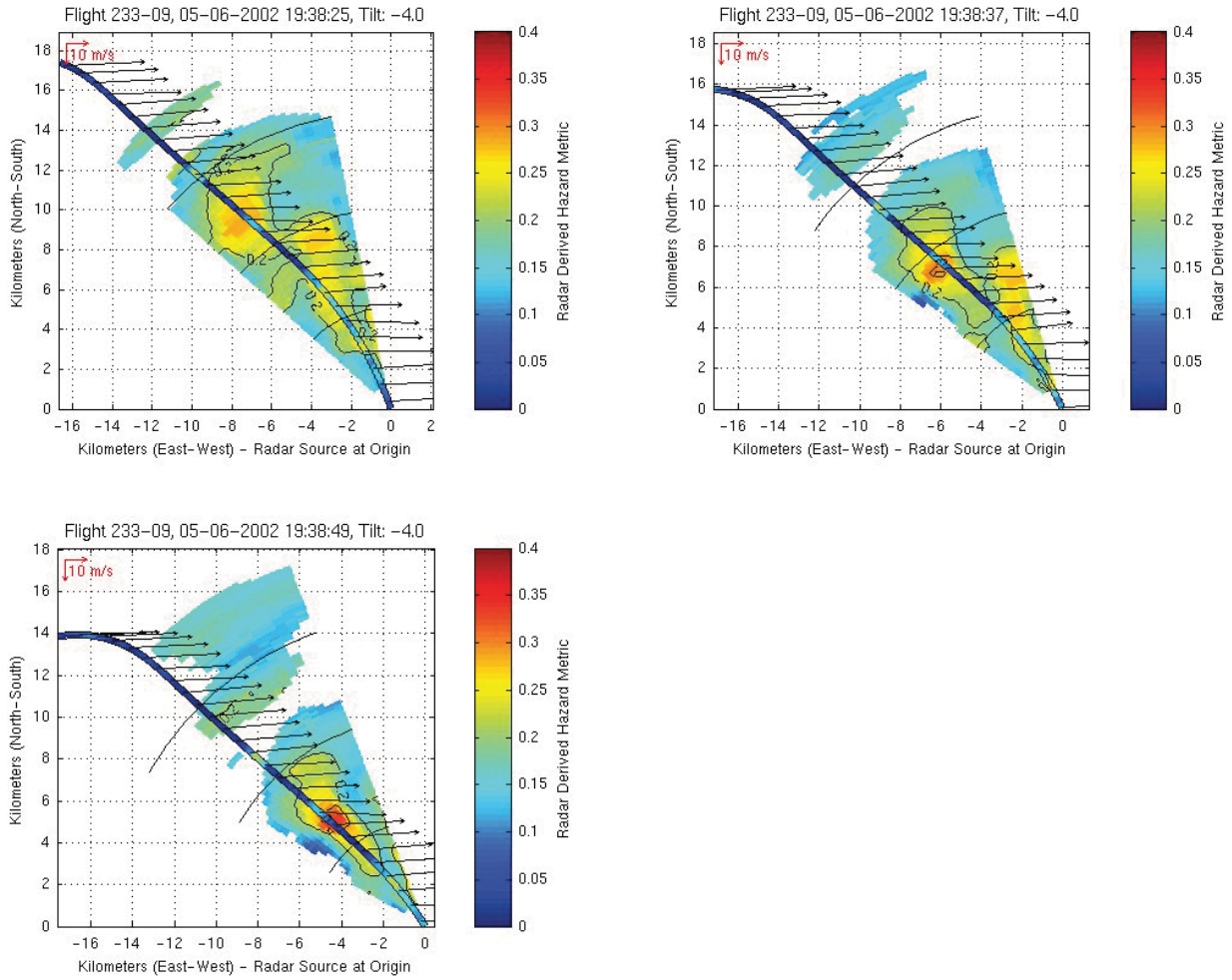

Figure 98. Sequential scans at 12*s* intervals for airborne radar predicted $\sigma_{\Delta n}$ (color contour cones) and *in situ* $\sigma_{\Delta n}$ (color on flight path line) for Event 233-09. Ambient wind vectors are shown along path.

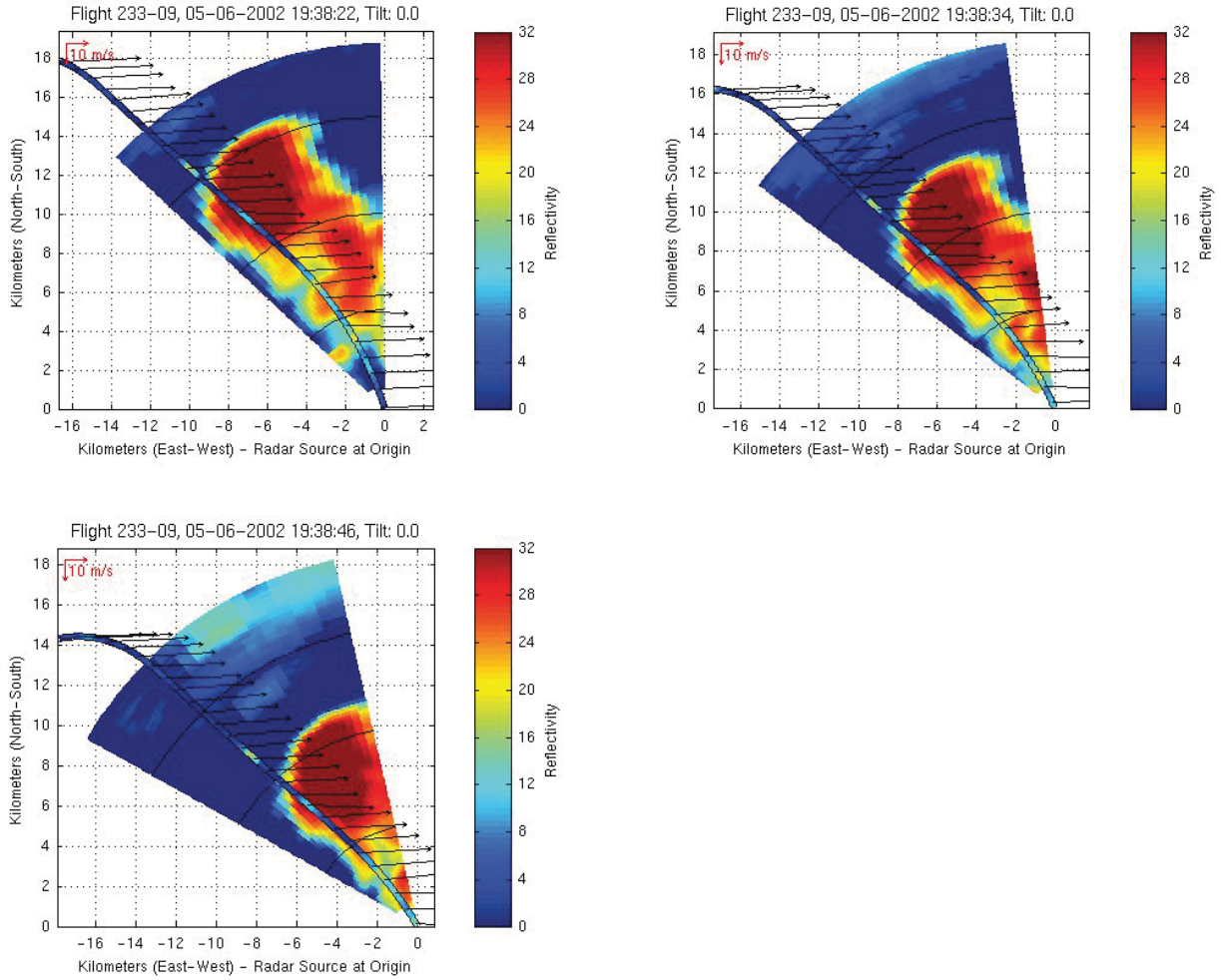

Figure 99. Sequential scans at 12*s* interval for airborne radar reflectivity factor (color contour cones) and *in situ* $\sigma_{\Delta n}$ (color on flight path line) for Event 233-09. Ambient wind vectors are shown along path.

2.10: Flight 234, May 7, 2002

Between 1800 and 1900 UTC on 07 May 2002, ARIES investigated a line of broken, convective cells near Knoxville, Tennessee (Figure 100 and Figure 101). The cells were isolated and short-lived but continued to redevelop along the line during the data collection period. Pilot reports of light turbulence had been issued in the vicinity of these cells (Figure 102). Visual meteorological conditions prevailed, although thin cirrus cloud layers were present.

Five significant turbulence encounters by ARIES were associated with cloud top penetration of these cells (Figure 103 - Figure 112). Weak to moderate airborne radar reflectivity was associated with the cells. The precipitation encountered was in the form of snow and ice crystals. The maximum storm tops were 9.1 *km* (30 *kft*) and the flight altitude was 7.6 *km* (25 *kft*). The cell motion was towards the east-northeast at 18 *m/s* (35 *kts*). The prevailing winds in the storm environment were from 23 *m/s* (45 *kts*) from 270° relative to true North.

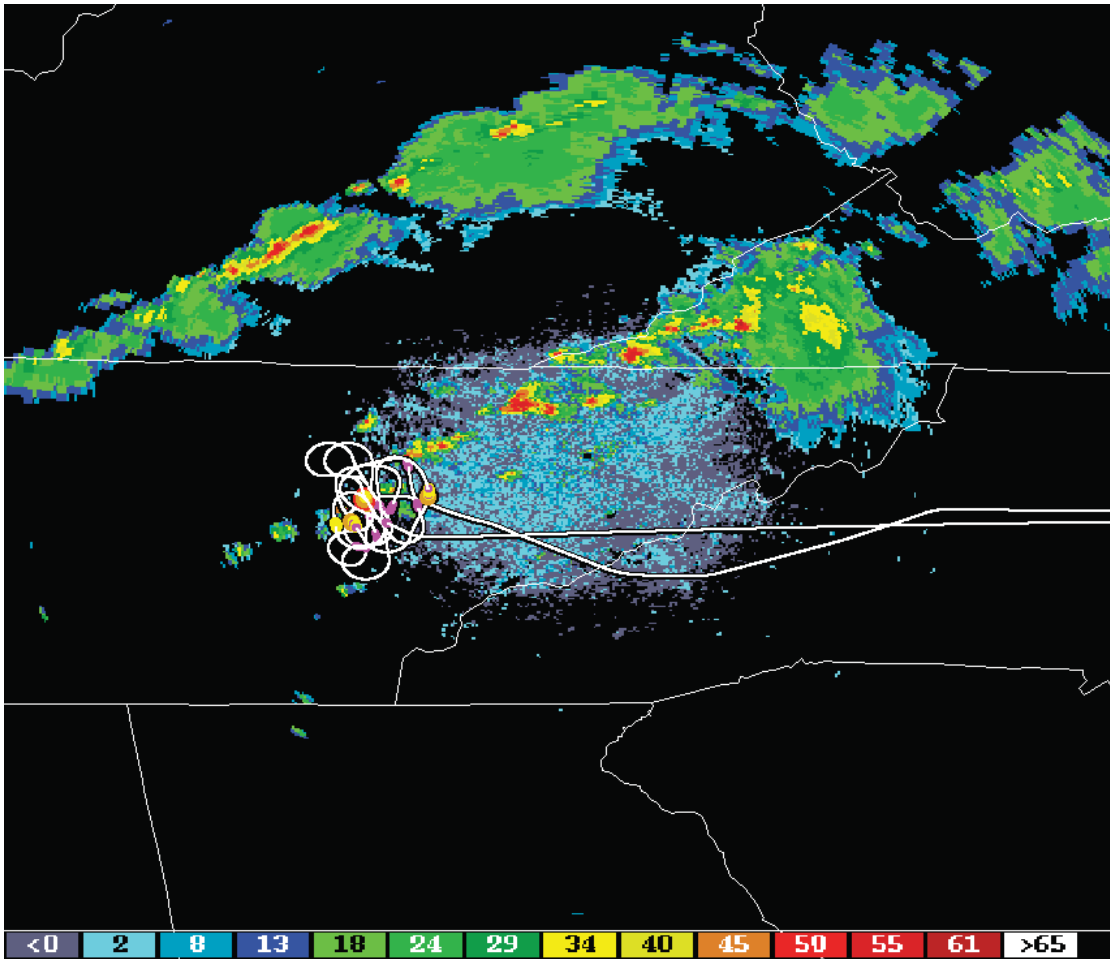

Figure 100. Path for Flight 234. Ground based composite radar reflectivity (*dBz*) from the KMRX (Knoxville, Tennessee) NEXRAD radar at 18:13:30 UTC on 7 May 2002. See Figure 3 for legend to intensity of the aircraft RMS normal loads.

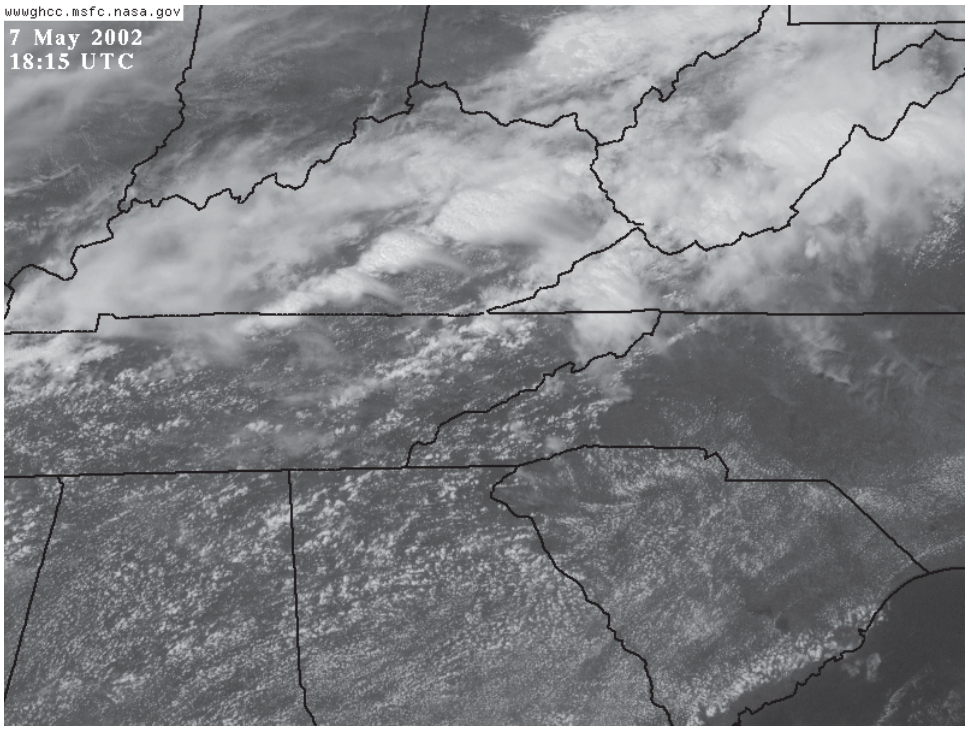

Figure 101. GOES-12 visible satellite image at 1815 UTC on 07 May 2002.

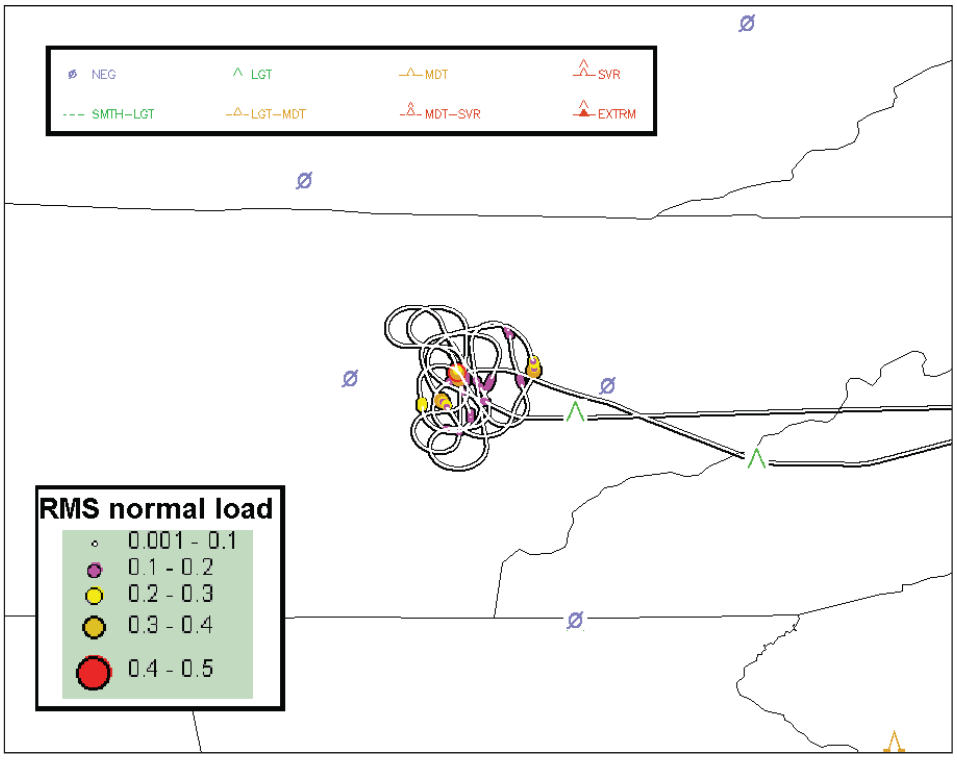

Figure 102. RMS normal loads encountered along the path for Flight 234 with turbulence PIREPS for 07 May 2002.

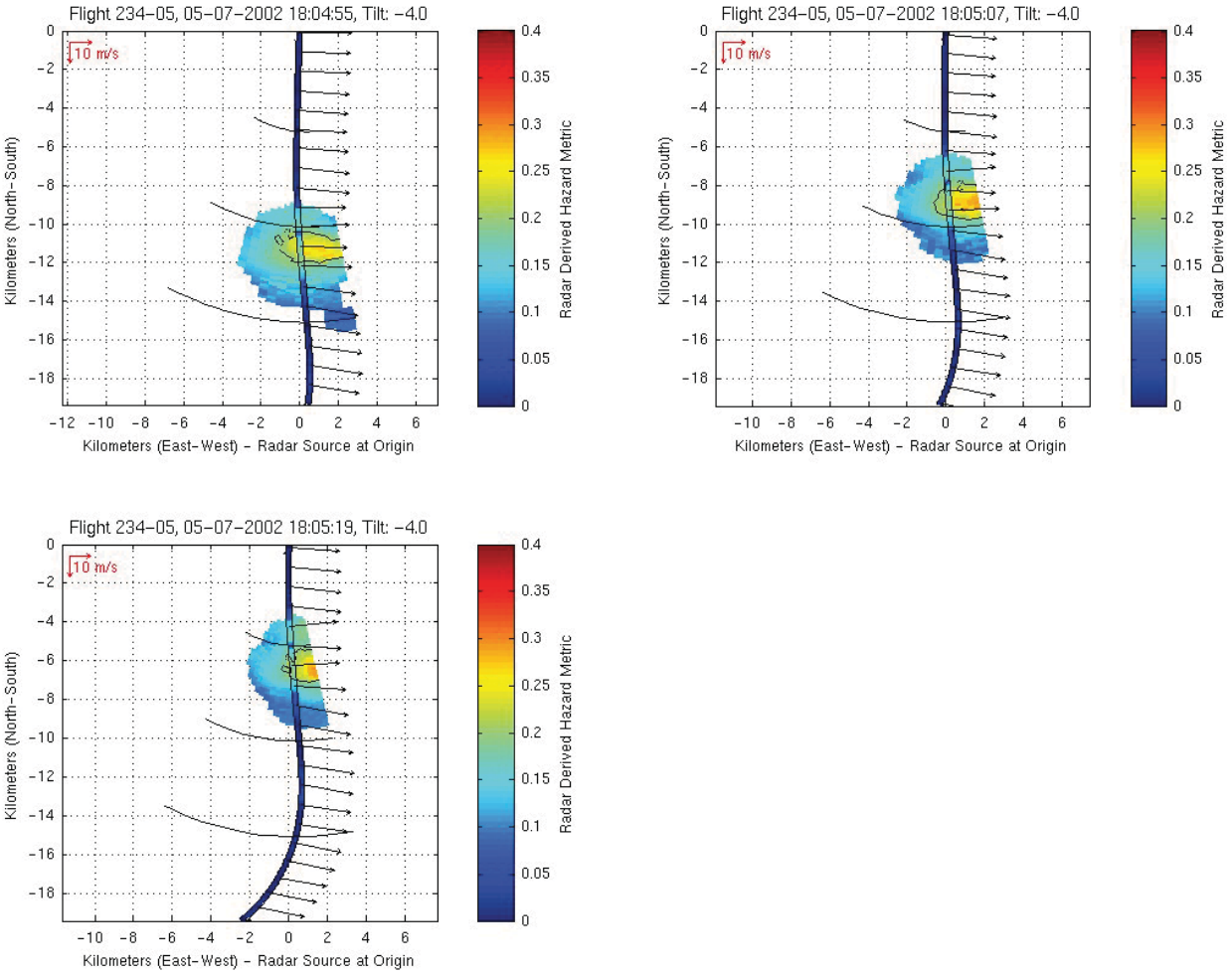

Figure 103. Sequential scans at 12*s* intervals for airborne radar predicted $\sigma_{\Delta n}$ (color contour cones) and *in situ* $\sigma_{\Delta n}$ (color on flight path line) for Event 234-05. Ambient wind vectors are shown along path.

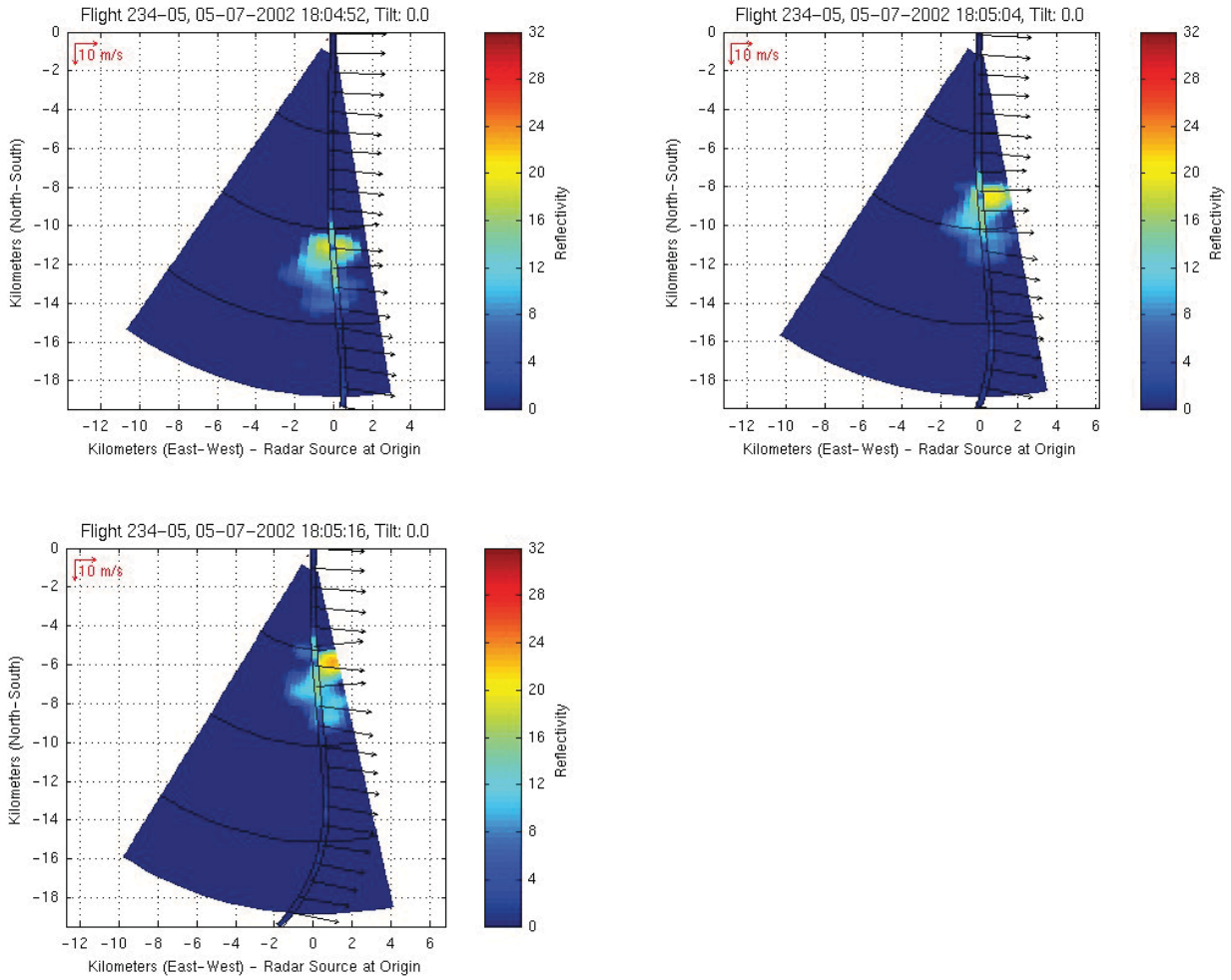

Figure 104. Sequential scans at 12*s* interval for airborne radar reflectivity factor (color contour cones) and *in situ* $\sigma_{\Delta n}$ (color on flight path line) for Event 234-05. Ambient wind vectors are shown along path.

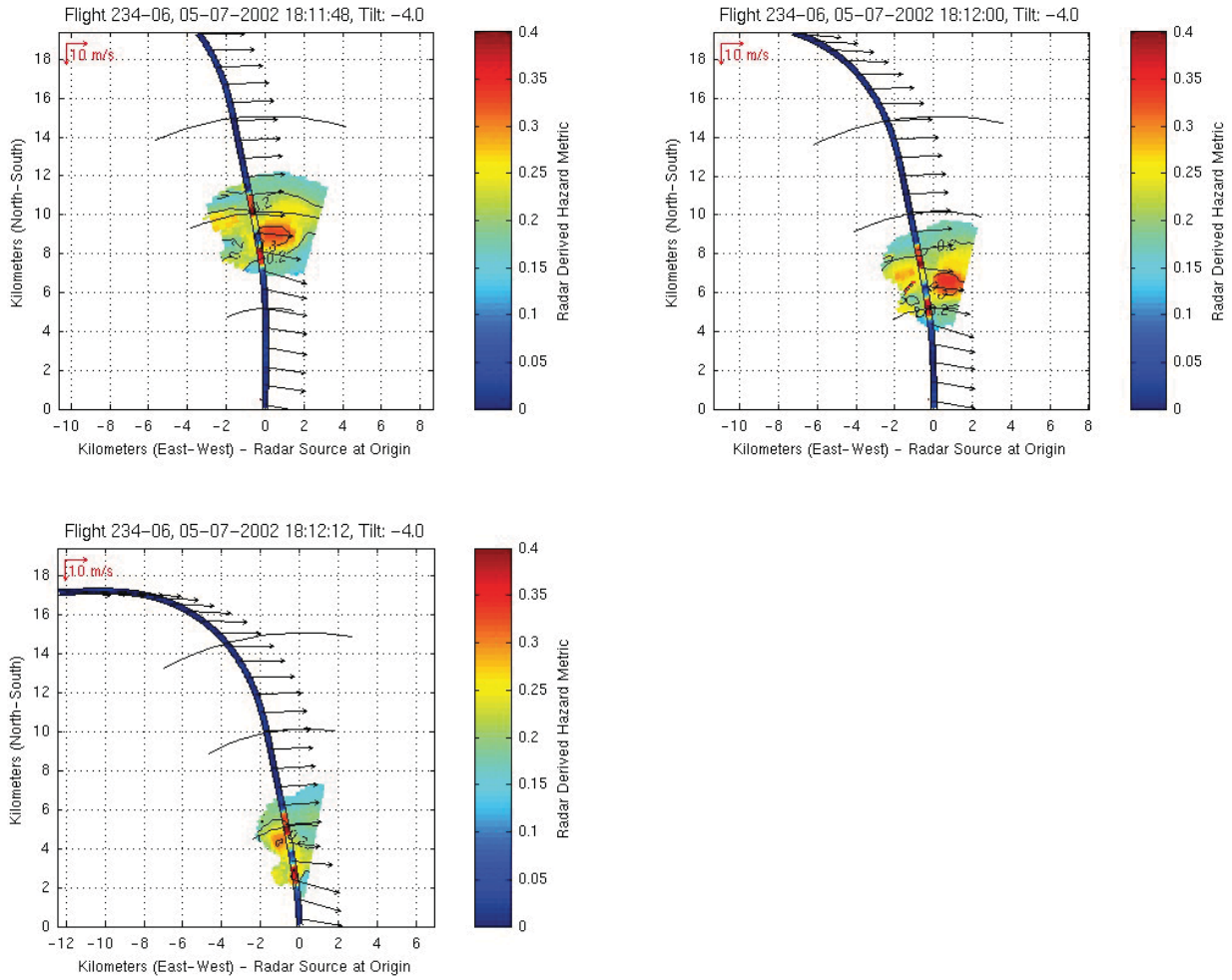

Figure 105. Sequential scans at 12*s* intervals for airborne radar predicted $\sigma_{\Delta n}$ (color contour cones) and *in situ* $\sigma_{\Delta n}$ (color on flight path line) for Event 234-06. Ambient wind vectors are shown along path.

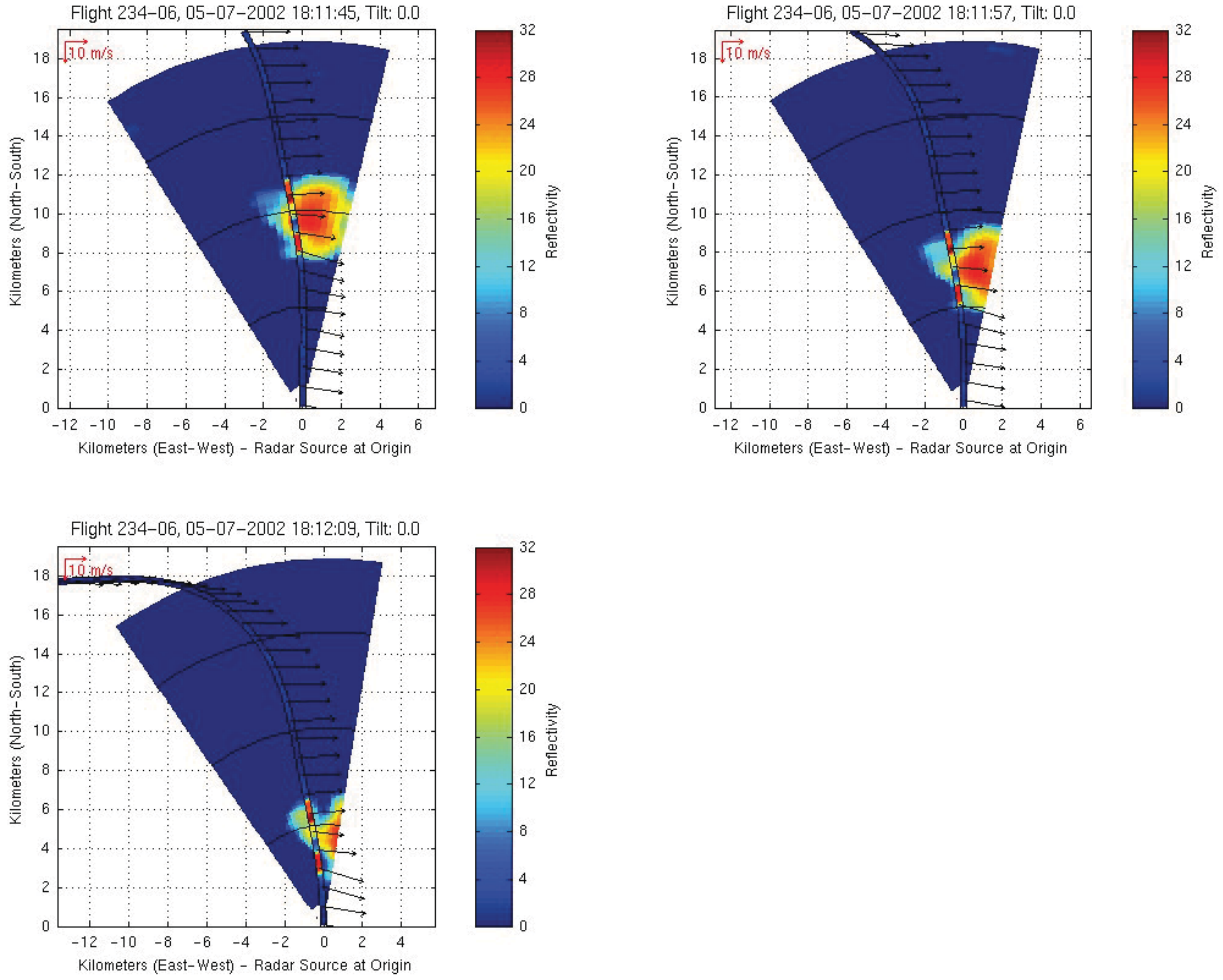

Figure 106. Sequential scans at 12*s* interval for airborne radar reflectivity factor (color contour cones) and *in situ* $\sigma_{\Delta n}$ (color on flight path line) for Event 234-06. Ambient wind vectors are shown along path.

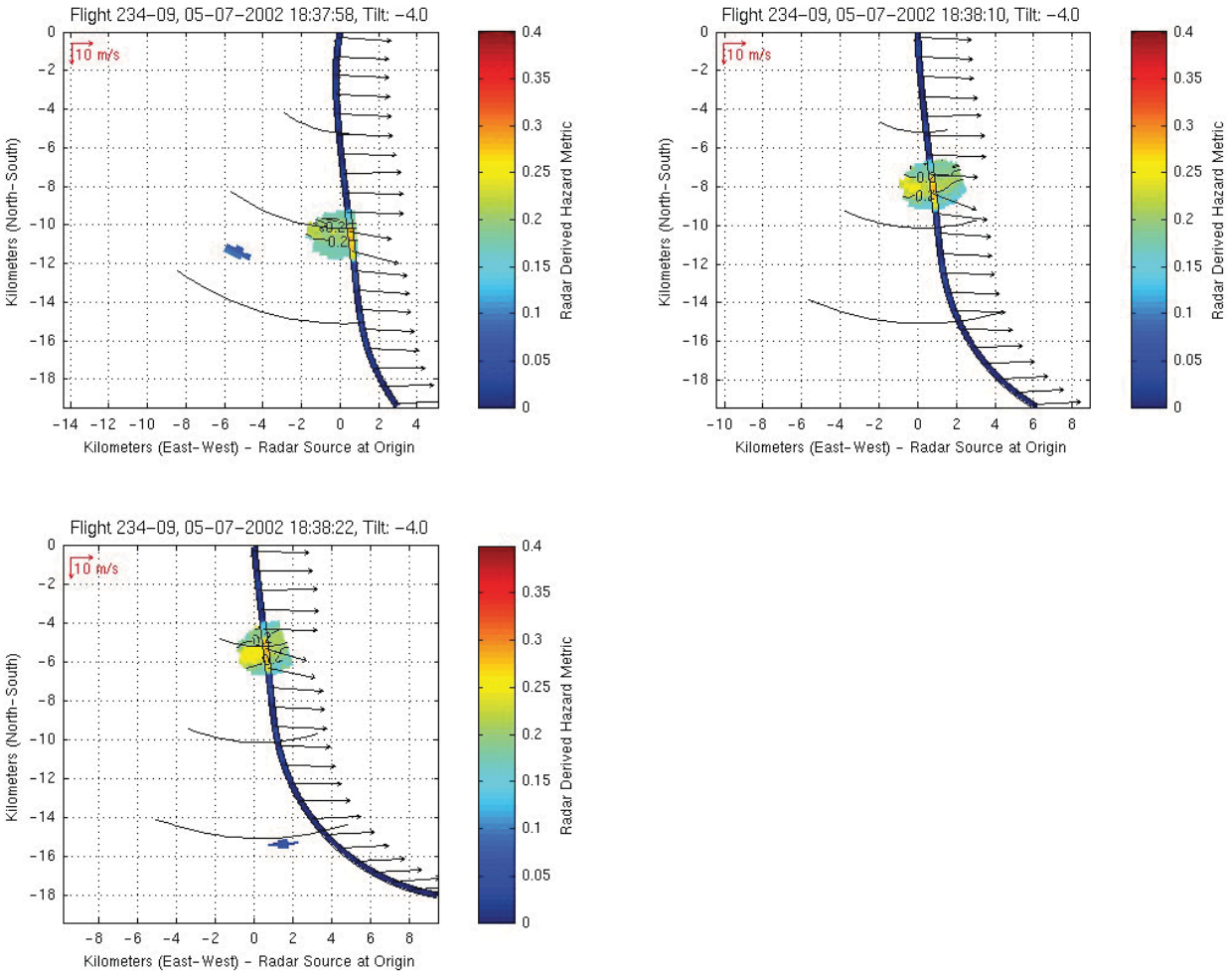

Figure 107. Sequential scans at 12*s* intervals for airborne radar predicted $\sigma_{\Delta n}$ (color contour cones) and *in situ* $\sigma_{\Delta n}$ (color on flight path line) for Event 234-09. Ambient wind vectors are shown along path.

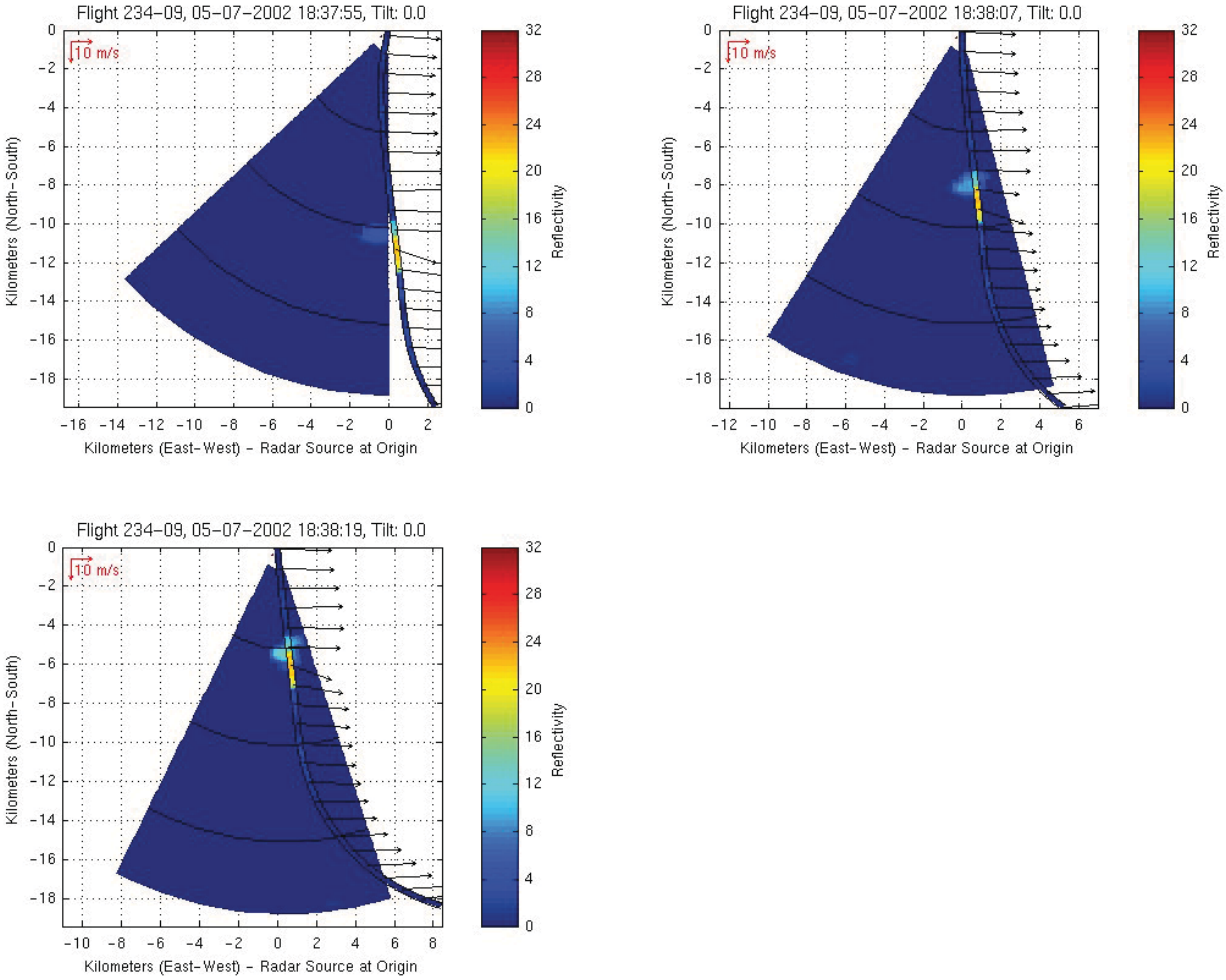

Figure 108. Sequential scans at 12*s* interval for airborne radar reflectivity factor (color contour cones) and *in situ* $\sigma_{\Delta n}$ (color on flight path line) for Event 234-09. Ambient wind vectors are shown along path.

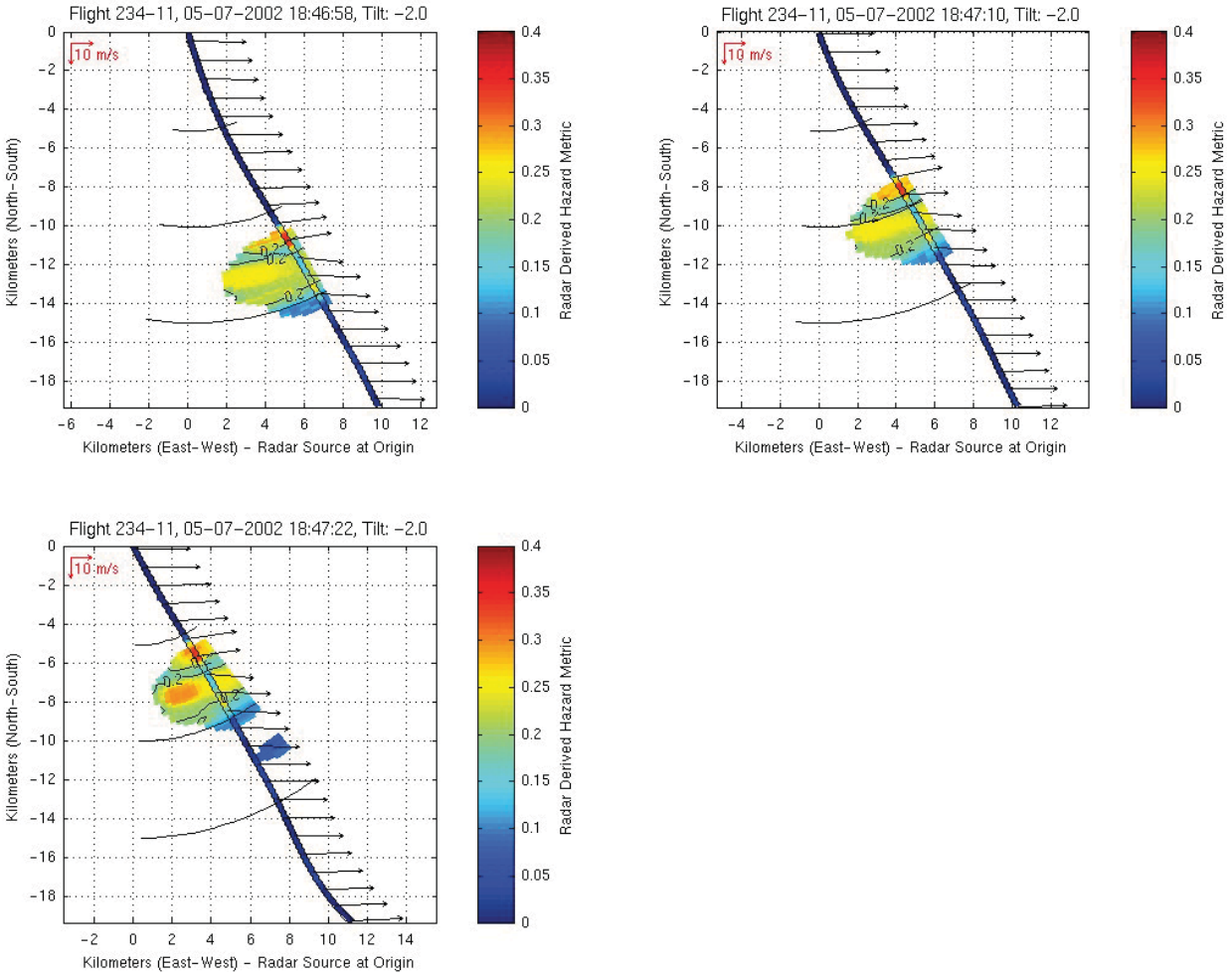

Figure 109. Sequential scans at 12*s* intervals for airborne radar predicted $\sigma_{\Delta n}$ (color contour cones) and *in situ* $\sigma_{\Delta n}$ (color on flight path line) for Event 234-11. Airborne with –2° tilt only. Ambient wind vectors are shown along path.

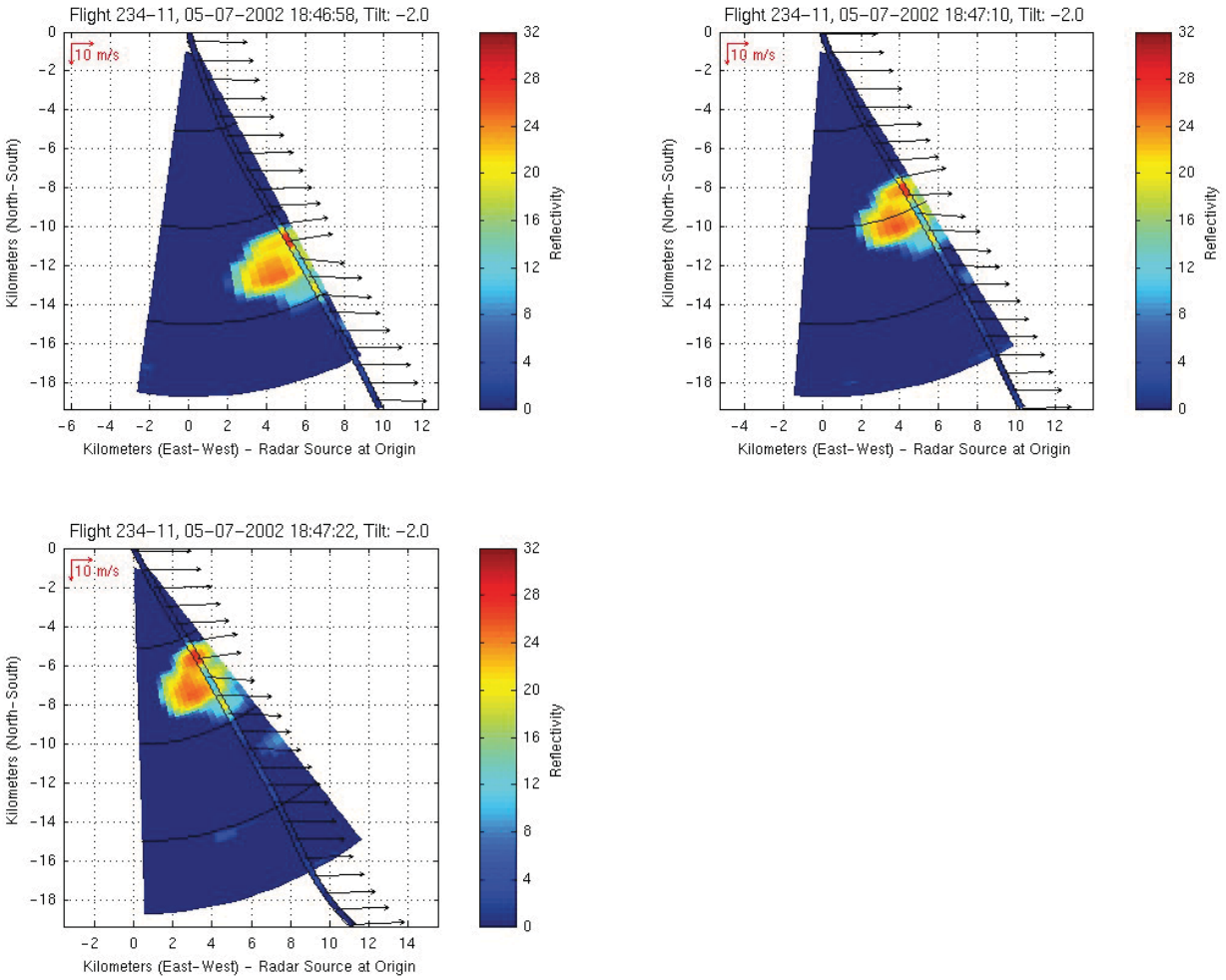

Figure 110. Sequential scans at 12*s* interval for airborne radar reflectivity factor (color contour cones) and *in situ* $\sigma_{\Delta n}$ (color on flight path line) for Event 234-11. Airborne with –2° tilt only. Ambient wind vectors are shown along path.

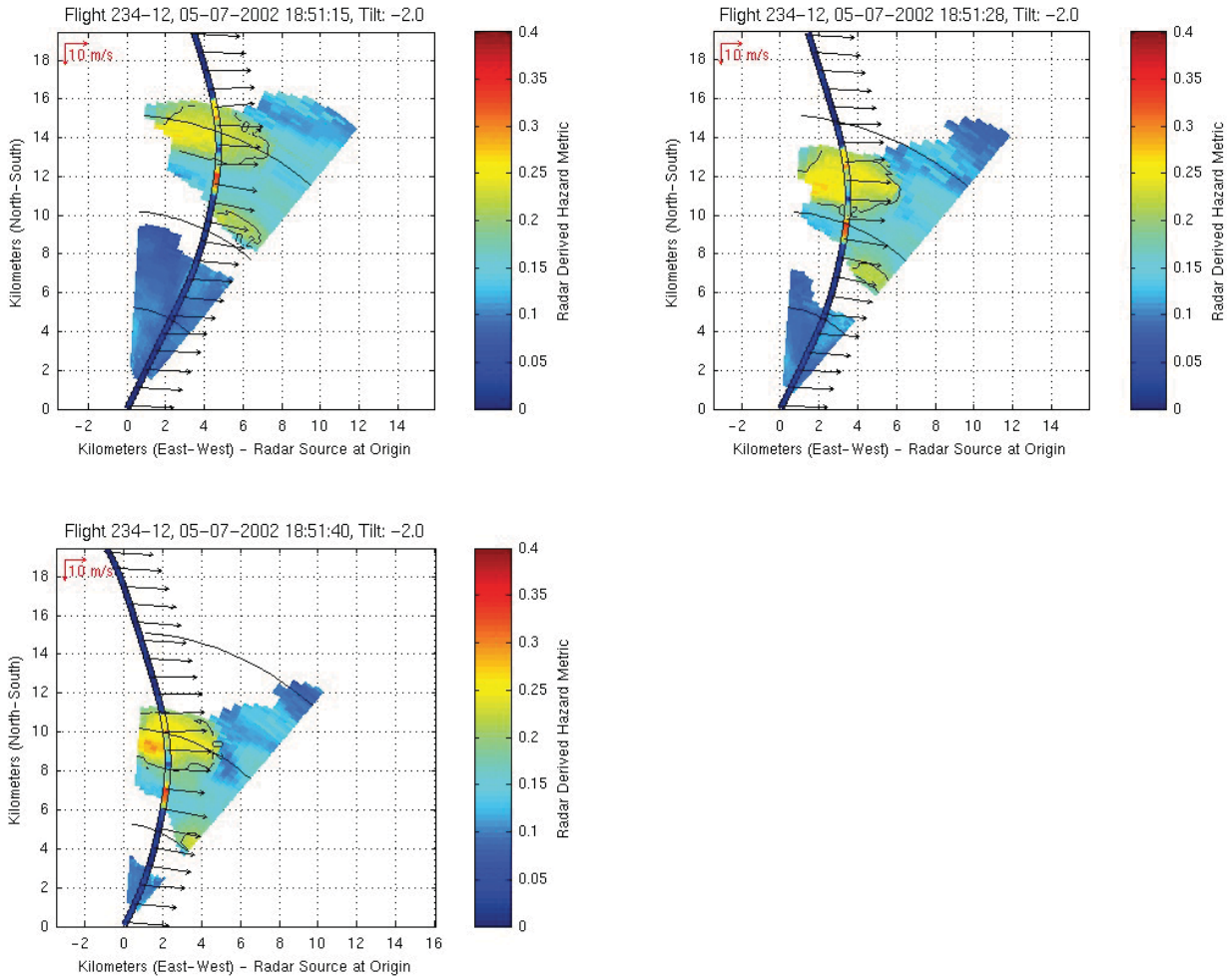

Figure 111. Sequential scans at 12*s* intervals for airborne radar predicted $\sigma_{\Delta n}$ (color contour cones) and *in situ* $\sigma_{\Delta n}$ (color on flight path line) for Event 234-12. Ambient wind vectors are shown along path.

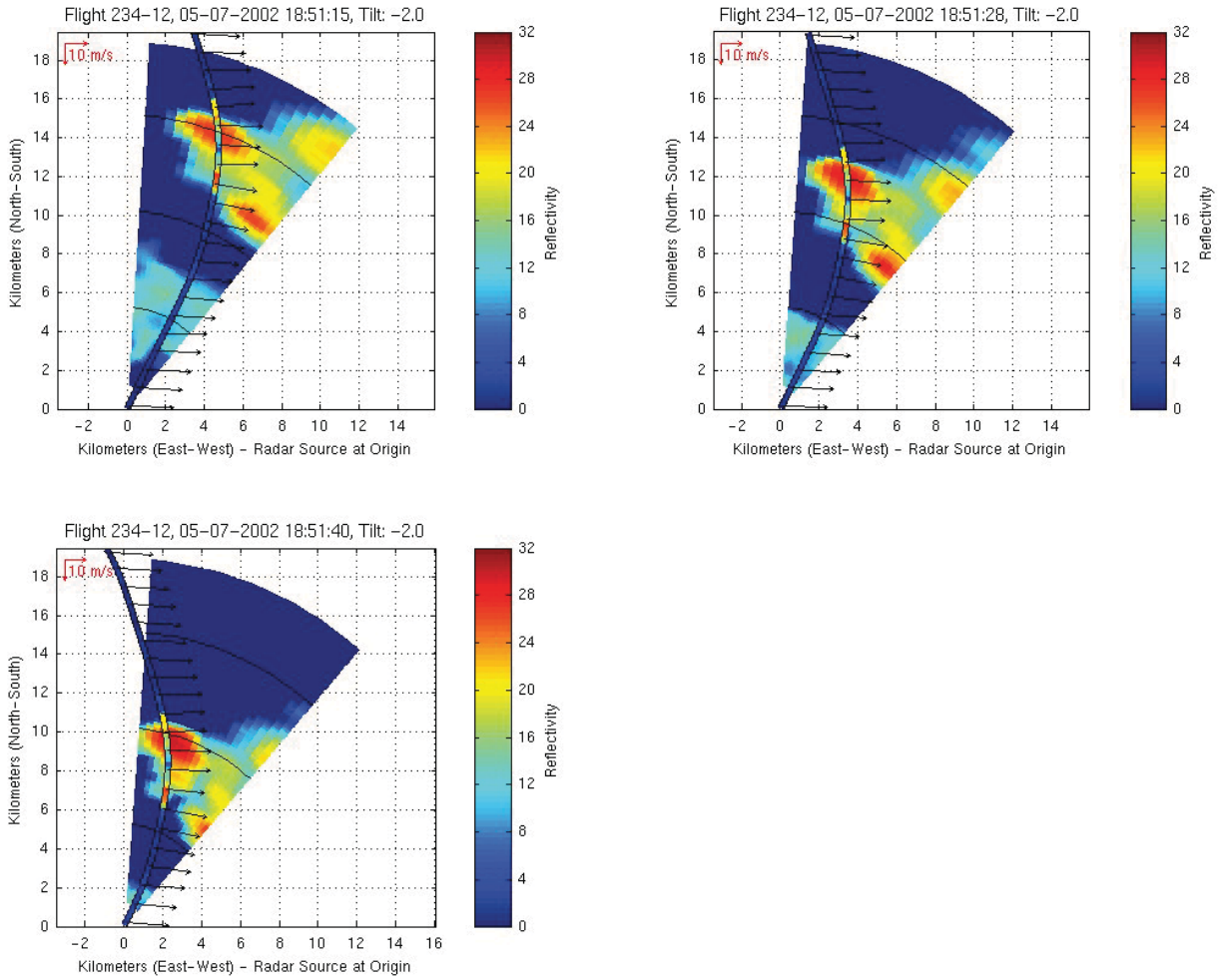

Figure 112. Sequential scans at 12*s* interval for airborne radar reflectivity factor (color contour cones) and *in situ* $\sigma_{\Delta n}$ (color on flight path line) for Event 234-12. Airborne with –2° tilt only. Ambient wind vectors are shown along path.

2.11: Flight 235, May 10, 2002

Between 1800 and 1945 UTC on 10 May, 2002, ARIES investigated two widely separated regions that were favorable for convective turbulence (Figure 113 - Figure 115). The first region was in east-central Alabama, where isolated convective cells were forming along a slow moving cold front. During the initial penetration in this region, visual meteorological conditions prevailed. However, due to strong convection throughout the region, convective outflow caused a decrease in visibility. The second region was along the South Carolina coast where isolated convective cells were forming along a sea-breeze front. Visual meteorological conditions prevailed during penetrations in this region. No pilot reports of turbulence were issued in the vicinity of either of the two regions that were investigated (Figure 116).

Six significant turbulence encounters were associated with the penetration of the isolated convective cells. The convection encountered in Alabama is shown in a photograph captured from the aircraft (Figure 117). A photograph of one of the video panels taken inside ARIES just prior to a turbulence encounter is shown in Figure 118. Two events were recorded with the convection shown in the photograph (Figure 119-Figure 122). The remaining events were associated with isolated convective cells forming on a sea-breeze front along the South Carolina coast (Figure 123). No figures are available for Events 235-05, 235-07, 235-08, and 235-09 because the radar "hazard" scans were taken in a configuration not compatible with the hazard algorithm's required format. During Event 235-05, moderate turbulence was encountered while flying above the ascending cloud top in clear air. Weak to moderate airborne radar reflectivity was associated with the penetrated cells. In Alabama, the storm top was 10.6 *km* (35 *kft*) and the flight altitudes were 7.3 and 7.9 *km* (24 and 26 *kft*). Precipitation encountered within this cell was in the form of snow and ice crystals. In South Carolina, the storm tops were 6 *km* (20 *kft*) and flight altitudes were 5.8 and 6.7 *km* (19 and 22 *kft*). Precipitation encountered within these cells was a mix of snow and rain. In both regions, prevailing winds at flight level were from 260° from true North. Wind speeds were between 13 and 18 *m/s* (25 and 35 *kts*) over South Carolina and 21 *m/s* (40 *kts*) over Alabama.

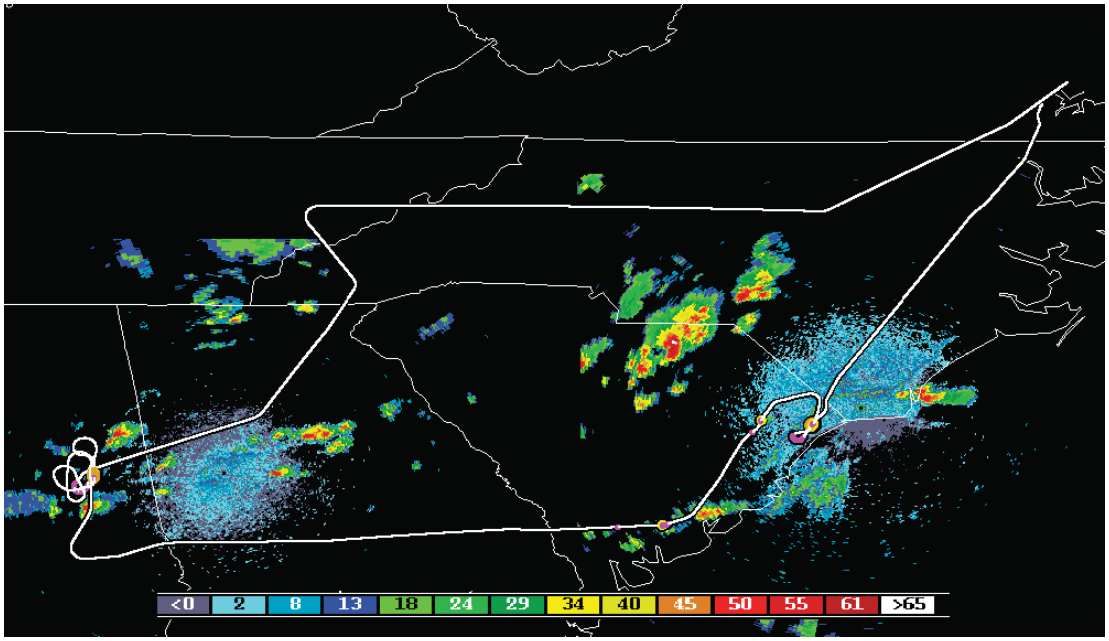

Figure 113. Path for Flight 235. Blended plot of ground based composite radar reflectivity (*dBz*) from the 18:22:08 UTC KFFC (Atlanta, Georgia) and 19:39:54 UTC KLTX (Wilmington, North Carolina) NEXRAD radars on 10 May 2002. See Figure 3 for legend to intensity of the aircraft RMS normal loads.

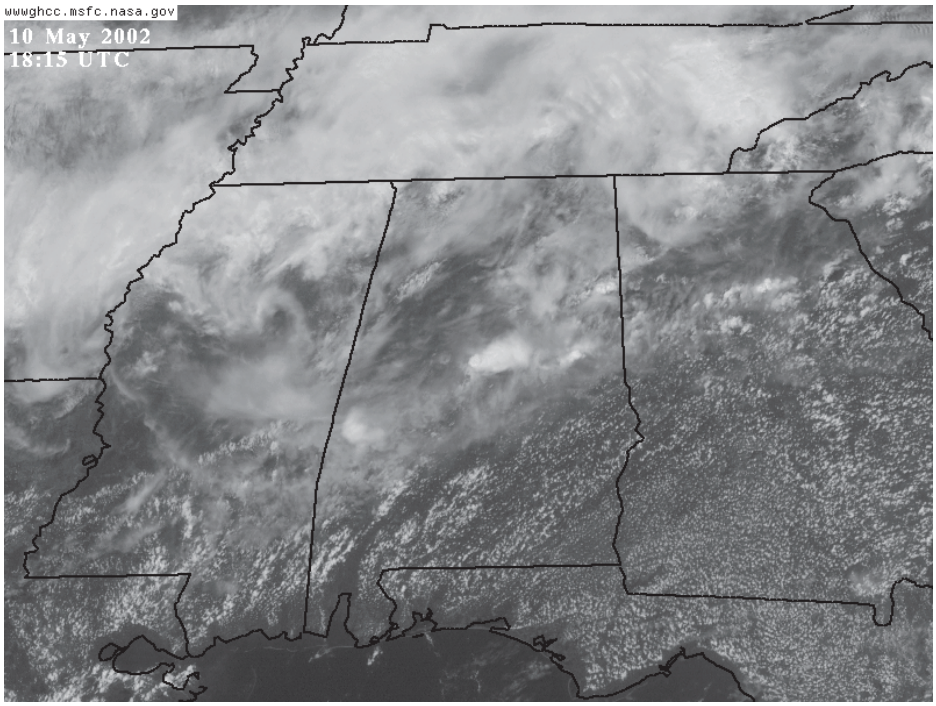

Figure 114. GOES-12 visible satellite image at 1815 UTC on 10 May 2002.

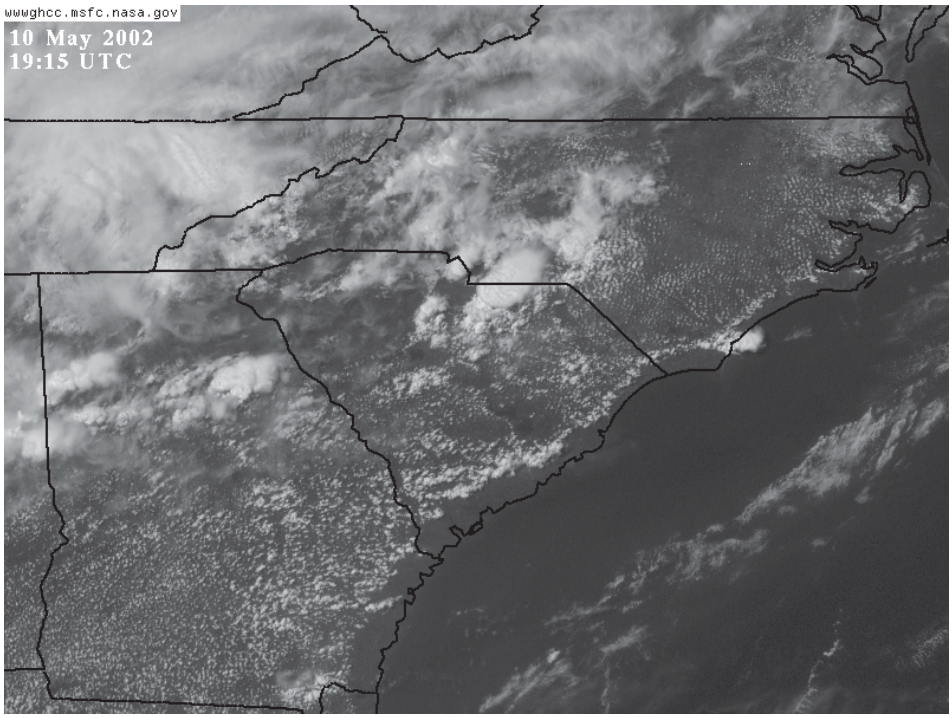

Figure 115. GOES-12 visible satellite image at 1915 UTC on 10 May 2002.

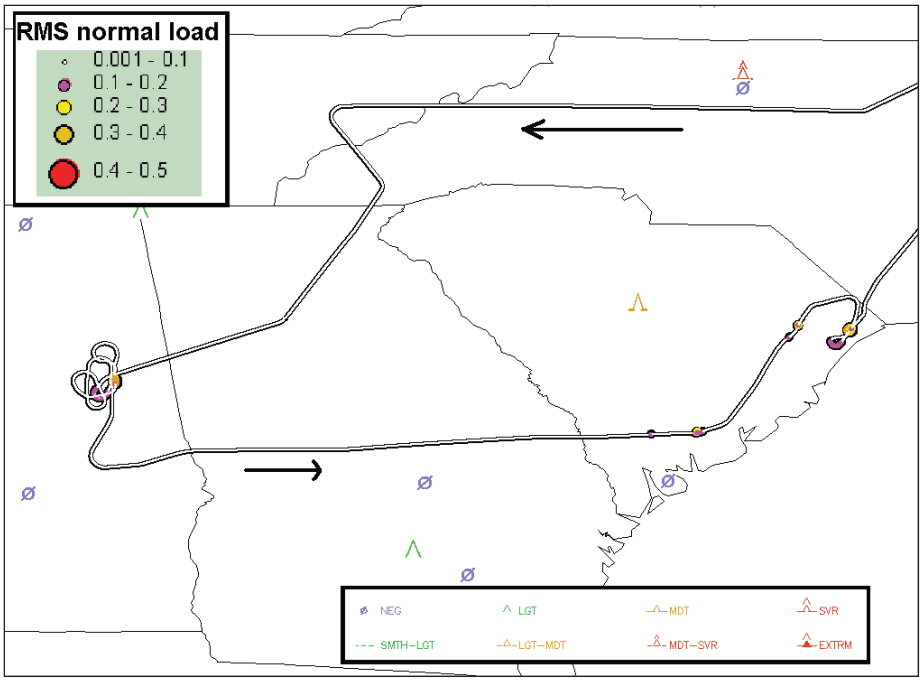

Figure 116. RMS normal loads encountered along the path for Flight 235 with turbulence PIREPS for 10 May 2002.

Figure 117. Photograph of the Alabama convection from a side window.

Figure 118. Real-time displays inside ARIES while approaching a turbulence encounter during Flight 235. Video from tail camera displayed on left, and airborne Doppler radar products on right.

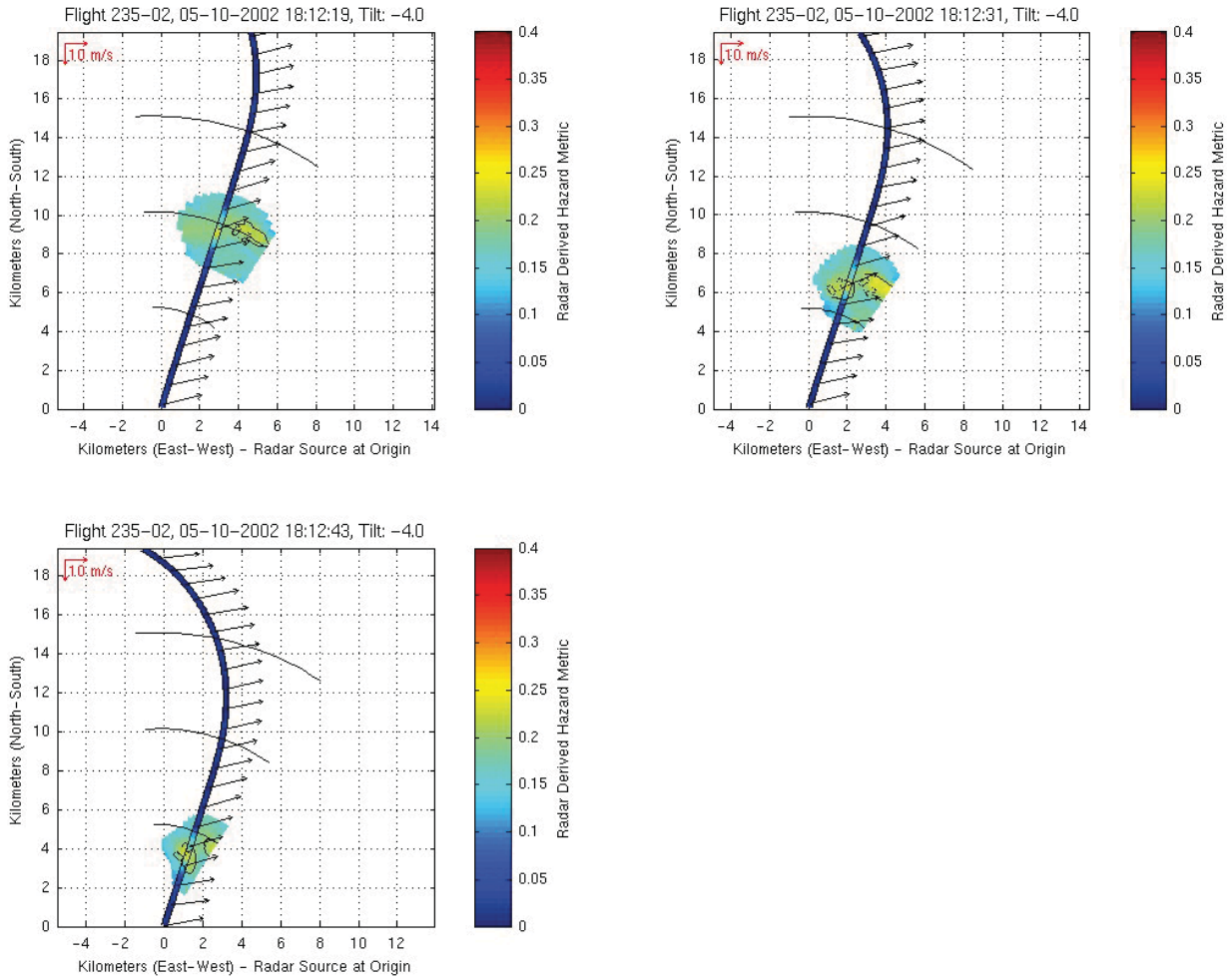

Figure 119. Sequential scans at 12*s* intervals for airborne radar predicted $\sigma_{\Delta n}$ (color contour cones) and *in situ* $\sigma_{\Delta n}$ (color on flight path line) for Event 235-02. Ambient wind vectors are shown along path.

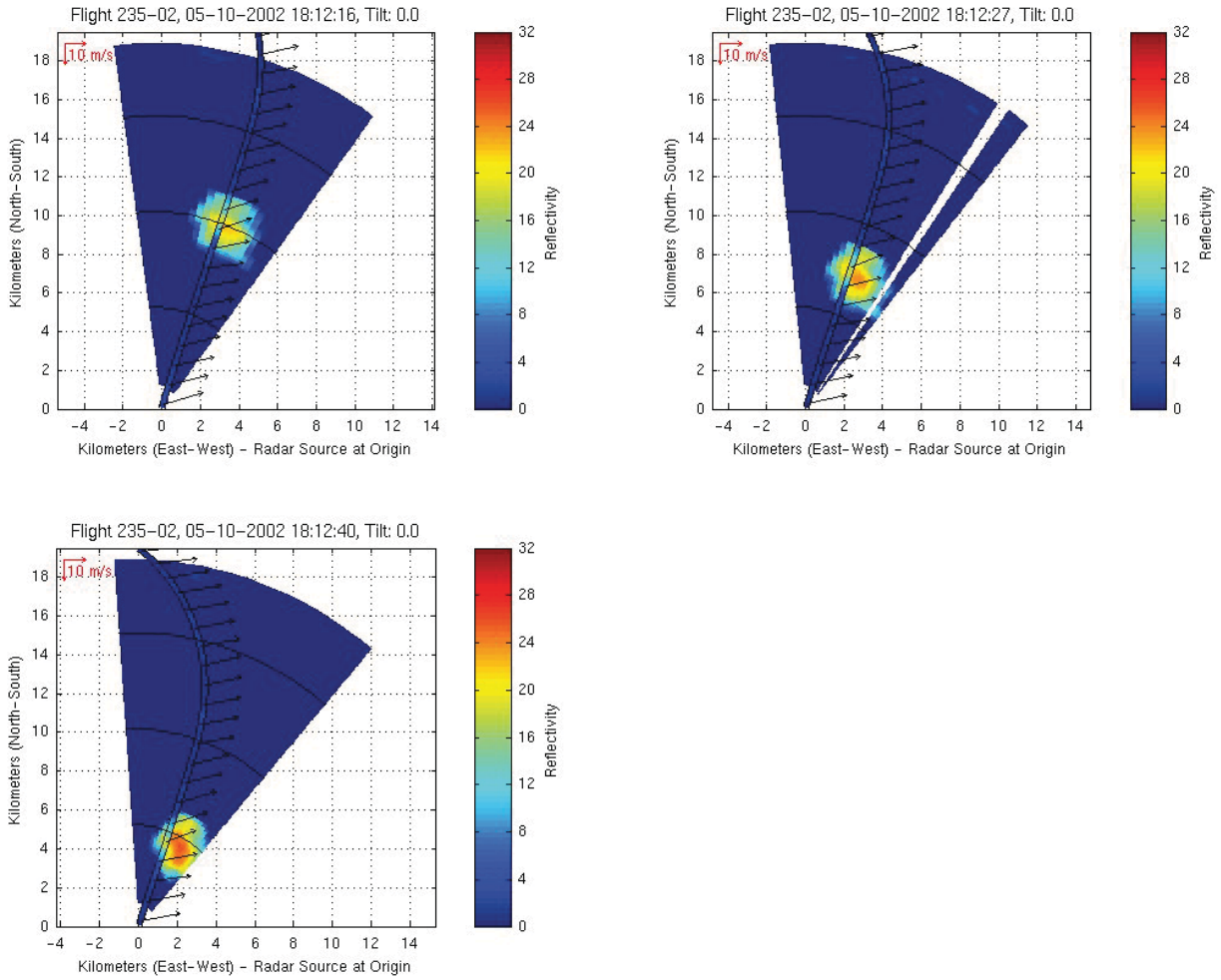

Figure 120. Sequential scans at 12*s* interval for airborne radar reflectivity factor (color contour cones) and *in situ* $\sigma_{\Delta n}$ (color on flight path line) for Event 235-02. Ambient wind vectors are shown along path.

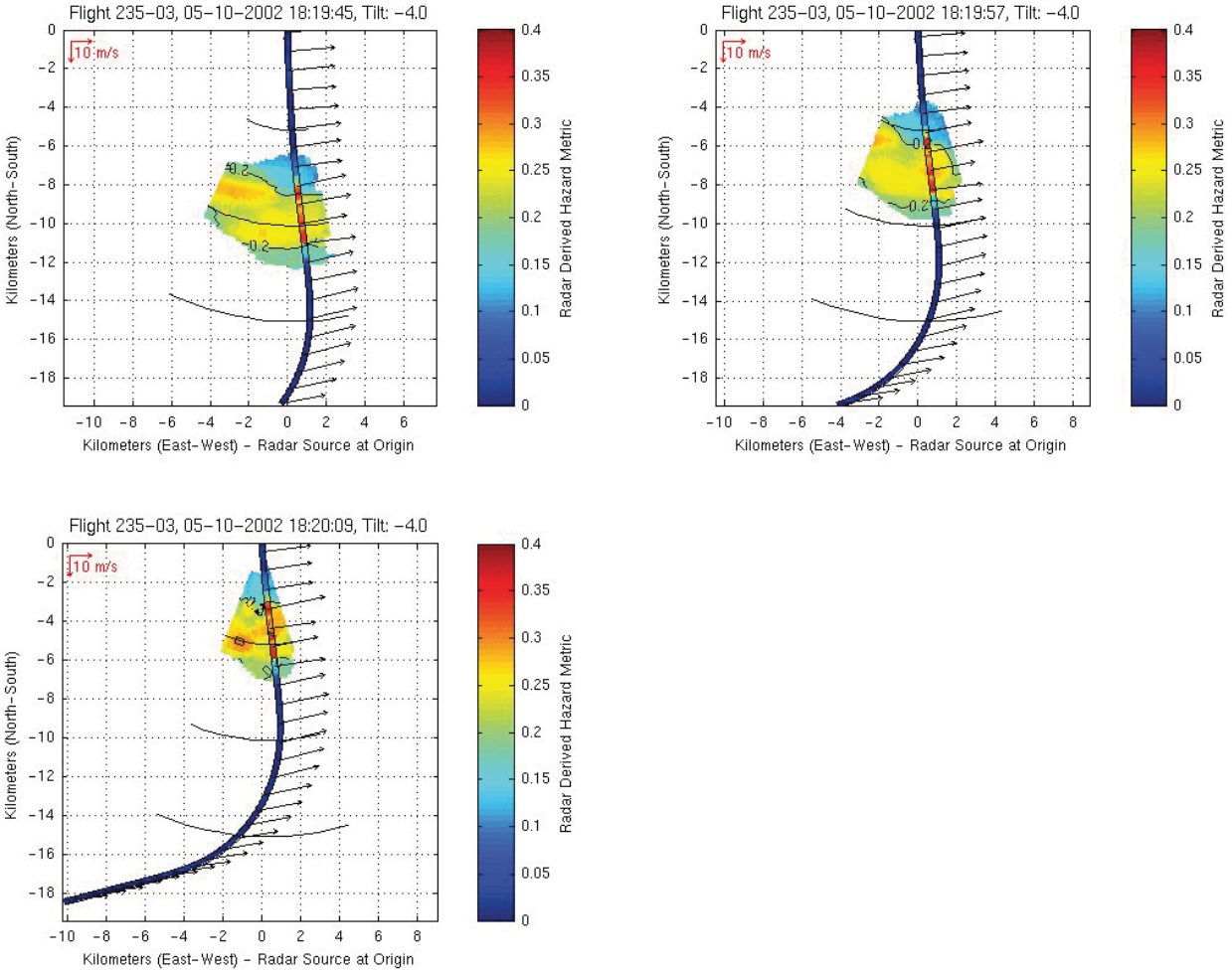

Figure 121. Sequential scans at 12*s* intervals for airborne radar predicted $\sigma_{\Delta n}$ (color contour cones) and *in situ* $\sigma_{\Delta n}$ (color on flight path line) for Event 235-03. Ambient wind vectors are shown along path.

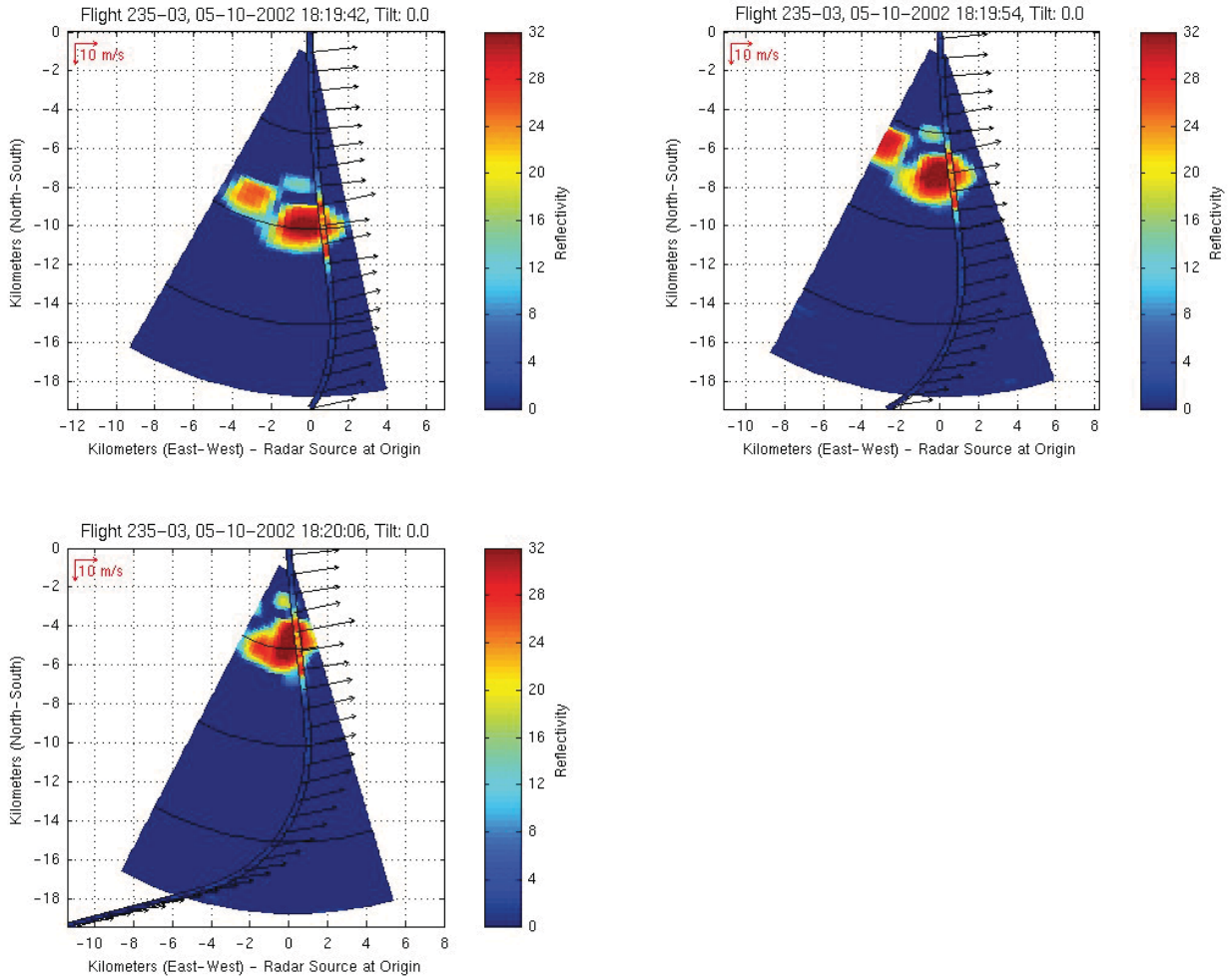

Figure 122. Sequential scans at 12*s* interval for airborne radar reflectivity factor (color contour cones) and *in situ* $\sigma_{\Delta n}$ (color on flight path line) for Event 235-03. Ambient wind vectors are shown along path.

Figure 123. Photograph of the sea breeze convection along the South Carolina Coast. Photograph taken from aft-starboard window during Flight 235.

2.12: Flight 240, May 17, 2002

Between 1700 and 1800 UTC, on 17 May 2002, ARIES investigated an isolated convective cell over central Alabama (Figure 124 and Figure 125). Convective indices favored strong updrafts, but otherwise conditions were typical for summertime southeastern convection. No pilot reports of significant turbulence had been issued (Figure 126) and visual meteorological conditions prevailed in the vicinity of this cell (Figure 127).

Two significant turbulence encounters were associated with penetrations near the top and on the upwind side of the growing convective cell (Figure 128 - Figure 131). Moderate radar reflectivity was detected in association with updrafts within the cell, due to the growth and transport of hydrometeors. Weak airborne radar reflectivity was associated with the tops and flanks of the cell. The elevation of the storm top was 12.2 *km* (40 *kft*) and cell motion was towards the northeast at 13 *m/s* (25 *kts*). Most penetrations were made well below the storm top at an altitude of 8.8 *km* (29 *kft*). The final turbulence event occurred at an altitude of 7.6 *km* (25 *kft*). Prevailing winds in the near storm environment were around 21 *m/s* (40 *kts*) from 220° relative to true North.

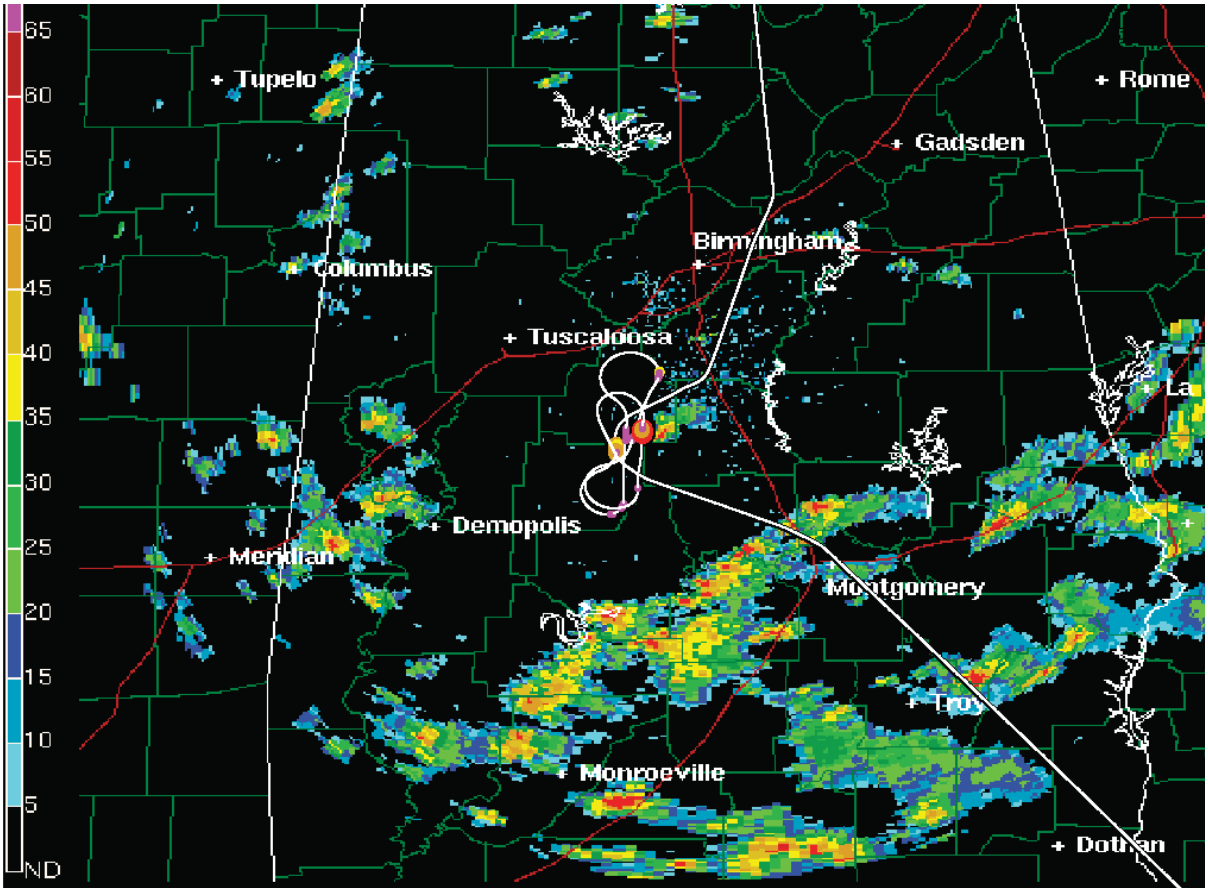

Figure 124. Path for Flight 240. Ground based radar reflectivity (*dBz*) from the 0.5° radar image from KBMX Birmingham, Alabama NEXRAD at 1807 UTC on 17 May 2002. See Figure 3 for legend to intensity of the aircraft RMS normal loads.

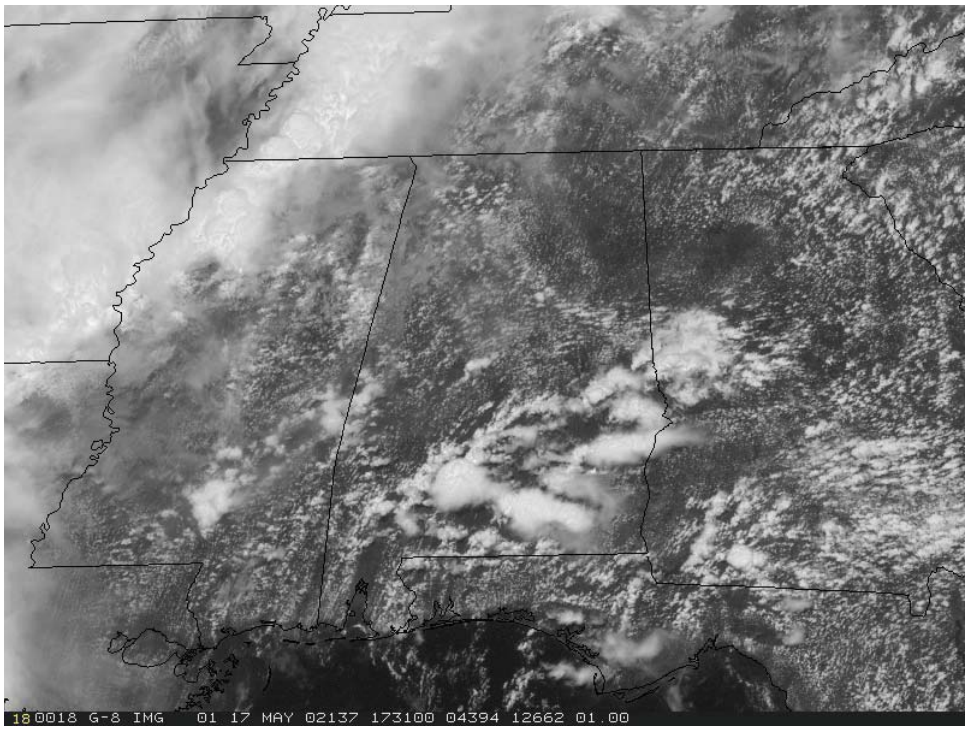

Figure 125. GOES-12 visible satellite image at 17:31:00 UTC on 17 May 2002. The convective cell investigated during flight is near the center of figure.

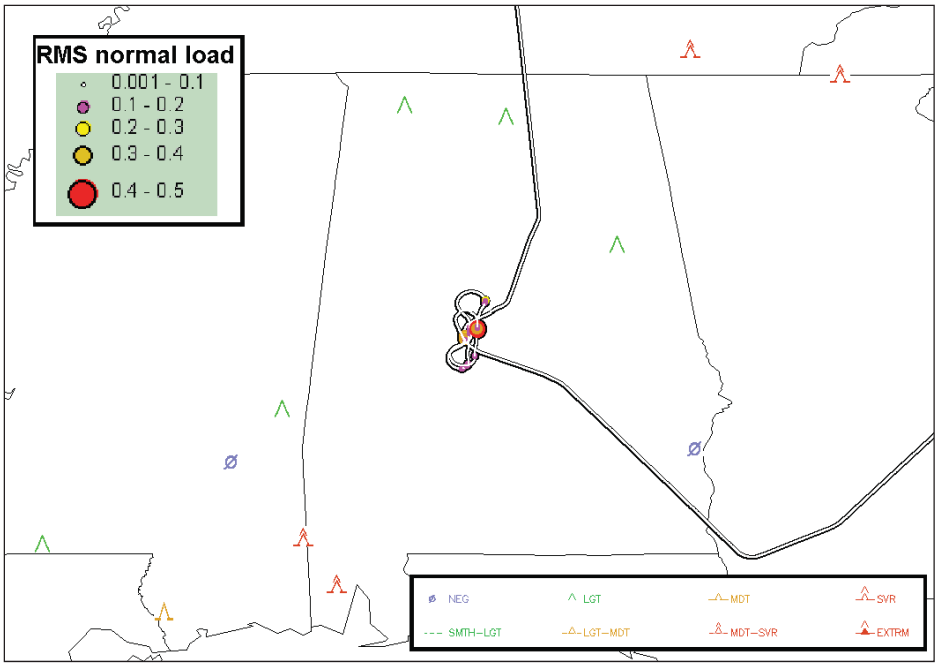

Figure 126. RMS normal loads encountered along the path for Flight 240 with turbulence PIREPS for 17 May 2002.

Figure 127. Photograph of a growing cumulus cloud as viewed from the cockpit window during Flight 240.

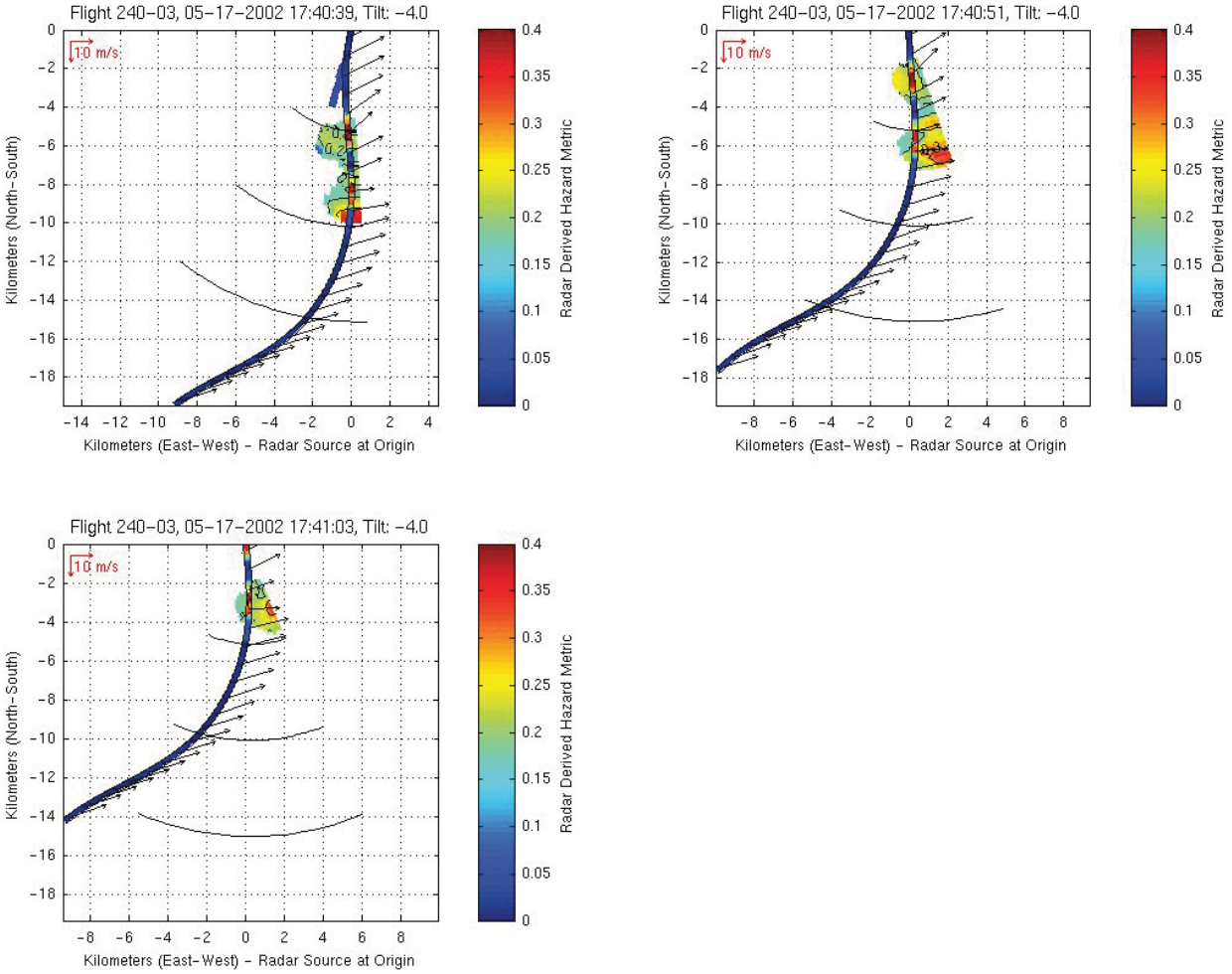

Figure 128. Sequential scans at 12*s* intervals for airborne radar predicted $\sigma_{\Delta n}$ (color contour cones) and *in situ* $\sigma_{\Delta n}$ (color on flight path line) for Event 240-03. Ambient wind vectors are shown along path.

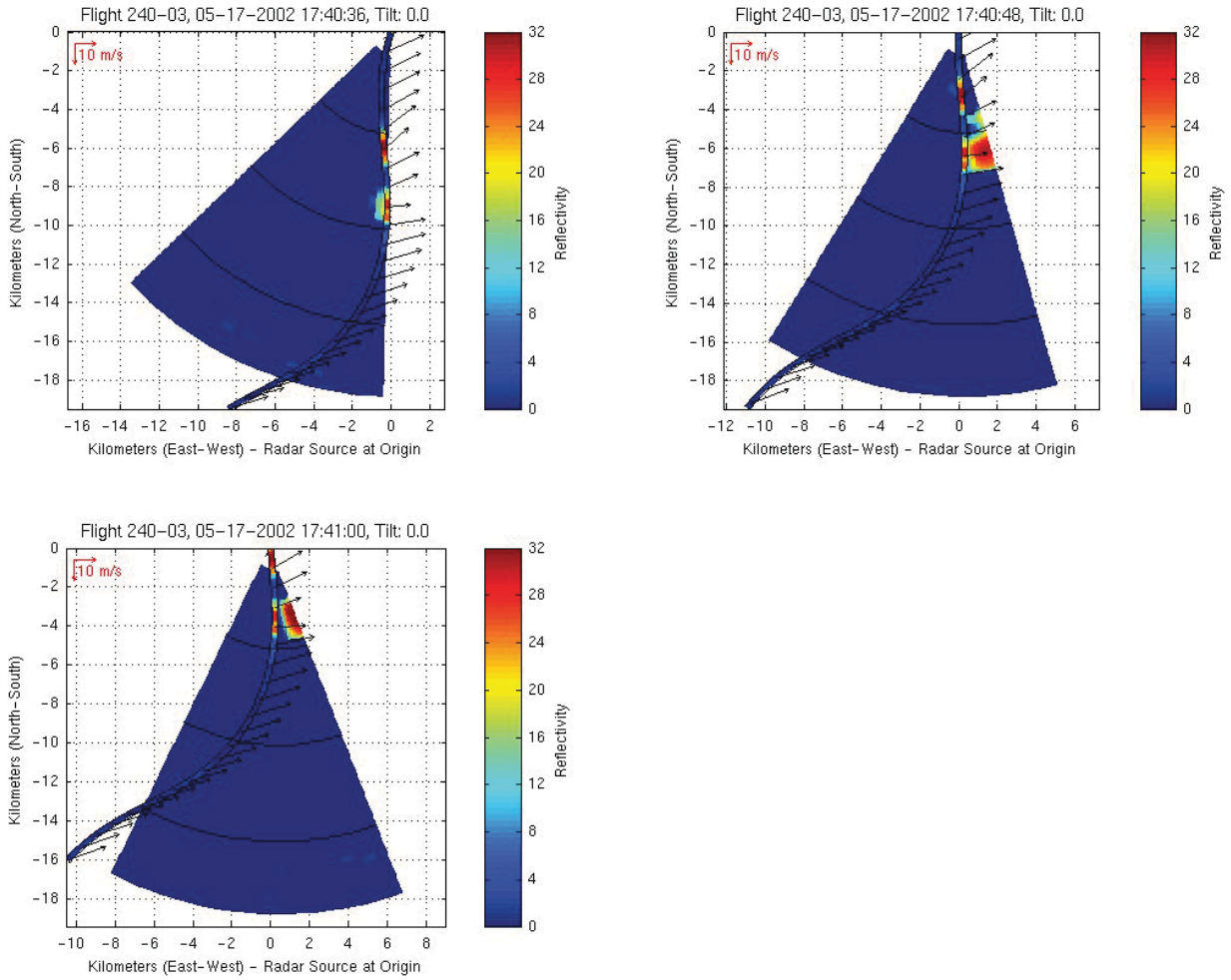

Figure 129. Sequential scans at 12*s* interval for airborne radar reflectivity factor (color contour cones) and *in situ* $\sigma_{\Delta n}$ (color on flight path line) for Event 240-03. Ambient wind vectors are shown along path.

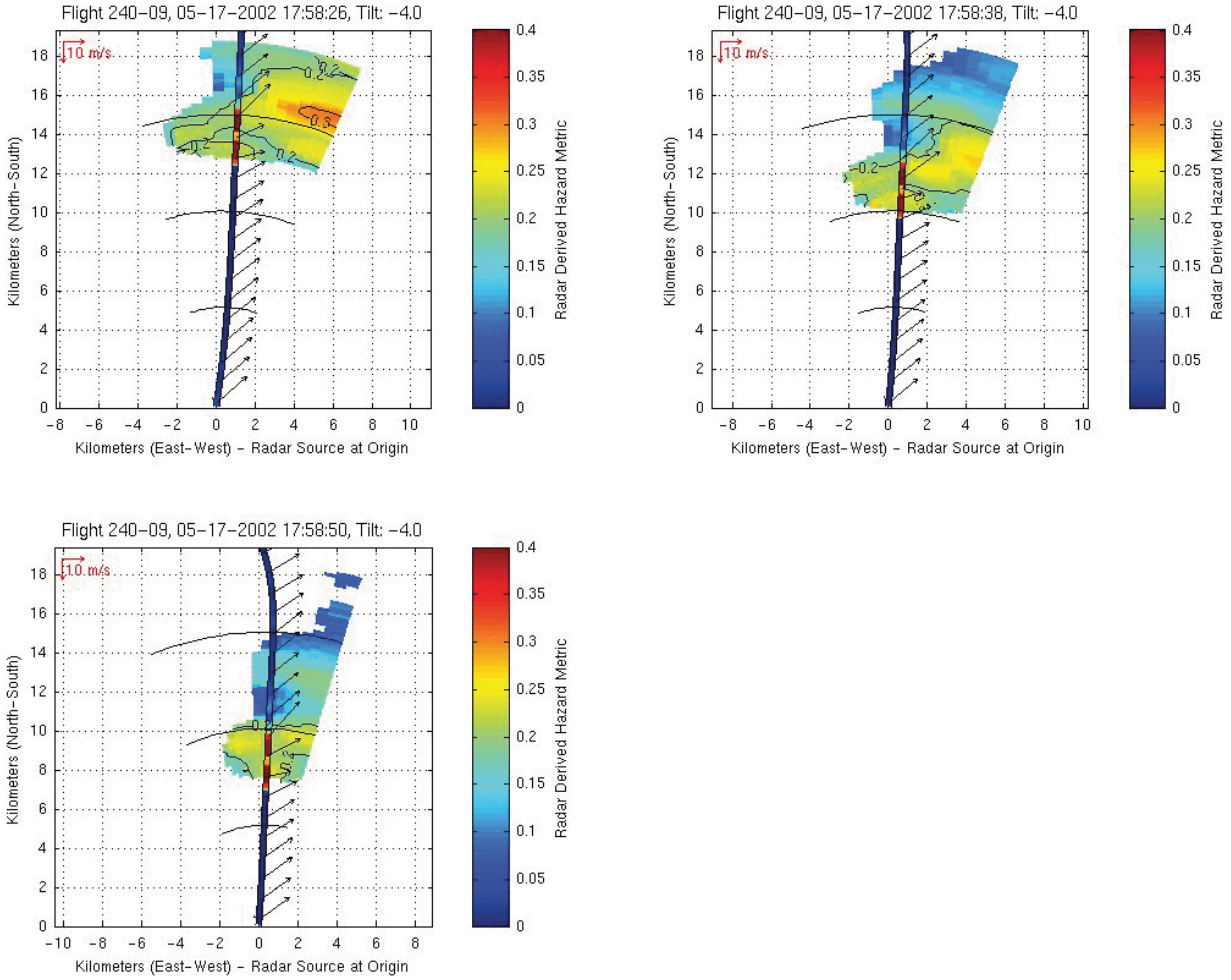

Figure 130. Sequential scans at 12*s* intervals for airborne radar predicted $\sigma_{\Delta n}$ (color contour cones) and *in situ* $\sigma_{\Delta n}$ (color on flight path line) for Event 240-09. Ambient wind vectors are shown along path.

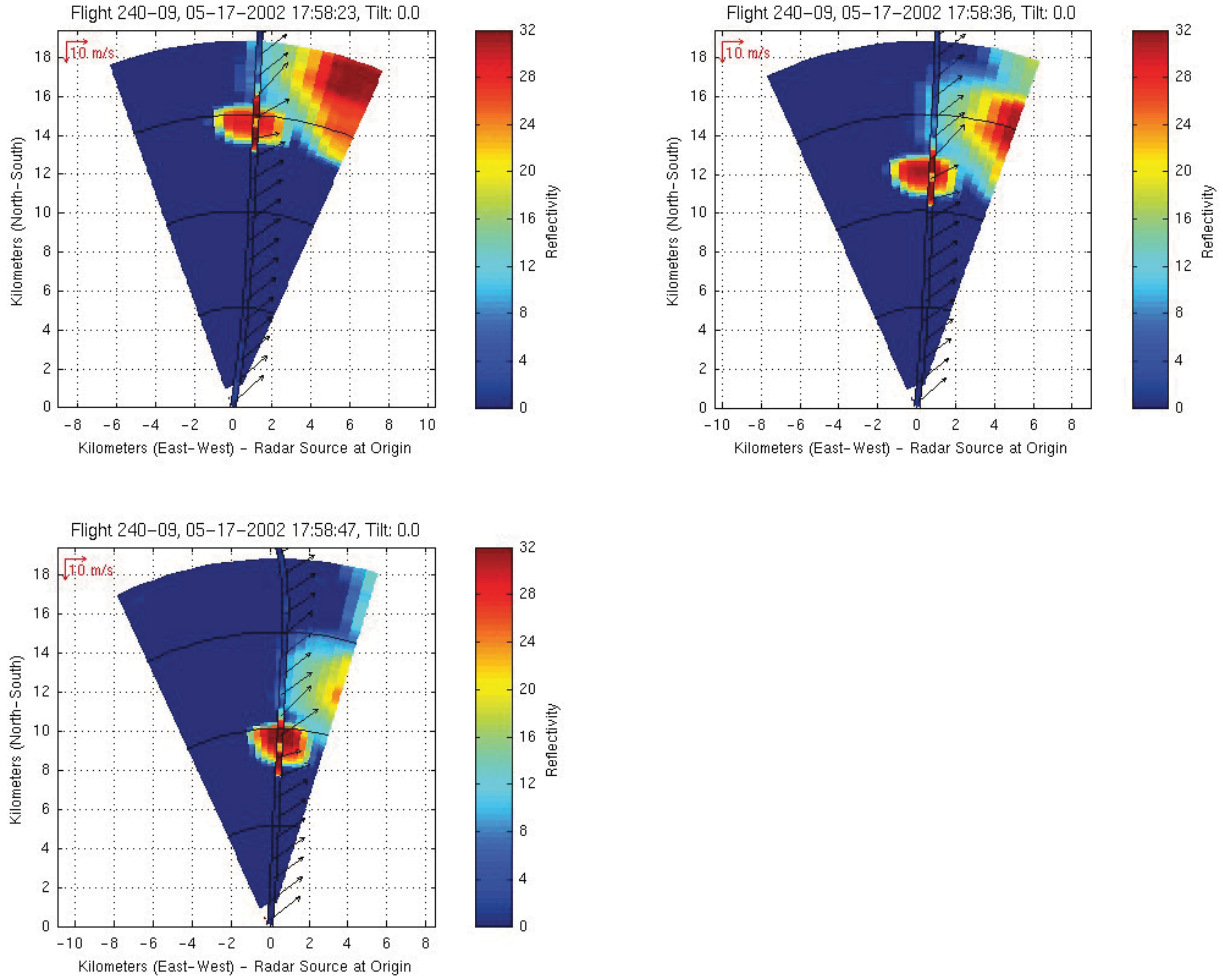

Figure 131. Sequential scans at 12*s* interval for airborne radar reflectivity factor (color contour cones) and *in situ* $\sigma_{\Delta n}$ (color on flight path line) for Event 240-09. Ambient wind vectors are shown along path.

3. Radar Scoring

A subjective scoring of the 2002 NASA flight test data (Flights 227-240) has been performed utilizing the post-processed airborne radar/track data presented in Section 2. The scoring is based on whether ATDS was able to predict the hazardous turbulence prior to its encounter and measurement with the *in-situ* system. False alarms (nuisances) and missed detections are also counted in the evaluation. Results from the scoring are shown in Table 2. A few cases were added in which the peak $\sigma_{\Delta n}$ did not exceed the alert criteria, in order to include cases that could become nuisance events. Some of the elements considered when scoring an event have been detailed in Georgia Tech Research Institute Final Contractor Report (2004) and are:

- The aircraft's measured in-situ turbulence magnitude (RMS normal loads; $\sigma_{\Delta n}$): above 0.2 *g* were considered moderate or greater (MoG), while those above 0.3 *g* were considered severe.
- The magnitude of the radar algorithm's predicted $\sigma_{\Delta n}$: values above 0.2 *g* defined "hazard warning" regions.
- The extent, coherence, and persistence of the radar hazard warning regions: large or coherent regions were given higher weight, while regions that were not persistent over at least two consecutive scans were ignored.
- Proximity of the hazard warning regions to the aircraft's flight track where MoG turbulence was encountered: no precise requirement was defined, but reasonable proximity of the two was required to score detection. Somewhat more leeway may have been given to larger, more coherent hazard warning regions.
- A hazard warning "lead time" of at least 30 seconds was required for the ATDS prediction.
- The detection algorithm was only required to detect hazardous turbulence in regions having radar reflectivity values greater than 15 *dBz*.

The scoring exercise shows that the ATDS meets FAA recommended performance levels of greater than 80% probability of detection and about 10% probability of a nuisance. False alarm (nuisance) cases, where the radar predicted a significant turbulence hazard but the aircraft did not encounter significant turbulence, were examined to understand why the system had a detection failure. For these cases, there were two reasons for the false alarms: 1) the turbulence 'patch' detected by radar and predicted to cause a hazardous turbulence upset was advected out of the path of the aircraft and 2) predicted levels of turbulence were just above hazard criteria (*e.g.*, 0.21 *g*), but *in situ* detection was just below hazard criteria (*e.g.*, 0.19 *g*). Although the latter was counted as a miss, this classification may be questioned, since turbulence was detected and turbulence was encountered. This example supports the need for a "may alert" or "caution" zone that does not penalize the system for missing an event when evidence supports the presence of turbulence that may be near the threshold of the hazard criteria.

Table 2. Final contingency table, annotation key, and overall statistics for the human scoring of the NASA 2002 flight test results. The table shows that the ATDS radar predicted 34 of the 42 significant turbulence encounters, while predicting false alarms in 4 of the 13 nonsignificant events.

AIRCRAFT	RADAR: Detected	RADAR: Not Detected
Hit	230-23 - 2 u 230-19 - u 230-21 - 0 u 230-15 - u 230-20 - u 231-10 - 231-08 - 233-07 - u 233-01 - 233-06 - 233-04 - r 234-06 - 234-11 - 234-12 - 234-09 - 234-05 - 230-12 - u 228-04 - u 228-12 - u 228-10 - 228-11 - 228-06 - 228-09 - 232-10 - 232-04 - 232-03 - 232-08 - 232-05 - o 235-03 - u 235-02 - 240-03 - 240-09 - u 232-06 - 233-09 - Total: 34	230-06 - 2 ? 230-10 - 2 m 230-08 - 2 m 230-04 - 230-24 - 2 m 233-05 - m 229-05 - m 231-04 - u Total: 8
Not hit	234-02 240-04 - 240-05 233-08 Total: 4	229-02 229-03 229-04 229-06 241-01 234-10 - 234-13 231-06 - n 228-07 - n Total: 9

Key

r - registration poor
u - underestimate
o - overestimate
m - marginal miss
0 - 0 tilt only
2 - -2 tilt only
? - not enough data
n - non-validated detection (moved off)
- - consensus agreement

Statistics

PODyes	=	**80.95%** 34/(34+8)
NAR	=	**10.53%** 4/(34+4)
PODno	=	**69.23%** 9/(4+9)
% correct	=	**78.18%** (34+9)/(34+9+4+8)

4. Turbulence Characteristics and its Implications on Aviation Operations

4.1: Radar Reflectivity

A general aviator's rule of thumb in preventing turbulence accidents is to avoid large thunderstorms. Operationally, this is not always achievable due to large regions of atmospheric convection, for which avoidance maneuvers are not practical because they greatly affect an airliner's capability to meet schedules or result in excessive fuel consumption. Although it is well known that flying into areas of high radar reflectivity (> 40 *dBz*) certainly poses a threat other than turbulence (*e.g.*, hail and poor visibility), avoiding turbulence by avoiding radar echoes may not necessarily avert a hazardous encounter. Figure 132 reveals a weak correlation between radar reflectivity and aircraft load accelerations. Note that some of the more intense turbulence encounters were not in environments with high levels of radar reflectivity (*e.g.*, Flight 232-10) and often nothing significant was indicated on the aircraft radar display (< 20 *dBz*). It is our belief that many similar events are reported by pilots as clear air turbulence (CAT) rather than CIT.

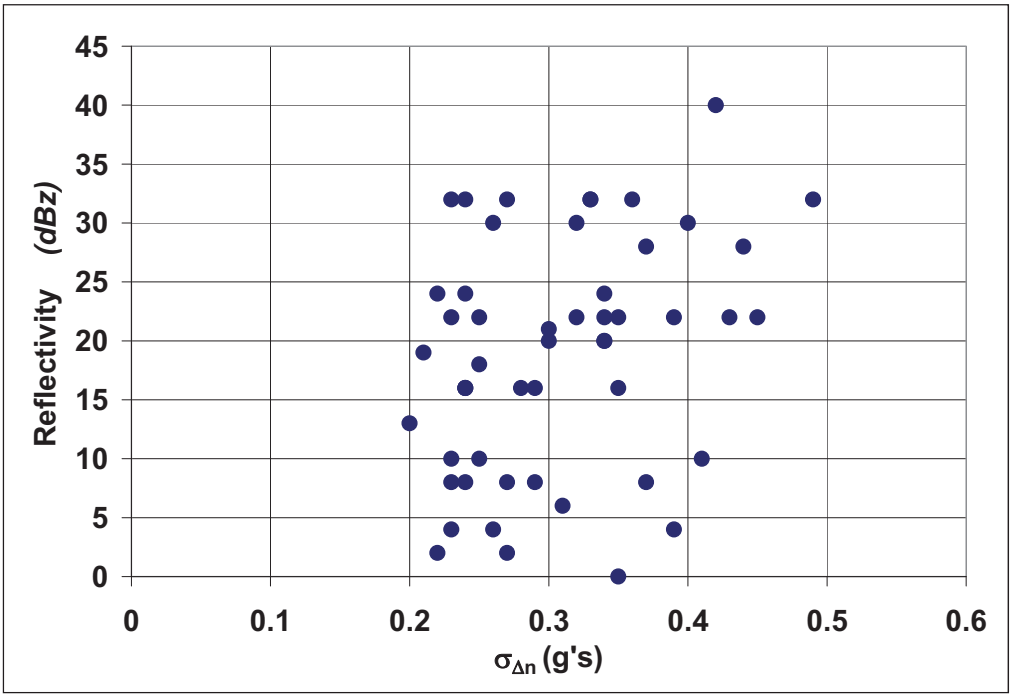

Figure 132. Peak radar reflectivity along path for all significant encounters during 2002 flight campaign.

4.2: Isotropy and Radar Performance

A challenge for turbulence detection with Doppler radar is that the radar senses air motion along the radial coordinates of the radar scan cone; whereas the aircraft primarily responds (via normal loads) to the vertical air motion along the flight path. Therefore, assumptions must be made in order to convert radar measurements into an aircraft hazard metric. If atmospheric turbulence were truly isotropic at the scale of the radar pulse volume, then one would expect perfect correlation between the statistics of all three wind components. However, *in situ* data collected by NASA's B-757 in 2000 and 2002 indicates that CIT is often anisotropic. One method of showing the anisotropic nature of CIT is comparing the *in situ* vertical (σ_w) and head wind (σ_u) component deviations that were measured during turbulence encounters. Figure 133 compares the peak standard deviations of the vertical and head winds for each of the events recorded in the 2002 flight experiments. Isotropy would reveal a one to one relationship between the σ_u and σ_w peaks. However, the figure shows a bias towards higher values of σ_w in most of the events, which is

consistent with previous research (Steiner and Rhyne 1962). This finding is not surprising since the turbulence source in thunderstorms derives from the strong updrafts associated with deep convection.

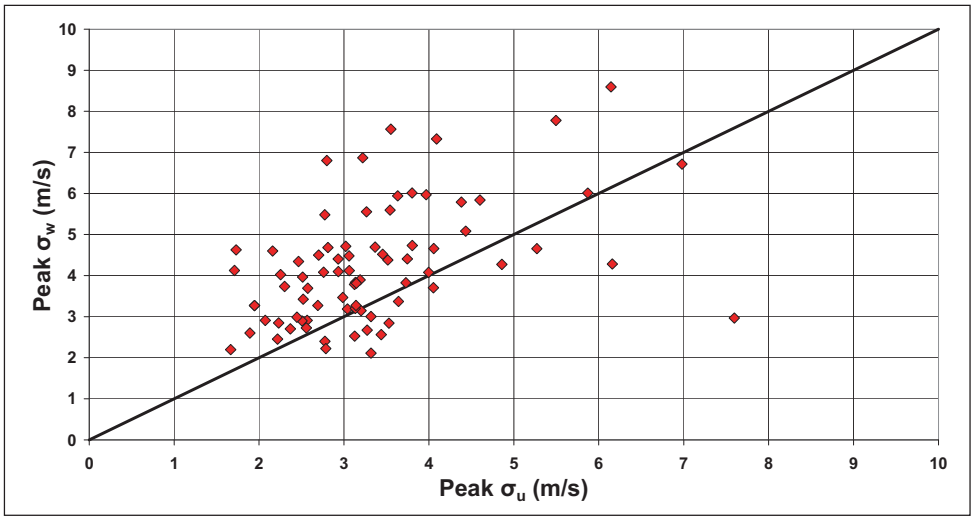

Figure 133. Corresponding peak values of σ_u and σ_w peaks for all 2002 turbulence events. Computed from *in situ* 20 *Hz* wind data assuming a 5 second window.

In Figure 134, a probability distribution reveals the likelihood of the along-path distance (L_x) between the locations of the σ_u and σ_w peaks depicted in Figure 133. Obviously, the measured peak σ_u and σ_w values are not the same and aren't collocated given the same event. In nearly all events the distance between the locations of the peak σ_u and σ_w was less than 2 *km*, and for 85% of the data within 900 *m*. This aspect of convective turbulence should be considered when developing alerting criteria, and hazard displays for ATDS.

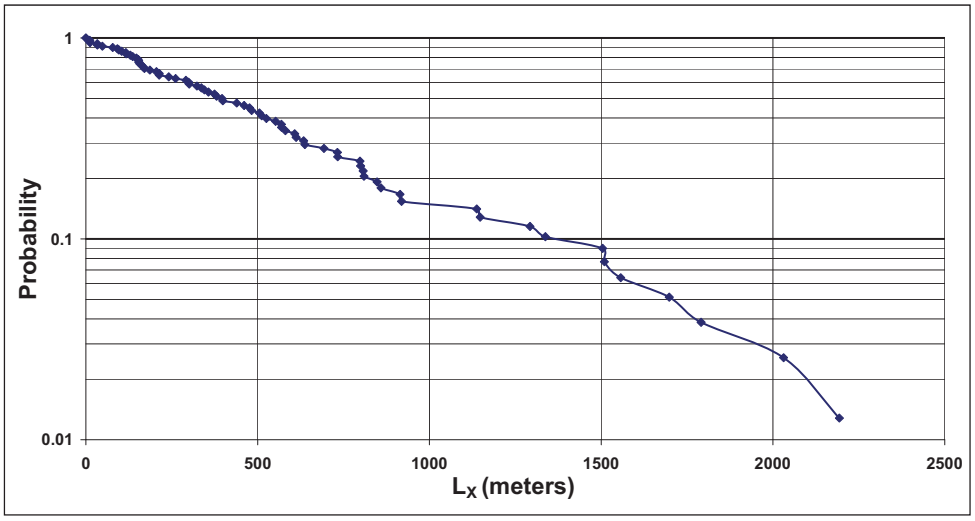

Figure 134. Probability distribution of the distance between locations of peak values of σ_u and σ_w for each event depicted in Figure 133.

4.3: Airborne and Ground Radar Comparison

Previous studies have examined the role of ground-based radar in identifying and quantifying the effect of CIT on aircraft (Doviak and Lee 1985). In this section NASA's ARIES radar data is compared with NEXRAD ground radar data and their merits in turbulence avoidance applications are discussed. For this evaluation, available NEXRAD data around the time and location of the events was compared against the airborne radar data.

Table 3 shows both radars' characteristics. Detailed information on the NEXRAD radar is given in Maddox et al. (2002). Notations are made where pulse lengths may vary. Pulse length refers to the time in which energy is transmitted from the antenna and when multiplied by the speed of light, represents the true length of the pulse in meters. Long pulses determine target locations, while short pulse lengths determine target intensity and motion characteristics. The hazard algorithms used for both flight campaigns were designed to make predictions from short pulse radar data.

Table 3. NEXRAD and airborne radar characteristics.

Radar	Nexrad WSR-88D	ARIES Radar (Collins WXR-700)
Radar Type	S-Band	X-Band
Peak Power	750 *kW*	125 *W*
Beamwidth	1^o	3.4^o
Pulse Length	Short Pulse: 1.67 μs (500 *m*) Long Pulse: 4 μs (1200 *m*)	Short Pulse: 1 μs (300 *m*) Long Pulse: 3 μs (900 *m*)
Range Resolution	Short Pulse: 250 *m* x 1^o Long Pulse: 600 *m* x 1^o	Short Pulse: 150 *m* x 3.4^o Long Pulse: 450 *m* x 3.4^o
Doppler Range	230 *km*	40 *km*

Similar to the findings of Doviak and Lee (1985), the NEXRAD spectrum widths for data measured at ground sites, on occasion, exceeded 5 *m/s* in the vicinity of the significant events. However, these events were typically associated with convection that had high levels of radar reflectivity and were located near the ground radar. In most of the events, NEXRAD did not detect levels of spectrum width that are typically associated with severe turbulence. However, further analysis is required for a quantitative comparison with the scoring in Section 3. Finally, NEXRAD data associated with events at the far edges of the radar volume were lost due to range folding, yielding no information about spectrum width.

Data resolution is important for tactical turbulence avoidance, particularly if alerting is considered. To illustrate this point, data from Event 232-10 are used (details of this event are in Section 2.8: Flight 232, April 30, 2002). In the vicinity of the ARIES encounter with turbulence, peak radar reflectivity levels from both the airborne radar (Figure 84 and Figure 86) and NEXRAD (Figure 135A) compare well. However, since the Huntsville, Alabama NEXRAD radar is about 170 *km* away, resolution is clearly much better in the data from the airborne radar. At a 170 *km* range, the NEXRAD radar's 1^o beam width becomes quite broad in scale. Horizontal resolution is such that each pixel represents approximately a 1 *km* wide portion of the atmosphere. This is significantly lower in resolution than the airborne radar product.

At the time and location of maximum turbulence loads, the NEXRAD scans of 3.3° (Figure 135A) and 2.4° (Figure 135B) place the center of the radar beam at elevations of 29 and 38 *kft* (8.84 k*m* and 11.58 k*m*), respectively. The ARIES flight encounter with turbulence occurred at an altitude of 35 *kft* (10.67 *km*), which is located between the center lines of the two scans. As for temporal resolution, the airborne radar quickly scans the portion of atmosphere directly ahead of the aircraft and produces a turbulence product that is readily available for the aircrew. Whereas for the NEXRAD product, the radar requires at least five minutes for each volume scan, and it may miss the location and amplitude of the turbulence event all together. This problem with ground radar is clearly illustrated with Event 232-10. This event demonstrates the quick buildup of a convective tower, and thus the need for the rapid-scan ATDS. The rapid development of the convective plume responsible for Event 232-10 can be seen in the vertical cross sections presented in Figure 136. In the five minute period between two volume scans, the plume ascended

nearly 5 *kft* (1500 *m*) from below to above the aircraft altitude. However, this data would have been too late for tactical avoidance since the first scan was completed five seconds prior to the encounter and the second scan was completed nearly five minutes after the turbulence encounter.

The timeliness of the radar-based turbulence detection product available to aircrews is a major concern in real-time turbulence avoidance applications. The advantage of the airborne product is its rapid availability to the aircrew. Automated conversion of the radar detected turbulence 'burst' to an aircraft specific load prediction, results in a flight deck decision support tool requiring no radar analysis and little if any interpretation on the part of the aircrew. As for the NEXRAD, the data must be transmitted or uplinked to the aircraft, requiring time that may be critical to the crew for cabin preparation.

Lastly, an advantage that the NEXRAD radar appears to have over the airborne radar is its ability to cover a much larger volume of atmosphere. However, Maddox et al. (2002) showed that the NEXRAD volumetric radar 'dome' had a significant reduction in aerial coverage at higher altitudes, therefore leaving a large portion of the United States with insufficient coverage.

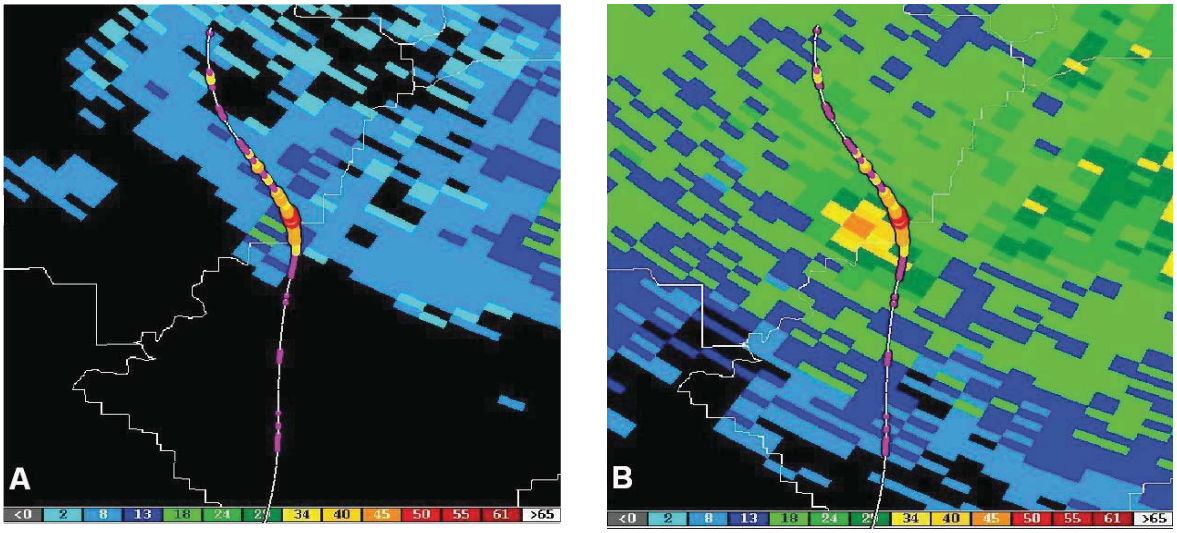

Figure 135. Huntsville, Alabama (KHTX) NEXRAD (A) 3.3° and (B) 2.4° PPI scans with ARIES flight path overlay. See Figure 3 for legend to *in situ* RMS normal loads along path.

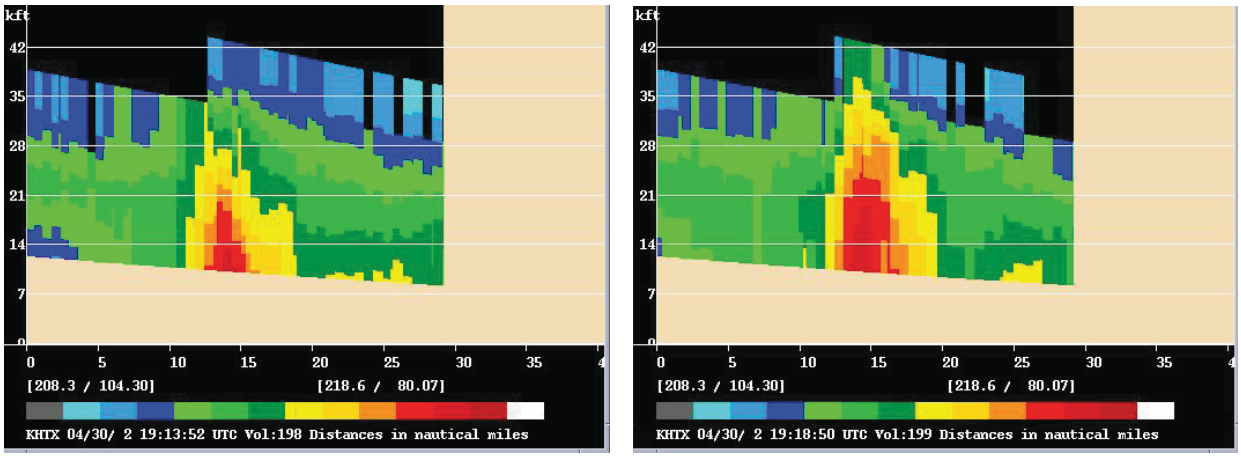

Figure 136. Vertical cross sections of radar reflectivity at 19:13:52 UTC (left panel) and 19:18:50 UTC (right panel), before and after turbulence encounter. Flight level is along the 35 *kft* line from left to right through the cross section.

5. Environmental Characteristics

In preparation for each flight, relatively simple forecast techniques were employed using the tools described in Section 2. Preferred flight regions included areas forecasted to have deep convection interacting with the jet stream. These regions were typically chosen based on persistence and were narrowed to areas where MASS predicted negative values of lifted index (LI) and high values of the North Carolina State University (NCSU) turbulence index (Kaplan et al. 2000, 2006). The LI characterizes the amount of instability in a given environment, but doesn't necessarily predict the development of convection. However, triggered convection is expected to be more intense with stronger updrafts in environments with decreasing values of LI. Therefore, one can expect the intensity of turbulence to have a correlation with negative LI.

The LI is calculated by computing the temperature of an air parcel lifted dry adiabatically from the surface to its level of free convection, then lifted moist adiabatically to a given level aloft, commonly the 500 *mb* pressure level. The LI is the temperature difference at that level between the ambient environment and the lifted parcel. Negative values indicate potential instability, while increasingly positive values indicate greater stability. Since some flights had numerous turbulence encounters within the same region of airspace, the peak turbulence event is determined for each active region and is plotted against the LI (Figure 137). Analysis of this data indicated a weak correlation between peak $\sigma_{\Delta n}$ and LI, with stronger aircraft load accelerations associated with convection in environments with larger magnitudes of negative LI. Similarly, peak vertical velocities, as derived from the ARIES *in situ* data, increased with decreasing LI (Figure 138).

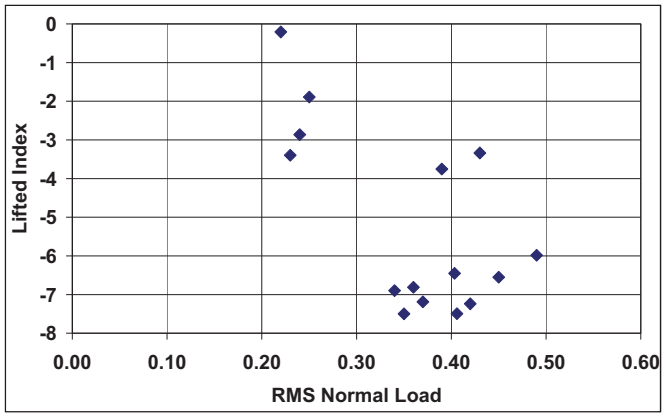

Figure 137. Plot of peak $\sigma_{\Delta n}$ versus forecast lifted indices for all turbulence event locations during the 2002 flight experiments.

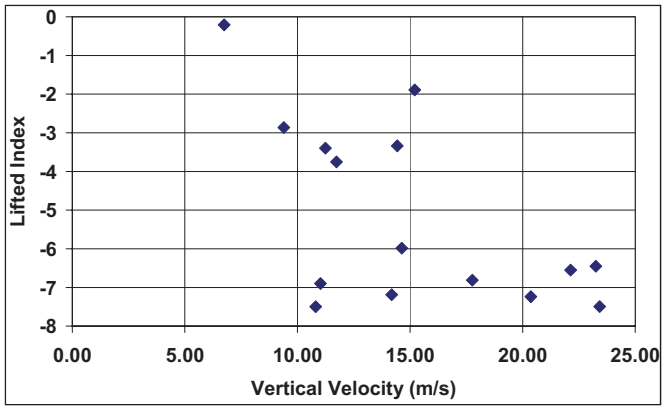

Figure 138. Same as Figure 137 but for vertical velocity versus lifted index (LI).

6. Summary and Conclusions

Flight tests of NASA's Turbulence Prediction And Warning System were conducted in the Fall of 2000 and Spring of 2002. Flight experiments were conducted to evaluate technologies that would allow the detection and alerting for hazardous turbulence in convective environments. During twelve flights, NASA's B-757 tallied fifty three encounters with convectively induced turbulence. These flights, avoided regions containing high levels of radar reflectivity (> 40 *dBz*) as is routine for commercial aircraft. Turbulence was often experienced when flying within convection and associated precipitation, while smooth conditions were typically encountered when flying outside of these regions. In general, the largest turbulence loads were encountered at the interfaces between updrafts and downdrafts. Continuous loads on the aircraft were experienced while flying within updrafts and downdrafts.

The ATDS research system performed to specified FAA standards by detecting 80% of the events at least 30 seconds prior to the encounter during the ARIES flights. In several cases the ATDS exceeded the FAA recommended performance standards by alerting to hazardous turbulence in environments with radar reflectivity levels below 15 *dBz*. In all events, radar reflectivity levels were moderate or low (< 40 *dBz*), and at times, lower than the aircraft's radar display threshold (< 20 *dBz*). Furthermore, turbulence intensities were weakly correlated with radar reflectivity levels indicating that the level of reflectivity is not always a good measure of the turbulence threat associated with convection. Strong turbulence events were encountered with as little as 0 *dBz* radar reflectivity.

In the context of developing requirements for an alerting protocol, the ATDS made predictions of aircraft turbulence loads from the along-beam component of air motion detected with airborne Doppler radar. This was verified by

analyses showing that the peak standard deviations in the vertical wind were typically located within 2 *km* of the peak variance in the along-path wind measured by the *in situ* sensor.

Comparisons between NEXRAD and airborne radar data show conclusively that the airborne tool is critical for tactical avoidance of (or preparation for) a turbulence encounter. However, for aircraft not equipped with PWS, more analysis should be conducted to examine how uplinked NEXRAD products may provide benefit in avoiding hazardous CIT.

In the context of turbulence forecasting to support strategic avoidance, the strongest events were associated with convection triggered in regions of high convective instability as indicated by forecasted lifted indices. Therefore, this and other convective forecast indices should be considered as predictors of turbulence intensities associated with CIT.

The meteorological factors that caused the turbulence during the NASA flight campaign are common in the atmosphere, and similar condition could have contributed to previous turbulence accidents. In several cases, severe turbulence PIREPS were issued from commercial aircraft in the vicinity of the NASA flights. In some of the flights that encountered isolated convective cells, turbulence avoidance would not be an issue for commercial aircraft since alternate paths were easily identified. However, the isolated storms served as a test bed for obtaining data to validate the ATDS prediction capability. Similarities between the NASA flight experiments and reported turbulence accident accounts are as follows:

1) Event duration was typically less than 30 seconds and coincided with time spent within the cloud.
2) Consistent with many pilot reports, turbulence events occurred inside cloudy regions where radar reflectivity levels were often weak enough to be below the threshold on the aircraft's radar display (< 20 *dBz*). Intensity of the turbulence encounter was not correlated with the magnitude of radar reflectivity factor.
3) The most severe events occurred within the sharp gradient between a strong updraft and a downwind downdraft.
4) Rapidly rising cloud tops and intense convective updrafts were associated with most of the turbulence events.
5) CIT may occur within environments that are unfavorable for CAT.

As demonstrated in at least one of the NASA flights (Flight 232), unexpected encounters with turbulence can occur in IMC conditions (such as within areas of poor visibility due to anvil outflow and cloud blow-off) and where radar reflectivity is weak. However, alerts provided by an ATDS could potentially provide warnings that would reduce injuries and costs in those circumstances.

Acknowledgements

We would like to thank Dr. Roland Bowles (retired NASA) for his many ideas, motivation, and stimulating discussions. Also, we would like to thank the NASA TPAWS element lead, Mr. James Watson (now retired), whose leadership facilitated the successful outcome of the TPAWS project. Many thanks to Ed Johnson, Neil O'Connor, Randy Vanvalkenburg, and other NASA reviewers for their comments and suggestions. The airborne radar reflectivity and hazard plots were generated by NCAR as a deliverable under NASA contract NAS1-02056.

References

Ahmad, N.N., and Proctor, F.H., 2011: Large Eddy Simulations of Severe Convection Induced Turbulence. AIAA 2011-3201.

Benjamin, S.G., Grell, G.A., Brown, J.M., Brundage, K.J., Devenyi, D., Kim, D., Schwartz, B., Smirnova, T.G., Smith, T.L., Weygandt, S.S., and Manikin, G.A., 2000: The 20-km Version of the Rapid Update Cycle. *Preprints, 9th Conerence. on Aviation, Range, and Aerospace Meteorology,* Amer. Meteor. Soc., Orlando, Florida, September 2000, pp. 421-423.

Bowles, R.L., and Buck, B., 2009: A Methodology for Determining Statistical Performance Compliance for Airborne Doppler Radar with Forward-Looking Turbulence Detection Capability. NASA CR 2009-215769.

Brewster, K.A., 1984: Kinetic Energy Evolution in a Developing Severe Thunderstorm. Master's Thesis, University of Oklahoma, Norman OK.

Cornman, L.B., Williams, J.K., and Goodrich, R.K., 2000: The detection of Convective Turbulence Using Airborne Doppler Radars. *Proceedings of the 9th Conference on Aviation, Range, and Aerospace Meteorology*, Orlando, Florida, September 2000, pp. 569-574.

Cornman, L.B., Gerding, S., Maymaris, G. and Williams, J., 2002: Evaluation of an Airborne Radar Turbulence Detection Algorithm. *Preprints, 10th Conference on Aviation, Range, and Aerospace Meteorology, Amer. Meteor. Soc.*, Portland, Oregon, May 2002, pp. 237-240.

Doviak, R.J. and Lee, J.T., 1985: Radar for Storm Forecasting and Weather Hazard Warning. *J. Aircraft*, **22**, 1059-1063.

Georgia Tech Research Institute, 2004: Development and Implementation of Automated Scoring Algorithm. *Contract NAS1-02056*, Prepared for NASA Langley Research Center, January 29, 2004. 102 pp.

Hamilton, D.W., and Proctor, F.H., 2002a: Meteorology Associated with Turbulence Encounters During NASA's Fall-2000 Flight Experiments. AIAA 2002-0943.

Hamilton, D.W., and Proctor, F.H., 2002b: Convectively Induced Turbulence Encounters During NASA's Fall 2000 Flight Experiments. *Preprints, 10th Conference on Aviation, Range, and Aerospace Meteorology, Amer. Meteor. Soc.*, Portland, Oregon, May 2002, pp. 371-374.

Hamilton, D.W., and Proctor, F.H., 2003: An Aircraft Encounter with Turbulence in the Vicinity of a Thunderstorm. AIAA 2003-4075.

Hamilton, D.W., and Proctor, F.H., 2006a: Progress in the Development of an Airborne Turbulence Detection System. *12th Conference on Aviation Range and Aerospace Meteorology*, Amer. Meteor. Soc., Atlanta, Georgia, Paper 6.5, January 2006, 9 pp.

Hamilton, D.W., Proctor, F.H., 2006b: Airborne Turbulence Detection System Certification Tool Set. AIAA 2006-75.

Kaplan, M.L., Charney, J.J., Waight, III, K.T., Lux, K.M., Cetola, J.D., Huffman, A.W., Slusser, S.D., Riordan, A.J., and Lin, Y-L., 2006: Characterizing the Severe Turbulence Environments Associated with Commercial Aviation Accidents. A Real-Time Turbulence Model (RTTM) Designed for the Operational Prediction of Moderate-Severe Aviation Turbulence Environments. *Meteorology and Atmospheric Physics*, **94**, 235-270.

Kaplan, M.L., Huffman, A.W., Lux, K.M., Charney, J.J., Riordan, A.J., and Lin, Y.-L., 2005: Characterizing the Severe Turbulence Environments Associated With Commercial Aviation Accidents---Part I: 44 Case Study Synoptic Observational Analyses. *Meteorology and Atmospheric Physics*, **88**, 129-152.

Kaplan, M.L., Lin, Y-L., Charney, J.J., Pfeiffer, K.D., DeCroix, D.S., and Weglarz, R.P., 2000: A Terminal Area PBL Prediction System at Dallas-Fort Worth and its Application in Simulating Diurnal PBL Jets. *Bull. Amer. Meteor. Soc.,* **81**, 2179-2204.

Kauffmann, P., 2002: The Business Case for Turbulence Sensing Systems in the US Air Transport Sector. *J. Air Transport Management*, **8**, 99-107.

Maddox, R.A., Zhang, J., Gourley, J.J., and Howard, K.W., 2002: Weather Radar Coverage Over the Contiguous United States. *Weather Forecasting*, **17**, 927-934.

NTSB, 2011: Review of U.S. Civil Aviation Accidents, 2007-2009. National Transportation Board, Report NTSB/ARA-11/01, 59 pp.

Nutter, P.A., and Manobianco, J., 1999: Evaluation of the 29 km ETA Model. Part I: Objective Verification at Three Selective Stations. *Weather Forecasting*, **14**, 5-17.

Pantley, K.C., 1989: *Turbulence Near Thunderstorm Tops*, M.S. thesis, Department of Meteorology, San Jose State University, 132 pp.

Press, H., and Binckley, E.T. 1948: A Preliminary Evaluation of the Use of Ground Radar for the Avoidance of Turbulent Clouds. NACA TN 1684.

Proctor, F.H., and Hamilton, D.W., 2005: Hazard Metric Unification. Weather Accident Prevention Review, NASA's Aviation Safety and Security Program, Williamsburg, VA, September 2005 (attached to appendix)

Proctor, F.H., Hamilton, D.W., and Bowles, R.L., 2002a: Numerical Study of a Convective Turbulence Encounter. AIAA-2002-0944.

Proctor, F.H., Hamilton, D.W., and Bowles, R.L., 2002b: Numerical Simulation of a Convective Turbulence Event. *Preprints, 10th Conference on Aviation, Range, and Aerospace Meteorology*, *Amer. Meteor. Soc.,* Portland, Oregon, May 2002, pp. 41-44.

Robinson, P.A. Buck, B.K., Bowles, R.L., Boyd, D.L.B., and Cornman, L.B., 2000: Optimization of the NCAR In Situ Turbulence Measurement Algorithm. AIAA 2000-0492.

Rogers, E., Black, T.L., Deaven, D.G., and DiMego, G.J., 1996: Changes to the Operational "Early" ETA Analysis/Forecast System at the National Centers for Environmental Prediction. *Weather and Forecasting*, **11**, 391-403.

Steiner, R. and Rhyne, R.H., 1962: Some Measured Characteristics of Severe Storm Turbulence. National Severe Storm Project Report No. 10, 17 pp.

Thompson, J.K. and Lipscomb, V.W., 1949: An Evaluation of the Use of Ground Radar for Avoiding Severe Turbulence Associated with Thunderstorms. NACA TN 1960, 10 pp.

Tvaryanas A.P., 2003: Epidemiology of Turbulence-related Injuries in Airline Cabin Crew, 1992–2001, *Aviation Space Environ Med*, **74**, 970–976.

Wusk, M.S., 2002: ARIES: NASA Langley's Airborne Research Facility, AIAA 2002-5822.

Appendix: Hazard Metric Unification

HAZARD METRIC UNIFICATION

Fred Proctor and David Hamilton

NASA Langley Research Center

Presented at:
NASA's WxAP Annual Review
Williamsburg, VA
September 20-21, 2005

Proctor/Hamilton

ABSTRACT

The intensity of the atmospheric turbulence can be characterized by many parameters (i.e., turbulence kinetic energy, turbulence eddy dissipation rate, velocity variance, turbulence integral length scale, etc). However, 1) it is difficult to characterize atmospheric turbulence with the use of just one parameter and more importantly, 2) these parameters cannot be easily related to the influence that turbulence has on aircraft response.

Two metrics for quantifying turbulence intensity in the context of aviation safety are at the forefront of current debate; the eddy dissipation rate (EDR) of the atmospheric turbulence and the root mean square (RMS) of the aircraft's normal acceleration. This presentation will describe each of the two metrics and discuss the merits and disadvantages of each. A recommendation of the preferred metric will be given based on its intended function.

Proctor/Hamilton

Motivation

- To provide a recommendation for the best turbulence hazard metric given its intended function

Proctor/Hamilton

OUTLINE

- Definition of Turbulence
- Aircraft Response to Turbulence
- Hazard Metric
  - RMS Normal Load
  - Eddy Dissipation Rate
  - Aircraft Centric or Atmospheric Centric
- Advantages and Disadvantages of Each Metric
- Summary and Recommendations

Proctor/Hamilton

Definition: Atmospheric Turbulence

- According to Stull, airflow or wind, can be divided into three broad categories:
  - Mean wind
  - Waves
  - Turbulence
- Turbulence in the atmosphere is often defined as the deviation of fluid velocity from some mean, where the mean is determined from either a fixed time or space interval
- The intensity of the atmospheric turbulence can be characterized by many parameters (i.e., turbulence kinetic energy, velocity variance, turbulence eddy dissipation rate, turbulence integral length scale, etc)

Proctor/Hamilton

Aircraft Response To Turbulence

- Aircraft flying through such a perturbed flow field will respond depending upon the fluid scale of motion, aircraft type, altitude, air speed, and weight.
- Different aircraft may respond dissimilarly to the same turbulence field.
- Aircraft only respond to a specific range of turbulence scales. Small (λ<40*m*) and very large scales of motion (λ>4000*m*) impart negligible accelerations on the aircraft.

Proctor/Hamilton

Aircraft Response

Cumulative distribution of normalized aircraft loads as a function of wave number. Aircraft calculation based on B-757-200 frequency domain model. Assumes von Karman turbulence spectrum with an outer scale of 300 m and σ_w=1 m/s. (provided by Roland Bowles)

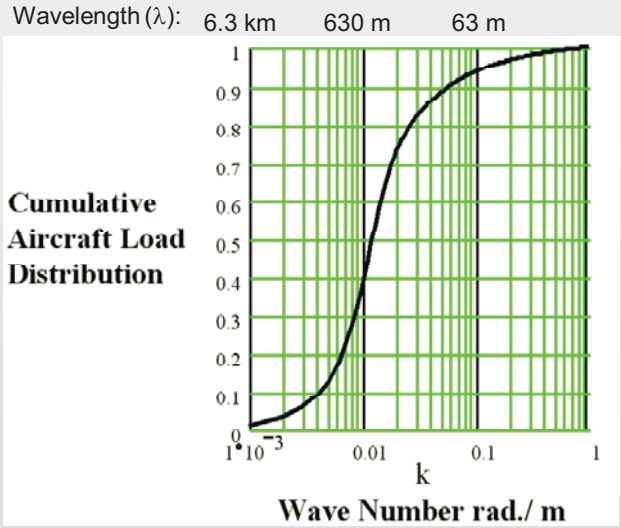

Proctor/Hamilton

Idealized Encounter with Turbulence

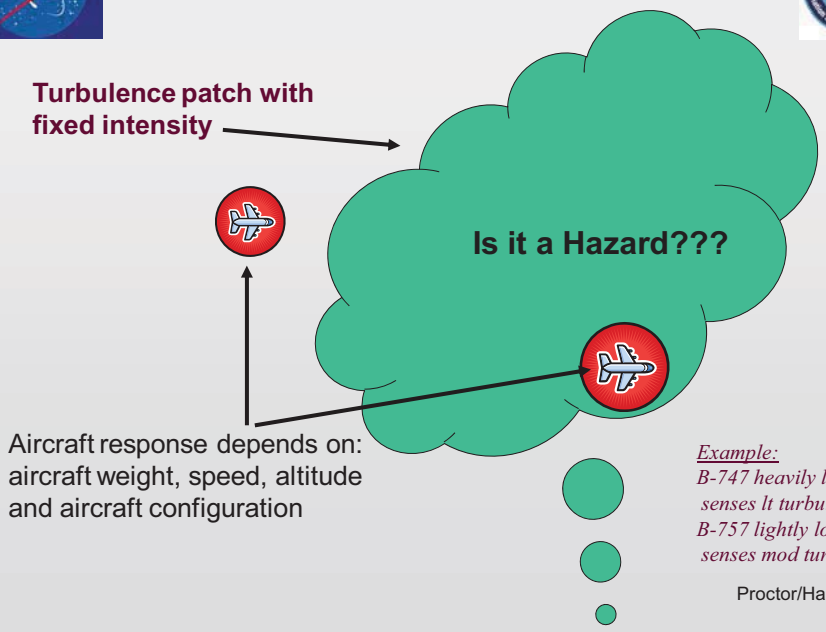

Example:
B-747 heavily loaded senses lt turbulence
B-757 lightly loaded senses mod turbulence

Proctor/Hamilton

Hazard Metric

- Issues of Debate
  - Aircraft Centric or
  - Atmospheric Centric
- Metrics
  - Root Mean Square (RMS) of Aircraft Normal Load
  - Eddy Dissipation Rate (EDR)
- Choice depends on if one wants to characterize the atmospheric turbulence conditions, or does one wish to characterize the turbulence effect on the aircraft?

Proctor/Hamilton

RMS Normal Load

- The root mean square of the aircraft's normal acceleration represents the "turbulence" response of an aircraft to turbulent air motions
  - statistically quantifies the sharp bumps and accelerations that passengers feel when flying in an aircraft
  - simple to calculate from direct measurements available from the aircraft's accelerometers
  - assumes a 5 second window

Proctor/Hamilton

Correlation of Peak Load With Peak RMS Load (5 sec. window)

Based on Measurements for 291Turbulence Encounter Cases

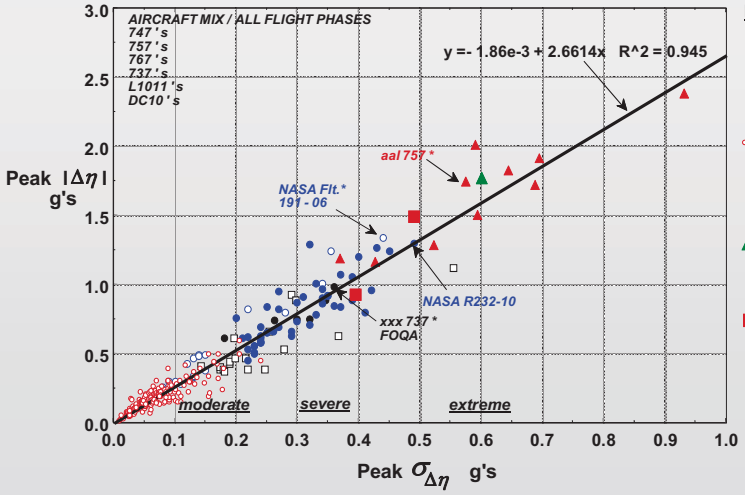

DATA SOURCES

- 6 FOQA Incidents
- 18 ICAO Events
- 49 NASA EVENTS (02)
- 18 NASA EVENTS (00)
- 10 NTSB Accidents
- Delta (184 events)

* Cases Chosen for Detail Modeling to Support FAA Radar Certification Effort

UAL 747 Pacific Accident

two recent events

REGRESSION

ESTIMATED FROM RADAR OBSERVABLES FOR TPAWS CONCEPT

Bowles

The Eddy Dissipation Rate (EDR)

- EDR attempts to quantitatively describe the rate at which turbulence energy is transferred from large to small scales of turbulence where it is then damped by molecular viscosity and irreversibly converted into heat
- EDR is not directly measurable, but must be inferred
  - more than one method for deriving EDR, each of which may provide very different values for an identical turbulence field
  - in the calculation of EDR, assumptions are often invoked which include homogeneity, isotropy, and the existence of an inertial subrange of turbulence scales

Proctor/Hamilton

Aircraft Centric or Atmospheric Centric?

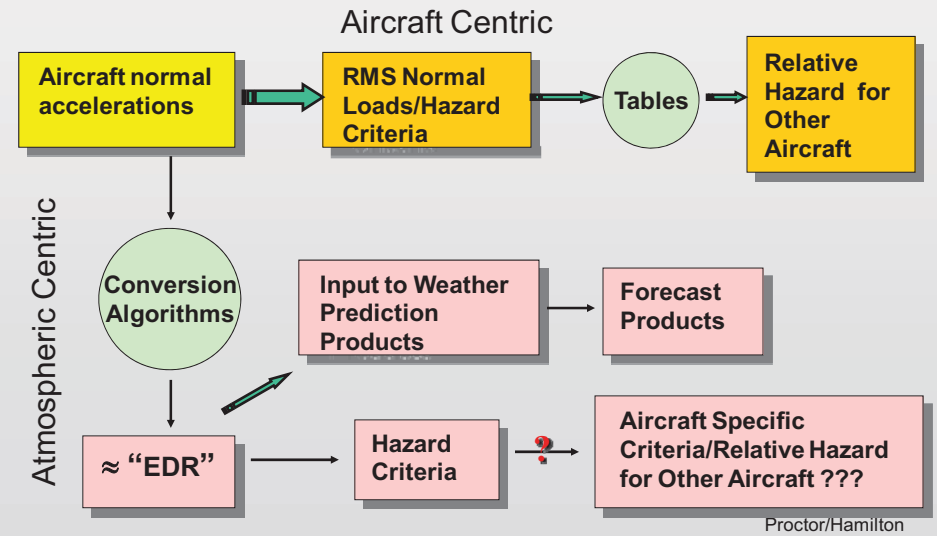

Proctor/Hamilton

Advantages of EDR

- EDR can be an acceptable parameter in quantifying the properties of turbulent fluid flow under certain validated assumptions
- EDR can provide an estimate for the intensity of atmospheric turbulence
- Aircraft reports of EDR can be used to initiate weather forecast turbulence products
- Knowing the EDR of the atmosphere could be useful in other applications unrelated to flight turbulence (i.e. weather forecasting, wake separation, and air pollution dispersion)

Proctor/Hamilton

Can aircraft response be determined from EDR?

Each of these three spectra have same EDR. However, they have different turbulence outer length scales

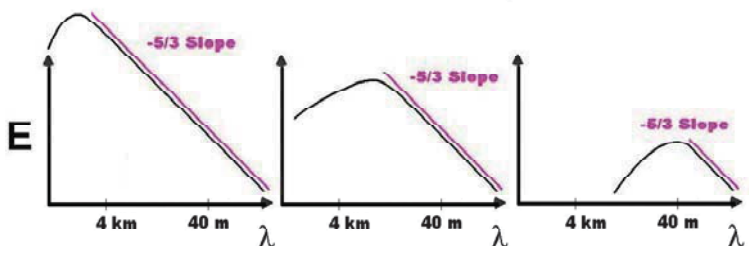

Strong → Weak

Aircraft Response

Proctor/Hamilton

Types of Flow

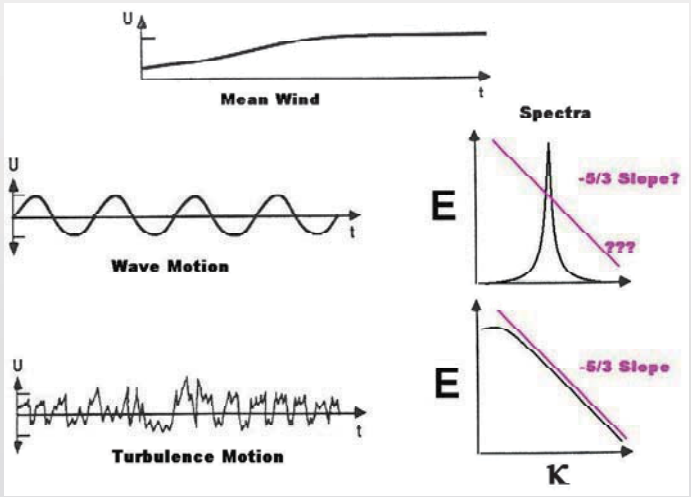

Proctor/Hamilton

Disadvantages of using EDR

- EDR cannot be directly calculated or measured and must be inferred.
- There is no standard method for estimating EDR.
- How do you verify?
- Certain assumptions are required (isotropy, homogeneity, steady state turbulence) for the calculation of EDR to be theoretically valid. Furthermore, knowledge of the turbulence outer scale is critical for estimating EDR. (i.e. data must resolve the inertial subrange).
- A large sample of data is required to calculate EDR. Many have found ranges between 5 and 15 minutes is required for stable estimation. In this amount of time, some aircraft may have traveled up to 120 *nmiles.*
- Input data sampling frequency may dramatically affect the value of calculated EDR.
- Averaging time/space can significantly affect the value of calculated EDR, i.e. a large sample of data is necessary for providing a stable output of EDR.

Proctor/Hamilton

Disadvantages of using EDR (continued)

- Even if a turbulence patch is correctly characterized with an appropriate value for EDR, aircraft will respond dissimilarly as they penetrate this patch.
  - Therefore, a formulation is required to determine the relationship between EDR and aircraft turbulence response, i.e. light, moderate, or severe.
  - Although theory exists to convert an EDR estimate to a load estimate, there are several assumptions that are needed to be made; turbulence length scale, aircraft response function, limits of integration, and correction factors. Also required for conversion are parameters such as aircraft type, weight, altitude, and airspeed. The accuracy of this conversion has not yet been established.

Proctor/Hamilton

Advantages of RMS Normal Load

- The normal load metric is a direct calculation from measured aircraft response.
- Simple to implement because it is calculated from direct measurement.
- The normal load metric confidently quantifies the hazard imposed from the turbulence encounter upon the aircraft and its passengers.
- Transfer functions exist that allow for conversion of normal loads from one aircraft to another. For example, if two dissimilar aircraft encounter the same turbulence field, the normal load can be predicted for the following aircraft based on the normal load sensed by the preceding aircraft. This conversion is determined from known aircraft characteristics.
- Aircraft manufacturers, operators, and maintenance personnel understand the consequences of normal loads upon aircraft. Also, aircraft design limitation is usually expressed in terms of normal loads.
- The FAA has provided guidelines for reporting turbulence duration and intensity regarding the turbulence impact upon aircraft and passengers. These guidelines are consistent with the intended function of the normal load metric.
- An operational system based on the normal load metric has been demonstrated during the TPAWS program.

Proctor/Hamilton

Disadvantages of RMS Normal Load

- Does not directly relate to conventional fluid metrics that characterize the intensity of the atmospheric turbulence (i.e., turbulence kinetic energy, turbulence eddy dissipation rate, turbulence integral length scale, etc)
  - However, this is usually not a concern to passenger and aircraft safety
- Not clear how this could be used to initialize NWS turbulence forecast products

Proctor/Hamilton

Summary and Recommendations

- **Based on our study to determine the most appropriate turbulence metric for application to flight safety, the normal load metric is the most preferred**
  - **metric is aircraft centric**
  - **relatively easy to deduce from standard flight systems**
  - **this metric is understood by the aircraft operators**
  - **operationally tested**

Proctor/Hamilton

REPORT DOCUMENTATION PAGE

Form Approved
OMB No. 0704-0188

1. REPORT DATE *(DD-MM-YYYY)*	2. REPORT TYPE	3. DATES COVERED *(From - To)*
01- 02 - 2012	Technical Memorandum	

4. TITLE AND SUBTITLE

Flight Tests of the Turbulence Prediciton and Warning System (TPAWS)

5a. CONTRACT NUMBER

5b. GRANT NUMBER

5c. PROGRAM ELEMENT NUMBER

6. AUTHOR(S)

Hamilton, David W.; Proctor, Fred H.; Ahmad, Nash'at N.

5d. PROJECT NUMBER

5e. TASK NUMBER

5f. WORK UNIT NUMBER

411931.02.61.07.02

7. PERFORMING ORGANIZATION NAME(S) AND ADDRESS(ES)

NASA Langley Research Center
Hampton, VA 23681-2199

8. PERFORMING ORGANIZATION REPORT NUMBER

L-20125

9. SPONSORING/MONITORING AGENCY NAME(S) AND ADDRESS(ES)

National Aeronautics and Space Administration
Washington, DC 20546-0001

10. SPONSOR/MONITOR'S ACRONYM(S)

NASA

11. SPONSOR/MONITOR'S REPORT NUMBER(S)

NASA/TM-2012-217337

12. DISTRIBUTION/AVAILABILITY STATEMENT

Unclassified - Unlimited
Subject Category 03
Availability: NASA CASI (443) 757-5802

13. SUPPLEMENTARY NOTES

David Hamilton is currently with WeatherPredict Consulting, Inc., Raleigh, NC.

14. ABSTRACT

Flight tests of the National Aeronautics and Space Administration's Turbulence Prediction And Warning System (TPAWS) were conducted in the Fall of 2000 and Spring of 2002. TPAWS is a radar-based airborne turbulence detection system. During twelve flights, NASA's B-757 tallied 53 encounters with convectively induced turbulence. Analysis of data collected during 49 encounters in the Spring of 2002 showed that the TPAWS Airborne Turbulence Detection System (ATDS) successfully detected 80% of the events at least 30 seconds prior to the encounter, achieving FAA recommended performance criteria. Details of the flights, the prevailing weather conditions, and each of the turbulence events are presented in this report. Sensor and environmental characterizations are also provided.

15. SUBJECT TERMS

TPAWS; detection; flight test; warning system

16. SECURITY CLASSIFICATION OF:			17. LIMITATION OF ABSTRACT	18. NUMBER OF PAGES	19a. NAME OF RESPONSIBLE PERSON
a. REPORT	b. ABSTRACT	c. THIS PAGE			STI Help Desk (email: help@sti.nasa.gov)
					19b. TELEPHONE NUMBER *(Include area code)*
U	U	U	UU	152	(443) 757-5802